

DISS. ETH NO. 27297

Highly selective flame-aerosol-made gas sensors enabled by particle-based filters

A thesis submitted to attain the degree of
DOCTOR OF SCIENCES of ETH ZURICH
(Dr. sc. ETH Zurich)

presented by
JAN VAN DEN BROEK
MSc ETH Zurich

born on 16.09.1990
citizen of
Weggis, Lucerne, Switzerland

accepted on the recommendations of
Prof. Dr. Sotiris E. Pratsinis, examiner
Prof. Dr. Christopher A. Mayhew, co-examiner

2021

Acknowledgements

First and foremost, I am grateful to my supervisor Prof. Dr. Sotiris E. Pratsinis for his continuous encouragement and support. With his always critical, but constructive, advice, he was a true mentor that guided me during the past years to become the researcher I am today. I would also like to thank Prof. Dr. Christopher A. Mayhew for stimulating discussions and co-examining this thesis.

This work was performed at the Particle Technology Laboratory (PTL) at ETH Zürich, and I would like to thank all its members and students for the great atmosphere and their hospitality. Special thanks go to Dr. Andreas Güntner, leader of the sensor team whose vision convinced me to start this Ph.D. Without his continuous support and motivation, this work could not have been achieved. It was a great pleasure to be part of the sensor team and I am thankful to all its past and present members, including Nicolay Pineau, Sebastian Abegg and Ines Weber for the phenomenal scientific collaborations and camaraderie.

Additionally, I like to thank René Pluss for his always helping hand with technical problems, and Dr. med. Philipp Gerber and Nina Derron from the Department of Endocrinology, Diabetes, and Clinical Nutrition at the University Hospital Zürich for their professional help with ethics approvals and human testing.

I am deeply grateful to all bachelor and master students that choose to do their project with me or supported me as assistants: Sebastian Keller, Dario Bischof, Leandro Magro, David Klein Cerrejon, Noah Codoni and Amy Wang Chang Ting. They all significantly contributed to this work.

Financial support by the Swiss National Science Foundation (SNF 200020_175754 and 206021_170729) is gratefully acknowledged.

To my family, particularly my parents, thank you for your love, continuous support and faith in me. Above all, I thank my wife Xue for her unwavering and unconditional love. Thank you for always believing in me and the endless joy you bring to my life.

Contents

Acknowledgements	i
Contents	iii
Summary	vii
Zusammenfassung	xi
1 Highly selective gas sensing enabled by filters	1
1.1 Introduction.....	2
1.2 Sorption filters	5
1.2.1 Definitions & principles.....	5
1.2.2 Adsorbent materials & properties.....	7
1.2.3 Analyte separation in time.....	10
1.3 Size-selective filters	14
1.3.1 Definitions & principles.....	14
1.3.2 Pore-size control	15
1.3.3 Filter configuration	19
1.4 Catalytic filters.....	22
1.4.1 Definitions & principles.....	22
1.4.2 Tailored selectivity	23
1.4.3 Filter configuration	27
1.5 References	31
2 Highly selective and rapid breath isoprene sensing enabled by activated alumina filter	43
2.1 Introduction.....	44
2.2 Experimental.....	46
2.2.1 Sensor fabrication	46
2.2.2 Filter fabrication	46
2.2.3 Gas evaluation	47
2.3 Results and discussion.....	48
2.3.1 Filter effect on isoprene selectivity.....	48
2.3.2 Separation mechanism	49
2.3.3 Gas mixtures.....	50
2.3.4 Low-ppb isoprene detection	51
2.3.5 Operational stability with simulated breath	52
2.4 Conclusions.....	53
2.5 References	54
3 Highly selective detection of methanol over ethanol by a handheld gas sensor	57
3.1 Introduction.....	58
3.2 Experimental.....	60
3.2.1 Sensor fabrication	60
3.2.2 Separation column fabrication.....	60

3.2.3	Gas evaluation	61
3.2.4	Evaluation of the headspace of drinks and human breath.....	63
3.3	Results and discussions	63
3.3.1	Detector design	63
3.3.2	Selective methanol detection.....	64
3.3.3	Dynamic range.....	66
3.3.4	High ethanol background	67
3.3.5	Methanol-spiked liquor and breath	69
3.4	Conclusions.....	72
3.5	References	73
4	Screening methanol poisoning with a portable breath detector	77
4.1	Introduction.....	78
4.2	Experimental.....	80
4.2.1	Detector design and measurement	80
4.2.2	Study design	81
4.2.3	Breath sampling and methanol spiking.....	82
4.2.4	Statistical analysis.....	83
4.3	Results and discussions	83
4.3.1	Selective methanol over ethanol detection.....	83
4.3.2	Breath methanol quantification and intra-sample repeatability.....	85
4.3.3	Agreement to PTR-TOF-MS and diagnostic capability	87
4.4	Conclusions.....	90
4.5	References	91
5	Selective formaldehyde detection at ppb in indoor air with a portable sensor	95
5.1	Introduction.....	96
5.2	Experimental.....	98
5.2.1	Microsensor & column fabrication.....	98
5.2.2	Characterization.....	99
5.2.3	Gas evaluation	99
5.2.4	Wood product emission testing	100
5.2.5	Indoor air testing.....	101
5.2.6	PTR-TOF-MS validation	101
5.3	Results and discussion.....	102
5.3.1	Detector design	102
5.3.2	Selectivity and lower detection limit	103
5.3.3	Formaldehyde emissions from wood products.....	105
5.3.4	Indoor air measurements	107
5.4	Conclusions.....	109
5.5	References	109
6	Research Recommendations	113
6.1	References	116
A	A pocket-sized device enables detection of methanol adulteration in alcoholic beverages	117
A.1	Introduction.....	118
A.2	Results and discussion.....	119

A.3	Methods	121
A.4	Supplementary Methods.....	123
A.4.1	Column design.....	123
A.4.2	Sensor design.....	123
A.4.3	PCB design.....	123
A.4.4	Sample preparation and analysis	124
A.4.5	Calibrations	125
A.5	Supplementary Discussion	125
A.5.1	Sensor design and detection concept	125
A.5.2	Selective methanol and ethanol detection in laboratory mixtures.....	126
A.5.3	Comparison to state-of-the-art methanol sensors	128
A.5.4	Beer with various methanol contents.....	128
A.5.5	Wines from five continents	128
A.5.6	Response analysis of pure and methanol-spiked pear spirit.....	129
A.6	Supplementary Figures.....	130
A.7	References	137
B	Supplementary Data Chapter 2: Highly selective and rapid breath isoprene sensing enabled by activated alumina filter	139
B.1	Full sensor responses with filter	139
B.2	Filter characterization at different loadings.....	140
B.3	Effect of relative humidity.....	140
B.4	Filter validation by PTR-TOF-MS.....	141
B.5	Sensor operational stability	141
C	Supplementary Data Chapter 3: Highly selective detection of methanol over ethanol by a handheld gas sensor	143
C.1	Effect of temperature and relative humidity.....	143
C.2	Methanol detection with high ethanol interference.....	144
C.3	Regeneration after liquor and breath sampling.....	144
C.4	Operational stability in ambient air.....	145
D	Supplementary Data Chapter 4: Rapid diagnosis of methanol poisoning with a portable breath detector	147
D.1	Calculation of blood/breath concentrations.....	147
D.2	Physiological data of subjects.....	148
D.3	Analyte stability in Tedlar bags.....	149
D.4	Level of detection.....	149
D.5	Measured methanol and ethanol concentrations of all subjects.....	150
D.6	Weekly calibration	152
D.7	Relative Bland-Altman.....	152
E	Supplementary Data Chapter 5: Selective formaldehyde detection at ppb in indoor air with a portable sensor.....	153
E.1	Sensor baseline stability	153
E.2	Oriented strand board emission measurement.....	154
E.3	PTR-TOF-MS calibration for indoor air measurements	155
E.4	Retention times of relevant compounds	156
E.5	Validation of wood emission measurement.....	157

E.6	Sensor intra-sample repeatability.....	158
E.7	Validation of indoor air measurement.....	159
	Curriculum Vitae	161
	Publications and Presentations.....	162

Summary

Portable and inexpensive gas sensors are essential for the next generation of non-invasive medical diagnostics, smart air quality monitoring & control and food quality assessment. While state-of-the-art chemical gas sensors can detect molecules at very low parts-per-million or even billion (ppm/ppb) concentration, the major challenge remains in detecting them with high *selectivity*. Filters are an effective and versatile, though often unrecognized, route to overcome selectivity issues of sensors by exploiting additional molecular properties of analytes, such as their size, chemical reactivity or surface affinity. In this thesis, such filters based on packed particle beds are combined with flame-aerosol-made chemoresistive gas sensors, integrated into portable detectors and validated in the application.

Chapter 1 provides a tutorial for the material engineering of sorption, size-selective and catalytic filters. First, the underlying filter concepts and principles for analyte separation are introduced, making use of high surface area adsorbents, microporous materials and heterogeneous catalysts. Then, specific implementations of filters with sensors are presented, highlighting trends and critically comparing their performance. Emphasis is thereby placed on material design for targeted gas separation, portable device integration and performance in the application. Finally, research frontiers and opportunities for low-cost gas sensing systems in emerging applications are highlighted.

In chapter 2, a filter is presented enabling selective isoprene detection in breath. Isoprene is a promising breath marker for detection and monitoring of different photo- and physiological conditions such as high blood cholesterol. However, its detection in human breath with its hundreds of compounds is still challenging for chemical sensors. This is solved by a filter containing high surface area activated alumina that retains hydrophilic compounds in breath (e.g., ketones, alcohols, ammonia), while hydrophobic isoprene is not affected. Combined with a highly sensitive but non-specific Pt-doped SnO₂ sensor, isoprene is detected within 10 s down to 5 ppb at 90% relative humidity and without interference of breath-relevant acetone, ammonia, ethanol and methanol.

Chapter 3 presents a hydrophobic filter enabling highly selective detection of methanol over ethanol. Methanol consumption can cause blindness, organ failure or even death. However, currently no detector exists for quick screening of methanol-laced beverages or diagnosis of methanol poisoning by breath analysis as chemical sensors cannot distinguish

methanol from the much higher ethanol background. Here, this is enabled by a compact separation column (Tenax TA) that separates analytes as in gas chromatography, while a downstream chemoresistive gas sensor (Pd-doped SnO₂ nanoparticles) detects analytes sequentially, thus selectively. This way, methanol is measured within 2 min from 1 to 1,000 ppm without interference of much higher levels of hydrogen, acetone or ethanol (up to 62,000 ppm). As a proof-of-concept, the detector reliably measured methanol concentrations in methanol-spiked liquor and breath samples.

Methanol poisoning outbreaks after consumption of adulterated alcohol frequently overwhelm health care facilities in developing countries. Chapter 4 presents how the developed methanol detector can serve as a non-invasive and rapid diagnostic tool for methanol poisoning in breath. The detector was validated with methanol-spiked breath of 20 volunteers (105 breath samples) after consumption of alcoholic beverages. Thereby, spiked methanol concentrations were quantified accurately within 2 min in the full breath-relevant range (10–1,000 ppm) in excellent agreement ($R^2 = 0.966$) with benchtop mass spectrometry. This simple-in-use detector is a promising diagnostic tool for rapid screening of methanol poisoning, assessment of severity and monitoring of treatment. The methanol detector can also be used by consumers, distillers and law-enforcing authorities to easily screen methanol in alcoholic beverages. Appendix A presents the methanol detector fully integrated into a hand-sized, multi-use sensor–smartphone system for on-demand headspace analysis of beverages. Thereby, methanol concentrations above and below legal limits are accurately quantified in 89 pure and methanol-contaminated alcoholic drinks from 6 continents for 107 consecutive days.

Finally, the concept of the hydrophobic separation column is applied to other analytes in chapter 5. Formaldehyde is a carcinogenic indoor air pollutant emitted from wood-based furniture, building materials, paints and textiles. Yet, no low-cost sensor exists for on-site monitoring to fulfill stringent current and upcoming exposure guidelines. Here, an inexpensive and handheld formaldehyde detector with proven performance in real indoor air is presented. Selectivity is achieved by a compact separation column that separates formaldehyde from interferants present in ambient air. Downstream, a highly sensitive nanoparticle-based chemoresistive Pd-doped SnO₂ sensor detects formaldehyde in the relevant concentration range down to 5 ppb within 2 min. As a proof-of-concept, formaldehyde is measured in indoor air and from different wood product emissions, in excellent agreement ($R^2 > 0.98$) with high-resolution mass spectrometry.

Chemical sensors rarely leave the laboratories because they struggle to provide the required selectivity in the application. In this thesis, it is shown how filters can be combined

with state-of-the-art sensors to overcome these limitations. This immediately results into useful detectors with validated performance. Given the immense potential of filters, they will almost certainly play a pivotal role in the future development of advanced sensor systems with unprecedented selectivity.

Zusammenfassung

Tragbare und günstige Gassensoren sind essenziell für die nächste Generation von nicht-invasiver Medizinaldiagnostik, automatischer Raumluftüberwachung und Steuerung, sowie in der Nahrungsmittelkontrolle. Dabei können hochmoderne chemische Gassensoren heutzutage Gasmoleküle im extrem tiefen Konzentrationsbereich von nur einigen Molekülen pro Million oder gar Milliarde (ppm/ppb) detektieren. Die Herausforderung bleibt jedoch, bestimmte Moleküle *selektiv* in Gasgemischen mit hunderten von verschiedenen Komponenten zu detektieren. Filter stellen eine effektive und vielseitige, jedoch oft unerkannte, Methode dar, um Selektivitätslimitationen von Sensoren zu überwinden. Sie nutzen dabei zusätzliche Molekulareigenschaften von Molekülen aus, wie zum Beispiel deren Grösse, chemische Reaktivität oder Oberflächenaffinität. In dieser Arbeit werden solche Filter basierend auf Partikel-Packungen mit flammenhergestellten chemoresistiven Gassensoren kombiniert, in tragbare Detektoren integriert und in verschiedenen Applikationen validiert und getestet.

Kapitel 1 ist ein Leitfaden für die Materialentwicklung von Sorptions-, Grössenselektive- und katalytischen Filtern. Zuerst werden die zugrundeliegenden Filterkonzepte und Grundlagen zur Separation von Gasmolekülen unter Verwendung von Adsorber mit grosser Oberfläche, mikroporösen Materialien und heterogenen Katalysatoren eingeführt. Dann werden spezifische Umsetzungen von Filtern mit Sensoren vorgestellt, Trends aufgezeigt und deren Vor- und Nachteile kritisch verglichen. Der Fokus wird dabei auf das Materialdesign für gezielte Gasseparation, die tragbare Geräteintegration und deren Leistungsvermögen in der Anwendung gesetzt.

In Kapitel 2 wird ein Filter vorgestellt, der die selektive Detektion von Isopren im Atem ermöglicht. Isopren ist ein vielversprechender Atemmarker für verschiedene pathologische und physiologische Zustände wie zum Beispiel hohes Blut-Cholesterin. Jedoch war das Messen von Isopren mit chemischen Sensoren im menschlichen Atem mit hunderten von anderen Komponenten bisher nicht möglich. Dies wird hier durch einen Filter ermöglicht, welcher aus aktiviertem Aluminiumoxid mit grosser Oberfläche besteht. Der Filter hält hydrophile Atemkomponenten (z.B., Ketone, Alkohole, Ammoniak) zurück, während hydrophobes Isopren nicht beeinflusst wird. Kombiniert mit einem hochempfindlichen, aber nicht-selektiven, Pt-dotierten SnO₂ Gassensor wird Isopren damit innerhalb von 10 s bis auf 5 ppb bei 90% relativer

Luftfeuchtigkeit exakt detektiert, ohne Beeinträchtigung durch Azeton, Ammoniak, Ethanol und Methanol in atemrelevanten Konzentration.

Kapitel 3 stellt einen hydrophoben Filter vor, der das hochselektive Messen von Methanol in der Gegenwart von Ethanol ermöglicht. Die Einnahme von Methanol kann zu Erblindung, Organschäden oder sogar zum Tod führen. Zurzeit gibt es jedoch keinen Methanol-Sensor der schnelles Methanol-Screening in Getränken oder zur Diagnose einer Methanolvergiftung aus der Atemluft ermöglicht. Dies, weil chemische Sensoren Methanol nicht von Ethanol unterscheiden können. Dies wird hier durch eine kompakte Separationskolonne (Tenax TA) gelöst, welche Gasmoleküle wie in der Gaschromatographie auftrennt, während ein dahinterliegender chemoresistiver Gassensor (Pd-dotiertes SnO₂) die Gasmoleküle sequenziell, und dadurch selektiv, detektiert. Dadurch kann Methanol innert 2 min im Konzentrationsbereich von 1 bis 1'000 ppm gemessen werden, ohne Störung durch höhere Konzentrationen von Wasserstoff, Azeton oder Ethanol (bis zu 62'000 ppm). In einer Machbarkeitsstudie erkannte der Detektor dabei Methanolkonzentrationen präzise in vergiftetem Rum und Atem.

Ausbrüche von Methanolvergiftungen durch vergifteten Alkohol überwältigen regelmässig sanitäre Einrichtungen in Entwicklungsländern. Kapitel 4 befasst sich damit, wie der entwickelte Methanol-Detektor als schneller und nicht-invasiver Diagnostest zur Erkennung einer Methanolvergiftung im Atem dienen kann. Der Detektor wurde dabei mit Methanol-zugesetztem Atem von 20 Freiwilligen (105 Atemproben) nach Konsum von Alkohol validiert. Methanolkonzentrationen im relevanten Bereich (10–1'000 ppm) wurden dabei innert 2 min akkurat und in exzellenter Übereinstimmung ($R^2 = 0.966$) zum Massenspektrometer bestimmt. Dieser einfach anwendbare Detektor ist dadurch vielversprechend zur schnellen Diagnose einer Methanolvergiftung, zur Beurteilung des Vergiftungsgrades und zur Überwachung der Behandlung. Der Methanol-Detektor kann auch von Konsumenten, Schnapsbrenner und Vollzugsbehörden zum Aufspüren von Methanol in alkoholischen Getränken verwendet werden. Anhang A zeigt die Integration des Detektors in ein tragbares, batteriebetriebenes Messgerät zur Bestimmung von Methanol in Getränken. Dabei wurden Methanolkonzentration über und unter gesetzlichen Grenzen akkurat in 89 alkoholischen Getränken aus 6 Kontinenten während 107 aufeinanderfolgenden Tagen bestimmt.

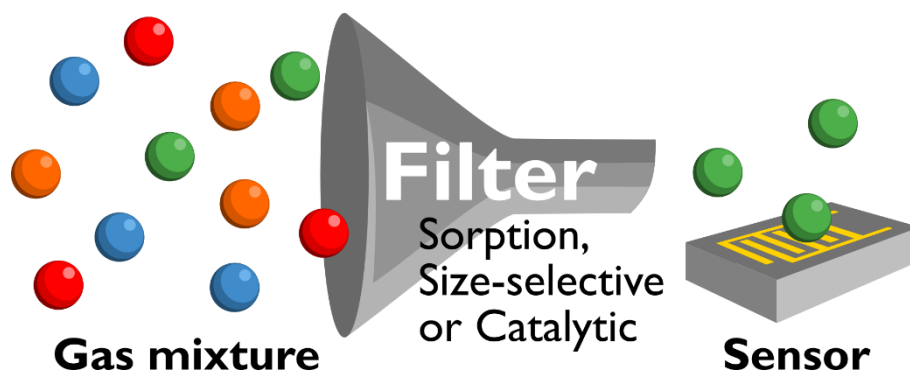
Zum Schluss wird in Kapitel 5 das Konzept einer hydrophoben Separationskolonne zur Detektion von weiteren Molekülen angewandt. Formaldehyd ist ein krebserregender Luftschadstoff der von Holzmöbeln, Baumaterialien, Farben und Textilien emittiert wird.

Jedoch gibt es keinen günstigen Sensor zur Formaldehyd-Überwachung vor Ort, um strikte bestehende und bevorstehende Emissionsrichtlinien einzuhalten. Hierfür wurde ein günstiger und tragbarer Formaldehyd-Detektor entwickelt und in echter Innenraumluft getestet. Selektivität wird durch eine kompakte Separationskolonne erreicht, welche Formaldehyd von anderen Komponenten in Raumluft separiert. Stromabwärts wird Formaldehyd von einem hochsensiblen, nanopartikelbasierenden Pd-dotierten SnO₂ Sensor bis auf 5 ppb innert 2 min detektiert. Als Machbarkeitsstudie wurden Formaldehydemissionen in Raumluft und von verschiedenen Holzprodukten in exzellenter Übereinstimmung mit hochauflösender Massenspektrometrie bestimmt.

Chemische Sensoren verlassen selten die Laboratorien, da ihre Selektivität unzureichend für die Anwendung ist. In dieser Arbeit wird gezeigt, wie Filter mit hochmodernen Gassensoren kombiniert werden können, um dessen Selektivitätslimitationen zu überwinden. Dadurch resultieren sofort brauchbare Detektoren mit validierter Leistung. In Anbetracht des immensen Potentials von Filter werden diese mit Sicherheit eine zentrale Rolle in der zukünftigen Entwicklung von hochentwickelten Sensorsystemen mit ausgezeichneter Selektivität spielen.

Chapter 1

Highly selective gas sensing enabled by filters



Abstract

Portable and inexpensive gas sensors are essential for the next generation of non-invasive medical diagnostics, smart air quality monitoring & control, human search & rescue and food quality assessment to name a few of their immediate applications. Therein, analyte selectivity in complex gas mixtures like breath or indoor air remains the major challenge. Filters are an effective and versatile, though often unrecognized, route to overcome selectivity issues by exploiting additional properties of target analytes (e.g., molecular size and surface affinity) besides reactivity with the sensing material. This review provides a tutorial for the material engineering of sorption, size-selective and catalytic filters. Of specific interest are high surface area sorbents (e.g., activated carbon, silica gels and porous polymers) with tunable properties, microporous materials (e.g., zeolites and metal-organic frameworks) and heterogeneous catalysts, respectively. Emphasis is placed on material design for targeted gas separation, portable device integration and performance. Finally, research frontiers and opportunities for low-cost gas sensing systems in emerging applications are highlighted.

1.1 Introduction

Gas sensors allow modern electronic devices to smell their environment. By utilizing portable and inexpensive sensors, a multitude of promising applications¹ can be realized (Figure 1.1): Smart air quality control (indoor² and outdoor³) with distributed, interconnected or drone-borne sensors that communicate wirelessly chemical data in real-time to map toxic pollutants (e.g., formaldehyde,⁴ NO_x⁵ or CFC-11⁶); food quality assessment⁷ to monitor the production and distribution from plant growth (e.g., plant hormone ethylene⁸), regulate processing (e.g., acetic acid for aroma development in coffee⁹) and detect spoiling (e.g., ammonia for meat¹⁰) to minimize waste; non-invasive medical diagnostics by breath analysis¹¹ to detect diseases (e.g., cancer¹² or diabetes¹³) and monitor their progression, or personalized tracking of physiological data (e.g., dieting¹⁴ or exercise¹⁵); and in human search and rescue¹⁶ to assist first responders with robots capable to detect the unique human chemical signature¹⁷ similar to dogs (e.g., after earthquakes or avalanches¹⁸), just to highlight some.

For integration into electronic devices, gas sensors need to be compact, inexpensive and simple-in-use. Most importantly, they need to detect selectively volatile organic compounds (VOCs) and gases at low ppb to ppm (parts-per-billion/million by volume) concentrations in mixtures without interference over hundreds of others (e.g., >800 in breath¹⁹ or >250 in indoor air²⁰). State-of-the-art gas sensors (e.g., chemoresistive²¹ or optical²²) provide this sensitivity by making use of nanomaterials having high specific surface area (e.g., 5 ppb acetone at 90% relative humidity (RH) by leached nanostructured Pd/SnO₂²³ or sub-ppb detection of Cl₂ by nanoparticle-based liquid crystal sensors²⁴).

Most challenging, however, is selectivity, which can be tuned to some extent by material composition of single sensors including metastable phases,²⁵ solid solutions,²⁶ mixed oxides²⁷ or heterostructures with unique morphology (e.g., hollow nanofibers²⁸ or ordered macroporous oxides²⁹). For example, the epsilon phase of WO₃ (i.e., ϵ -WO₃) stabilized by Cr-doping showed some acetone selectivity (>6) to ethanol, methanol NO_x, NH₃ and CO.²⁵ Also, In₄Sn₃O₁₂ reacts selectively to formaldehyde,³⁰ Ti/ZnO to isoprene,³¹ Si/ α -MoO₃ to ammonia,³² or Ag/LaFeO₃ to methanol.³³ However, such selectivities are typically only moderate, apart rare exceptions exploiting unique analyte-sensor interactions (e.g., CuBr for ammonia³⁴ or WO₃ for NO₂³⁵). This is often not sufficient in applications where interferant concentrations may be orders of magnitude higher than the target analyte (e.g., <8 ppb carcinogenic³⁶ formaldehyde in indoor air with ~1,000 ppb CO background³⁷).

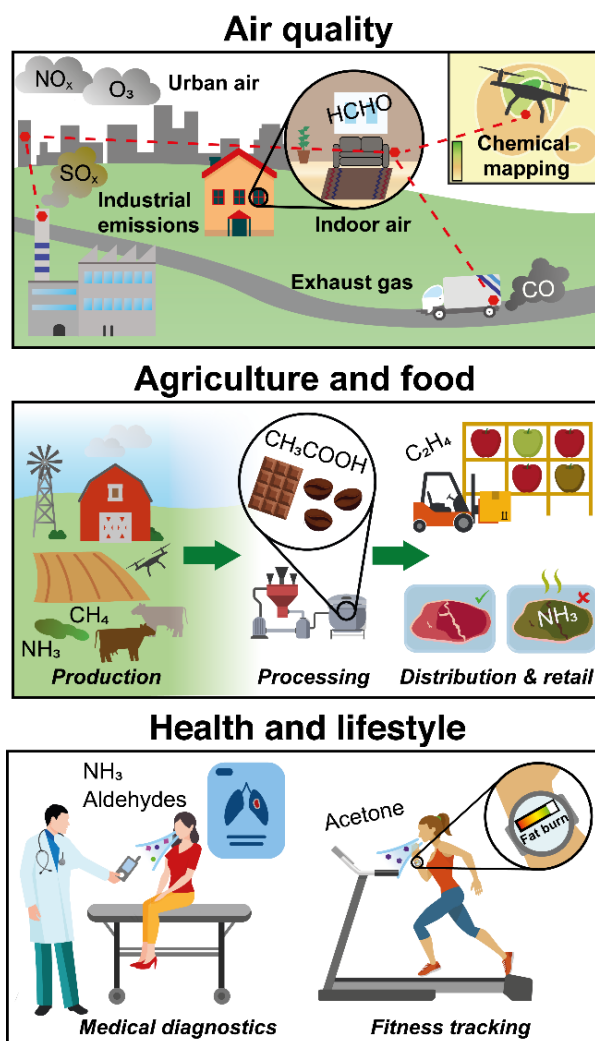


Figure 1.1: Compact and low-cost gas sensors in air quality monitoring, agriculture & food quality assessment and health & lifestyle applications.

To discriminate between analytes in gas mixtures, different sensors can also be combined to arrays (also called electronic noses or E-noses), overcoming selectivity limitations of single sensors.³⁸ Reviews on material design,³⁹ data processing algorithms⁴⁰ and applications (e.g., food quality and safety monitoring,⁴¹ or breath analysis⁴²) of sensor arrays address their potential. Generally, arrays process different sensor signals by statistical models to classify different odors. A variety of algorithms is used based on descriptive⁴³ (e.g., principle component analysis, hierarchical cluster analysis) and predictive methods⁴⁴ (e.g., artificial neural networks), often requiring a large set of data to “train” the models. Typically, arrays do not detect and discriminate specific analytes, but rather distinguish and classify analyte patterns (i.e., odors). For instance, a sensor array might differentiate lung cancer patients from healthy subjects⁴⁵ or distinguish different quality grades of Indian black tea⁴⁶. Thereby, often broadly sensitive sensors are used, making the array susceptible to overfitting and bogus correlations from confounders.⁴⁷ To discriminate multiple analytes and detect them with high accuracy in

gas mixtures, distinctly selective sensors, ideally with orthogonal features,⁴⁸ are most desirable for inclusion into arrays.

Filters represent a third approach to enhance the selectivity of gas sensors. They were first discussed in a review about selectivity in semiconductor gas sensors in 1987.⁴⁹ Since then, filters were treated only as a side aspect in many books and reviews of gas sensors in general,⁵⁰ gas sensor types (e.g., metal-oxide,⁵¹ arrays,⁵² zeolite,⁵³ metal-organic frameworks,⁵⁴ mesoporous materials,⁵⁵ combustible⁵⁶) and applications (e.g., environment, health and safety,⁵⁷ automotive,⁵⁸ explosives,⁵⁹ pollution,⁶⁰ indoor air quality,² health monitoring and disease diagnostic⁶¹). Placed either in front (e.g., packed beds) or directly on top (e.g., overlayers) of sensors, filters alter the composition and/or concentration of analytes in gas mixtures before reaching the sensor. In the ideal case, the target analyte is not affected while interferants are removed, resulting in high selectivity (>1,000) even with non-selective sensors.⁶² Already in 1980, a packed bed of zeolite 3A was tested to filter H₂S to selectively detect H₂ by a commercial SnO₂ sensor (Taguchi, Figaro).⁶² Also, SiO₂-covered SnO₂ sensors eliminated interference by CO, CH₄, ethanol and isobutane for selective H₂ detection,⁶³ charcoal and carbon cloth were used to protect CH₄ sensors from poisoning by siloxanes,⁶⁴ and zeolite 5A filters blocked H₂S and ethylene for selective CO detection.⁶⁵ Today, filters are well-established in most industrial sensors (e.g., CO⁶⁶ and CH₄⁶⁷ alarm sensors), however, their immense potential remains rather unexplored.

Only recently, filters were used to overcome selectivity issues of sensors for other, so far inaccessible, applications such as revealing methanol-adulterated liquors by separating methanol from ethanol in a packed bed sorption filter,⁶⁸ detecting H₂ leaks to fulfil, for the first time, stringent national standards by a polymer membrane on top of a plasmonic sensor,⁶⁹ and monitoring body fat burn from breath acetone by combusting interferants on a Pt/Al₂O₃ filter⁷⁰ preceding a Si/WO₃ sensor. Thereby, the distinct advantage of filters is the exploitation of additional and complementary molecular properties (e.g., size, sorption affinity), often not accessible by sensors alone. By using advanced materials (e.g., microporous metal-organic frameworks, MOF) and material design on the nanoscale (e.g., heterostructures, nanocluster dopants), filters can be designed systematically to achieve high sensor selectivity. Most importantly, filters can be modular to the sensor and thus flexibly combined with different sensor technologies (e.g., optical,⁶⁹ chemoresistive,⁷¹ electrochemical⁷²) and even sensor arrays⁷³.

Here, we systematically review **sorption**, **size-selective** and **catalytic filters** with guidelines for their design in assembling highly selective sensor systems. Selectivity

improvement by filters comes at increased complexity of the sensing system and each filter type introduces distinct advantages and disadvantages, broadly summarized in Table 1.1. We address these characteristics by first introducing the underlying filter concepts and basic principles necessary for analyte separation. Then, specific implementations of such filters are presented, highlighting trends and critically comparing their performance. Finally, device integration and performance in practical cases are elaborated. We close by highlighting current challenges and opportunities.

Table 1.1: Performance characteristic of different filter types (○, ↑, ↓ indicating no change, increase and decrease in comparison to the sensor without filter, respectively).

Filter type	Configuration	Selectivity	Flexibility for selectivity	Multi-analyte detection	Sensitivity	Analysis time	Power consumption	Size
Sorption	Packed bed	↑↑	↑	○	○	○	○	↑
	Separation column	↑↑	↑↑	↑↑	↓	↑↑	↑↑	↑↑
Size-selective	Overlayer	↑	↑	○	○	○	○	○
	Membrane	↑↑	↑↑	○	↓	↑	○	↑
Catalytic	Overlayer	↑	↑	○	↑	○	○	○
	Packed bed	↑↑	↑↑	○	○	○	↑	↑

1.2 Sorption filters

1.2.1 Definitions & principles

A sorption filter exploits the difference between analytes flowing or diffusing through. So mixtures of analytes either adsorb⁷⁴ onto or are absorbed in the filter to enhance the sensor selectivity downstream. Most sorption filters are based on adsorption, while absorption dominates gas chromatography (GC)-sensor systems. These filters are inexpensive and modular to the gas sensor,⁷¹ thus easy to implement and characterize. Most importantly, they are flexible as a wide range of sorbents is available to separate analytes based on polarity,⁷⁵ hydrophilicity,⁷¹ boiling point,⁷⁶ molecular weight⁶⁸ or size⁷⁷. A drawback is their saturation,⁷⁸ requiring replacement or regeneration by purging with clean air and/or by heating⁷⁹ that tends to prolong sensor response and recovery times. However, by combining purging and heating, adsorbents can be regenerated within minutes⁸⁰ as established for thermal desorption tubes in air quality monitoring.⁸¹

For adsorption, the chemical surface groups (nonpolar, polar and analyte-specific), accessible surface area and pore size distribution of the adsorbent (filter) are important (Figure 1.2a). Adsorption of analytes takes place through weak (10–100 meV) and reversible physical forces (i.e., van der Waals).⁸² Sorption filters are often packed beds of adsorbent particles, porous granules or fibers. To characterize their adsorption capacity for certain analytes, a

breakthrough curve is recorded.⁸³ Thereby, the analyte concentration at the filter outlet is measured for constant inlet analyte concentration and flow rate. The time for the outlet analyte concentration to reach a certain fraction (often 5%) of its inlet is defined as the breakthrough time.

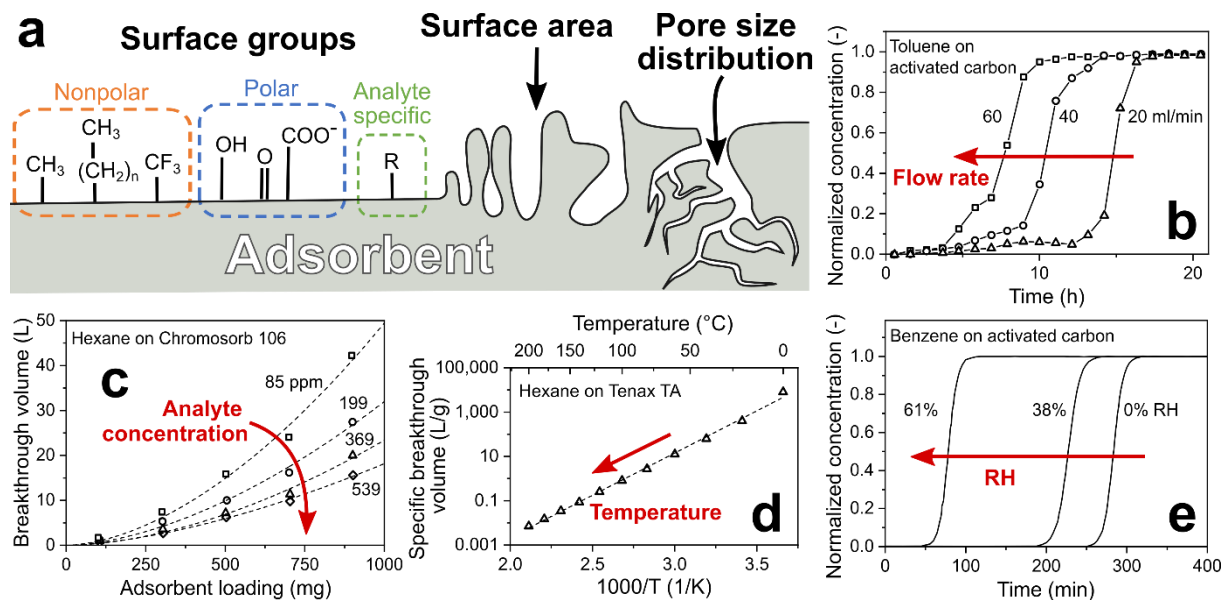


Figure 1.2: (a) Critical adsorbent (filter) properties: Surface chemical groups, surface area and pore size distribution. (b) Effect of overall flow rate through the filter on the breakthrough time.⁸⁴ (c) Effect of filter (adsorbent) loading and analyte concentration on breakthrough volume.⁸⁵ (d) Effect of temperature on specific breakthrough volume.⁸⁰ (e) Effect of RH on the breakthrough time.⁸⁶

Decreasing the flow rate through the filter (adsorbent) prolongs the breakthrough time linearly (Figure 1.2b),⁸⁵ but typically lowers the sensor response as fewer analyte molecules reach the sensor.⁸⁷ Breakthrough time multiplied by the flow rate gives the breakthrough volume that is flow rate-independent and increases proportionally with adsorbent loading since more surface area is available for analyte adsorption (Figure 1.2c).⁸⁵ However, larger filter loadings result in larger pressure drop⁸⁸ through the filter and prolong the sensor response time. Typically, the breakthrough volume is normalized with respect to adsorbent loading.⁸⁹ This material-specific property is useful in design of sorption filters and independent (for a wide range) of flow rate and adsorbent loading. At low analyte concentrations (<10 ppm), breakthrough volumes are independent of concentration, as typically seen in GC.⁹⁰ This is important for gas sensing in breath analysis or indoor air monitoring where analyte concentrations are in that range (e.g., ~500 ppb acetone in breath⁹¹ or ~80 ppb formaldehyde in indoor air⁹²). But concentrations can reach also hundreds of ppm in certain conditions (e.g., ethanol from cleaning products⁹³ or propane/butane from gas cookers), where breakthrough occurs earlier as the capacity of adsorbent is exhausted. This is shown exemplarily in Figure

1.2c for adsorption of 85–539 ppm hexane on a porous non-polar polymer adsorbent with large surface area (Chromosorb 106, $>700 \text{ m}^2 \text{ g}^{-1}$).⁸⁵

Adsorption by physical forces is temperature-dependent (van't Hoff law⁹⁴) resulting in a steep decrease of breakthrough volumes with increasing temperature. This is shown in Figure 1.2d for adsorption of hexane on a porous non-polar polymer adsorbent (Tenax TA), where increasing the temperature from 0 to 20 °C reduces the breakthrough volume by 95%.⁸⁰ Heating is used to accelerate regeneration of sorption filters (e.g., packed zeolite bed⁷⁵ for CH₄ sensing within 2 h by heating to 250 °C) and control the separation of compounds by GC⁹⁵. Another factor is relative humidity (RH) that is omnipresent in most applications (e.g., up to 95% at 36 °C in exhaled human breath⁹⁶). Adsorption of water leads to partial blocking of adsorption sites and reduces the breakthrough time, depending on adsorbent hydrophilicity. For instance, increasing the RH from 0 to 61% for weakly polar activated carbon fibers reduced the breakthrough time of benzene by 76% (Fig. 1.2e). In contrast, when using the non-polar polymer adsorbent Tenax TA, this time was not affected.⁹⁷

1.2.2 Adsorbent materials & properties

Sorption filters preceding gas sensors are tabulated in Table 1.2, showing their composition, target analytes and figure of merit. First⁶⁴ sorption filters for gas sensing were carbon-based⁷⁷ (i.e., activated carbon, graphene, carbon molecular sieve, carbon fiber, etc.) as these were well established already for vapor filtration (e.g., gas masks⁹⁸). Other important adsorbents include silica (silica gel⁹⁹ and mesoporous silica¹⁰⁰), porous polymers (e.g., Tenax TA¹⁰¹), activated alumina,¹⁰² zeolites¹⁰³ and metal-organic frameworks (MOFs)¹⁰⁴. These feature high porosity and surface area (Figure 1.3a–d), resulting in high adsorption capacity. They are commercially available in a variety of shapes (e.g., powders, granules, pellets, fibers), specific surface areas, pore sizes and chemical functionalization (e.g., surface polarity).⁸⁹ Specific surface areas range usually from $20 \text{ m}^2 \text{ g}^{-1}$ for some porous polymers (e.g., Tenax GR⁸⁹) up to $7,000 \text{ m}^2 \text{ g}^{-1}$ for ultra-high surface area MOFs¹⁰⁵ (Figure 1.3e).

Carbon-based adsorbents, silica gels, porous polymers and activated alumina typically feature a mix of meso- (2–50 nm) and micropores (<2 nm) with similar log-normal pore size distributions.¹⁰⁶ Zeolites¹⁰⁷ and MOFs¹⁰⁸, on the other hand, have a well-defined micropore size in the same order of magnitude as gas molecules (e.g., kinetic diameter of benzene¹⁰⁹ is 0.59 nm) that depends on their composition. The accessible surface area, and thus adsorption capacity, depends often on adsorbent's pore size and analyte's molecular size. For instance, p-xylene can access the pores of adsorbent MOF-107, while m- and o-xylene cannot, resulting in

enhanced adsorption capacity of p-xylene.¹¹⁰ When applied as dense layers or membranes, such an effect can even be used to create a sharp size cut-off (e.g., dehydration of solvents by zeolite membranes¹¹¹). Also the adsorbent surface properties are crucial and can be controlled thermally (e.g., higher surface area of activated carbon at higher pyrolysis temperature¹¹²) and chemically¹¹³ (e.g., alkali treatment of activated carbon to increase adsorption of hydrophobic VOCs,¹¹⁴ plasma/microwave treatment,¹¹⁵ ammonization¹¹⁶ or oxidization¹¹⁷).

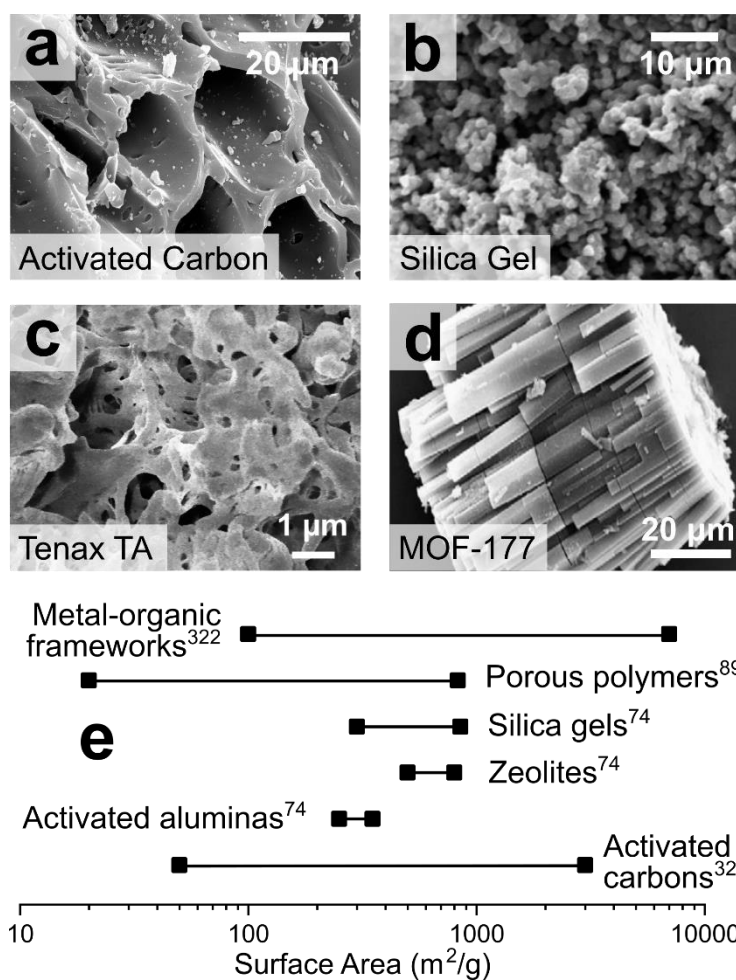


Figure 1.3: SEM images of commercial adsorbents: (a) Activated carbon,¹¹⁸ (b) Silica gel,¹¹⁹ (c) Porous polymer (Tenax TA),⁶⁸ (d) Metal-organic framework (MOF-177).¹²⁰ a–d: Reproduced with permission. Open Access CC BY. (e) Range of surface areas for sorption materials.

Sorption filters of relatively non-polar carbon-based adsorbents (e.g., charcoal, activated carbon) are used to remove VOCs that interfere with the selective detection of relatively inert, non-polar gases such as H₂, CO or CH₄ (Figure 1.4a). On non-polar adsorbents, VOCs are adsorbed mostly by non-specific dispersion forces that are proportional to VOC's molecular weight.¹²¹ Such filters have been used in commercial CO sensors to meet national standards.⁷⁶ For instance, the ethanol response of a SnO₂ sensor is reduced by more than an order of magnitude with a charcoal filter (Figure 1.4b, open vs. filled squares), in contrast to

CO (circles) and H₂ (triangles) that are not affected.⁷⁶ Also other VOCs, such as butane, heptane, ethyl acetate⁷⁶ and silicones⁵⁹ are filtered out, resulting in highly selective detection of small, non-polar gases (e.g., CH₄⁷⁶).

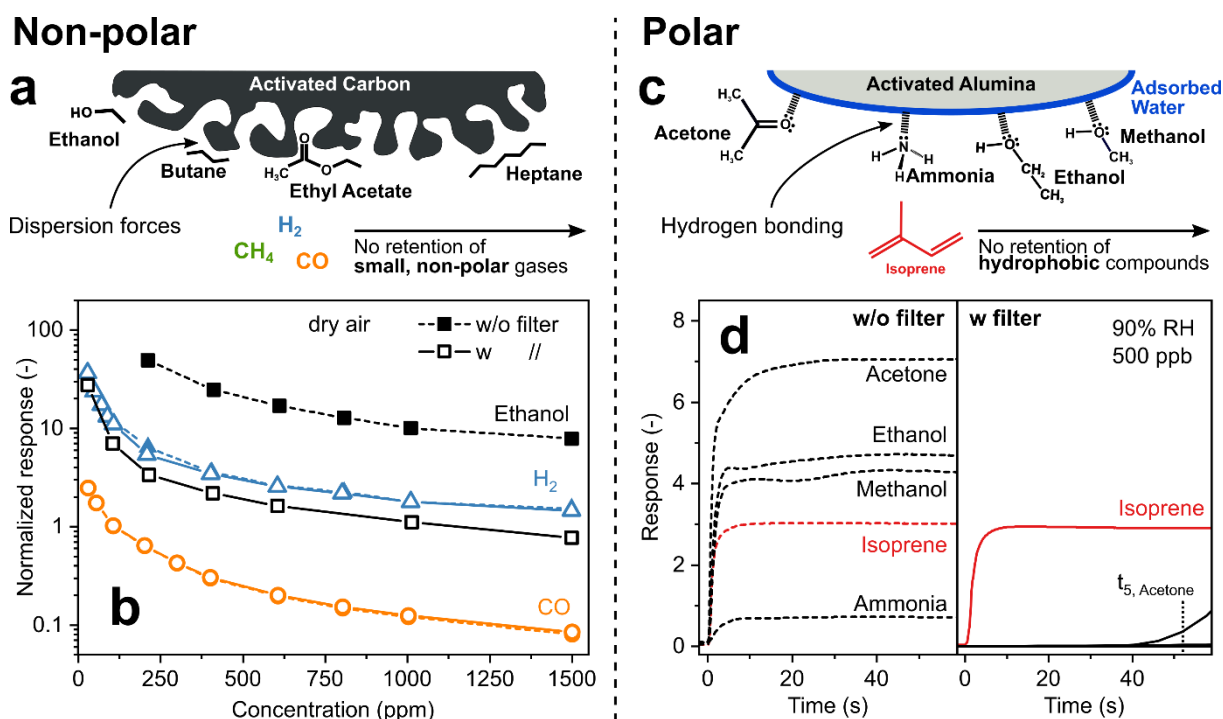


Figure 1.4: (a) Concept of non-polar activated carbon VOC filter for sensing of low molecular weight gases. (b) Responses of a SnO₂ sensor to H₂ (triangles), CO (circles) and ethanol (squares) without (filled symbols) and with (open) preceding activated carbon filter.⁷⁶ Note that symbols for H₂ and CO with and without filter are on top of each other indicating that they passed unscathed through the filter that caught most (~90%) ethanol. (c) Concept of polar activated alumina filter that retains hydrophilic compounds while hydrophobic isoprene passes unhindered. (d) Response of a Pt/SnO₂ sensor to breath-relevant analytes at 500 ppb without (left panel) and with that filter (right panel).⁷¹

In contrast, polar adsorbents interact with analytes mostly through dipole-dipole¹²² and hydrogen bonding¹²³, resulting in more specific molecule removal (e.g., alcohols, carbonyls, aldehydes). Such polar adsorbents, including activated alumina,¹²⁴ silica gel,¹²⁵ P₂O₅,¹²⁶ Nafion,¹²⁷ metal-organic pastes,¹²⁸ CaCl₂¹²⁹ and NaOH,¹³⁰ also strongly adsorb water. So, they are used as desiccants to minimize the impact of humidity that compromises sensor performance (e.g., SnO₂)¹³¹. For example, activated alumina is covered by a thin water layer in the presence of humidity¹³² that adsorbs hydrophilic analytes such as alcohols, ketones and ammonia by hydrogen bonding, while hydrophobic hydrocarbons are not affected (Figure 1.4c). This facilitated selective sensing of isoprene, a non-invasive marker for cholesterol and other metabolic conditions,¹³³ by a packed bed filter of commercial activated alumina (1 g only) upstream of a non-selective Pd/SnO₂ sensor at 90% RH.⁷¹ While that sensor without filter is not selective (Figure 1.4d), only isoprene is detected with the filter during 40 s of exposure

before hydrophilic analytes break through (e.g., acetone after 52 s). This is much shorter than typically obtained with carbon-based filters ($>1 \text{ h}^{134}$) due to their much higher surface area ($>1,000$ vs. $155 \text{ m}^2 \text{ g}^{-1}$, for activated carbon and alumina, respectively), but sufficient for end-tidal breath measurements¹³⁵ and buffered samplers.¹³⁶ The resulting isoprene selectivity by using this filter outperforms⁷¹ other TiO_2 ,¹³⁷ Ti/ZnO^{31} and h-WO_3 ¹³⁸ sensors for isoprene.

More specific interaction includes silver ions that adsorb ethylene quite selectively due to π - π interactions.¹³⁹ This was used for selective detection of ethylene for monitoring fruit ripeness using a Ag-doped alumina filter.¹⁴⁰ After sampling and trapping of ethylene, it is released by heating the filter to $60 \text{ }^\circ\text{C}$, and detected by a non-specific amperometric sensor without interference by NO , NO_2 , SO_2 and acetylene.¹⁴⁰ Another example is indigo, whose reactive $\text{C}=\text{C}$ bond selectively reacts with ozone.¹⁴¹ This is used by NO_2 sensors in the form of indigo-impregnated filter paper,¹⁴² indigo layers directly deposited on a semiconducting sensor¹⁴³ or indigo dispersed in a packed bed of carbon nanotubes¹⁴⁴ to mitigate interference by ozone. Using differential sensing techniques, such indigo filters were even used for selective ozone detection.¹⁴² Such analyte-specific interactions were obtained also during formation of chemical complexes,¹⁴⁵ for instance, ammonia with CaCl^{146} or CuBr^{34} forming $\text{Cu}(\text{NH}_3)_2^+$. The first was used to reduce ammonia concentrations in breath from 10 ppm to only 0.8 ppm while other breath analytes were not influenced.¹²⁹ The second has been applied for sensing ammonia down to 5 ppb at room temperature and 90% RH,¹⁴⁷ but can be used as filter as well. Also quite promising for sorption filters is chemical derivatization, used for instance for selective removal of aldehydes in gas mixtures (e.g., indoor air) by 2,4-dinitrophenylhydrazine.⁴ Another option is surface acidity/basicity tuning for preferential adsorption of bases/acids (e.g., acetic acid on basic Y/ZnO^{148}).

1.2.3 Analyte separation in time

Sorption filters can also act as GC columns to separate analytes in time rather than remove them completely.¹⁴⁹ For this, the analyte-containing gas sample is carried through the filter by a gas (e.g., helium, nitrogen and rarely air) with a pump or pressurized gas cylinder. Most GC-sensor systems (partition or gas-liquid GC)⁹⁵ use open tubular columns (coated with a liquid phase on the inside),¹⁴⁹ which are heated to control analyte separation.¹⁵⁰ If the elution (retention) times of analytes are quite apart, analytes can be detected sequentially by the sensor resulting in very high selectivity and multi-analyte detection capacity (e.g., H_2 and CH_4 in breath¹⁵¹). An inherent drawback of GC-sensors is their batch nature, preventing continuous monitoring of analytes. However, by miniaturizing GC-systems for low sample and dead

volumes and optimizing column heating protocols, analysis time can be reduced to a few seconds.¹⁵²

The first GC-sensor systems were combinations of GC columns with a portable gas sensor.¹⁵³ They selectively detected a variety of analytes, including formaldehyde,¹⁵⁴ breath acetone,¹⁵⁵ VOCs from groundwater headspace,¹⁵⁶ H₂ and CH₄,¹⁵⁷ alcohols¹⁵⁸ and aromatics¹⁵⁹ with limits of detection as low as 15 ppt.¹⁶⁰ Even highly complex mixtures of up to 50 analytes¹⁶¹ could be separated by 2-dimensional GC techniques (two columns in series) with validated performance for occupational exposure monitoring.¹⁶² Such GC-sensor systems are available commercially, for instance the Defiant TOCAM¹⁶³ or Dräger X-pid¹⁶⁴ for broad chemical analysis or the Quintron Breath Tracker¹⁵¹ for breath H₂ and CH₄ in the diagnosis of lactose malabsorption. However, such systems are expensive (several hundred dollars for the column alone), bulky (coiled column of several meters length), heavy (several kg) and require high power (for heating of the column), making them not suitable for battery-powered and handheld detectors.

Micro GC-sensor systems can be based entirely on microelectromechanical systems (MEMS)¹⁶⁵ using planar (i.e., microchip) GC columns,¹⁵³ resulting in much smaller and portable systems, i.e., mountable on a belt¹⁶⁶ (Figure 1.5a). Such systems can reach separation performance close to benchtop GCs, as illustrated in Figure 1.5b where 21 different VOCs are separated within 200 s by a GC-flame ionization detector (FID, red chromatogram) and the micro GC-sensor system (blue chromatogram).¹⁶⁶ They have been tested with a variety of analyte mixtures, including indoor air pollutants,¹⁶⁷ lung cancer biomarkers,¹⁶⁸ chemical warfare agents,¹⁶⁹ aromatics,¹⁷⁰ trichloroethylene in indoor air,¹⁷¹ explosive markers¹⁷² or VOCs for workplace exposure safety.¹⁷³ However, GC-sensor devices with proven performance under real conditions validated with a benchtop device (e.g., as shown in Figure 1.5c for personal exposure monitoring of trichloroethylene with a GC-FID and the belt-mounted GC-sensor device¹⁶⁶) are rare.

Simpler implementation is achieved by focusing on single analytes for specific applications. An example is a detector consisting of a non-specific Pd/SnO₂ gas sensor and a compact separation column for screening of methanol in alcoholic beverages and exhaled breath to detect liquor adulteration and diagnose methanol poisoning non-invasively.⁶⁸ The detector is handheld (94 g), fully integrated, inexpensive and can communicate results by Wi-Fi to a smartphone (Figure 1.5d).¹⁷⁴ It uses a compact packed bed (4.5 cm long, 4 mm diameter) of commercial Tenax TA sorbent with room air as carrier gas instead of a capillary or microchip GC column.⁶⁸ As a result, methanol is detected selectively in the headspace of alcoholic drinks

laced with 1 vol% methanol within 2 min (Figure 1.5e).¹⁷⁴ After flushing the column with room air for 10 min,⁶⁸ it is fully regenerated and ready for the next measurement. The device revealed harmless from harmful concentrations of methanol down to 0.01 vol% in different wines, beers and liquors from six continents (Figure 1.5f).¹⁷⁴

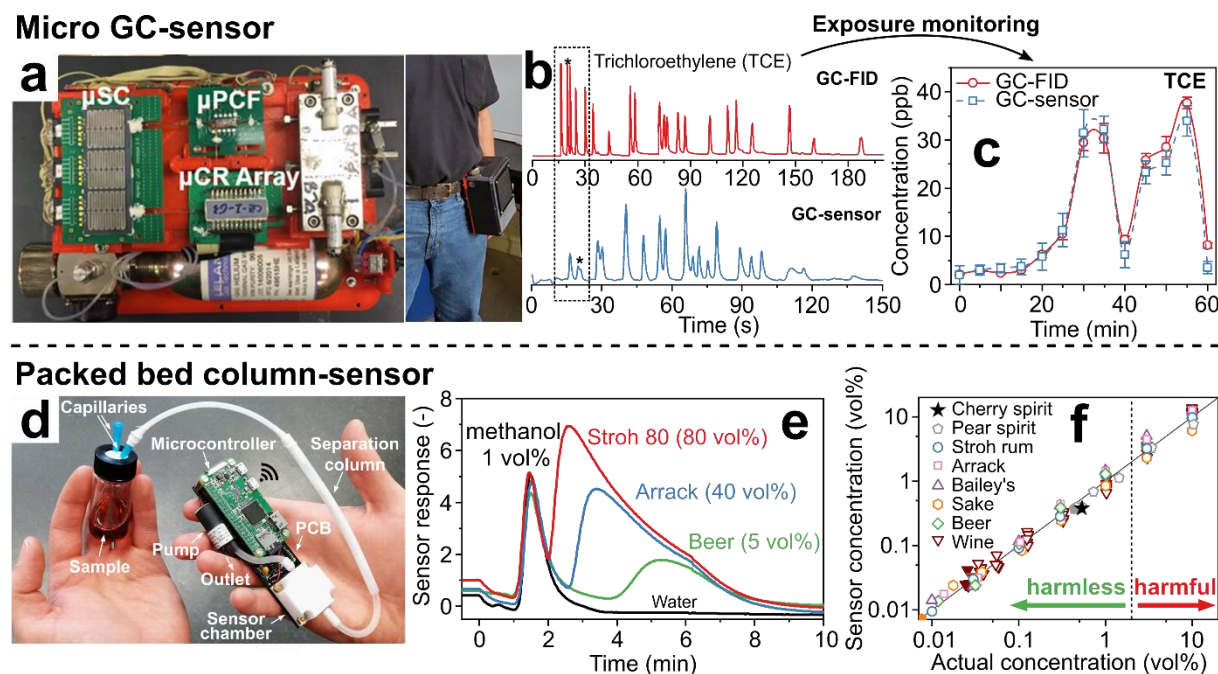


Figure 1.5: (a) State-of-the-art micro GC-sensor system consisting of micropreconcentrator-focuser (μ PCF), microseparation column (μ SC) and microchemiresistor array (μ CR array) that can be mounted on a belt. Reproduced with permission.¹⁶⁶ Copyright 2019 American Chemical Society. (b) Chromatograms of a mixture of 21 VOCs by a benchtop GC-FID and by the micro GC-sensor system showing similar separation performance for both systems.¹⁶⁶ (c) Selective monitoring of trichloroethylene over 60 min by a belt-mounted micro GC-sensor system (dashed line) in comparison to measurements by benchtop GC-FID (solid line).¹⁶⁶ (d) Handheld analyzer for measurement of methanol in laced beverages. Reproduced with permission.¹⁷⁴ Copyright 2020 Springer Nature. (e) Sensor response after sampling of Stroh 80, Arrack, beer and water laced with 1 vol% methanol.¹⁷⁴ (f) Scatter plot of the sensor-measured methanol concentrations versus the actual concentration for beverages laced with harmless and harmful methanol concentrations.¹⁷⁴

This concept of simple packed bed separation columns can be adapted easily to other applications. For example, using a larger (500 mg) Tenax TA separation column, formaldehyde was measured within 2 min at concentrations as low as 5 ppb at 40% RH without interference by H₂, CH₄, CO, methanol, acetaldehyde, ethanol, and acetone. As a result, ppb-level formaldehyde concentrations were detected for the first time in wood-product emissions and in indoor air with a low-cost solid-state sensor.¹⁷⁵ This is possible by the very high selectivity provided by the simple and modular packed bed sorption column, which cannot be reached typically by sensors alone (e.g., ZnO/ZIF-8 core-shell structures,¹⁷⁶ NiO-SnO₂ microflowers¹⁷⁷) or their arrays (e.g., four SnO₂-based sensors¹⁷⁸).

Table 1.2: Sorption filters in combination with gas sensors.

Filter configuration	Filter material	Target analyte	Sensor	LOD ^a (ppm)	Response time	Tested interferants (selectivity)	Ref	
Packed bed	Activated carbon	CH ₄	Pellistor	25,000	–	Hexamethyldisiloxane (∞^b)	59	
		CO	SnO ₂	20	2.5 min	Ethanol (0.11), H ₂ (0.07)	76	
	Ag/Al ₂ O ₃	Ethylene	Electrochemical	0.02	10 min	Acetylene, NO, NO ₂ , SO ₂ (all ∞^b)	141	
	Carbon cloth	CO	SnO ₂	1.5	–	Butane, ethanol, ethyl acetate, heptane (all ∞^b)	66	
	Carbon cloth, charcoal granules	CH ₄	Pellistor	10,000	12-50 s	Hexamethyldisiloxane (∞^b)	64	
	Indigo	Ozone	Electrochemical	0.04	~5 min	NO ₂ (∞^b)	143	
	Indigo/carbon nanotubes	NO ₂	Organic semiconductor	0.01	–	Ozone (∞^b)	145	
	Zeolite 4A	H ₂	SnO ₂	10	–	H ₂ S (∞^b)	62	
	Zeolite 5A	CO	Electrochemical	0.03	5 s	Ethylene (∞^b), H ₂ S (∞^b), CH ₄ (>1,000), ethane (>1,000), H ₂ (>1,000)	65	
	Zeolite MOR	CH ₄	SnO ₂	1,000	–	Ethanol, hexane (both ∞^b)	75	
Commercial GC column	Hayesep Q	H ₂ , CH ₄	SnO ₂	2	<1 min	–	158	
	MXT-1	VOCs (<14 carbon atoms)	PID ^c	<0.015	30 min	–	161	
	OV-1 megabore	Alcohols, acetaldehyde, acetone, ethyl acetate	In ₂ O ₃	0.1	<5 min	–	159	
	OV-101	Alkanes	TCD ^d	–	5 s	–	154	
	Rtx-VMS	cis-1,2-Dichloroethylene, benzene, trichloroethylene, toluene, tetrachloroethylene, p-xylene	PID	1 µg/L (in liquid)	15 min	Various ground water compounds	157	
	Rtx-5	8 organophosphates/sulfates, 5 VOCs	NEMS ^e	0.1	5 s	–	158	
	Rxi-624	Benzene, ethylbenzene, toluene, xylenes	PID	0.0025	19 min	–	160	
	Rtx-5MS, Rtx-200	50 VOCs	PID	–	14 min	–	162, 163	
	Rtx-VMS, Rt Q-BOND	Formaldehyde	PID	0.0005	11 min	–	155	
	Not specified	Acetone	ZnO	0.1	2 min	–	156	
	Separation column	Activated alumina	Isoprene	Pt/SnO ₂	0.005	4 s	Acetone, ethanol, methanol, NH ₃ (all ∞^b)	71
		Tenax TA	Methanol	Pd/SnO ₂	1	102 s	Acetone, ethanol, H ₂ (both ∞^b)	68
			Ethanol, methanol	Pd/SnO ₂	0.01 vol% (in liquid)	10 min	–	175
		Formaldehyde	Pd/SnO ₂	0.005	2 min	Acetaldehyde, acetone, CH ₄ , CO, ethanol, methanol (all ∞^b)	176	
	Overlayer	Indigo	NO ₂	Organic semiconductor	0.04	>1 h	Ozone (>20)	144

^aLowest measured concentration, ^bNot detectable by the sensor, ^cPhotoionization detector, ^dThermal conductivity detector, ^eNanoelectromechanical system

1.3 Size-selective filters

1.3.1 Definitions & principles

Size-selective filters separate analytes by their kinetic diameter. These filters are microporous¹⁷⁹ with pore sizes (usually <2 nm) comparable to analyte diameters. If applied as membranes in front of the sensor, analytes larger than the pore size are blocked (i.e., size cut-off) from reaching the sensor (Figure 1.6a). This can result in very high selectivity to target analytes over hundreds of interferants typically present in such mixtures (e.g., VOCs in indoor air¹⁸⁰ such as terpenes, alkenes, aromatic hydrocarbons). A drawback of such filters is their ineffectiveness for interferants smaller than the target analyte, which can be addressed by combination with other filter types or selective sensing materials. All size-selective filter–sensor systems are tabulated in Table 1.3 together with various figures of merit for comparison.

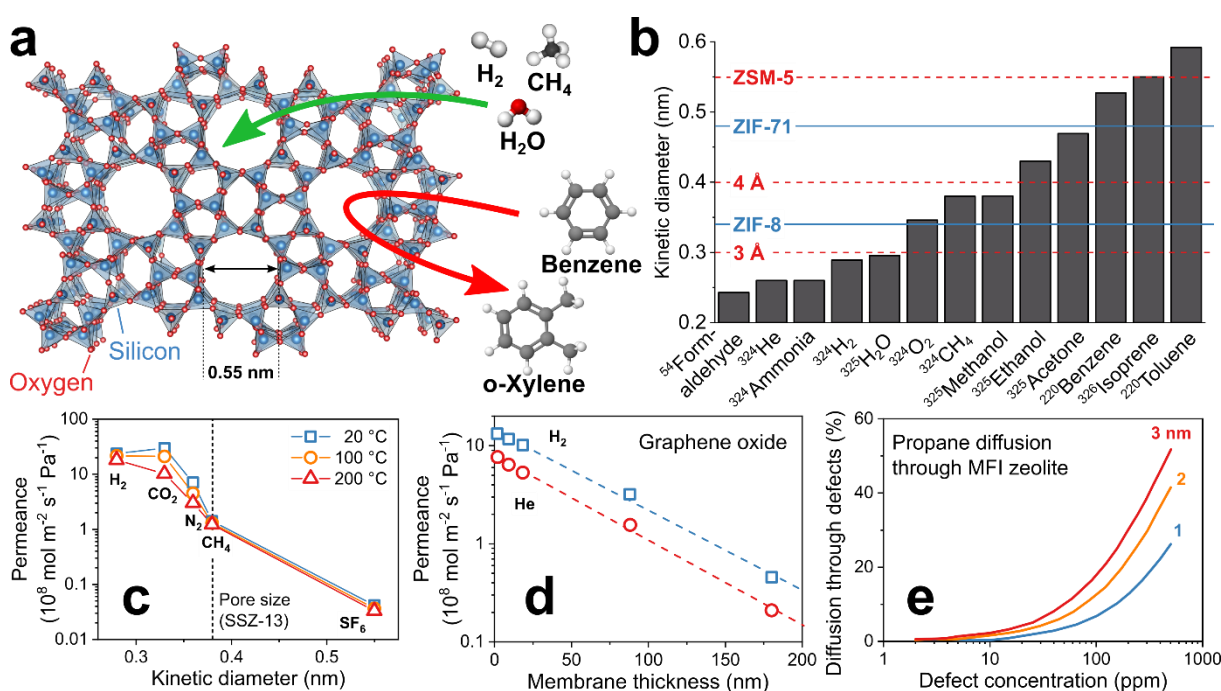


Figure 1.6: (a) Working principle of a size-selective zeolite filter. Arrows indicate blocked (red) and possible (green) diffusion through the microporous structure. (b) Kinetic diameters of common analytes in gas sensing and pore sizes of commonly used zeolites¹⁰⁷ (dashed lines) and MOFs¹⁸¹ (solid lines). (c) Effect of analyte kinetic diameter on membrane permeance at three temperatures.¹⁸² (d) Effect of membrane thickness on permeance.¹⁸³ (e) Effect of membrane defect size and concentration on diffusion of analytes through such defects.¹⁸⁴

Most promising microporous materials are zeolites,¹⁸⁵ MOFs¹⁸⁶ and covalent organic frameworks¹⁸⁷ (COF) featuring pore sizes that depend on crystal structure and composition. An advantage is the myriad of available frameworks (e.g., 248 zeolites,¹⁰⁷ thousands of MOFs and COFs¹⁸⁸) offering distinct pore sizes that can be matched flexibly to target analytes. This is illustrated in Figure 1.6b, showing the kinetic diameters of common analytes in gas sensing

and the pore size of selected zeolites (red) and MOFs (blue). Because of their high internal surface area and intrinsic microporosity, zeolites and MOFs are used frequently for catalysis¹⁸⁹ (e.g., production of styrene with zeolite ZSM-5 catalyst¹⁹⁰), gas storage¹⁹¹ (e.g., H₂ in MOF Cu-EMOF¹⁹²) and even sensors (e.g., chemoresistive⁵⁴ or optical¹⁹³ MOFs and zeolites⁵⁸).

The selectivity of such filters is characterized by the analyte permeance (molar flux per unit driving force).¹⁹⁴ The permeance strongly depends on analyte size as shown in Figure 1.6c exemplarily for a zeolite (SSZ-13) membrane with 0.38 nm pore size (dashed line).¹⁸² In fact, H₂ (0.28 nm) features almost three order of magnitude higher permeance than SF₆ (0.55 nm). However, differences in adsorption strength between analytes can influence the permeance.¹⁹⁵ For instance, CO₂ preferentially adsorbs on SSZ-13, hindering diffusion of other compounds in gas mixtures through the zeolite.¹⁸²

A key property of size-selective filters is their thickness that is inversely proportional to analyte permeance, as shown exemplarily for H₂ and He on 1.9–180 nm thick microporous graphene oxide (GO) layers (Figure 1.6d).¹⁸³ Thus, thin layers are needed for fast sensor responses. This often comes at the cost of higher defect density (e.g., cracks or pinholes), compromising separation selectivity since analytes can pass through the defects. The relation between defect concentration and diffusion is shown in Figure 1.6e for propane and zeolite MFI membranes.¹⁸⁴ Even extremely low defect concentrations reduce drastically analyte selectivity.¹⁸⁴ Thus, a major challenge for effective size-selective filters is the synthesis of thin and defect-free ones (e.g., MOFs,¹⁹⁶ zeolites¹⁸⁴ and GO¹⁹⁷). Mixed matrix membranes (MMM)¹⁹⁸ that consist of a microporous material dispersed in a polymer matrix are promising also. The MMMs can be easily processed to thin membranes with a small number of defects, resulting in high permeance while preserving selectivity.

1.3.2 Pore-size control

First size-selective filters were layers of amorphous SiO₂ directly on top of sensing films (e.g., SnO₂,¹⁹⁹ Ga₂O₃,²⁰⁰ WO₃,²⁰¹ or In₂O₃²⁰²). These were obtained at elevated temperature (>500 °C) under exposure of the sensing film to a silicone source (e.g., hexamethyldisiloxane).²⁰³ The resulting microporous SiO₂ layer is impenetrable for most analytes except for very small H₂, resulting in a more than 100 times higher H₂ selectivity²⁰⁴ to VOCs (e.g., ethanol, acetone and benzene). This is remarkable for chemoresistive H₂ sensors, which offer low limit of detection (e.g., 10 ppb by CeO₂/In₂O₃²⁰⁵) that is critical for leak detection,²⁰⁶ but typically suffer from poor selectivity²⁰⁷ (e.g., <13 to CO for that sensor²⁰⁵). However, the introduced diffusion barrier also increased response and especially recovery

times of sensors from seconds to several minutes²⁰⁸ or even hours²⁰⁹ depending on SiO₂ thickness. This is too long for most applications (e.g., seconds for leak detection²¹⁰).

Capitalizing on the effect of filter layer thickness on analyte permeance (Figure 1.6d), SiO₂ layers with graded thickness²¹¹ had also been deposited on chemoresistive microarrays, allowing slight selectivity modulation from sensor to sensor. While individual sensors remain unspecific, different analytes (e.g., formaldehyde, CO, ammonia, acetone, etc.) were distinguished by pattern analysis in offline breath analysis²¹² and air quality monitoring.²¹³ The pore size and shape of SiO₂ can even be adjusted flexibly by molecular imprinting adsorbed molecules as template during deposition.²¹⁴ For instance, templating such layers on SnO₂ sensors with benzaldehyde resulted in high selectivity to linear hexane over its branched isomers.²¹⁵ Templating with smaller butanal, however, reduced responses to all analytes.²¹⁵

Other microporous materials allow even more flexible control over pore size to adjust selectivity. For instance, pristine graphene oxide (GO) membranes have a narrow pore size distribution <0.3 nm²¹⁶ that is typically adjusted (i.e., size and density) by physical (e.g., ion-bombardment²¹⁷) and chemical treatments (e.g., oxidative etching²¹⁸). Such dense and porous GO membranes with small (0.3–0.4 nm) and large (0.5–0.6 nm) pores were placed upstream of PdO/WO₃ sensors for selective detection of H₂S (Figure 1.7a).²¹⁹ The sensor with dense GO layer (Figure 1.7b, squares) showed lower H₂S selectivity and sensitivity than the sensor alone (circles), as all analytes cannot pass the small intrinsic GO pores. For GO layers with large (triangles) and small (diamonds) pores, the H₂S selectivity is increased to formaldehyde and large analytes (i.e., ethanol, acetone and toluene 0.59 nm²²⁰) compared to the sensor alone. For instance, the selectivity to acetone is tripled (from 4.7 to 14) by covering the sensor with a GO layer having small pores, while response and recovery times did not change much. However, analytes smaller than the pore size (i.e., ammonia 0.29, H₂S 0.36 and methanethiol 0.45 nm) can pass through the pores more easily, so the H₂S selectivity is increased less. The exception is formaldehyde (0.23 nm), probably due to its preferential adsorption²²¹ on GO. Overall, the obtained H₂S selectivity is only moderate (<15 over ammonia and ethanol) and surpassed by other chemoresistive H₂S sensors (e.g., >700 over ammonia and ethanol by CuO²²²). However, these modular GO layers could be combined readily also with other, more selective H₂S sensors.

Zeolites and MOFs feature very narrow pore size distributions. While MOFs have been used as selective sensor materials (e.g., interference-²²³ or luminescent²²⁴-based), the first implementation as auxiliary size-selective filters were ZIF-8 layers directly grown on ZnO nanowire sensors operated at 250 °C.²²⁰ The ZIF-8 membrane features pore openings of 0.34

nm,²²⁵ smaller than most analyte diameters (Figure 1.6b). While the sensor without filter showed low (<5) H₂ selectivity to toluene and benzene, their responses are completely blocked by the ZIF-8 layer irrespective of their concentration, resulting in high H₂ selectivity. Using ZIF-8 as filter also blocked CO,²²⁶ ethanol²²⁷ and acetone²²⁷. These results outperform even SiO₂-covered sensors, especially as response and recovery times are unscathed due to the very thin (2–3 nm²²⁷) ZIF-8 thicknesses. They are only outperformed by other sensor technologies such as optical nanoplasmonic sensors²²⁸, which however suffer from higher detection limits (~0.1 vol%⁶⁹).

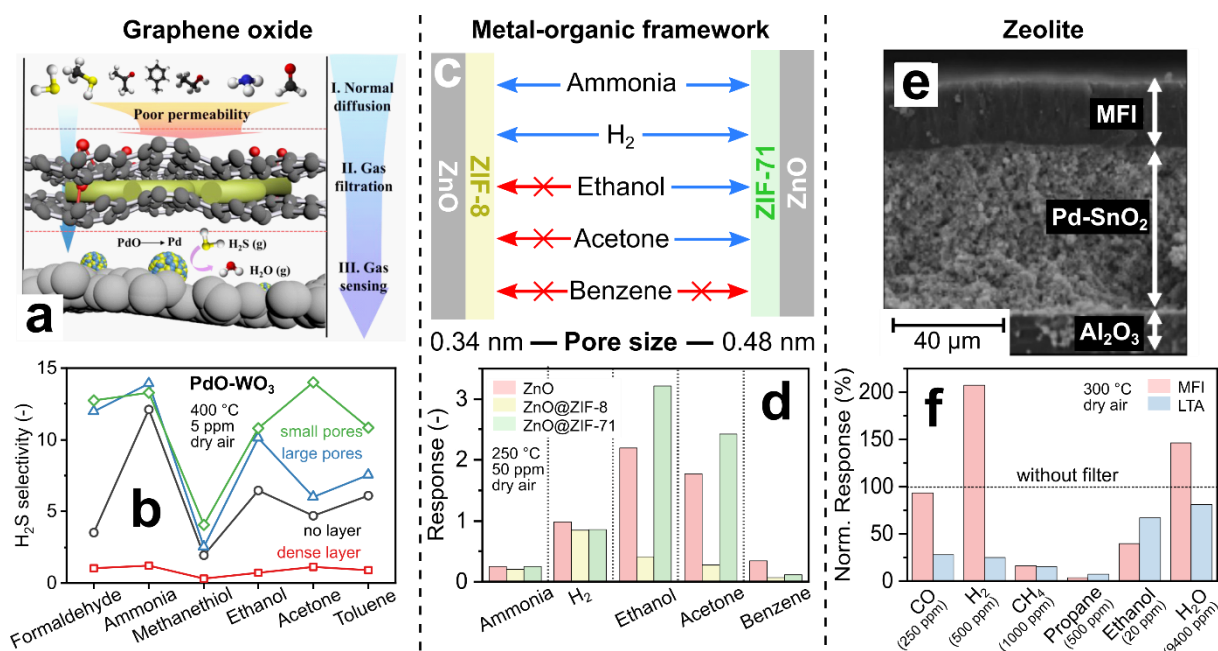


Figure 1.7: (a) Concept for H₂S selective sensor by GO filter membrane. Reproduced with permission.²¹⁹ Copyright 2020 American Chemical Society. (b) H₂S selectivity over various confounders of a PdO-doped WO₃ sensor with GO filter membranes.²¹⁹ (c) Pore size-dependent selectivity of ZnO nanorods covered by metal-organic frameworks ZIF-8 and ZIF-71. Arrows indicate if an analyte's diameter is smaller (blue) or larger (red) than the MOF pores. (d) ZnO sensor response without (pink) and with ZIF-8 (yellow) or ZIF-71 (green) MOF overlayers.¹⁸¹ (e) Cross-section image of a Pd-doped SnO₂ sensing film on Al₂O₃ support coated with MFI zeolite. Reproduced with permission.²²⁹ Copyright 2007 Elsevier. (f) Pd/SnO₂ sensor responses with hydrophobic MFI or hydrophilic LTA overlayers normalized to sensor responses without filter (line).²²⁹

By using MOFs with different pore sizes, the selectivity can be changed drastically using the same sensor, as shown exemplary in Figure 1.7c,d for MOF-coated ZnO nanorods.¹⁸¹ With ZIF-8 coating (Figure 1.7d, yellow bars), most of ammonia and H₂ pass through, giving similar responses to bare sensors (red bars, reduced by <20%). The responses for larger analytes (i.e., ethanol, acetone and benzene), however, decreased by a factor of 4–6. In contrast, for ZIF-71 coatings with larger pore opening (0.48 nm, green bars), ethanol and acetone pass through and even show slightly higher sensor response than the uncoated sensor. Such

increased responses were also observed for H₂S on ZIF-71 covered WO₃ sensors²³⁰ and were attributed to enhanced analyte adsorption onto the ZIF-71.²³¹

Besides framework composition, the pore size of MOFs²³² and zeolites²³³ can also be adjusted by encapsulation of ions or nanoparticles in their pores. For instance, the selectivity of a ZnO sensor coated with ZIF-71 was tuned by incorporation of silver nanoparticles.²³⁴ With increasing nanoparticle size and concentration, the response to acetone decreased by 64%, while that to H₂ increased by 83%.²³⁴ These results show how size-selective filters enable the control of sensor selectivity based on analyte size—otherwise impossible by sensor materials, arrays or other filter types that interact mostly chemically with the analytes.

Figure 1.7e,f shows the effect of different zeolite frameworks on the selectivity of a Pd-doped SnO₂ sensor operated at 300 °C in dry air.²²⁹ MFI and LTA zeolite layers (~25 μm thickness with pore sizes 0.47 and 0.42 nm,¹⁰⁷ respectively) were grown directly on screen-printed sensors (Figure 1.7e) by seeding their surface with zeolite crystals and subsequent solvothermal synthesis.²³⁵ Figure 1.7f shows the response with MFI (red bars) and LTA (blue bars) to different analytes normalized to the response without zeolite layer. While this sensor is non-specific, by adding an MFI layer, it responds selectively to H₂, CO and H₂O. In contrast, LTA increased primarily the selectivity to ethanol and H₂O. Both layers significantly reduced the responses to propane and CH₄, but also increased response times from 38 s to 3 and 16 min with LTA and MFI layers, respectively. The selectivity changes were mostly attributed to zeolite adsorption characteristics (LTA is hydrophilic and MFI hydrophobic) and not to size-selective diffusion, as the zeolite layers showed a large number of intra-crystalline voids (i.e., defects leading to unselective diffusion as shown in Figure 1.6e). Layers with similar performance were prepared also by simple micro-dropping of zeolite suspensions directly on sensors to preserve their film integrity.²³⁶

A variety of zeolites coated on different sensors (e.g., FER on Au-La₂O₃/SnO₂,²³⁷ LTA and MFI on WO₃,²³⁸ Cr₂TiO₅²³⁸ and Zn_{1-x}Cu_xO,²³⁹ array of FAU, BEA and MOR on ZnO²⁴⁰ and mixtures of LTA, FAU and MFI on SnO₂²⁴¹) showed a modulation of sensor response. For instance, ethanol selectivity over isopropanol of SnO₂ sensors was improved from 1.0 to 4.2 by covering with ~26 μm of MFI zeolite.²⁴¹ However, the achieved selectivities were only moderate (<20), in the range typically observed for different sensor compositions without the need for filters and not yet suitable for low concentration analyte detection in complex mixtures (e.g., breath or indoor air). Furthermore, the selectivity improvements often cannot be attributed to size-selective filtering alone. In fact, they are often a complex interplay between i) diffusion resistance, ii) size-selectivity, iii) preferential adsorption as a result of different

filter surface properties (Chapter 2) and iv) catalytic effects as a result of the thermal coupling of filter to the (typically) heated sensor (Chapter 4).

1.3.3 Filter configuration

Size-selective filters can be implemented as direct coatings (i.e., overlayer)²³⁷ or as membranes (free-standing²¹⁹ or on a macroporous support²⁴²) placed in front of sensors. Both configurations offer distinct dis/advantages as shown here exemplarily with two filter–sensor systems for selective formaldehyde detection:

The first system uses a ZIF-8 MOF overlayer (~200 nm thick) directly formed on a ZnO sensor (Figure 1.8a).¹⁷⁶ While such coating of sensors with size-selective materials is attractive to maintain a compact sensor configuration, it leads to elevated filter temperature through its contact with the heated sensor (here 300 °C). This often degrades the size-selectivity as most microporous materials are catalytically active.²⁴³ The ZnO sensor without filter is mostly non-selective, giving high responses to a variety of analytes (Figure 1.8b). With filter layer (Figure 1.8c), responses to formaldehyde and ammonia, that are smaller than the ZIF-8 pores, are reduced only slightly. Also the sensor response times stay similar (14 to 21 s) because of the thin (~200 nm) filter layer. Large molecules such as toluene are blocked by the filter, resulting in pronounced formaldehyde selectivity >100, even in the presence of high humidity (>90% RH). However, other analytes larger than the pore size (i.e., methanol, ethanol and acetone) are not held back, probably because of catalytic conversion²⁴⁴ to smaller molecules on the heated ZIF-8 layer interacting with the ZnO. As a result, only moderate selectivities (5–11) are achieved that might be insufficient for measurement of formaldehyde in indoor air where interferant concentrations can be orders of magnitude higher.²⁴⁵ However, such size-selective ZIF-8 layers could be combined with other formaldehyde-selective sensors (e.g., In₄Sn₃O₁₂,³⁰ NiO-SnO₂,¹⁷⁷ Co/In₂O₃²⁴⁶ or ZnO quantum dots loaded hollow SnO₂ nanospheres²⁴⁷) or sensor arrays¹⁷⁸ to further boost their selectivity. Alternatively, size-selective overlayers can be applied on room temperature sensors to avoid catalytic conversion of interferants.

In contrast, size-selective membrane filters can be produced individually with good control over morphology (e.g., thickness²⁴⁸) and can be combined as separate units more flexibly with sensors (e.g., electrochemical, optical). Figure 1.8d–f shows an example where a size-selective membrane of MFI zeolite was formed on a macroporous Al₂O₃ support (Figure 1.8d) and placed upstream of a Pd-doped SnO₂ sensor.²⁴² Similar to uncoated ZnO, the Pd-doped SnO₂ sensor (Figure 1.8e) alone is not selective. In contrast to the overlayer, however,

the membrane features a size-cutoff, as analytes larger than the pore size (i.e., isoprene and TIPB) are barely detected by the sensor (Figure 1.8f). Interestingly, also smaller analytes (i.e., methanol, ethanol, acetone and ammonia) are blocked effectively by the membrane, probably as a result of adsorption effects. So, excellent formaldehyde selectivity up to more than 1,000 is achieved even at low concentrations down to 30 ppb at 90% RH, unmatched by most chemoresistive sensors. A drawback of this configuration, however, is the larger zeolite thickness ($\sim 3 \mu\text{m}$) that introduces a high diffusion resistance. As a result, the formaldehyde response is reduced by a factor of 5 and the response and recovery times increased to 8 and 72 min,²⁴² respectively, significantly higher than those with overlayers (Figure 1.8a–c).¹⁷⁶

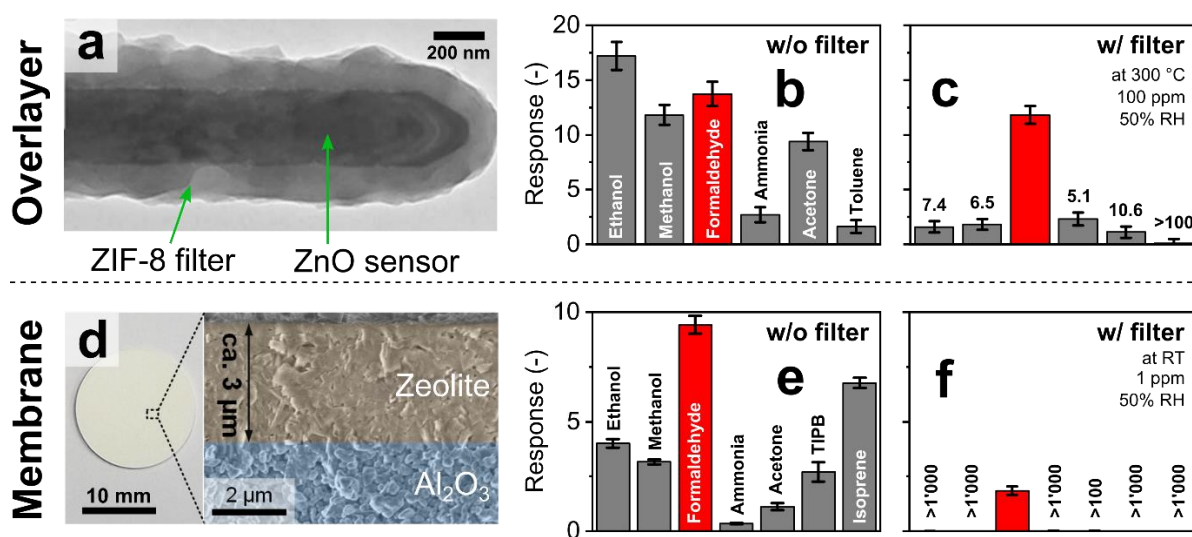


Figure 1.8: (a) ZnO sensing nanorods covered by a microporous overlayer of ZIF-8 MOF. Reproduced with permission.¹⁷⁶ Copyright 2016 American Chemical Society. Sensor response without (b) and with ZIF-8 overlayer (c) to indoor air-relevant analytes with the corresponding formaldehyde selectivities.¹⁷⁶ (d) Microporous MFI zeolite membrane grown on a macroporous alumina substrate. Reproduced with permission.²⁴² Copyright 2018 Elsevier. Response of a Pd-doped SnO₂ sensor without (e) and in combination with MFI zeolite membrane (f) to indoor air-relevant analytes with corresponding formaldehyde selectivities.²⁴²

Table 1.3: Size-selective filters in combination with gas sensors.

Filter configuration	Filter material	Target analyte	Sensor	LOD ^a (ppm)	Response time	Tested interferants (selectivity)	Ref
Overlayer	PMMA	H ₂	Plasmonic	10	<1 s	CH ₄ (63), CO ₂ (32), CO (2.1), NO ₂ (0.12)	69
	SiO ₂	H ₂	SnO ₂	20,000	–	CH ₄ (>1,000)	199
MOF ZIF-8		Formaldehyde	ZnO	50	60 s	Butane (>500), CH ₄ (>500), CO (>500), ethanol (18), methanol (11)	203
				1,000	<1 min	Acetone, benzene, ethanol (all >1,000)	204
				3,100	>1 min	CH ₄ , propane (both >1,000)	208
				0.250	>1 h	CH ₄ (>100), ethanol (>100), CO (>50)	209
				500	<30 s	Acetone, CH ₄ , CO, CO ₂ , ethanol, isobutene, propane, NH ₃ , NO	200
				100	5 s	CH ₄ (>100), isobutane (12), CO (6.8), ethanol (<1)	202
				10	21 s	Toluene (>100), acetone (10.6), ethanol (7.4), methanol (6.5), NH ₃ (5.1)	177
				10	–	Benzene (12), NH ₃ (4.2), acetone (3.1), ethanol (2)	181
				10	>5 min	Benzene, toluene (both ∞ ^b)	220
				5	>5 min	CO (37)	227
MOF ZIF-71		H ₂ S	Pd/ZnO	10	>5 min	Acetone, benzene, ethanol, toluene (all ∞ ^b)	228
				2	2 min	Ethanol (19), acetone (11), NO ₂ (3.4)	230
				20	–	Acetone (1.9)	234
				10	–	Benzene (27), NH ₃ (13), H ₂ (3.7), acetone (1.3)	181
Zeolite FER		Ethanol	L ₂ O ₃ -Au/SnO ₂	50	–	Isopropanol (20), ethylene (15), ethanol (13), H ₂ (9)	237
				0.050	<1 min	Acetone, CO ₂ , ethanol, H ₂ , NH ₃	239
Zeolite LTA		Ethanol	Pd/SnO ₂	10	1.7 min	CH ₄ (>1,000), propane (>400), CO (>100), H ₂ (>100)	236
				20	16 min	H ₂ O (>4000), CH ₄ (>200), propane (74), CO (35), H ₂ (31)	223
Zeolite MFI		Ethanol	WO ₃ , Cr ₂ TiO ₅	21	>30 min	CO (>1,000)	238
				20	3 min	H ₂ O (>1,000), CH ₄ (>100), propane (83), CO (6.2), H ₂ (2.2)	223
Zeolite FAU, BEA, MOR		Acetone, ethanol, NH ₃ , NO ₂	ZnO	21	>5 min	CO (>100)	238
				1	–	–	240
Mix. (LTA, FAU, MFI)		–	SnO ₂	2.5	<5 min	Acetone, butane, CO, ethane, ethanol, isopropanol, propane, toluene	241
				100	–	–	201
Overlayer (graded thickness)	SiO ₂	CO	WO ₃	0.5	–	–	211
				0.2	>1 min	Ethanol, H ₂ O	212
Overlayer (patterned)	SiO ₂	Indoor air contaminants	SnO ₂ , WO ₃	<1	<5 s	–	213
				–	–	–	214
Membrane	Graphene oxide	Alcohols, aldehydes	SnO ₂	–	>1 min	2,2-dimethylbutane (>82), 2-methylpentane (82)	215
				1	30 s	Acetone (14), NH ₃ (14), formaldehyde (13), ethanol (11), toluene (11), methanethiol (4)	219
Zeolite MFI		Formaldehyde	Pd/SnO ₂	0.03	8 min	Ethanol (>1,000), isoprene (>1,000), methanol (>1,000), NH ₃ (>1,000), TIPB (>1,000), acetone (>100)	242
				–	–	–	–

^aLowest measured concentration, ^bNot detectable by the sensor

1.4 Catalytic filters

1.4.1 Definitions & principles

Catalytic filters exploit differences in *chemical reactivity* between analytes to enhance the selectivity of downstream sensors. Ideally, the target analyte passes the filter intact, while interferants convert fully on the filter (catalyst) to inert species undetected by the sensor, as illustrated in Figure 1.9a. Nevertheless, partial analyte conversion and formation of intermediates has been observed.²⁴⁹ As a result, interferants are eliminated or their concentration is reduced substantially, resulting in high sensor selectivity. Most importantly with respect to other filters, catalytic ones operate continuously²⁵⁰ (and do not saturate like sorption filters, Chapter 2). This is a distinct feature if interferants are present constantly in the background air (e.g., ethanol from cleaning products⁹³ or disinfectants²⁵¹). However, catalytic filters usually require some heating to optimize selectivity, which can be circumvented if the catalytic filter is deposited directly onto the heated sensing film as an overlayer.

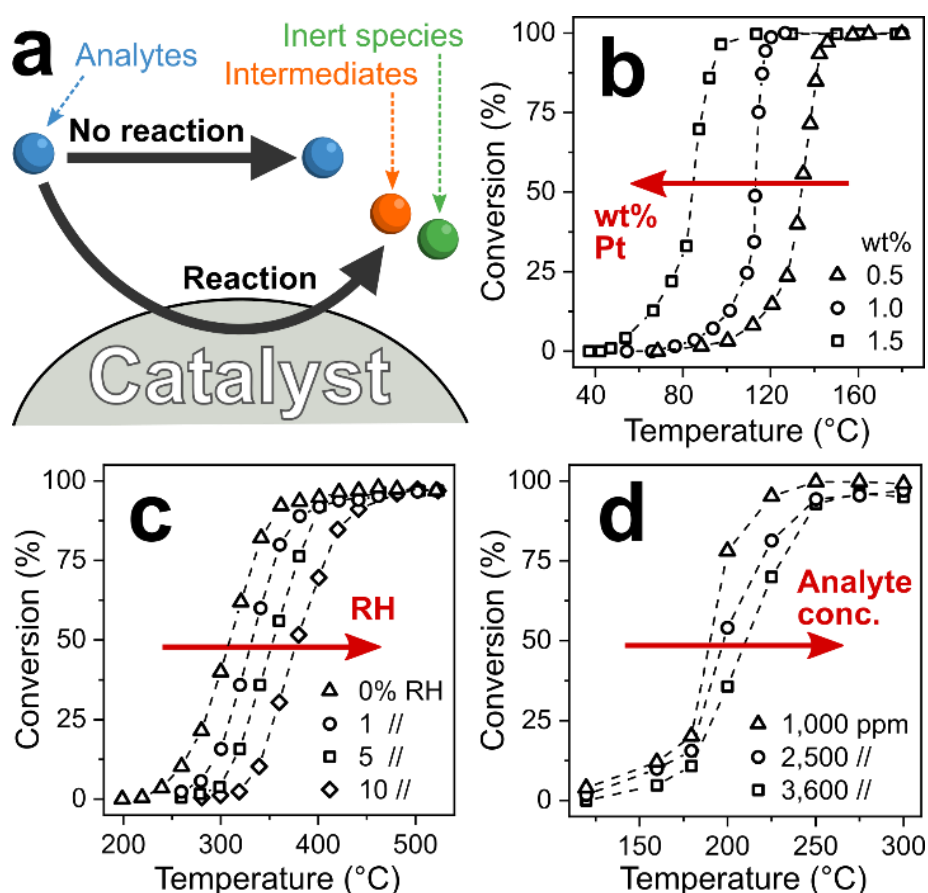


Figure 1.9: (a) Chemical reaction pathways between analytes and catalytic filter. Analytes thereby pass the catalyst unscathed without reaction (desired for the target analyte) or are converted to intermediate or inert species (desired for interferants). (b) Increased noble metal loading lowers filter temperature for complete conversion.²⁵² (c) Increased RH²⁵³ and (d) analyte concentration²⁵⁴ increases that temperature.

A variety of crystalline²⁵⁵ or amorphous²⁵⁶ catalytic materials is available from heterogeneous catalysis, including metal oxides,²⁵⁷ mixed-metal catalysts,²⁵⁸ zeolites,¹⁸⁹ mesoporous silica¹⁸⁹ and MOFs.²⁵⁹ They typically feature high specific surface areas (e.g., $>100 \text{ m}^2 \text{ g}^{-1}$)²⁶⁰ with surface composition, structure and operational temperature determining the overall reactivity, and subsequently, selectivity. These properties make catalytic filters attractive for material engineering at the nanoscale (e.g., surface area,²⁶¹ acidity²⁶² or surface hydrophobicity²⁶³). In particular, noble metals (e.g., Pt,²⁶⁴ Pd,²⁶⁴ Rh,²⁶⁴ Au²⁵⁸ and Ag²⁶¹) are frequently added to enhance reactivity by tuning their size down to single atoms.²⁶⁵ For example, increasing the loading of Pt on Al₂O₃ from 0.5 (triangles, Figure 1.9b) to 1.5 wt% (squares) reduces the temperature of full propene combustion from 160 to 100 °C.²⁵²

In contrast to heterogeneous catalysis, catalytic filters for sensors are typically operated in mixtures with many compounds (e.g., several hundred in human breath²⁶⁶), low analyte concentrations and high or varying humidity. These parameters markedly influence the reactivity and selectivity of catalytic filters. For example, catalyst activity is strongly influenced by humidity as water molecules can competitively interact and block catalyst active sites,²⁶⁷ reducing their reactivity. As an example, the onset of CH₄ conversion on Pd/SnO₂ shifts from 240 °C in dry air to 320 °C at just 10% RH (Figure 1.9c).²⁵³ For sensor applications, humidity often varies greatly (e.g., 30–95% RH²⁶⁸ in indoor air) or is present at high levels (e.g., exhaled breath $>97\%$ RH⁹⁶), which needs to be considered in the design of catalytic filters. Furthermore, analyte concentration influences conversion at high concentrations when the reaction kinetics (i.e., diffusion to, adsorption on, conversion at and desorption from the catalyst) become rate-limited.²⁶⁹ For instance, on Pt/Al₂O₃–CeO₂, complete conversion of 1,000 ppm toluene is attained at 250 °C, while for 3,600 ppm it is 300 °C (Figure 1.9d).²⁵⁴ For gas sensors, the catalytic filter needs to convert interferants at high concentrations and leave intact the target analyte often present at orders of magnitude lower concentration (e.g., <10 ppb formaldehyde in indoor air⁹² with >10 ppm H₂, ethanol or acetone²⁴⁵). So, heterogeneous catalysis can inspire the design of catalytic filters, but their performance needs to be tailored systematically to sensor conditions.

1.4.2 Tailored selectivity

Sensors with catalytic filters are tabulated in Table 1.4, showing their composition, target analytes and various figures of merit. First catalytic filters for gas sensors were developed to remove VOCs (e.g., CO and ethanol) for reliable alkane detection.²⁵⁰ Monitoring alkanes (e.g., CH₄, propane and butane) in domestic²⁷⁰ and industrial areas (e.g., from gas leaks²⁷¹ and

coal mines²⁷²) is important due to their high flammability²⁷³ and regulated exposure limit (e.g., CH₄, 1,000 ppm²⁷⁴). This is challenging, as chemoresistive sensors respond weakly to alkanes (high energy needed to activate C-H bonds²⁵⁴) and suffer from high cross-sensitivity²⁷⁵ to pollutants, particularly CO (e.g., >7,000 ppm in coal mines²⁷⁶ and >100 ppm in industrial areas²⁷⁷) and ethanol (e.g., >100 ppm from hand disinfection²⁵¹).

Typical catalysts consist of noble metals (e.g., Pt, Pd and Au) on ceramic supports (e.g., Al₂O₃, SiO₂ and Fe₂O₃) that are deposited directly onto sensing films as porous layers. Their working principle is illustrated in Figure 1.10a on the example²⁷⁸ of a SnO₂ sensor (operated at 350 °C) covered by a layer (100-150 μm) of mesoporous Pt/ or Pd/SiO₂. Without filter (Figure 1.10b), the sensor shows similar resistance changes (i.e., responses) to 20–400 ppm CO (dashed line) and 200–4,000 ppm CH₄ (solid line), typical for such SnO₂-based sensors. With filter, CO is fully converted in the filter layer to non-responsive species (i.e., CO₂ and H₂O), while chemically stable CH₄ passes unscathed. As a result (Figure 1.10c), no resistance changes to CO are detected anymore, while they are unchanged for CH₄, resulting in selective CH₄ detection.²⁷⁸ Such CH₄ sensor systems outperform sensors without filter (e.g., methane to CO selectivity of 8 for Pd-Ag activated ZnO²⁷⁹ and ZnO/ZnO₂ heterostructures²⁸⁰) and enabled industrial development of selective gas leak sensors to prevent false alarms.²⁸¹

A variety of catalysts appear suitable for this application, as similar results were obtained with several Al₂O₃- and SiO_x-based catalysts (e.g., thermally evaporated pure Al₂O₃ and SiO_x,⁵¹ drop-coated Pt,⁷³ Pd⁷³ and RuO₂²⁸² on SiO₂,⁷³ flame deposited Pd/Al₂O₃²⁸³ and screen printed Pt/Al₂O₃,²⁵⁰ Pd/Al₂O₃²⁸⁴ and Pt/ZSM-5 zeolites²⁸⁵), Ga₂O₃,²⁸⁶ WO₃,⁵¹ Pd/SnO₂²⁸⁷ and Au/Ce-Zr.²⁸⁸ The preferential conversion of VOCs over alkanes is expected due to the alkane's higher chemical stability.²⁸⁹ Disadvantages of such filters are their limited applicability to alkane detection, as well as typically high operation temperatures (i.e., >350 °C)²⁷⁸. However, the performance of filters can be improved further and their selectivity tuned more flexibly by exploiting specific analyte–catalyst interactions. For instance, gold catalysts are highly reactive to CO already at room temperature.²⁹⁰ In fact, catalytic filters such as Au/Fe₂O₃,²⁹¹ Au/ZnO²⁹² and Au/TiO₂²⁹² removed CO selectively over alkanes (e.g., propane) even at room temperature, with the highest removal efficiency in the order of Au/Fe₂O₃>Au/ZnO>Au/TiO₂.

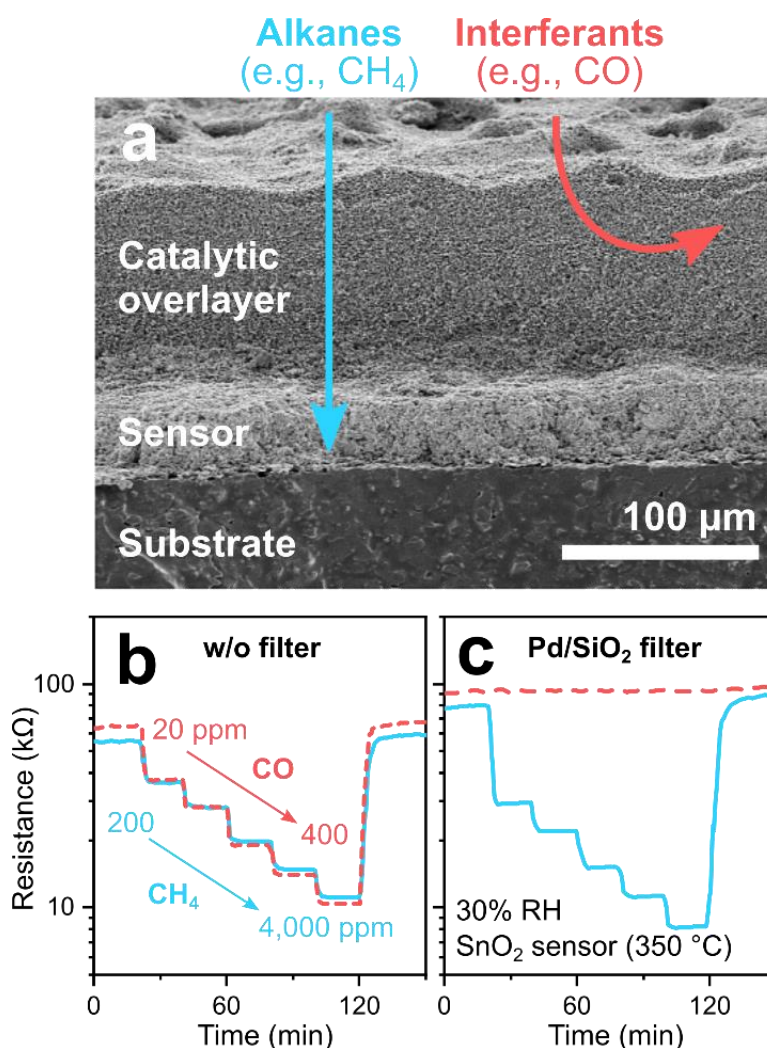


Figure 1.10: (a) SEM cross-section of a SnO₂ sensor with a mesoporous catalytic overlayer (filter). Alkanes (e.g., CH₄) pass through the filter unscathed and are detected by the sensor, while interferants (e.g., CO) are converted to non-responsive species (e.g., CO₂). Reproduced with permission.²⁷⁸ Copyright 2003 Elsevier. SnO₂ sensor response to CO (20–400 ppm, dashed line) and CH₄ (200–4000 ppm, solid line) without (b) and with (c) a Pd/SiO₂ mesoporous catalyst filter at 30% RH.²⁷⁸

More challenging are filters that distinguish between VOCs with similar stability (e.g., ketones, aldehydes, aromatics), requiring more precise material engineering. For instance, high ethanol background in ambient air or breath (>100 ppm from disinfectants²⁵¹ and alcohol consumption²⁹³, respectively) is a common issue preventing accurate measurements of target analytes. This was addressed by a catalytic filter that exploits surface acidity and basicity (Figure 1.11) for selective measurement of acetone,²⁹⁴ a metabolic breath marker for fat oxidation.²⁹⁵ The acetone carbonyl group coordinates primarily with Lewis acid sites abundantly present on acidic oxides (e.g., WO₃²⁹⁶). In contrast, ethanol conversion is favored on basic oxides featuring surface-adsorbed oxygen- and hydroxyl-related species.²⁹⁷ Hence, the highest ethanol over acetone selectivity was found for ZnO featuring highest basicity (Figure 1.11a-d),²⁹⁴ in line with literature.²⁹⁶ Sampling breath of an alcohol intoxicated

volunteer through such a small (150 mg) packed bed filter of ZnO heated to 260 °C completely eliminates ethanol interference (Figure 1.11e). Most importantly, the filter leaves acetone intact as verified by responses of a Si/WO₃ sensor without and with filter (Figure 1.11f) and confirmed by benchtop mass spectrometry. Ethanol responses are strongly reduced (i.e., by 88% at 20 ppm ethanol, remaining response from the combustion to H₂²⁹⁸), resulting in selective acetone detection down to 25 ppb in breath-relevant 90% RH with a selectivity to ethanol of 81. This ZnO filter fully combusts also other interferants (e.g., formaldehyde), while leaving aromatics (e.g., toluene, benzene), CH₄ and H₂ intact. The selectivity can be further increased by removing the ethanol conversion products (i.e. H₂) by other (catalytic) filters or by operating the filter at higher temperature, although this can reduce the sensitivity by partially converting the target analyte (i.e., acetone).

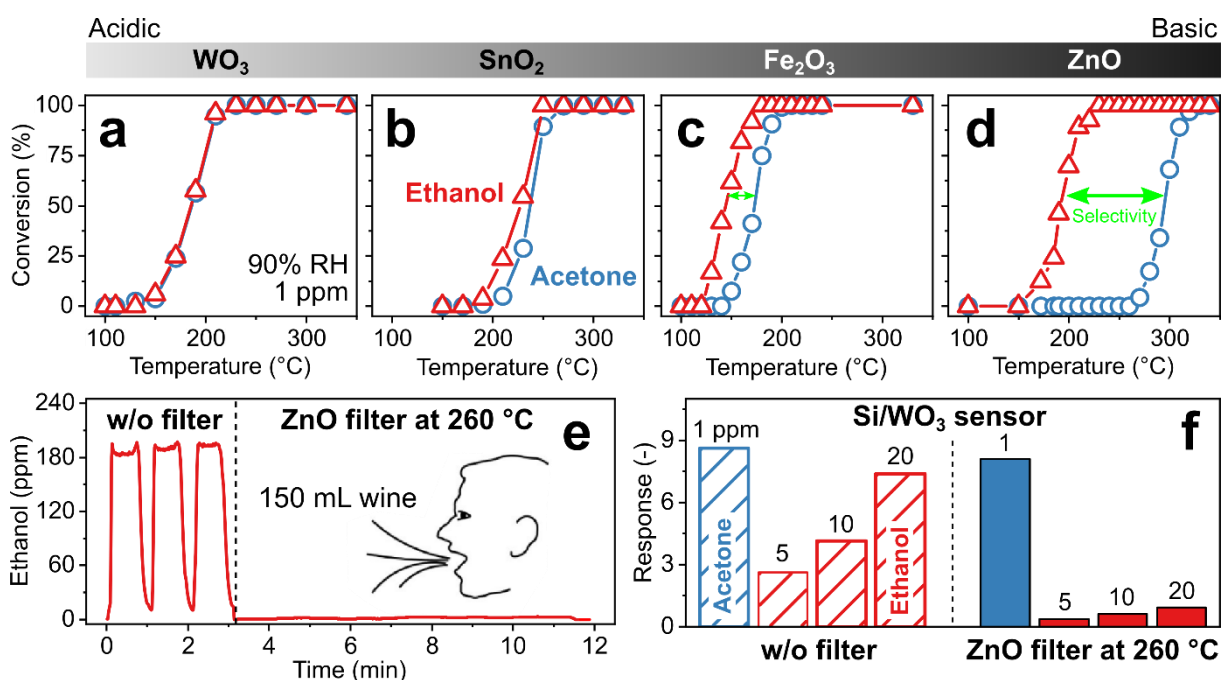


Figure 1.11: (a–d) Conversion of 1 ppm ethanol (triangles) and acetone (circles) on metal oxides with increasing basicity, $\text{WO}_3 < \text{SnO}_2 < \text{Fe}_2\text{O}_3 < \text{ZnO}$, that increases the acetone selectivity over ethanol. (e) Ethanol concentration measured during three consecutive breath exhalations without filter ($t \leq 3$ min) and with 150 mg ZnO filter at 260 °C ($t > 3$ min) that totally eliminated ethanol. (f) Si/WO₃ sensor response to 1 ppm acetone and 5, 10 and 20 ppm ethanol without (open bars) and with a ZnO catalyst at 260 °C (filled bars) upstream of the sensor.²⁹⁴

Catalytic filters can even increase selectivity to analytes from the same chemical group. For instance, the selective detection of carcinogenic⁹² benzene over toluene and xylene in indoor air is challenging for chemical gas sensors due to the chemical similarity of these analytes (aromatic hydrocarbons with 0–2 methyl groups).²⁹⁹ A promising approach is the use of catalytic Co₃O₄ overlayers electron-beam evaporated onto Pd/SnO₂ sensing films.³⁰⁰ Toluene and p-xylene were partially converted in the filter layer to non-reactive species,

reducing their responses by as much as 97%, depending on Co_3O_4 thickness (0–60 nm). In contrast, the response to benzene increased by 30% at optimal filter thickness (20 nm), attributed to its activation in the catalytic layer through formation of more responsive intermediates, as has been observed for benzene detection already with Pt/ Al_2O_3 filters.³⁰¹ As a result, benzene selectivity to p-xylene, toluene, ethanol, formaldehyde and CO was doubled from ~1 to >2 that could be further improved with sensors featuring intrinsic benzene selectivity (e.g., Au/multi-walled carbon nanotubes³⁰² with benzene selectivity towards o-xylene and toluene >30). Most interesting, by switching the filter–sensor arrangement, i.e., Co_3O_4 was used as sensor with a catalytic filter layer of SnO_2 , also the selectivity could be reversed.³⁰³ Toluene and p-xylene responses increased up to a factor of 5 (possibly through formation of more responsive benzyl alcohol³⁰⁴), while responses of interferants decreased significantly. As a result, toluene and p-xylene selectivity >20 could be achieved towards benzene, ethanol, formaldehyde and CO.

Similarly, increased selectivity through higher sensitivity to target analytes was observed also for other catalytic filters. For instance, a Pd/ WO_3 sensor covered by undoped zeolite layers (HZSM-5) increased the CO response by a factor of 7 resulting in selectivity of more than 4 over methanol, ethanol and acetone. Covering the same sensor with Pt/HZSM-5 increased methanol responses by a factor of 15 resulting in selectivity >9 over the same analytes.³⁰⁵ Packed bed filters of Pt/ LaFeO_3 heated to 200 °C upstream of Pt/ SnO_2 sensors turned them selective to CO with negligible interference from propane.³⁰⁶ However, when operating the filter at 350 °C, sensor responses to propane increased by a factor of 25 while CO was completely removed. Also, nanolayers (5–20 nm) of Pd or Ag deposited by successive ionic layer deposition on SnO_2 sensors removed ozone interference and increased responses to reducing gases (e.g., CO and H_2).³⁰⁷ While such catalytic filters offer a powerful tool to enhance sensitivity and tailor selectivity, none of these studies investigated the composition of the effluent, to identify the reformed species and characterize their interaction with the sensor, motivating further research.

1.4.3 Filter configuration

Catalytic filters are typically deposited directly²⁸³ as overlayers (e.g., as porous layers,²⁸³ membranes,³⁰⁸ zeolites³⁰⁹ or metallic nanoclusters³¹⁰) onto sensor materials. This results in compact filter–sensor systems where sensing film and catalyst temperature are coupled, requiring no additional heating source. However, this also implies that filter and sensor cannot be fabricated and operated individually to achieve maximum selectivity.

Additionally, overlayers may act as diffusion barrier, increasing response times (e.g., from 1 to 4 min for 20–70 μm thick zeolite layers on $\text{SrTi}_{1-x}\text{Fe}_x\text{O}_{3-\delta}$ sensors)³¹¹. While depositing thin³¹² or highly porous²⁷⁸ catalytic overlayers can address this, filter efficiency could be compromised. Finally, solid-state diffusion of the catalytic layer into the sensing film may alter sensor performance (e.g., catalytic Pd diffusion into SnO_2 sensor).²⁸⁷ This can be solved by an additional inert separation layer (e.g., Al_2O_3 ³⁰⁸ or SiO_2 ⁷³).

Such a SnO_2 gas sensor (operated at 375 °C) with a Cr_2O_3 catalytic overlayer deposited by electron-beam evaporation had been tested as ethylene sensor (Figure 1.12a–d).³¹² Ethylene monitoring is used for controlling growth, development and ripening of fruits.³¹³ Figure 1.12a shows a cross-section SEM image of the Al_2O_3 substrate, the SnO_2 sensing layer ($\sim 21 \mu\text{m}$) and a thin Cr_2O_3 overlayer (300 nm). Without the Cr_2O_3 overlayer, the SnO_2 sensor features high sensitivity to ethylene, but responds also to trimethylamine (TMA), dimethylamine (DMA), ammonia (NH_3), ethanol, formaldehyde (HCHO) and CO (Figure 1.12b). With this catalytic overlayer, the responses to all interfering analytes are reduced, while the ethylene response remains similar. As a result, ethylene selectivity to the tested analytes increases from 1–3.8 to 3.4–24 with an estimated ethylene limit of detection of only 24 ppb. Increasing the Cr_2O_3 layer thickness (from 300 to 600 nm) further reduces responses to interferants but also to ethylene, resulting in overall poorer selectivities. The filter-sensor system was further integrated into a hand-held device with wireless communication, which monitored fruit ripening (exemplarily shown for a banana in Figure 1.12c) under controlled conditions (i.e., in a closed chamber). While promising, further validation with a high-resolution instrument (e.g., GC-MS) and testing in indoor air is required.

Catalytic filters can be implemented also as a packed bed upstream of the sensor affording individual optimization and operation, as well as flexible combination with different sensors (e.g., chemoresistive, electrochemical or optical). A drawback is the sometimes necessary additional heating source²⁹⁴ and pressure drop when air is drawn through the filter to the sensor by a pump.³¹⁴ The former can be addressed by tailoring materials at the nanoscale (e.g., introducing highly reactive noble metals²⁹⁰). Such a compact (30 mg) catalytic packed bed filter of Pt/ Al_2O_3 nanoparticles had been used for a selective breath acetone sensor (Figure 1.12d–f).⁷⁰ Acetone is a breath marker for fat metabolism²⁹⁵ with applications in personalized exercise³¹⁵ and diet monitoring,³¹⁶ as well as search and rescue.³¹⁷ While Pt/ Al_2O_3 is used already to remove VOCs over alkanes, tailoring the Pt-loading is necessary to allow for selective combustion of breath-relevant interferants over acetone. For example, 0.2 mol% Pt/ Al_2O_3 removed selectively isoprene, alcohols, aldehydes, aromatics, CO, H_2 and NH_3 over

acetone with high robustness to humidity (30–90% RH) at 135 °C. Figure 1.12d shows the crystalline Al_2O_3 particles decorated with 0.2 mol% Pt clusters (average size 9 nm).⁷⁰ When coupled to a Si/WO_3 sensor, this results in unprecedented acetone selectivity (> 250 , Figure 1.12e), which cannot be achieved by sensors alone (e.g., selectivity to ethanol < 10 by Si/WO_3 and isoprene < 4 by Al/ZnO ³¹⁸) or orthogonal sensor arrays⁴⁸.

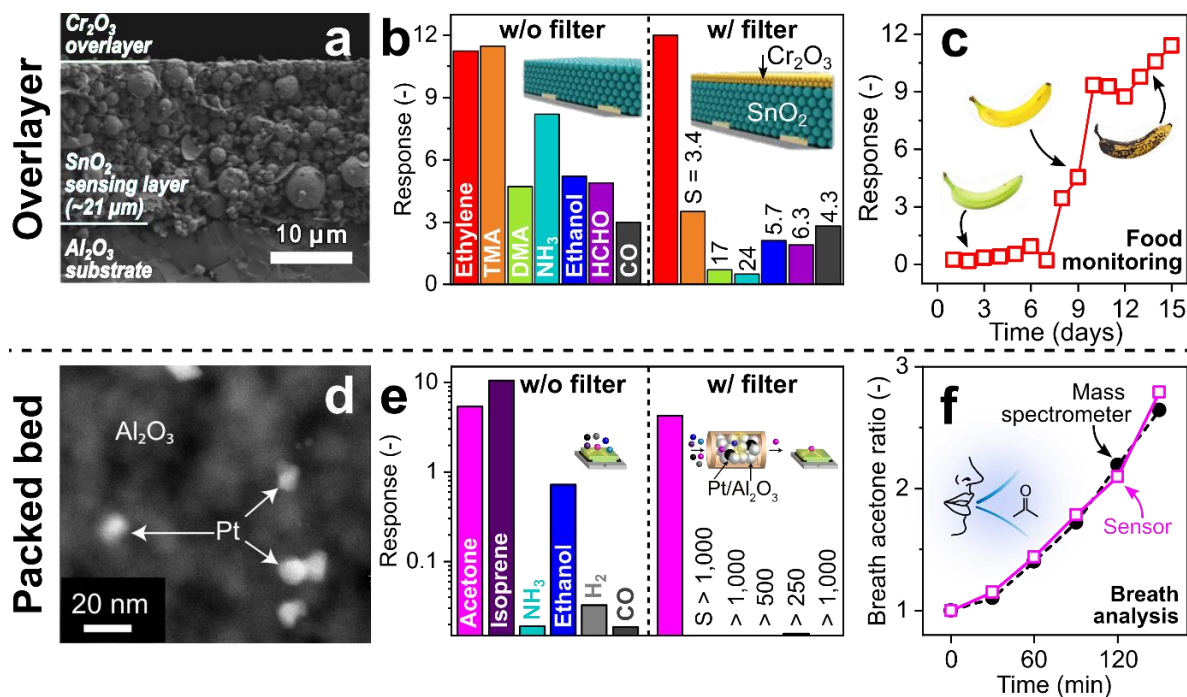


Figure 1.12: (a) SnO_2 sensor (375 °C) with catalytic Cr_2O_3 overlayer. Reproduced with permission.³¹² Open Access CC BY. (b) SnO_2 sensor response to 2.5 ppm ethylene, trimethylamine (TMA), dimethylamine (DMA), ammonia (NH_3), ethanol, formaldehyde (HCHO) and CO without and with the Cr_2O_3 overlayer with the resulting ethylene selectivities.³¹² (c) Sensor response with filter layer when exposed to an underripe ($t < 7$ days), a ripe ($t > 7$ days) and an overripe banana ($t > 10$ days).³¹² (d) Catalytic $\text{Pt}/\text{Al}_2\text{O}_3$ filter. Reproduced with permission.⁷⁰ Open Access CC BY. (e) Si/WO_3 sensor (400 °C) response to 1 ppm acetone, isoprene, NH_3 , ethanol, H_2 and CO without and with the packed bed $\text{Pt}/\text{Al}_2\text{O}_3$ filter (135 °C, please note the logarithmic y-axis) resulting in superior acetone selectivity.⁷⁰ (f) Breath acetone concentration ratio (normalized to initial concentration) as measured by the $\text{Pt}/\text{Al}_2\text{O}_3$ - Si/WO_3 detector (open squares) and benchtop mass spectrometer (filled circles) during post-exercise rest.⁷⁰ Illustrations in (b)³¹² and (f)⁷⁰ were reproduced with permission. Open Access CC BY.

Most importantly, the sensor exhibits sufficiently low limit of detection (i.e., 5.5 ppb that is superior even to 30 ppb by more bulky GC-IMS³¹⁹), and the response time is not affected by the filter (i.e., 1.3 min at 100 ppb). For validation, breath samples after exercise were analyzed by the filter–sensor system and simultaneously with benchtop mass spectrometry (Figure 1.12f). The sensor correctly detects the increase of breath acetone indicating fat burn, in excellent agreement to the benchtop method and is applicable also in extreme scenarios (i.e., in presence of alcohol disinfectants as well as > 50 ppm H_2 and CH_4 in exhaled breath³²⁰). Such filter–sensor systems can be implemented readily in commercial portable breath analyzers.³²¹

Table 1.4: Catalytic filters in combination with gas sensors.

Filter configuration	Filter material	Target analyte	Sensor	LOD ^a (ppm)	Response time	Tested interferants (selectivity)	Ref
Overlayer	Al ₂ O ₃	CH ₄	Pellistor	25,000	–	Hexamethyldisiloxane (<1)	59
	Co ₃ O ₄	Benzene	Pd/SnO ₂	0.25	3 s	Ethanol (5.1), xylene (4.8), toluene (2.6), CO (2.4), formaldehyde (2.4)	300
	CuO	CO	SnO ₂	900	–	Ethanol (<1)	308
	Cr ₂ O ₃	Ethylene	SnO ₂	0.1	9 s	NH ₃ (24), dimethylamine (17), formaldehyde (6.3), ethanol (5.7), CO (4.3), trimethylamine (3.4)	312
	Ga ₂ O ₃	CH ₄	Ga ₂ O ₃	500	–	Ethanol (2), acetone (<1)	286
	Zeolite MFI	CO	Pd/WO ₃	100	–	Acetone, ethanol, methanol (all <1)	305
	SnO ₂ , TiO ₂	Toluene, xylene	Co ₃ O ₄	5	<6 min	Formaldehyde (>20), CO (>10), benzene (>8), ethanol (>7.6)	303
	Pt	CO	SnO ₂	10	–	NO ₂ (<1), ozone (<1)	310
		Propane	In _{0.1} Sb _{0.003} Pd _{0.1} /SnO ₂	500	–	CO (40), ethanol (<1)	73
	Pd	Propane	In _{0.1} Sb _{0.003} Pd _{0.1} /SnO ₂	500	–	CO (>1,000), ethanol (1)	73
	Pd, Ag	CO, H ₂	SnO ₂	1,000	–	Ozone (<1)	307
	Pt/Al ₂ O ₃	CH ₄ , ethane	SnO ₂	100	<3 min	CO (>1,000), ethanol (>20), benzene (>10), acetone (>5)	250
		Benzene	WO ₃	1	–	Ethanol (5.8), NH ₃ (<1), NO ₂ (<1)	301
	Pt & Pd/SiO ₂	CH ₄	SnO ₂	200	–	CO (>1,000)	278
	Pt/Zeolite MFI	Propane	SrTi _{0.8} Fe _{0.2} O _{3-δ}	500	–	CO (>100), NO (>100), H ₂ (>20), propene (>50)	285
		Methanol	Pd/WO ₃	2	–	CO (>1,000), ethanol (13), acetone (8)	305
	Pd/Al ₂ O ₃ , SiO _x , WO ₃	CH ₄ , butane, propane	SnO _x , InO _x	10,000	–	CO, ethanol	51
	Pd/Al ₂ O ₃	CH ₄	Pd/SnO ₂	50	–	CO (>1,000), ethanol (1)	283
		CO, CH ₄	SnO ₂	100	<100 ms	CO (10), H ₂ (5)	284
		Propane	SnO ₂	300	–	ethanol (1)	287
	Heptane, octane	SnO ₂	150	–	NO ₂ (5), CO (2.75)	282	
Packed bed	Mo/Zeolite Y	Heptane, octane	Cr _{1.95} Ti _{0.05} O ₃	–	–	Nonane (1), decane (2), undecane (3)	309
	ZnO	Acetone, benzene, H ₂ , CH ₄ , toluene	Si/WO ₃	0.25	–	Ethanol (81), formaldehyde	294
	Au/Ce _{0.8} Zr _{0.2} O ₂	CH ₄	Pt/SnO ₂	5,000	35 s	Acetone, CO, ethanol, formaldehyde, toluene (all > 100)	288
	Au/Fe ₂ O ₃	CH ₄ , propane	Pt/SnO ₂	2,000	10 s	CO, ethanol (both >1,000)	291
	Au/TiO ₂	Propane	SnO ₂	100	–	CO (2.1)	292
	Au/ZnO	Propane	SnO ₂	100	–	CO (7.4)	292
	Pt/Al ₂ O ₃	Acetone	Si/WO ₃	0.05	55 s	CO (>1,000), isoprene (>1,000), NH ₃ (>1,000), ethanol (>500), H ₂ (>250),	70
		Propane	Pt/LaFeO ₃	1,000	30 s	CO (>1), NO (>100)	306

^aLowest measured concentration.

1.5 References

1. M. Mayer and A. J. Baeumner, *Chem. Rev.*, **2019**, 119, 7996-8027.
2. A. Schütze and T. Sauerwald, in *Advanced Nanomaterials for Inexpensive Gas Microsensors*, ed. E. Llobet, Elsevier, **2020**, pp. 209-234.
3. A. C. Rai, P. Kumar, F. Pilla, A. N. Skouloudis, S. Di Sabatino, C. Ratti, et al., *Sci. Total Environ.*, **2017**, 607-608, 691-705.
4. T. Salthammer, S. Mentese and R. Marutzky, *Chem. Rev.*, **2010**, 110, 2536-2572.
5. R. Beelen, G. Hoek, D. Vienneau, M. Eeftens, K. Dimakopoulou, X. Pedeli, et al., *Atmos. Environ.*, **2013**, 72, 10-23.
6. M. Rigby, S. Park, T. Saito, L. Western, A. Redington, X. Fang, et al., *Nature*, **2019**, 569, 546-550.
7. H. Yousefi, H.-M. Su, S. M. Imani, K. Alkhaldi, C. D. M. Filipe and T. F. Didar, *ACS Sens.*, **2019**, 4, 808-821.
8. O. L. Gamborg and T. A. LaRue, *Nature*, **1968**, 220, 604-605.
9. C. Lindinger, D. Labbe, P. Pollien, A. Rytz, M. A. Juillerat, C. Yeretizian and I. Blank, *Anal. Chem.*, **2008**, 80, 1574-1581.
10. A. R. Shalaby, *Food Res. Int.*, **1996**, 29, 675-690.
11. A. T. Güntner, S. Abegg, K. Königstein, P. A. Gerber, A. Schmidt-Trucksäss and S. E. Pratsinis, *ACS Sens.*, **2019**, 4, 268-280.
12. S. M. Gordon, J. P. Szidon, B. K. Krotoszynski, R. D. Gibbons and H. J. O'Neill, *Clin. Chem.*, **1985**, 31, 1278-1282.
13. M. J. Henderson, B. Karger and G. Wrenshall, *Diabetes*, **1952**, 1, 188-200.
14. C. N. Tassopoulos, D. Barnett and T. Russell Fraser, *Lancet*, **1969**, 293, 1282-1286.
15. S. T. Senthilmohan, D. B. Milligan, M. J. McEwan, C. G. Freeman and P. F. Wilson, *Redox Rep.*, **2000**, 5, 151-153.
16. S. Giannoukos, A. Agapiou and S. Taylor, *J. Breath Res.*, **2018**, 12, 027106.
17. A. M. Curran, S. I. Rabin, P. A. Prada and K. G. Furton, *J. Chem. Ecol.*, **2005**, 31, 1607-1619.
18. K. E. Jones, K. Dashfield, A. B. Downend and C. M. Otto, *J. Am. Vet. Med. Assoc.*, **2004**, 225, 854-860.
19. B. de Lacy Costello, A. Amann, H. Al-Kateb, C. Flynn, W. Filipiak, T. Khalid, et al., *J. Breath Res.*, **2014**, 8, 014001.
20. O. O. Hänninen, S. Alm, K. Katsouyanni, N. Künzli, M. Maroni, M. J. Nieuwenhuijsen, et al., *J. Exposure Sci. Environ. Epidemiol.*, **2004**, 14, 440-456.
21. T. Seiyama, A. Kato, K. Fujiishi and M. Nagatani, *Anal. Chem.*, **1962**, 34, 1502-1503.
22. C. Nylander, B. Liedberg and T. Lind, *Sens. Actuators*, **1982**, 3, 79-88.
23. N. J. Pineau, S. D. Keller, A. T. Güntner and S. E. Pratsinis, *Microchim. Acta*, **2020**, 187, 96.
24. M. E. Prévôt, A. Nemati, T. R. Cull, E. Hegmann and T. Hegmann, *Adv. Mater. Technol.*, **2020**, 5, 2000058.
25. L. Wang, A. Teleki, S. E. Pratsinis and P. I. Gouma, *Chem. Mater.*, **2008**, 20, 4794-4796.
26. V. Jayaraman, G. Mangamma, T. Gnanasekaran and G. Periaswami, *Solid State Ionics*, **1996**, 86, 1111-1114.
27. T. Ishihara, K. Shiokawa, K. Eguchi and H. Arai, *Chem. Lett.*, **1988**, 17, 997-1000.
28. H.-J. Cho, Y. H. Kim, S. Park and I.-D. Kim, *ChemNanoMat*, **2020**, 6, 1014-1027.
29. Z. Dai, T. Liang and J.-H. Lee, *Nanoscale Adv.*, **2019**, 1, 1626-1639.
30. J. A. Kemmler, S. Pokhrel, J. Birkenstock, M. Schowalter, A. Rosenauer, N. Barsan, et al., *Sens. Actuators B Chem.*, **2012**, 161, 740-747.

31. A. T. Güntner, N. J. Pineau, D. Chie, F. Krumeich and S. E. Pratsinis, *J. Mater. Chem. B*, **2016**, 4, 5358-5366.
32. A. T. Güntner, M. Righettoni and S. E. Pratsinis, *Sens. Actuators B Chem.*, **2016**, 223, 266-273.
33. R. Qian, Z. Yumin, L. Tianping, S. Kaiyuan, Z. Baoye, Z. Zhongqi, et al., *Nanotechnology*, **2018**, 29, 145503.
34. M. Bendahan, C. Jacolin, P. Lauque, J.-L. Seguin and P. Knauth, *J. Phys. Chem. B*, **2001**, 105, 8327-8333.
35. M. Akiyama, J. Tamaki, N. Miura and N. Yamazoe, *Chem. Lett.*, **1991**, 20, 1611-1614.
36. M. Hauptmann, P. A. Stewart, J. H. Lubin, L. E. Beane Freeman, R. W. Hornung, R. F. Herrick, et al., *J. Natl. Cancer Inst.*, **2009**, 101, 1696-1708.
37. C. J. Weschler, *Indoor air*, **2000**, 10, 269-288.
38. K. Persaud and G. Dodd, *Nature*, **1982**, 299, 352-355.
39. W. Hu, L. Wan, Y. Jian, C. Ren, K. Jin, X. Su, et al., *Adv. Mater. Technol.*, **2019**, 4, 1800488.
40. A. Hierlemann and R. Gutierrez-Osuna, *Chem. Rev.*, **2008**, 108, 563-613.
41. S. Matindoust, M. Baghaei-Nejad, M. H. S. Abadi, Z. Zou and L.-R. Zheng, *Sens. Rev.*, **2016**, 36, 169-183.
42. R. E. Amor, M. K. Nakhleh, O. Barash and H. Haick, *Eur. Respir. Rev.*, **2019**, 28, 190002.
43. S. Haykin and K. R. Liu, *Handbook on array processing and sensor networks*, John Wiley & Sons, **2010**.
44. Z. Chen, Z. Chen, Z. Song, W. Ye and Z. Fan, *J. Semicond.*, **2019**, 40, 111601.
45. G. Peng, U. Tisch, O. Adams, M. Hakim, N. Shehada, Y. Y. Broza, et al., *Nat. Nanotechnol.*, **2009**, 4, 669-673.
46. M. B. Banerjee, R. B. Roy, B. Tudu, R. Bandyopadhyay and N. Bhattacharyya, *J. Food Eng.*, **2019**, 244, 55-63.
47. F. Röck, N. Barsan and U. Weimar, *Chem. Rev.*, **2008**, 108, 705-725.
48. N. J. Pineau, J. F. Kompalla, A. T. Güntner and S. E. Pratsinis, *Microchim. Acta*, **2018**, 185, 563-563.
49. S. R. Morrison, *Sens. Actuators*, **1987**, 12, 425-440.
50. G. Korotcenkov, in *Handbook of Gas Sensor Materials: Properties, Advantages and Shortcomings for Applications Volume 1: Conventional Approaches*, Springer New York, New York, NY, **2013**, pp. 293-303.
51. C. A. Papadopoulos, D. S. Vlachos and J. N. Avaritsiotis, *Sens. Actuators B Chem.*, **1996**, 32, 61-69.
52. F. Röck, N. Barsan and U. Weimar, *Chem. Rev.*, **2008**, 108, 705-725.
53. K. Sahner, G. Hagen, D. Schonauer, S. Reiss and R. Moos, *Solid State Ionics*, **2008**, 179, 2416-2423.
54. W.-T. Koo, J.-S. Jang and I.-D. Kim, *Chem*, **2019**, 5, 1938-1963.
55. T. Wagner, S. Haffer, C. Weinberger, D. Klaus and M. Tiemann, *Chem. Soc. Rev.*, **2013**, 42, 4036-4053.
56. C. Allman and G. Khilnani, *Adv. Instrum.*, **1983**, 38, 399-406.
57. A. Ryzhikov, M. Labeau and A. Gaskov, *Selectivity Improvement of Semiconductor Gas Sensors by Filters*, presented in part at the Sensors for Environment, Health and Security, Dordrecht, **2009**.
58. D. J. Wales, J. Grand, V. P. Ting, R. D. Burke, K. J. Edler, C. R. Bowen, et al., *Chem. Soc. Rev.*, **2015**, 44, 4290-4321.
59. J. B. Miller, *IEEE Sens. J.*, **2001**, 1, 88-93.

60. C. Pijolat, B. Riviere, M. Kamionka, J. P. Viricelle and P. Breuil, *J. Mater. Sci.*, **2003**, 38, 4333-4346.
61. J.-W. Yoon and J.-H. Lee, *Lab Chip*, **2017**, 17, 3537-3557.
62. G. N. Advani and A. G. Jordan, *J. Electron. Mater.*, **1980**, 9, 29-49.
63. K. Fukui and K. Komatsu, Proceedings of the International Meeting on Chemical Sensors, Analytical Chemistry Symposia Series, vol. 17, p. 52-36, Fukuoka, Japan, **1983**.
64. S. J. Gentry and S. R. Howarth, *Sens. Actuators*, **1984**, 5, 265-273.
65. K. Nagashima and S. Suzuki, *Anal. Chim. Acta*, **1984**, 162, 153-159.
66. M. Schweizer-Berberich, S. Strathmann, W. Göpel, R. Sharma and A. Peyre-Lavigne, *Sens. Actuators B Chem.*, **2000**, 66, 34-36.
67. H. Debéda, P. Massok, C. Lucat, F. Ménil and J.-L. Aucouturier, *Meas. Sci. Technol.*, **1997**, 8, 99-110.
68. J. van den Broek, S. Abegg, S. E. Pratsinis and A. T. Güntner, *Nat. Commun.*, **2019**, 10, 4220.
69. F. A. A. Nugroho, I. Darmadi, L. Cusinato, A. Susarrey-Arce, H. Schreuders, L. J. Bannenberg, et al., *Nat. Mater.*, **2019**, 18, 489-495.
70. I. C. Weber, H. P. Braun, F. Krumeich, A. T. Güntner and S. E. Pratsinis, *Adv. Sci.*, **2020**, 7, 2001503.
71. J. van den Broek, A. T. Güntner and S. E. Pratsinis, *ACS Sens.*, **2018**, 3, 677-683.
72. Y. Li, J. Liu, M. Liu, F. Yu, L. Zhang, H. Tang, et al., *Electrochem. Commun.*, **2016**, 64, 42-45.
73. C. H. Kwon, D. H. Yun, H.-K. Hong, S.-R. Kim, K. Lee, H. Y. Lim and K. H. Yoon, *Sens. Actuators B Chem.*, **2000**, 65, 327-330.
74. R. T. Yang, *Gas separation by adsorption processes*, Butterworth-Heinemann, **2013**.
75. O. Hugon, M. Sauvan, P. Benech, C. Pijolat and F. Lefebvre, *Sens. Actuators B Chem.*, **2000**, 67, 235-243.
76. T. Oyabu, Y. Matuura and R. Murai, *Sens. Actuators B Chem.*, **1990**, 1, 218-221.
77. X. Zhang, B. Gao, A. E. Creamer, C. Cao and Y. Li, *J. Hazard. Mater.*, **2017**, 338, 102-123.
78. S. Brunauer, L. S. Deming, W. E. Deming and E. Teller, *J. Am. Chem. Soc.*, **1940**, 62, 1723-1732.
79. S. J. Gregg, K. S. W. Sing and H. Salzberg, *J. Electrochem. Soc.*, **1967**, 114, 279C-279C.
80. Scientific Instrument Services (SIS), Tenax® TA breakthrough volume data, <https://www.sisweb.com/index/referenc/tenaxta.htm>, (accessed 2019/08/20).
81. M. Harper, *J. Chromatogr. A*, **2000**, 885, 129-151.
82. J. Rouquerol, F. Rouquerol, P. Llewellyn, G. Maurin and K. S. Sing, *Adsorption by powders and porous solids: principles, methodology and applications*, Academic press, **2013**.
83. I. M. Klotz, *Chem. Rev.*, **1946**, 39, 241-268.
84. N. Mohan, G. K. Kannan, S. Upendra, R. Subha and N. S. Kumar, *J. Hazard. Mater.*, **2009**, 168, 777-781.
85. M. Harper, *Ann. Occup. Hyg.*, **1993**, 37, 65-88.
86. Z.-H. Huang, F. Kang, K.-M. Liang and J. Hao, *J. Hazard. Mater.*, **2003**, 98, 107-115.
87. K. Frank, H. Kohler and U. Guth, *Sens. Actuators B Chem.*, **2009**, 141, 361-369.
88. K. Allen, T. Von Backström and D. Kröger, *Powder Technol.*, **2013**, 246, 590-600.
89. K. Dettmer and W. Engewald, *Anal. Bioanal. Chem.*, **2002**, 373, 490-500.
90. R. J. Peters and H. A. Bakkeren, *Analyst*, **1994**, 119, 71-74.
91. C. Turner, P. Španěl and D. Smith, *Physiol. Meas.*, **2006**, 27, 321-337.

92. World Health Organization, *WHO guidelines for indoor air quality: Selected pollutants*, **2010**.
93. K.-D. Kwon, W.-K. Jo, H.-J. Lim and W.-S. Jeong, *J. Hazard. Mater.*, **2007**, 148, 192-198.
94. F. Gritti and G. Guiochon, *Anal. Chem.*, **2006**, 78, 4642-4653.
95. D. S. Hage, in *Principles and Applications of Clinical Mass Spectrometry*, Elsevier, **2018**.
96. L. Ferrus, H. Guenard, G. Vardon and P. Varene, *Respir. Physiol.*, **1980**, 39, 367-381.
97. I. Maier and M. Fieber, *J. High Resolut. Chromatogr.*, **1988**, 11, 566-576.
98. G. Odell Wood, *Carbon*, **1992**, 30, 593-599.
99. A. A. Pesaran and A. F. Mills, *Int. J. Heat Mass Transfer*, **1987**, 30, 1037-1049.
100. X. Zhao, Q. Ma and G. Lu, *Energy Fuels*, **1998**, 12, 1051-1054.
101. K. Sakodinskii, L. Panina and N. Klinskaya, *Chromatographia*, **1974**, 7, 339-344.
102. A. Khaleel, P. N. Kapoor and K. J. Klabunde, *Nanostruct. Mater.*, **1999**, 11, 459-468.
103. S. Brosillon, M.-H. Manero and J.-N. Foussard, *Environ. Sci. Technol.*, **2001**, 35, 3571-3575.
104. N. M. Padial, E. Quartapelle Procopio, C. Montoro, E. López, J. E. Oltra, V. Colombo, et al., *Angew. Chem., Int. Ed.*, **2013**, 52, 8290-8294.
105. O. K. Farha, I. Eryazici, N. C. Jeong, B. G. Hauser, C. E. Wilmer, A. A. Sarjeant, et al., *J. Am. Chem. Soc.*, **2012**, 134, 15016-15021.
106. J. Rouquerol, D. Avnir, C. Fairbridge, D. Everett, J. Haynes, N. Pernicone, et al., *Pure Appl. Chem.*, **1994**, 66, 1739-1758.
107. C. Baerlocher, L. B. McCusker and D. H. Olson, *Atlas of zeolite framework types*, Elsevier, **2007**.
108. T. G. Glover and B. Mu, *Gas Adsorption in Metal-Organic Frameworks: Fundamentals and Applications*, CRC Press, **2018**.
109. J.-M. Li and O. Talu, in *Stud. Surf. Sci. Catal.*, ed. M. Suzuki, Elsevier, **1993**, vol. 80, pp. 373-380.
110. K. Yang, Q. Sun, F. Xue and D. Lin, *J. Hazard. Mater.*, **2011**, 195, 124-131.
111. Y. Morigami, M. Kondo, J. Abe, H. Kita and K. Okamoto, *Sep. Purif. Technol.*, **2001**, 25, 251-260.
112. Y. Sun, B. Gao, Y. Yao, J. Fang, M. Zhang, Y. Zhou, et al., *Chem. Eng. J.*, **2014**, 240, 574-578.
113. W. Shen, Z. Li and Y. Liu, *Recent Pat. Chem. Eng.*, **2008**, 1, 27-40.
114. L. Li, S. Liu and J. Liu, *J. Hazard. Mater.*, **2011**, 192, 683-690.
115. J. Boudou, A. Martinez-Alonzo and J. Tascon, *Carbon*, **2000**, 38, 1021-1029.
116. C. L. Mangun, K. R. Benak, J. Economy and K. L. Foster, *Carbon*, **2001**, 39, 1809-1820.
117. J. L. Figueiredo, M. Pereira, M. Freitas and J. Orfao, *Carbon*, **1999**, 37, 1379-1389.
118. Lalhmunsiama, S. M. Lee, S. S. Choi and D. Tiwari, *Metals*, **2017**, 7, 248.
119. Y. Li, J. He, Z. Kaisheng, T. Liu, Y. Hu, X. Chen, et al., *RSC Adv.*, **2019**, 9, 397-407.
120. S. Dipendu and D. Shuguang, *Tsinghua Sci. Technol.*, **2010**, 15, 363-376.
121. A. Stone, *The theory of intermolecular forces*, Oxford University Press, **2013**.
122. H.-J. Butt and M. Kappl, *Surface and interfacial forces*, Wiley Online Library, **2010**.
123. G. A. Jeffrey, *An introduction to hydrogen bonding*, Oxford University Press, **1997**.
124. S. Sircar, M. B. Rao and T. C. Golden, in *Stud. Surf. Sci. Catal.*, eds. A. Dąbrowski and V. A. Tertykh, Elsevier, **1996**, vol. 99, pp. 629-646.
125. M. Nishibori, W. Shin, N. Izu, T. Itoh and I. Matsubara, *Sens. Actuators B Chem.*, **2009**, 137, 524-528.
126. H. Suto and G. Inoue, *J. Atmos. Ocean. Technol.*, **2010**, 27, 1175-1184.

127. Ł. Guz, G. Łagód, K. Jaromin-Gleń, Z. Suchorab, H. Sobczuk and A. Bieganowski, *Sensors*, **2015**, 15, 1-21.
128. D. Vlachos, P. Skafidas and J. Avaritsiotis, *Sens. Actuators B Chem.*, **1995**, 25, 491-494.
129. A. Prabhakar, R. A. Iglesias, X. Shan, X. Xian, L. Zhang, F. Tsow, et al., *Anal. Chem.*, **2012**, 84, 7172-7178.
130. L.-Y. Chang, M.-Y. Chuang, H.-W. Zan, H.-F. Meng, C.-J. Lu, P.-H. Yeh and J.-N. Chen, *ACS Sens.*, **2017**, 2, 531-539.
131. N. Yamazoe, J. Fuchigami, M. Kishikawa and T. Seiyama, *Surf. Sci.*, **1979**, 86, 335-344.
132. R. H. Castro and D. V. Quach, *J. Phys. Chem. C*, **2012**, 116, 24726-24733.
133. R. Salerno-Kennedy and K. D. Cashman, *Wien. Klin. Wochenschr.*, **2005**, 117, 180-186.
134. M. Schweizer-Berberich, S. Strathmann, U. Weimar, R. Sharma, A. Seube, A. Peyre-Lavigne and W. Göpel, *Sens. Actuators B Chem.*, **1999**, 58, 318-324.
135. M. Righettoni, A. Tricoli, S. Gass, A. Schmid, A. Amann and S. E. Pratsinis, *Anal. Chim. Acta*, **2012**, 738, 69-75.
136. S. Schon, S. J. Theodore and A. T. Güntner, *Sens. Actuators, B*, **2018**, 273, 1780-1785.
137. A. Teleki, S. E. Pratsinis, K. Kalyanasundaram and P. I. Gouma, *Sens. Actuators B Chem.*, **2006**, 119, 683-690.
138. P.-I. Gouma, L. Wang, S. Simon and M. Stanacevic, *Sensors*, **2017**, 17, 199.
139. L. Cisneros, F. Gao and A. Corma, *Micropor. Mesopo. Mater.*, **2019**, 283, 25-30.
140. R. L. Jordan, C. P. Hauser and A. G. Dawson, *Analyst*, **1997**, 122, 811-814.
141. G. Bergshoeff, R. W. Lanting, J. van Ham, J. M. Prop and H. F. Reijnders, *Analyst*, **1984**, 109, 1165-1169.
142. W. R. Penrose, L. Pan, J. R. Stetter and W. M. Ollison, *Anal. Chim. Acta*, **1995**, 313, 209-219.
143. J. Brunet, L. Spinelle, A. Pauly, M. Dubois, K. Guerin, M. Bouvet, et al., *Org. Electron.*, **2010**, 11, 1223-1229.
144. J. Brunet, A. Pauly, M. Dubois, M. L. Rodriguez-Mendez, A. L. Ndiaye, C. Varenne and K. Guerin, *Talanta*, **2014**, 127, 100-107.
145. G. A. Lawrance, *Introduction to coordination chemistry*, John Wiley & Sons, **2013**.
146. A. I. Popov and W. W. Wendlandt, *J. Am. Chem. Soc.*, **1955**, 77, 857-859.
147. A. T. Güntner, M. Wied, N. J. Pineau and S. E. Pratsinis, *Adv. Sci.*, **2020**, 7, 1903390.
148. N. J. Pineau, F. Krumeich, A. T. Güntner and S. E. Pratsinis, *Sens. Actuators B Chem.*, **2021**, 327, 128843.
149. H. M. McNair, J. M. Miller and N. H. Snow, *Basic gas chromatography*, John Wiley & Sons, **2019**.
150. B. P. Regmi and M. Agah, *Anal. Chem.*, **2018**, 90, 13133-13150.
151. Quintron, BreathTracker Analyzer, <https://www.breathtests.com/instrumentation>, (accessed 2020/06/02).
152. M. Li, E. B. Myers, H. X. Tang, S. J. Aldridge, H. C. McCaig, J. J. Whiting, et al., *Nano Lett.*, **2010**, 10, 3899-3903.
153. S. C. Terry, J. H. Jerman and J. B. Angell, *IEEE Trans. Electron Devices*, **1979**, 26, 1880-1886.
154. H. Zhu, J. She, M. Zhou and X. Fan, *Sens. Actuators B Chem.*, **2019**, 283, 182-187.
155. H. Jung, W. Cho, R. Yoo, H.-s. Lee, Y.-S. Choe, J. Y. Jeon and W. Lee, *Sens. Actuators B Chem.*, **2018**, 274, 527-532.

156. M. Zhou, J. Lee, H. Zhu, R. Nidetz, K. Kurabayashi and X. Fan, *RSC Adv.*, **2016**, 6, 49416-49424.
157. F. Gao, M. Wang, X. Zhang, J. Zhang, Y. Xue, H. Wan and P. Wang, *Anal. Methods*, **2018**, 10, 4329-4338.
158. H. Meng, W. Yang, X. Yan, Y. Zhang, L. Feng and Y. Guan, *Sens. Actuators B Chem.*, **2015**, 216, 511-517.
159. I. Lara-Ibeas, A. Rodríguez-Cuevas, C. Andrikopoulou, V. Person, L. Baldas, S. Colin and S. Le Calvé, *Micromachines*, **2019**, 10, 187.
160. K. M. Skog, F. Xiong, H. Kawashima, E. Doyle, R. Soto and D. R. Gentner, *Anal. Chem.*, **2019**, 91, 1318-1327.
161. J. Lee, M. Zhou, H. Zhu, R. Nidetz, K. Kurabayashi and X. Fan, *Anal. Chem.*, **2016**, 88, 10266-10274.
162. J. Lee, S. K. Saylor, M. Zhou, H. Zhu, R. J. Richardson, Richard L. Neitzel, et al., *Anal. Methods*, **2018**, 10, 237-244.
163. Defiant Technologies, TOCAM, <https://www.defiant-tech.com/tocam-portable-gas-chromatograph-gc/>, (accessed 2020/06/03).
164. Dräger, X-pid 9000/9500, https://www.draeger.com/en_seeur/Applications/Products/Portable-Gas-Detection/Multi-Gas-Detectors/X-pid-9000-9500, (accessed 2020/06/03).
165. S. Zampolli, I. Elmi, G. C. Cardinali, L. Masini, F. Bonafè and F. Zardi, *Sens. Actuators B Chem.*, **2020**, 305, 127444.
166. J. Wang, N. Nuño, R. Nidetz, S. J. Peterson, B. M. Brookover, W. H. Steinecker and E. T. Zellers, *Anal. Chem.*, **2019**, 91, 4747-4754.
167. Y. Qin and Y. B. Gianchandani, *Microsyst. Nanoeng.*, **2016**, 2, 15049.
168. T. Tzeng, C. Kuo, S. Wang, P. Huang, Y. Huang, W. Hsieh, et al., *IEEE J. Solid-State Circuits*, **2016**, 51, 259-272.
169. P. R. Lewis, P. Manginell, D. R. Adkins, R. J. Kottenstette, D. R. Wheeler, S. S. Sokolowski, et al., *IEEE Sens. J.*, **2006**, 6, 784-795.
170. S. Zampolli, I. Elmi, F. Mancarella, P. Betti, E. Dalcanale, G. C. Cardinali and M. Severi, *Sens. Actuators B Chem.*, **2009**, 141, 322-328.
171. S. K. Kim, H. Chang and E. T. Zellers, *Anal. Chem.*, **2011**, 83, 7198-7206.
172. W. R. Collin, G. Serrano, L. K. Wright, H. Chang, N. Nuño and E. T. Zellers, *Anal. Chem.*, **2014**, 86, 655-663.
173. J. Wang, J. Bryant-Genevier, N. Nuño, C. Zhang, B. Kraay, C. Zhan, et al., *Microsyst. Nanoeng.*, **2018**, 4, 17101.
174. S. Abegg, L. Magro, J. van den Broek, S. E. Pratsinis and A. T. Güntner, *Nat. Food*, **2020**, 1, 351-354.
175. J. van den Broek, D. K. Cerrejon, S. E. Pratsinis and A. T. Güntner, *J. Hazard. Mater.*, **2020**, 399, 123052.
176. H. L. Tian, H. Q. Fan, M. M. Li and L. T. Ma, *ACS Sens.*, **2016**, 1, 243-250.
177. D. Meng, D. Liu, G. Wang, Y. Shen, X. San, M. Li and F. Meng, *Sens. Actuators B Chem.*, **2018**, 273, 418-428.
178. A. T. Güntner, V. Koren, K. Chikkadi, M. Righettoni and S. E. Pratsinis, *ACS Sens.*, **2016**, 1, 528-535.
179. IUPAC, *Compendium of Chemical Terminology*, Blackwell Scientific Publications, **2019**.
180. R. Barro, J. Regueiro, M. Llompарт and C. Garcia-Jares, *J. Chromatogr. A*, **2009**, 1216, 540-566.
181. T. T. Zhou, Y. T. Sang, X. X. Wang, C. Y. Wu, D. W. Zeng and C. S. Xie, *Sens. Actuators B Chem.*, **2018**, 258, 1099-1106.

-
182. N. Kosinov, C. Auffret, C. Gücüyener, B. M. Szyja, J. Gascon, F. Kapteijn and E. J. M. Hensen, *J. Mater. Chem. A*, **2014**, 2, 13083-13092.
183. H. Li, Z. Song, X. Zhang, Y. Huang, S. Li, Y. Mao, et al., *Science*, **2013**, 342, 95-98.
184. N. Kosinov, J. Gascon, F. Kapteijn and E. J. M. Hensen, *J. Membr. Sci.*, **2016**, 499, 65-79.
185. S. M. Auerbach, K. A. Carrado and P. K. Dutta, *Handbook of zeolite science and technology*, CRC Press, Boca Raton, Florida, **2003**.
186. S. Qiu, M. Xue and G. Zhu, *Chem. Soc. Rev.*, **2014**, 43, 6116-6140.
187. S.-Y. Ding and W. Wang, *Chem. Soc. Rev.*, **2013**, 42, 548-568.
188. M. A. Ruiz, A. Sua and F. Tian, in *Encyclopedia of Interfacial Chemistry*, ed. K. Wandelt, Elsevier, Oxford, **2018**, pp. 646-671.
189. J. Liang, Z. Liang, R. Zou and Y. Zhao, *Adv. Mater.*, **2017**, 29, 1701139.
190. T. F. Degnan Jr, C. M. Smith and C. R. Venkat, *Appl. Catal. A*, **2001**, 221, 283-294.
191. R. E. Morris and P. S. Wheatley, *Angew. Chem., Int. Ed.*, **2008**, 47, 4966-4981.
192. S. S.-Y. Chui, S. M.-F. Lo, J. P. H. Charmant, A. G. Orpen and I. D. Williams, *Science*, **1999**, 283, 1148-1150.
193. J. Zhang, Y. Tan and W.-J. Song, *Microchim. Acta*, **2020**, 187, 234.
194. A. F. Ismail, K. C. Khulbe and T. Matsuura, *Gas separation membranes*, Springer, **2015**.
195. R. Krishna and J. Wesselingh, *Chem. Eng. Sci.*, **1997**, 52, 861-911.
196. Z. Kang, L. Fan and D. Sun, *J. Mater. Chem. A*, **2017**, 5, 10073-10091.
197. C. Chi, X. Wang, Y. Peng, Y. Qian, Z. Hu, J. Dong and D. Zhao, *Chem. Mater.*, **2016**, 28, 2921-2927.
198. P. S. Goh, A. F. Ismail, S. M. Sanip, B. C. Ng and M. Aziz, *Sep. Purif. Technol.*, **2011**, 81, 243-264.
199. C. D. Feng, *J. Electrochem. Soc.*, **1994**, 141, 220-225.
200. M. Fleischer, M. Seth, C. D. Kohl and H. Meixner, *Sens. Actuators B Chem.*, **1996**, 36, 297-302.
201. J. Goschnick, M. Frietsch and T. Schneider, *Surf. Coat. Technol.*, **1998**, 108-109, 292-296.
202. Z. L. Zhan, D. G. Jiang and J. Q. Xu, *Mater. Chem. Phys.*, **2005**, 90, 250-254.
203. A. Katsuki and K. Fukui, *Sens. Actuators B Chem.*, **1998**, 52, 30-37.
204. X. Meng, Q. Zhang, S. Zhang and Z. He, *Sensors*, **2019**, 19, 2478.
205. J. Hu, Y. Sun, Y. Xue, M. Zhang, P. Li, K. Lian, et al., *Sens. Actuators B Chem.*, **2018**, 257, 124-135.
206. W. J. Buttner, M. B. Post, R. Burgess and C. Rivkin, *Int. J. Hydrogen Energy*, **2011**, 36, 2462-2470.
207. Y. Luo, C. Zhang, B. Zheng, X. Geng and M. Debligny, *Int. J. Hydrogen Energy*, **2017**, 42, 20386-20397.
208. K. Wada and M. Egashira, *Sens. Actuators B Chem.*, **2000**, 62, 211-219.
209. G. Tournier and C. Pijolat, *Sens. Actuators B Chem.*, **2005**, 106, 553-562.
210. US Department of Energy. *Hydrogen, Fuel Cells and Infrastructure Technologies Program: Multi-Year Research, Development and Demonstration Plan*, **2007**
211. V. V. Sysoev, I. Kiselev, V. Trouillet and M. Bruns, *Sens. Actuators B Chem.*, **2013**, 185, 59-69.
212. S. Ehrmann, J. Jüngst, J. Goschnick and D. Everhard, *Sens. Actuators B Chem.*, **2000**, 65, 247-249.
213. C. Arnold, M. Harms and J. Goschnick, *IEEE Sens. J.*, **2002**, 2, 179-188.
214. N. Kodakari, T. Sakamoto, K. Shinkawa, H. Funabiki, N. Katada and M. Niwa, *Bull. Chem. Soc. Jpn.*, **1998**, 71, 513-519.

215. M. Sekiyama, N. Katada and M. Niwa, *Sens. Actuators B Chem.*, **2007**, 124, 398-406.
216. L. Huang, M. Zhang, C. Li and G. Shi, *J. Phys. Chem. Lett.*, **2015**, 6, 2806-2815.
217. S. C. O'Hern, M. S. Boutilier, J.-C. Idrobo, Y. Song, J. Kong, T. Laoui, et al., *Nano Lett.*, **2014**, 14, 1234-1241.
218. J. Zhao, G. He, S. Huang, L. F. Villalobos, M. Dakhchoune, H. Bassas and K. V. Agrawal, *Sci. Adv.*, **2019**, 5, eaav1851.
219. J. S. Jarig, J. Lee, W. T. Koo, D. H. Kim, H. J. Cho, H. Shin and I. D. Kim, *Anal. Chem.*, **2020**, 92, 957-965.
220. M. Drobek, J. H. Kim, M. Bechelany, C. Vallicari, A. Julbe and S. S. Kim, *ACS Appl. Mater. Interfaces*, **2016**, 8, 8323-8328.
221. M. Chi and Y.-P. Zhao, *Comput. Mater. Sci.*, **2009**, 46, 1085-1090.
222. Z. Li, N. Wang, Z. Lin, J. Wang, W. Liu, K. Sun, et al., *ACS Appl. Mater. Interfaces*, **2016**, 8, 20962-20968.
223. G. Lu and J. T. Hupp, *J. Am. Chem. Soc.*, **2010**, 132, 7832-7833.
224. A. Lan, K. Li, H. Wu, D. H. Olson, T. J. Emge, W. Ki, et al., *Angew. Chem., Int. Ed.*, **2009**, 48, 2334-2338.
225. H. Bux, F. Liang, Y. Li, J. Cravillon, M. Wiebcke and J. Caro, *J. Am. Chem. Soc.*, **2009**, 131, 16000-16001.
226. X. N. Wu, S. S. Xiong, Z. H. Mao, S. Hu and X. G. Long, *Chem.-Eur. J.*, **2017**, 23, 7969-7975.
227. M. Weber, J. H. Kim, J. H. Lee, J. Y. Kim, I. Iatsunskyi, E. Coy, et al., *ACS Appl. Mater. Interfaces*, **2018**, 10, 34765-34773.
228. C. Wadell, S. Syrenova and C. Langhammer, *ACS Nano*, **2014**, 8, 11925-11940.
229. M. Vilaseca, J. Coronas, A. Cirera, A. Cornet, J. R. Morante and J. Santamaria, *Sens. Actuators B Chem.*, **2007**, 124, 99-110.
230. Y. Zhou, T. Zhou, Y. Zhang, L. Tang, Q. Guo, M. Wang, et al., *Solid State Ionics*, **2020**, 350, 115278.
231. Z. Qiao, Q. Xu and J. Jiang, *J. Mater. Chem. A*, **2018**, 6, 18898-18905.
232. K. B. Sezginel, S. Keskin and A. Uzun, *Langmuir*, **2016**, 32, 1139-1147.
233. K. S. Walton, M. B. Abney and M. D. LeVan, *Micropor. Mesopo. Mater.*, **2006**, 91, 78-84.
234. T. Zhou, Z. Qin, X. Wang, C. Wu, X. Tang, T. Zhang, et al., *Chem. Commun.*, **2019**, 55, 11045-11048.
235. M. Vilaseca, J. Coronas, A. Cirera, A. Cornet, J. R. Morante and J. Santamaría, *Catal. Today*, **2003**, 82, 179-185.
236. M. Vilaseca, J. Coronas, A. Cirera, A. Cornet, J. Morante and J. Santamaria, *Sens. Actuators B Chem.*, **2008**, 133, 435-441.
237. K. Fukui and S. Nishida, *Sens. Actuators B Chem.*, **1997**, 45, 101-106.
238. R. Binions, H. Davies, A. Afonja, S. Dungey, D. Lewis, D. E. Williams and I. P. Parkin, *J. Electrochem. Soc.*, **2009**, 156, J46-J51.
239. S. Galioglu, I. Karaduman, T. Çorlu, B. Akata, M. A. Yıldırım, A. Ateş and S. Acar, *J. Mater. Sci.: Mater. Electron.*, **2018**, 29, 1356-1368.
240. D. C. Pugh, E. J. Newton, A. J. T. Naik, S. M. V. Hailes and I. P. Parkin, *J. Mater. Chem. A*, **2014**, 2, 4758-4764.
241. P. Tarttelin Hernández, S. M. V. Hailes and I. P. Parkin, *Sens. Actuators B Chem.*, **2017**, 242, 1281-1295.
242. A. T. Güntner, S. Abegg, K. Wegner and S. E. Pratsinis, *Sens. Actuators B Chem.*, **2018**, 257, 916-923.
243. E. G. Derouane and S. M. Roberts, *Microporous and mesoporous solid catalysts*, John Wiley & Sons, **2006**.

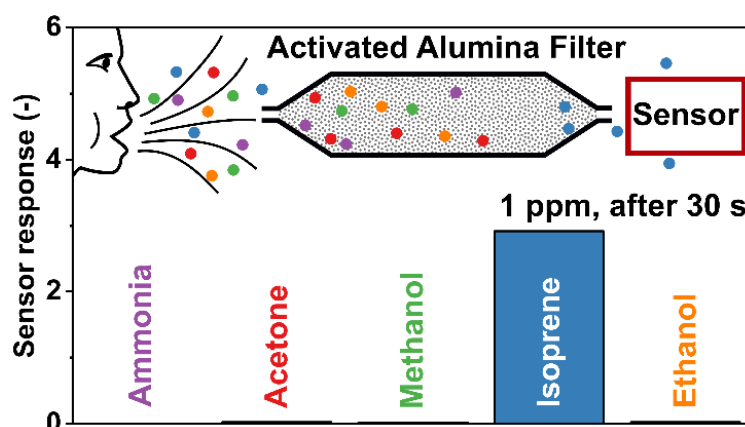
-
244. U. P. Tran, K. K. Le and N. T. Phan, *ACS Catal.*, **2011**, 1, 120-127.
245. S. K. Brown, M. R. Sim, M. J. Abramson and C. N. Gray, *Indoor Air*, **1994**, 4, 123-134.
246. Z. Wang, C. Hou, Q. De, F. Gu and D. Han, *ACS Sens.*, **2018**, 3, 468-475.
247. Y. Sun, H. Yang, Z. Zhao, K. Suematsu, P. Li, Z. Yu, et al., *Sens. Actuators B Chem.*, **2020**, 318, 128222.
248. F. Krumeich, S. Abegg and A. T. Güntner, *Z. Anorg. Allg. Chem.*, **2020**, 646, 412-418.
249. A. Y. Volkov, *Platinum Met. Rev.*, **2004**, 48, 3-11.
250. M. A. Portnoff, R. Grace, A. M. Guzman, P. D. Runco and L. N. Yannopoulos, *Sensors and Actuators: B. Chemical*, **1991**, 5, 231-235.
251. V. Bessonneau and O. Thomas, *Int. J. Environ. Res. Public Health*, **2012**, 9, 868-879.
252. L. F. Liotta, *Appl. Catal., B*, **2010**, 100, 403-412.
253. R. Kikuchi, S. Maeda, K. Sasaki, S. Wennerström and K. Eguchi, *Appl. Catal. A*, **2002**, 232, 23-28.
254. Z. Abbasi, M. Haghghi, E. Fatehifar and S. Saedy, *J. Hazard. Mater.*, **2011**, 186, 1445-1454.
255. R. Strobel, A. Baiker and S. E. Pratsinis, *Adv. Powder Technol.*, **2006**, 17, 457-480.
256. L. Machala, R. Zboril and A. Gedanken, *J. Phys. Chem. B*, **2007**, 111, 4003-4018.
257. J. C. Védrine, *Catalysts*, **2017**, 7, 314-314.
258. M. S. Kamal, S. A. Razzak and M. M. Hossain, *Atmos. Environ.*, **2016**, 140, 117-134.
259. J. W. Maina, C. Pozo-Gonzalo, L. Kong, J. Schütz, M. Hill and L. F. Dumée, *Mater. Horiz.*, **2017**, 4, 345-345.
260. M. A. Sidheswaran, H. Destailats, D. P. Sullivan, J. Larsen and W. J. Fisk, *Appl. Catal., B*, **2011**, 107, 34-41.
261. H. Huang, Y. Xu, Q. Feng and D. Y. C. Leung, *Catal.: Sci. Technol.*, **2015**, 5, 2649-2669.
262. H. A. Benesi, *J. Catal.*, **1967**, 8, 368-374.
263. R. K. Sharma, B. Zhou, S. Tong and K. T. Chuang, *Ind. Eng. Chem. Res.*, **1995**, 34, 4310-4317.
264. R. J. Farrauto, M. Deeba and S. Alerasool, *Nat. Catal.*, **2021**, 2, 603-613.
265. Z. Li, D. Wang, Y. Wu and Y. Li, *Natl. Sci. Rev.*, **2018**, 5, 673-689.
266. M. Phillips, *Anal. Biochem.*, **1997**, 247, 272-278.
267. A. G. Panov and J. J. Fripiat, *J. Catal.*, **1998**, 178, 188-197.
268. M. Frankel, G. Bekö, M. Timm, S. Gustavsen, E. W. Hansen and A. M. Madsen, *Appl. Environ. Microbiol.*, **2012**, 78, 8289-8297.
269. J. A. Moulijn, O. W. N. M. van Leeuwen and R. A. Santen, *Stud. Surf. Sci. Catal.*, **1993**, 79, 69-86.
270. F. A. Smith, S. Elliott, D. R. Blake and F. S. Rowland, *Environ. Sci. Policy*, **2002**, 5, 449-461.
271. T. G. Leighton and P. R. White, *Proc. R. Soc. A*, **2012**, 468, 485-510.
272. S. Basu and P. K. Basu, *J. Sens.*, **2009**, 2009, 861968.
273. B. Vanderstraeten, J. Berghmans, D. Tuerlinckx, B. Smit, E. Van't Oost and S. Vliegen, *J. Hazard. Mater.*, **1997**, 56, 237-246.
274. S. Prasad, L. Zhao and J. Gomes, *Epidemiology*, **2011**, 22, 251-251.
275. T. Sahm, W. Rong, N. Bârsan, L. Mädler, S. K. Friedlander and U. Weimar, *J. Mater. Res.*, **2007**, 22, 850-857.
276. P. Reimann and A. Schütze, *Sens. Rev.*, **2012**, 32, 47-58.
277. V. Weli and J. O. Adegoke, *J. Pollut. Control*, **2016**, 4, 1000171.
278. A. Cabot, J. Arbiol, A. Cornet, J. R. Morante, F. Chen and M. Liu, *Thin Solid Films*, **2003**, 436, 64-69.

279. S. Ghosh, C. Roychaudhuri, R. Bhattacharya, H. Saha and N. Mukherjee, *ACS Appl. Mater. Interfaces*, **2014**, 6, 3879-3887.
280. S. Ghosh, R. Bhattacharyya, H. Saha, C. R. Chaudhuri and N. Mukherjee, *Phys. Chem. Chem. Phys.*, **2015**, 17, 27777-27788.
281. N. Ikoma, M. Takeya and N. Satoshi, *Combustible gas sensor and method for detecting deterioration of catalyst*, EP0751390A3, **1995**.
282. S. Jansat, K. Pelzer, J. Garcia-Anton, R. Raucoules, K. Philippot, A. Maisonnat, et al., *Adv. Funct. Mater.*, **2007**, 17, 3339-3347.
283. T. Sahn, W. Rong, N. Bârsan, L. Mädler and U. Weimar, *Sens. Actuators B Chem.*, **2007**, 127, 63-68.
284. T. Suzuki, K. Kunihara, M. Kobayashi, S. Tabata, K. Higaki and H. Ohnishi, *Sens. Actuators B Chem.*, **2005**, 109, 185-189.
285. K. Sahner, R. Moos, M. Matam, J. J. Tunney and M. Post, *Sens. Actuators B Chem.*, **2005**, 108, 102-112.
286. M. Fleischer, S. Kornely, T. Weh, J. Frank and H. Meixner, *Sens. Actuators B Chem.*, **2000**, 69, 205-210.
287. G. G. Mandayo, E. Castaño, F. J. Gracia, A. Cirera, A. Cornet and J. R. Morante, *Sens. Actuators B Chem.*, **2002**, 87, 88-94.
288. F. S. Fateminia, Y. Mortazavi and A. A. Khodadadi, *Mater. Sci. Semicond. Process.*, **2019**, 90, 182-189.
289. B. A. Tichenor and M. A. Palazzolo, *Environ. Prog.*, **1987**, 6, 172-176.
290. H. H. Kung, M. Kung and C. Costello, *J. Catal.*, **2003**, 216, 425-432.
291. S. N. Oliaee, A. Khodadadi, Y. Mortazavi and S. Alipour, *Sens. Actuators B Chem.*, **2010**, 147, 400-405.
292. J. Jońca, J. Harmel, L. Joanny, A. Ryzhikov, M. L. Kahn, P. Fau, et al., *Sens. Actuators B Chem.*, **2017**, 249, 357-363.
293. J. Vuković, D. Modun, D. Marković and D. Sutlović, *J. Subst. Abuse Alcohol.*, **2015**, 3, 1029.
294. A. T. Güntner, I. C. Weber and S. E. Pratsinis, *ACS Sens.*, **2020**, 5, 1058-1067.
295. M. P. Kalapos, *Biochim. Biophys. Acta*, **2003**, 1621, 122-139.
296. N. C. Jeong, J. S. Lee, E. L. Tae, Y. J. Lee and K. B. Yoon, *Angew. Chem., Int. Ed.*, **2008**, 47, 10128-10132.
297. T. Mallat and A. Baiker, *Chem. Rev.*, **2004**, 104, 3037-3058.
298. J. Llorca, N. Homs and P. Ramirez de la Piscina, *J. Catal.*, **2004**, 227, 556-560.
299. A. Mirzaei, J.-H. Kim, H. W. Kim and S. S. Kim, *J. Mater. Chem. C*, **2018**, 6, 4342-4370.
300. S.-Y. Jeong, J.-W. Yoon, T.-H. Kim, H.-M. Jeong, C.-S. Lee, Y. Chan Kang and J.-H. Lee, *J. Mater. Chem. A*, **2017**, 5, 1446-1454.
301. J. Hubálek, K. Malysz, J. Prášek, X. Vilanova, P. Ivanov, E. Llobet, et al., *Sens. Actuators B Chem.*, **2004**, 101, 277-283.
302. P. Clément, S. Korom, C. Struzzi, E. J. Parra, C. Bittencourt, P. Ballester and E. Llobet, *Adv. Funct. Mater.*, **2015**, 25, 4011-4020.
303. H.-M. Jeong, S.-Y. Jeong, J.-H. Kim, B.-Y. Kim, J.-S. Kim, F. Abdel-Hady, et al., *ACS Appl. Mater. Interfaces*, **2017**, 9, 41397-41404.
304. L. Cao, Z. Gao, S. L. Suib, T. N. Obee, S. O. Hay and J. D. Freihaut, *J. Catal.*, **2000**, 196, 253-261.
305. Y. Zeng, Z. Hua, X. Tian, X. Li, Z. Qiu, C. Zhang, et al., *Sens. Actuators B Chem.*, **2018**, 273, 1291-1299.
306. M. H. Saberi, Y. Mortazavi and A. A. Khodadadi, *Sens. Actuators B Chem.*, **2015**, 206, 617-623.

-
307. G. Korotcenkov, B. K. Cho, V. Brinzari, L. B. Gulina and V. P. Tolstoy, *Ferroelectrics*, **2014**, 459, 46-51.
 308. M. Frietsch, F. Zudock, J. Goschnick and M. Bruns, *Sens. Actuators B Chem.*, **2000**, 65, 379-381.
 309. D. P. Mann, K. F. E. Pratt, T. Paraskeva, I. P. Parkin and D. E. Williams, *IEEE Sens. J.*, **2007**, 7, 551-556.
 310. J. Wöllenstein, H. Böttner, M. Jaegle, W. J. Becker and E. Wagner, *Sens. Actuators B Chem.*, **2000**, 70, 196-202.
 311. K. Sahner, D. Schönauer, P. Kuchinke and R. Moos, *Sens. Actuators B Chem.*, **2008**, 133, 502-508.
 312. S.-Y. Jeong, Y. K. Moon, T.-H. Kim, S.-W. Park, K. B. Kim, Y. C. Kang and J.-H. Lee, *Adv. Sci.*, **2020**, 7, 1903093.
 313. V. Paul, R. Pandey and G. C. Srivastava, *J. Food Sci. Technol.*, **2012**, 49, 1-21.
 314. H. P. Hofmann, *Catal. Rev. Sci. Eng.*, **1978**, 17, 71-117.
 315. A. T. Güntner, N. A. Sievi, S. J. Theodore, T. Gulich, M. Kohler and S. E. Pratsinis, *Anal. Chem.*, **2017**, 89, 10578-10584.
 316. A. T. Güntner, J. F. Kompalla, H. Landis, S. J. Theodore, B. Geidl, N. A. Sievi, et al., *Sensors*, **2018**, 18, 3655-3655.
 317. A. T. Güntner, N. J. Pineau, P. Mochalski, H. Wiesenhofer, A. Agapiou, C. A. Mayhew and S. E. Pratsinis, *Anal. Chem.*, **2018**, 90, 4940-4945.
 318. R. Yoo, A. T. Güntner, Y. Park, H. J. Rim, H. S. Lee and W. Lee, *Sens. Actuators B Chem.*, **2019**, 283, 107-115.
 319. P. Mochalski, V. Ruzsanyi, H. Wiesenhofer and C. A. Mayhew, *J. Breath Res.*, **2018**, 12, 027107.
 320. K. Tadesse, D. Smith and M. A. Eastwood, *Q. J. Exp. Physiol. Cogn. Med. Sci.*, **1980**, 65, 85-97.
 321. M. Righettoni, A. Ragnoni, A. T. Güntner, C. Loccioni, S. E. Pratsinis and T. H. Risby, *J. Breath Res.*, **2015**, 9, 047101.
 322. S. Kaskel, in *The Chemistry of Metal–Organic Frameworks*, Wiley, **2016**, pp. 271-307.
 323. M. L. Terranova, S. Orlanducci and M. Rossi, *Carbon nanomaterials for gas adsorption*, CRC Press, **2012**.
 324. D. W. Breck, *Zeolite molecular sieves: structure, chemistry and use*, Krieger, **1984**.
 325. M. Van Leeuwen, *Fluid Phase Equilib.*, **1994**, 99, 1-18.
 326. M. Arruebo, J. L. Falconer and R. D. Noble, *J. Membr. Sci.*, **2006**, 269, 171-176.

Chapter 2

Highly selective and rapid breath isoprene sensing enabled by activated alumina filter



Abstract

Isoprene is a versatile breath marker for non-invasive monitoring of high blood cholesterol levels as well as for influenza, end-stage renal disease, muscle activity, lung cancer and liver disease with advanced fibrosis. Its *selective* detection in complex human breath by portable devices (e.g., metal-oxide gas sensors), however, is still challenging. Here, we present a new filter concept based on activated alumina powder enabling fast and highly selective detection of isoprene at the ppb level and high humidity. The filter contains high surface area adsorbents that retain hydrophilic compounds (e.g., ketones, alcohols, ammonia) representing major interferants in breath while hydrophobic isoprene is not affected. As a proof-of-concept, filters of commercial activated alumina powder are combined with highly sensitive but rather non-specific, nanostructured Pt-doped SnO₂ sensors. This results in fast (10 s) measurement of isoprene down to 5 ppb at 90% relative humidity with outstanding selectivity (>100) to breath-relevant acetone, ammonia, ethanol and methanol, superior to state-of-the-art isoprene sensors. Most importantly, when exposed continuously to simulated breath mixtures (four analytes) for eight days, this filter–sensor system showed stable performance. It can be incorporated readily into a portable breath isoprene analyzer promising for simple-in-use blood cholesterol monitoring or other patho/physiological conditions.

2.1 Introduction

Cardiovascular diseases are the leading cause of death,¹ accounting for more than 30% of global deaths in 2015.² Most of them could be preventable by reducing the major risk factors, including smoking, high blood pressure and high blood cholesterol.³ Currently, cholesterol is measured from a lipid profile obtained by a blood test. This means 9–12 hours of fasting before going to a physician for the measurement,⁴ which is both painful and elaborate, especially as often follow-up analyses are necessary due to large day-to-day variation in blood cholesterol concentrations.⁵ What is thus needed, is a fast and non-invasive method to reliably and routinely monitor blood cholesterol levels at home.

Breath analysis is a non-invasive diagnostic and monitoring technique that relies on detection of certain breath markers indicative of pathologic states.⁶ Exhaled isoprene is a by-product of the cholesterol biosynthetic pathway⁷ with typical breath concentrations ranging from 22 to 234 parts-per-billion (ppb)⁸ but even lower levels can occur in children⁹ and young adults.¹⁰ Most interestingly, a strong correlation between breath isoprene and blood cholesterol was shown for patients undergoing treatment with cholesterol-lowering lova-¹¹ and atorvastatins.¹² Increased breath isoprene levels occur also in patients with influenza,¹³ end-stage renal disease¹⁴ and after muscle activity,¹⁵ while such levels are decreased for lung cancer¹⁶ and liver disease with advanced fibrosis.¹⁷ Currently, breath isoprene is detected by mass spectrometry-(MS)¹¹ or gas chromatography-(GC)¹⁸ that are rather expensive, of limited portability and require scientific personnel to operate. Chemiluminescence measurement of isoprene is also possible but shows high interference from sulfur gases and other lower olefins, making precise measurement inaccurate.¹⁹ As a result, available methods are hardly suitable for routine breath tests.

Isoprene ($\text{CH}_2=\text{C}(\text{CH}_3)-\text{CH}=\text{CH}_2$) is a reactive, aliphatic hydrocarbon²⁰ that can be detected at low ppb concentrations also by nanostructured semiconductive metal-oxide (MOx) gas sensors. In specific, sensing films of Ti-doped ZnO deposited by flame aerosol technology were shown to detect isoprene levels down to 5 ppb at breath-relevant 90% relative humidity.²¹ Such sensors are attractive for breath analysis by being inexpensive, simple-in-use and readily miniaturized²² and integrated into portable devices.²³ They also have been applied already quite successfully for non-invasive fat burn monitoring during exercise and rest.²⁴ MOx sensors, however, typically lack selectivity to detect target analytes in breath (>800 compounds)²⁵. Sufficient selectivity was obtained by material design only in few cases, for instance for acetone by ϵ -WO₃,²⁶ ammonia by α -MoO₃²⁷ or triethylamine by hollow SnO₂ microfibers.²⁸ In

particular for isoprene, Ti-doped ZnO²¹ features selectivities in the range of 4 to 15 for breath-relevant acetone, ethanol and ammonia, however, it needs to be improved considering that these interferants are much more concentrated in the breath than isoprene. The major challenge in sensor material design with isoprene is the absence of distinct functional groups (hydroxyl, carbonyl, etc.) that can be exploited for selective sensor interaction.

Further molecular properties such as hydrophilicity and size can be exploited by filters to optimize sensing performance *beyond* chemoresistive surface reactivity. This concept has been applied for selective CO sensing²⁹ through adsorption of hydrocarbon interferants on activated carbon filters and for selective formaldehyde detection using size-selective microporous zeolite membranes.³⁰ Also complex GC columns have been used in combination with sensors for selective detection of trichloroethylene,³¹ alcohols,³² aromatic vapors³³ or even for multiple compounds in breath.³⁴ Such GC–sensor systems, however, require complex instrumentation (i.e., GC column, pre-concentration, ramped heating) and feature typically sluggish response and recovery times (e.g., 60 min³³ for sampling and analysis of aromatic volatiles). Consequently, they seem hardly suitable for real-time portable breath isoprene detectors.

Here, we present a novel filter–sensor concept for rapid and highly selective isoprene detection in complex breath mixtures at high relative humidity exploiting the hydrophobic nature of isoprene (Figure 2.1a). It consists of a packed bed of activated alumina featuring high

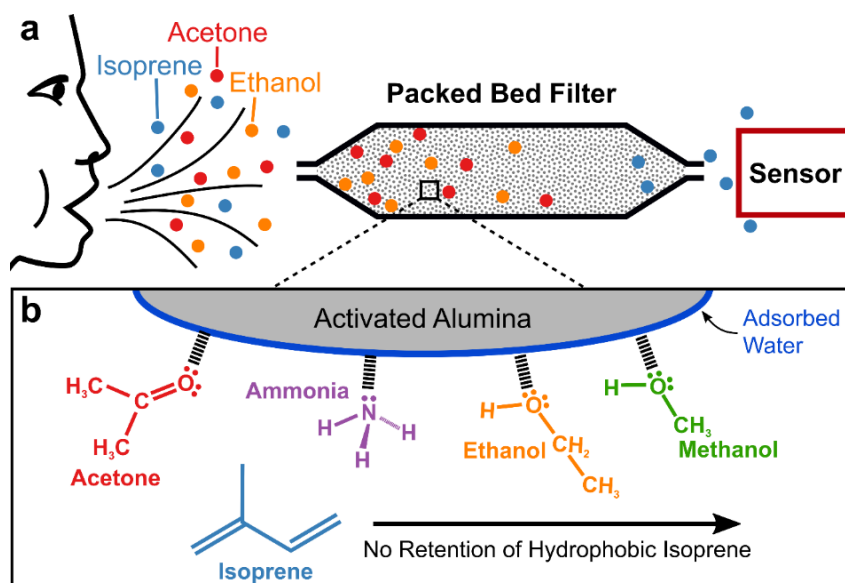


Figure 2.1: Filter–sensor concept of selective isoprene detection in complex gas mixtures: (a) Breath is filtered through a packed bed filter upstream of a highly sensitive but nonspecific gas sensor. (b) Hydrophilic analytes (e.g., acetone, ammonia, ethanol, methanol, etc.) are adsorbed and retained on the activated alumina and on the adsorbed water layer. In contrast, hydrophobic isoprene does not interact with the filter. This enables highly selective isoprene detection at low ppb concentration in real-time.

porosity and surface area ($\sim 155 \text{ m}^2/\text{g}$)³⁵ to adsorb and retain hydrophilic breath compounds while isoprene passes unhindered (Figure 2.1b). Placed upstream of a highly sensitive but non-specific, nanostructured Pt-doped SnO_2 sensor, this filter is characterized for isoprene in gas mixtures with up to four components at 90% relative humidity (RH). Finally, filter regeneration and long-term stability are evaluated for eight days of continuous operation.

2.2 Experimental

2.2.1 Sensor fabrication

Sensing films of Pt-doped (0.15 mol%) SnO_2 are prepared by flame spray pyrolysis (FSP) and directly deposited onto sensor substrates.³⁶ For the FSP precursor solution, tin (II) ethylhexanoate (Strem, $\sim 90\%$ in 2-ethylhexanoic acid) and platinum acetylacetonate (Alfa Aesar, min. 48.0 % Pt) are dissolved in xylene (Aldrich, $\geq 99.7\%$) to give a total metal concentration of 0.5 mol/L with a Pt-doping content of 0.15 mol%.³⁷ The precursor is fed through a FSP nozzle with 5 mL/min and dispersed with 5 L/min oxygen at a pressure drop of 1.5 bar. This spray is ignited by a premixed, ring-shaped methane/oxygen (1.25/3.2 L/min) flame³⁸ while additional 5 L/min of oxygen is supplied as sheath gas. Deposition takes place by thermophoresis³⁶ of Pt-doped SnO_2 nanoparticles onto sensor substrates mounted on a water-cooled holder at 20 cm height above the burner (HAB) for 2 min. The applied Al_2O_3 substrates (15 mm \times 13 mm \times 0.8 mm, Electronic Design Center, Case Western Reserve University) feature interdigitated Pt electrodes (sputtered, 350 μm width and spacing) and a Pt heater on the back. To improve adhesion and cohesion of these FSP-deposited nanoparticle films, they are in-situ annealed³⁹ with a particle-free flame. For this, the substrate is lowered to a HAB of 14.5 cm and annealed for 30 s by a xylene flame (11 ml/min xylene dispersed by 5 L/min oxygen at 1.5 bar) with the same methane/oxygen flame and sheath gas as for the sensing film deposition. Prior to testing, sensors are thermally stabilized by heating in an oven (Carbolite GmbH) at 500 °C for 5 h.

2.2.2 Filter fabrication

The filter consists of a packed bed of 1 g activated alumina (Sigma-Aldrich, neutral pH when in water, 50-300 mesh, $155 \text{ m}^2/\text{g}$) inside a Teflon tube (10 cm length, 15 mm inner diameter) and is firmly secured downstream by a porous, inert Teflon frit and upstream by an inert glass wool plug (Figure 2.2a). On both ends of the Teflon tube, tapered Swagelok connectors expand and contract the gas flow homogeneously to ensure utilization of the entire filter cross section and avoid stagnant zones. Freshly prepared filters are flushed with 1 L/min

air at 90 % RH for at least 12 h to saturate the alumina surface with humidity and guarantee equilibrium conditions.

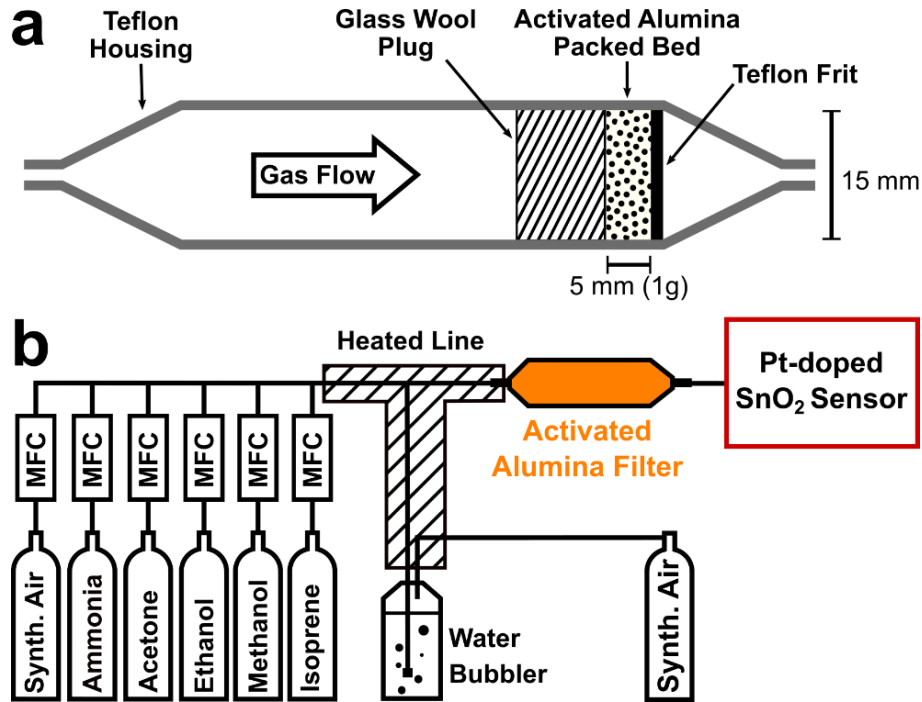


Figure 2.2: Schematic of the activated alumina filter (a) and the gas measurement setup (b).

2.2.3 Gas evaluation

The filter–sensor system (Figure 2.2b) consists of the gas delivery,²⁷ activated alumina filter and Pt-doped SnO₂ sensor. The sensor is mounted on a Macor holder and installed inside a Teflon sensor chamber⁴⁰ where it is heated to 400 °C by DC current (R&S HMC8043, Germany) by the substrate back-heater. The temperature is maintained by utilizing the Pt heater as resistance temperature detector (RTD), monitored with a multimeter (Keithley, 2700, USA). The ohmic resistance of the sensing film between the interdigitated electrodes is measured by the same multimeter. Sensor responses are evaluated as:

$$S = \frac{R_{Air}}{R_{Analyte}} - 1$$

where R_{Air} and $R_{Analyte}$ denote the sensor film resistances measured in synthetic air without and with a given analyte concentration, respectively. The sensor response (t_{90}) and filter breakthrough time (t_5) for an analyte are defined as the time to reach 90% and 5%⁴¹ of the steady-state response, respectively.

Sensor measurements were performed at a total gas flow rate of 1 L/min and 90% RH. Gas mixtures were prepared by first admixing the analyte gas standards with dry synthetic air (PanGas, hydrocarbon-free grade) by calibrated mass flow controllers (Bronkhorst,

Netherlands). Analyte gases are supplied from calibrated gas standards (PanGas) in synthetic air at concentrations of 10 ppm for acetone, isoprene, ammonia and 50 ppm for ethanol, methanol, ammonia. These analytes are present in breath at relatively high concentration and are selected because of their known interaction with Pt-doped SnO₂ sensors, unlike other breath compounds like H₂⁴². The humidity level was set by guiding synthetic air through a water bubbler and dosing it to the gas mixture stream to obtain the desired relative humidity level as verified by a humidity sensor (SHT2x, Sensirion AG). Teflon gas lines were heated to ~50 °C to avoid condensation and adsorption.²⁷

2.3 Results and discussion

2.3.1 Filter effect on isoprene selectivity

Figure 2.3a shows the sensor response profiles of Pt-doped SnO₂ to 500 ppb of isoprene (blue), acetone (red), ethanol (orange), methanol (green) and ammonia (purple) at breath-relevant⁴³ 90% RH. These analytes represent major components in exhaled breath with median concentrations higher than the 106 ppb⁴⁴ of isoprene (e.g., ammonia 833 ppb⁴⁵). The sensor detects *all* these analytes within a few seconds (e.g., $t_{90} = 2.9$ s for isoprene), sufficiently fast for real-time breath analysis. However, it *cannot* distinguish them. In fact, when evaluating the individual responses after 30 s (Figure 2.3b), representing a typical breath test duration,²⁴ the rather non-specific nature of Pt-doped SnO₂ becomes evident, in line with previous results.³⁷ Consequently, this sensor cannot measure isoprene selectively in breath mixtures.

Most importantly, when adding the activated alumina filter (Figure 2.3c), an *identical* response for isoprene is obtained with barely affected response dynamics (t_{90} of 4.2 s), while all hydrophilic analytes are held back. This results in *unprecedented* high isoprene-selectivity (>100) to all analytes Figure 2.3d). Only after 40 s, the sensor starts to detect acetone while it takes even longer for the other hydrophilic analytes (full responses in Figure B.1). In specific, breakthrough times t_5 strongly vary between the analytes from 50 to 300 s for acetone to ammonia, respectively (Figure 2.3d in parenthesis). Important also, after analyte exposure is stopped, the sensor fully recovers the initial baseline enabling repeated measurements. Note that the breakthrough and regeneration times of hydrophilic analytes can be controlled by the activated alumina filter loading, while the response time of isoprene is barely affected (shown in Figure B.2). One gram of activated alumina was selected for deeper investigation to guarantee an interferent-free detection of isoprene, fast filter regeneration for repeated measurements and a low pressure drop of ~20 mbar, sufficiently small²⁴ for breath analyzers.

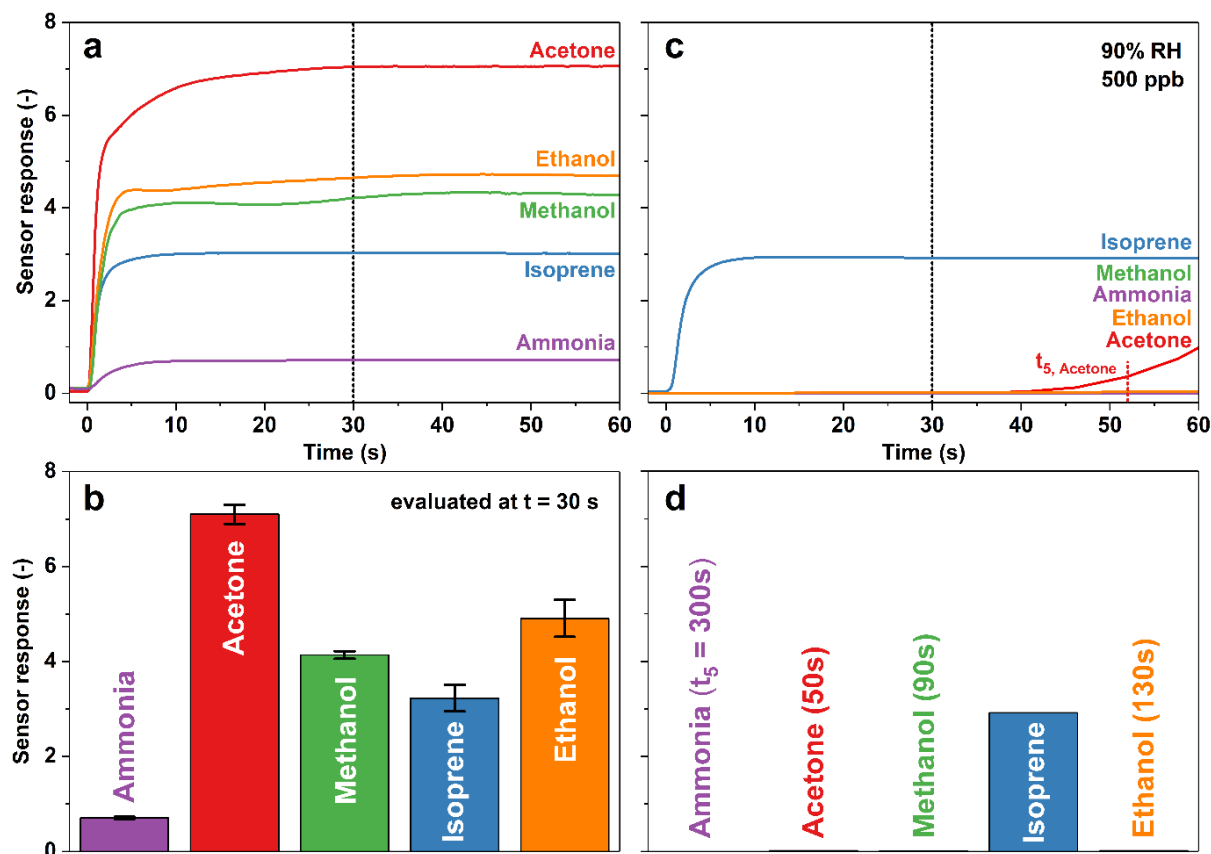


Figure 2.3: The responses of a Pt-doped SnO₂ sensor at 90% RH to 500 ppb of isoprene (blue), acetone (red), ethanol (orange), methanol (green) and ammonia (purple) without (a, b) and with a 1 g activated alumina filter (c, d). The single Pt-doped SnO₂ sensor without filter is rather non-specific when evaluating the responses after 30 s (b). Error bars indicate the response variability of three such sensors, which is smaller than 10%. Using the filter, hydrophilic analytes are held back until their characteristic breakthrough time t_5 , while the response of isoprene is unchanged (c). This results in very high isoprene-selectivity (>100) when evaluated, for instance, after 30 s (d).

The selectivities achieved by the proposed filter–sensor system clearly outperform state-of-the-art chemoresistive isoprene sensors. Highest isoprene selectivities obtained so far were in the range of 4 to 15 for acetone, ethanol and ammonia with Ti-doped ZnO.²¹ Other chemoresistive sensors of TiO₂⁴⁶ and *h*-WO₃⁴⁷ could detect isoprene but did not achieve selectivities >4. Only the chemiluminescence detector Fast Isoprene Sensor (FIS, Hills-Scientific) features similarly high isoprene selectivities, but this device is hardly suitable for routine measurements by a widespread population due to its high cost (base module \$42'000), weight (18 kg) and requirement of an external ozonizer.⁴⁸

2.3.2 Separation mechanism

When passing through the filter, hydrophilic analytes (i.e., alcohols, ketones, ammonia) are retained by adsorption on the activated alumina (Figure 2.1b) featuring extremely large surface area (155 m²/g).³⁵ Note that the alumina surface should be mostly covered by bound

water⁴⁹ at 90% RH because of its high affinity,⁵⁰ so gas ad-/absorption may occur on/in that layer as well.⁵¹ As a result, the strength of analyte-filter interaction should be governed by the ability for hydrogen bonding,⁵² with ammonia having four, ethanol and methanol three, acetone only two and isoprene zero hydrogen bonding sites (oxygen/nitrogen lone electron pairs & hydrogen atoms). This matches well with the t_5 of the analytes, following *the same* order (Figure 2.3d). Note that any water layer formed by RH (i.e., surface hydration) weakens sorption of hydrophilic compounds, as indicated by shorter t_5 for acetone at 50% RH (Figure B.3) and consistent with literature.⁵³

In contrast, isoprene is hydrophobic and passes through the filter unscathed, consistent with the sensing results (compare Figure 2.3a to c). Isoprene is the major hydrocarbon in breath (up to 70% of total)⁵⁴ but also other hydrophobic species (e.g., ethane, pentane)⁵⁵ should pass the filter unaffected and cause measurement errors, if interfering with the sensor. However, this can be prevented by combining this modular filter with an additional size-selective zeolite membrane to remove larger hydrocarbons (as applied already for sensing of formaldehyde)³⁰ or with an E-nose that can distinguish single components in gas mixtures with small prediction errors.³⁷

2.3.3 Gas mixtures

Human breath consists of >800 compounds,²⁵ so evaluation of the proposed filter-sensor system in gas mixtures is crucial. Figure 2.4a shows the Pt-doped SnO₂ response *with filter* to two consecutive 30 s exposures of simultaneous 500 ppb isoprene and acetone (grey-shaded). Most interestingly, two distinct responses are observed for each exposure. The first one increases immediately upon exposure, stays stable at ~3 and rapidly decreases after it. It is associated *solely* to isoprene, as evident from *single* isoprene exposure at the same conditions (blue line, Figure 2.4b) resulting in an *identical* response profile. The second response in Figure 2.4a is delayed, starting after ~40 s and spreading out over a couple of minutes. This response is related to acetone. In fact, it is identical to single acetone exposure (red line, Figure 2.4b) and the breakthrough time, t_5 , similar to longer exposures (Figure 2.3c). As a result, the outstanding separation properties of the filter are preserved also in binary mixtures and isoprene is detected *selectively* during such short breath-realistic exposures. Remarkable also, the filter-sensor system recovers fully within 5 min and gives repeatable signals for continuous application. Note that these results were cross-validated by a bench-top proton-transfer-reaction time-of-flight mass spectrometer (PTR-TOF-MS) (Figure B.4).

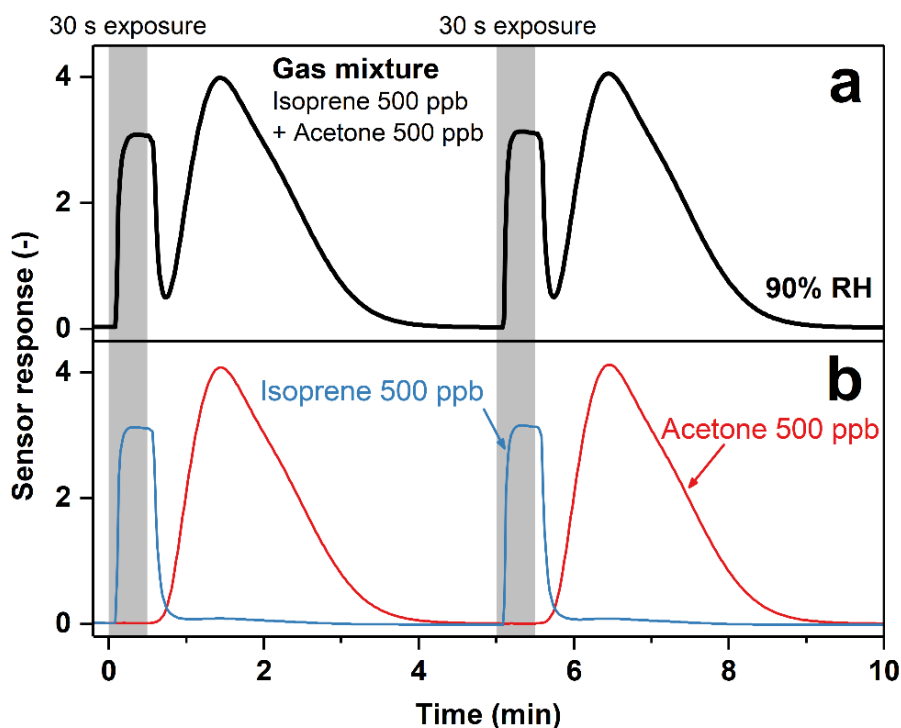


Figure 2.4: (a) Pt-doped SnO_2 sensor response with filter to a gas mixture of 500 ppb isoprene and acetone at 90% RH. Two consecutive pulses of 30 s (grey-shaded) were applied at 0 and 4.5 min, simulating breath pulses. (b) The single gas responses to 500 ppb of isoprene (blue) and acetone (red) at 90% RH.

2.3.4 Low-ppb isoprene detection

Breath isoprene levels can be at low ppb concentration, therefore, the Pt-doped SnO_2 sensor *with filter* was exposed to low but breath-relevant isoprene concentrations of 20, 10 and 5 ppb at 90% RH (Figure 2.5a). The sensor rapidly responds to these levels with high signal-to-noise ratio (>90) and can distinguish them clearly. When flushed with air, the filter–sensor system quickly regenerates (within 3 min) the original baseline and gives identical responses after repeated exposures to 20 and 10 ppb, indicating excellent reproducibility.

This filter–sensor system is applicable over the entire breath-relevant concentration range of isoprene from 5 to 500 ppb at 90% RH (blue crosses in Figure 2.5b). The resulting sensor responses follow a power law ($S \sim c^n$ with $n = 0.64$, $R^2 > 0.995$), in agreement with non-linear diffusion-reaction theory.⁵⁶ Remarkably as well, the presence of the filter does not compromise the sensor response to isoprene in comparison to that *without filter* (Figure 2.5b, red circles).

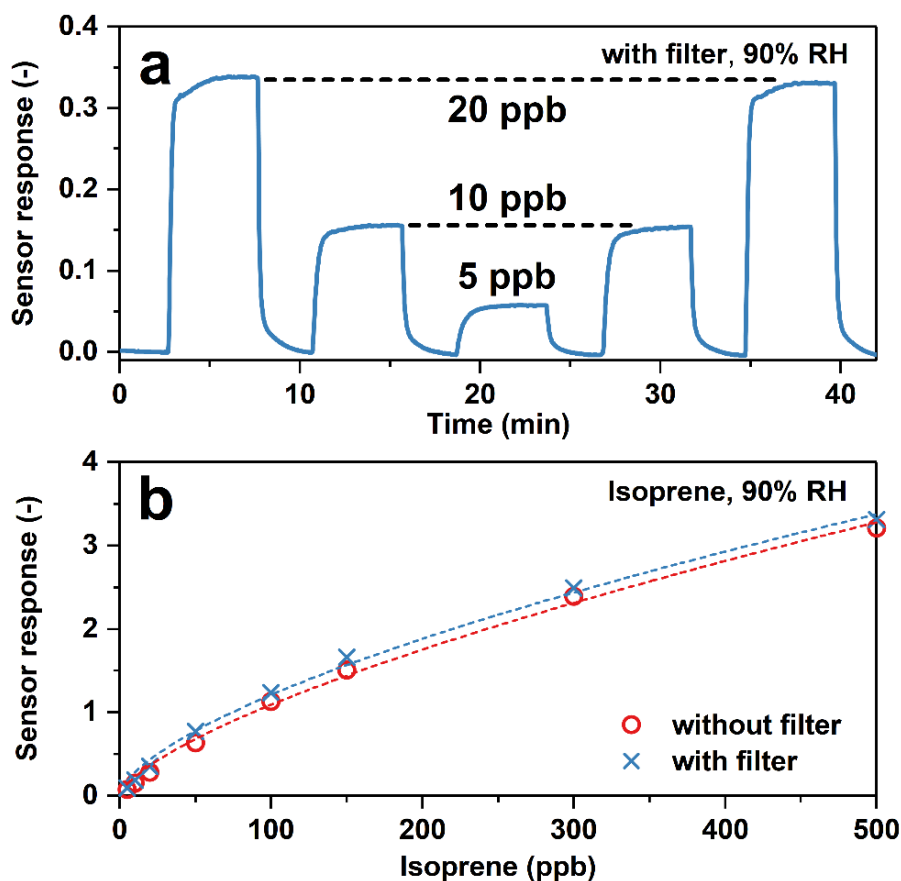


Figure 2.5: (a) Pt-doped SnO₂ sensor response with filter upon exposure to 5, 10 and 20 ppb of isoprene at 90% RH. These ultra-low but breath-relevant concentrations are detectable, reproducible and clearly distinguishable (signal-to-noise ratio >90). The filter quickly and fully regenerates after each pulse. (b) Sensor response curves without (red circles) and with filter (blue crosses) over the entire breath-relevant concentration range of isoprene from 5 to 500 ppb at 90% RH.

2.3.5 Operational stability with simulated breath

To challenge the filter–sensor system further, operational stability was evaluated during continuous operation for eight days at 90% RH. To simulate daily breath isoprene measurement, three consecutive pulses of a gas mixture containing breath-median concentrations of isoprene (106 ppb)⁴⁴, acetone (477 ppb)⁴⁵, methanol (461 ppb)⁵⁷ and ammonia (833 ppb)⁴⁵ were applied daily. Figure 2.6a shows the sensor responses during such a measurement cycle after six days. Isoprene is registered quickly and accurately from the first plateau during the exposure while all polar analytes are held back resulting in a delayed and accumulated spread response, similar to binary mixtures (Figure 2.4a). This enables precise measurement of isoprene even after several days of continuous operation despite the more concentrated interferants. Indeed, when evaluating the sensor baseline (red circles in Figure 2.6b) and isoprene response resistance (blue squares) during these eight days, both are quite stable (<6% change), corresponding to a change in sensor response <20% (Figure B.5). This is

consistent with previous results on Pt-doped SnO₂ sensors *without filters* when operated for 20 days,⁵⁸ and could be corrected by an additional processing algorithm.⁵⁹ The filter should not contribute to this drift since it regenerates completely after each simulated breath exposure (Figure 2.6a), as confirmed by bench-top PTR-TOF-MS (Figure B.4). Consequently, the filter–sensor system is promising for breath isoprene measurement, but this needs to be confirmed with tests on humans as was done recently²⁴ with acetone and Si-doped WO₃ sensors to monitor body fat burn during exercise and rest.

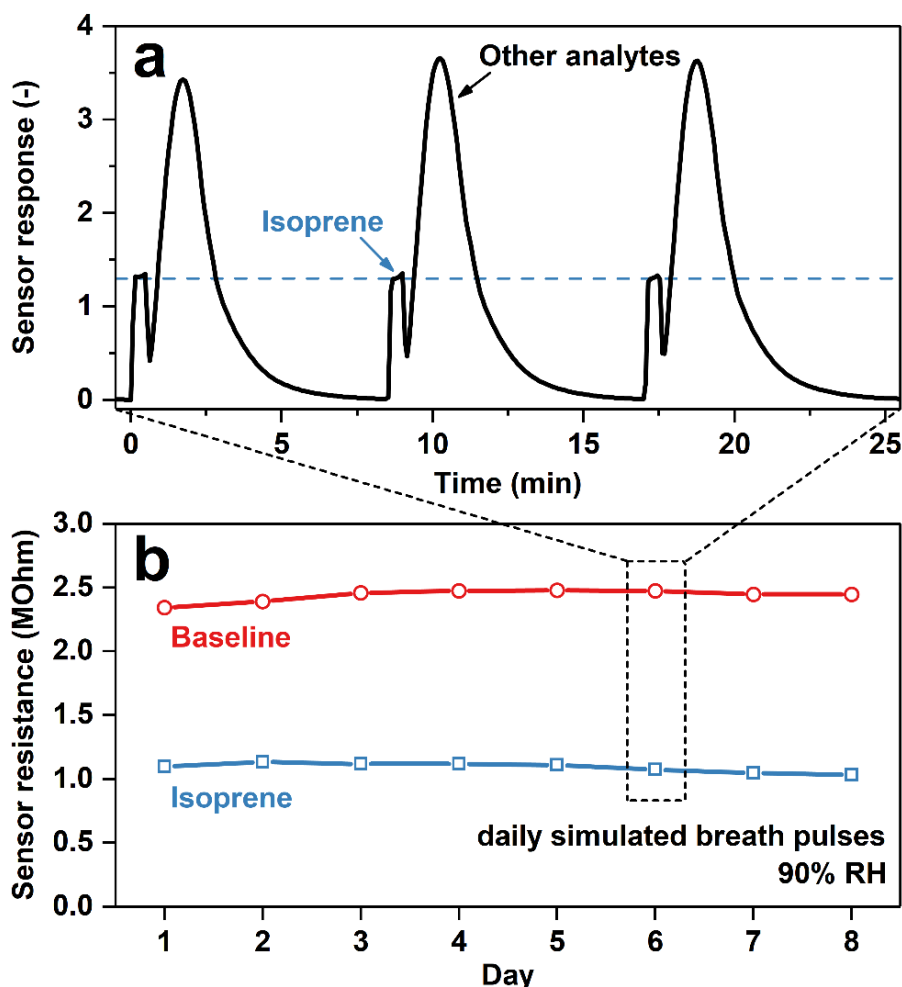


Figure 2.6: (a) Response of Pt-doped SnO₂ with filter to three consecutive 30 s pulses of simulated breath composed of 106 ppb isoprene, 477 ppb acetone, 461 ppb methanol and 833 ppb ammonia at 90% RH on the sixth day of continuous monitoring. (b) Evolution of the sensor baseline resistance (red circles) and the isoprene response resistance (blue squares) during eight days of continuous operation and daily simulated breath analysis.

2.4 Conclusions

A filter–sensor concept was introduced for rapid and highly selective isoprene detection in breath-relevant gas mixtures. The filter is a packed bed of activated alumina offering large surface area to retain hydrophilic compounds without affecting hydrophobic isoprene. As

proof-of-concept, filters of activated alumina turned a highly sensitive, non-specific Pt-doped SnO₂ sensor *isoprene-selective* (>100) to breath-relevant acetone, ammonia, ethanol and methanol at 90% RH. That way, isoprene is detected selectively down to 5 ppb within seconds, more than sufficient for real-time breath analysis. Even when operated continuously for eight days, this filter–sensor system showed stable performance with reproducible (regeneration within 10 min) and accurate isoprene detection in simulated breath mixtures. Based on their small size and modular design, they can be integrated readily into inexpensive and portable breath analyzers promising for non-invasive monitoring of blood cholesterol levels and other patho/physiological conditions.

2.5 References

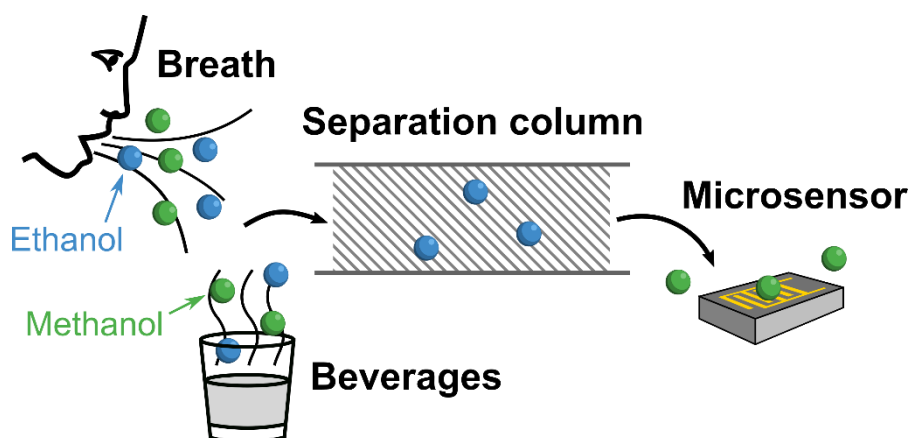
1. S. Mendis, P. Puska and B. Norrving, *Global atlas on cardiovascular disease prevention and control*, World Health Organization, **2011**.
2. V. Feigin, *Lancet*, **2016**, 388, 1459-1544.
3. H. C. McGill, C. A. McMahan and S. S. Gidding, *Circulation*, **2008**, 117, 1216-1227.
4. N. J. Stone, J. G. Robinson, A. H. Lichtenstein, C. N. Bairey Merz, C. B. Blum, R. H. Eckel, et al., *J. Am. Coll. Cardiol.*, **2014**, 63, 2889-2934.
5. L. Bookstein, S. S. Gidding, M. Donovan and F. A. Smith, *Arch. Intern. Med.*, **1990**, 150, 1653-1657.
6. T. H. Risby and S. F. Solga, *Appl. Phys. B*, **2006**, 85, 421-426.
7. E. S. Deneris, R. A. Stein and J. F. Mead, *Biochem. Biophys. Res. Commun.*, **1984**, 123, 691-696.
8. P. Španěl, S. Davies and D. Smith, *Rapid Commun. Mass Spectrom.*, **1999**, 13, 1733-1738.
9. N. Nelson, V. Lagesson, A. R. Nosratabadi, J. Ludvigsson and C. Tagesson, *Pediatr. Res.*, **1998**, 44, 363-367.
10. D. Smith, P. Španěl, B. Enderby, W. Lenney, C. Turner and S. J. Davies, *J. Breath Res.*, **2009**, 4, 017101.
11. B. G. Stone, T. J. Besse, W. C. Duane, C. D. Evans and E. G. DeMaster, *Lipids*, **1993**, 28, 705-708.
12. T. Karl, P. Prazeller, D. Mayr, A. Jordan, J. Rieder, R. Fall and W. Lindinger, *J. Appl. Physiol.*, **2001**, 91, 762-770.
13. A. Mashir, K. Paschke, D. Van Duin, N. Shrestha, D. Laskowski, M. Storer, et al., *J. Breath Res.*, **2011**, 5, 037107.
14. S. Davies, P. Španěl and D. Smith, *Nephrol., Dial., Transplant.*, **2001**, 16, 836-839.
15. J. King, A. Kupferthaler, K. Unterkofler, H. Koc, S. Teschl, G. Teschl, et al., *J. Breath Res.*, **2009**, 3, 027006.
16. A. Bajtarevic, C. Ager, M. Pienz, M. Klieber, K. Schwarz, M. Ligor, et al., *BMC Cancer*, **2009**, 9, 348.
17. N. Alkhouri, T. Singh, E. Alsabbagh, J. Guirguis, T. Chami, I. Hanouneh, et al., *Clin. Transl. Gastroenterol.*, **2015**, 6, e112.
18. J. M. Sanchez and R. D. Sacks, *Anal. Chem.*, **2003**, 75, 2231-2236.
19. S.-I. Ohira, J. Li, W. A. Lonneman, P. K. Dasgupta and K. Toda, *Anal. Chem.*, **2007**, 79, 2641-2649.

20. J. Clayden, N. Greeves and S. Warren, *Organic chemistry*, Oxford University Press, Oxford, **2012**.
21. A. T. Güntner, N. J. Pineau, D. Chie, F. Krumeich and S. E. Pratsinis, *J. Mater. Chem. B*, **2016**, 4, 5358-5366.
22. M. M. McCartney, Y. Zrodnikov, A. G. Fung, M. K. LeVasseur, J. M. Pedersen, K. O. Zamuruyev, et al., *ACS Sens.*, **2017**, 2, 1167-1174.
23. M. Righettoni, A. Ragnoni, A. T. Güntner, C. Loccioni, S. E. Pratsinis and T. H. Risby, *J. Breath Res.*, **2015**, 9, 047101.
24. A. T. Güntner, N. A. Sievi, S. J. Theodore, T. Gulich, M. Kohler and S. E. Pratsinis, *Anal. Chem.*, **2017**, 89, 10578-10584.
25. B. de Lacy Costello, A. Amann, H. Al-Kateb, C. Flynn, W. Filipiak, T. Khalid, et al., *J. Breath Res.*, **2014**, 8, 014001.
26. L. Wang, A. Teleki, S. E. Pratsinis and P. I. Gouma, *Chem. Mater.*, **2008**, 20, 4794-4796.
27. A. T. Güntner, M. Righettoni and S. E. Pratsinis, *Sens. Actuators B Chem.*, **2016**, 223, 266-273.
28. Y. Zou, S. Chen, J. Sun, J. Liu, Y. Che, X. Liu, et al., *ACS Sens.*, **2017**, 2, 897-902.
29. M. Schweizer-Berberich, S. Strathmann, W. Göpel, R. Sharma and A. Peyre-Lavigne, *Sens. Actuators B Chem.*, **2000**, 66, 34-36.
30. A. T. Güntner, S. Abegg, K. Wegner and S. E. Pratsinis, *Sens. Actuators B Chem.*, **2018**, 257, 916-923.
31. S. K. Kim, H. Chang and E. T. Zellers, *Anal. Chem.*, **2011**, 83, 7198-7206.
32. A. K. Wanekaya, M. Uematsu, M. Breimer and O. A. Sadik, *Sens. Actuators B Chem.*, **2005**, 110, 41-48.
33. S. Zampolli, I. Elmi, F. Mancarella, P. Betti, E. Dalcanale, G. C. Cardinali and M. Severi, *Sens. Actuators B Chem.*, **2009**, 141, 322-328.
34. T. Itoh, T. Miwa, A. Tsuruta, T. Akamatsu, N. Izu, W. Shin, et al., *Sensors*, **2016**, 16, 1891.
35. R. T. Yang, *Gas separation by adsorption processes*, Imperial College Press London, **1997**.
36. L. Mädler, A. Roessler, S. E. Pratsinis, T. Sahn, A. Gurlo, N. Barsan and U. Weimar, *Sens. Actuators B Chem.*, **2006**, 114, 283-295.
37. A. T. Güntner, V. Koren, K. Chikkadi, M. Righettoni and S. E. Pratsinis, *ACS Sens.*, **2016**, 1, 528-535.
38. L. Mädler, H. K. Kammler, R. Mueller and S. E. Pratsinis, *J. Aerosol Sci.*, **2002**, 33, 369-389.
39. A. Tricoli, M. Graf, F. Mayer, S. Kühne, A. Hierlemann and S. E. Pratsinis, *Adv. Mater.*, **2008**, 20, 3005-3010.
40. M. Righettoni, A. Tricoli, S. Gass, A. Schmid, A. Amann and S. E. Pratsinis, *Anal. Chim. Acta*, **2012**, 738, 69-75.
41. C. J. Geankoplis, *Transport processes and separation process principles*, Prentice Hall, **2003**.
42. B.-Y. Kim, J. S. Cho, J.-W. Yoon, C. W. Na, C.-S. Lee, J. H. Ahn, et al., *Sens. Actuators B Chem.*, **2016**, 234, 353-360.
43. L. Ferrus, H. Guenard, G. Vardon and P. Varene, *Respir. Physiol.*, **1980**, 39, 367-381.
44. C. Turner, P. Španěl and D. Smith, *Physiol. Meas.*, **2005**, 27, 13-22.
45. T. Claire, Š. Patrik and S. David, *Physiol. Meas.*, **2006**, 27, 321-337.
46. A. Teleki, S. E. Pratsinis, K. Kalyanasundaram and P. I. Gouma, *Sens. Actuators B Chem.*, **2006**, 119, 683-690.
47. P.-I. Gouma, L. Wang, S. Simon and M. Stanacevic, *Sensors*, **2017**, 17, 199.

48. Fast Isoprene Sensor, <http://www.hills-scientific.com/>, (accessed 17/11/27, 2017).
49. R. H. R. Castro and D. V. Quach, *J. Phys. Chem. C*, **2012**, 116, 24726-24733.
50. S. Sircar, M. Rao and T. Golden, *Stud. Surf. Sci. Catal.*, **1996**, 99, 629-646.
51. C. M. Roth, K.-U. Goss and R. P. Schwarzenbach, *J. Colloid Interface Sci.*, **2002**, 252, 21-30.
52. A. Delle Site, *J. Phys. Chem. Ref. Data*, **2001**, 30, 187-439.
53. K.-U. Goss and S. J. Eisenreich, *Environ. Sci. Technol.*, **1996**, 30, 2135-2142.
54. D. Gelmont, R. A. Stein and J. F. Mead, *Biochem. Biophys. Res. Commun.*, **1981**, 99, 1456-1460.
55. C. F. Kneepkens, G. Lepage and C. C. Roy, *Free Radicals Biol. Med.*, **1994**, 17, 127-160.
56. J. W. Gardner, *Sens. Actuators B Chem.*, **1990**, 1, 166-170.
57. C. Turner, P. Španěl and D. Smith, *Physiol. Meas.*, **2006**, 27, 637-648.
58. L. Mädler, T. Sahm, A. Gurlo, J. D. Grunwaldt, N. Barsan, U. Weimar and S. E. Pratsinis, *J. Nanopart. Res.*, **2006**, 8, 783-796.
59. T. Artursson, T. Eklöv, I. Lundström, P. Mårtensson, M. Sjöström and M. Holmberg, *J. Chemom.*, **2000**, 14, 711-723.

Chapter 3

Highly selective detection of methanol over ethanol by a handheld gas sensor



Abstract

Methanol poisoning causes blindness, organ failure or even death when recognized too late. Currently, there is no methanol detector for quick diagnosis by breath analysis or for screening of laced beverages. Typically, chemical sensors cannot distinguish methanol from the much higher ethanol background. Here, we present an inexpensive and handheld sensor for highly selective methanol detection. It consists of a separation column (Tenax) separating methanol from interferants like ethanol, acetone or hydrogen, as in gas chromatography, and a chemoresistive gas sensor (Pd-doped SnO₂ nanoparticles) to quantify the methanol concentration. This way, methanol is measured within 2 min from 1 to 1,000 ppm without interference of much higher ethanol levels (up to 62,000 ppm). As a proof-of-concept, we reliably measure methanol concentrations in spiked breath samples and liquor. This could enable the realization of highly selective sensors in emerging applications such as breath analysis or air quality monitoring.

3.1 Introduction

Ingestion, inhalation or skin absorption of methanol leads to irreversible tissue damage, especially to eyes and nervous system, or even death.¹ This is attributed to metabolization of methanol to toxic formic acid and formaldehyde,² if not immediately treated.³ Especially in developing countries, methanol poisoning outbreaks occur frequently with hundreds of victims due to adulterated alcohol as shown recently in Iran (Oct. 2018, 959 cases)⁴, Cambodia (May 2018, 237 cases)⁵ and India (Feb. 2019, >95 cases)⁶. Furthermore, methanol is often used as solvent or chemical feedstock⁷ in laboratories and chemical plants, posing a potential hazard of intoxication.

The gold-standard for detection of methanol intoxication is blood analysis by gas-liquid chromatography, but more frequent in hospitals is the indirect diagnosis through blood gas analysis.⁸ However, both require trained personnel, are expensive and rarely available in developing countries where most outbreaks occur.⁹ Blood methanol levels can also be determined non-invasively in exhaled breath,¹⁰ analogous to ethanol as widely applied by law enforcement.¹¹ The challenge is thereby the selective detection of methanol in the presence of much higher ethanol background typically present after consumption of tainted alcoholic beverages and during therapy where ethanol is used as an antidote.¹² Even more interesting might be simple methods for screening of alcoholic beverages to prevent methanol poisoning. But here too, the same challenge is met. Thus, inexpensive and portable devices are needed for rapid screening of methanol poisoning and liquor by paramedics or even laymen.

Chemical gas sensors are promising due to their low cost,¹³ high miniaturization potential¹⁴ and simple use¹⁵. In particular, metal-oxide sensors show high sensitivity when nanostructured, capable to detect analytes down to 5 ppb within seconds.¹⁶ But, such sensors are typically non-selective,¹⁷ especially for chemically similar molecules (like methanol and ethanol), representing a long-standing challenge in the field. Therefore, current chemoresistive¹⁸ and electrochemical¹⁹ gas sensors for methanol show cross-interferences to ethanol and other alcohols hindering them for the targeted application.

Filters can drastically improve the selectivity of chemical sensors by exploiting additional molecular properties of the target molecule. For instance, highly selective (>100–1,000) formaldehyde detection was possible even with a nonspecific SnO₂-based sensor by placing ahead a microporous zeolite membrane to filter molecules by size.²⁰ This way, formaldehyde was detected down to 30 ppb in 90% relative humidity (RH) without interference of 1 ppm ammonia, acetone, isoprene and ethanol.²⁰ Also a sorption packed bed separation

column of polar nanostructured alumina enabled separation of hydrophilic from hydrophobic compounds,²¹ analogous to a gas chromatographic (GC) column.²² This has led to highly selective (>100) sensing of isoprene down to 5 ppb at 90% RH despite the presence of much higher (4–8 times) methanol, ammonia and acetone concentrations.²¹ Non-polar adsorbents, such as Tenax TA, on the other hand, can separate molecules by their molecular weight and chemical functional groups.²³ They are widely used in air sampling, whereby heavy molecules are retained stronger than lighter ones due to stronger adsorption by van-der-Waals forces.²³ Thus, they are also promising to separate methanol from ethanol as done already in GC for the analysis of liquor (e.g., detected by olfactometry with humans²⁴) and human breath (e.g., by mass spectrometry²⁵).

Here, we present a handheld and inexpensive methanol detector (Figure 3.1a) capable to quantify methanol selectively in the presence of ethanol and other analytes (e.g., acetone, H₂). It consists of a small packed bed of Tenax (Figure 3.1b) to separate the analytes and a

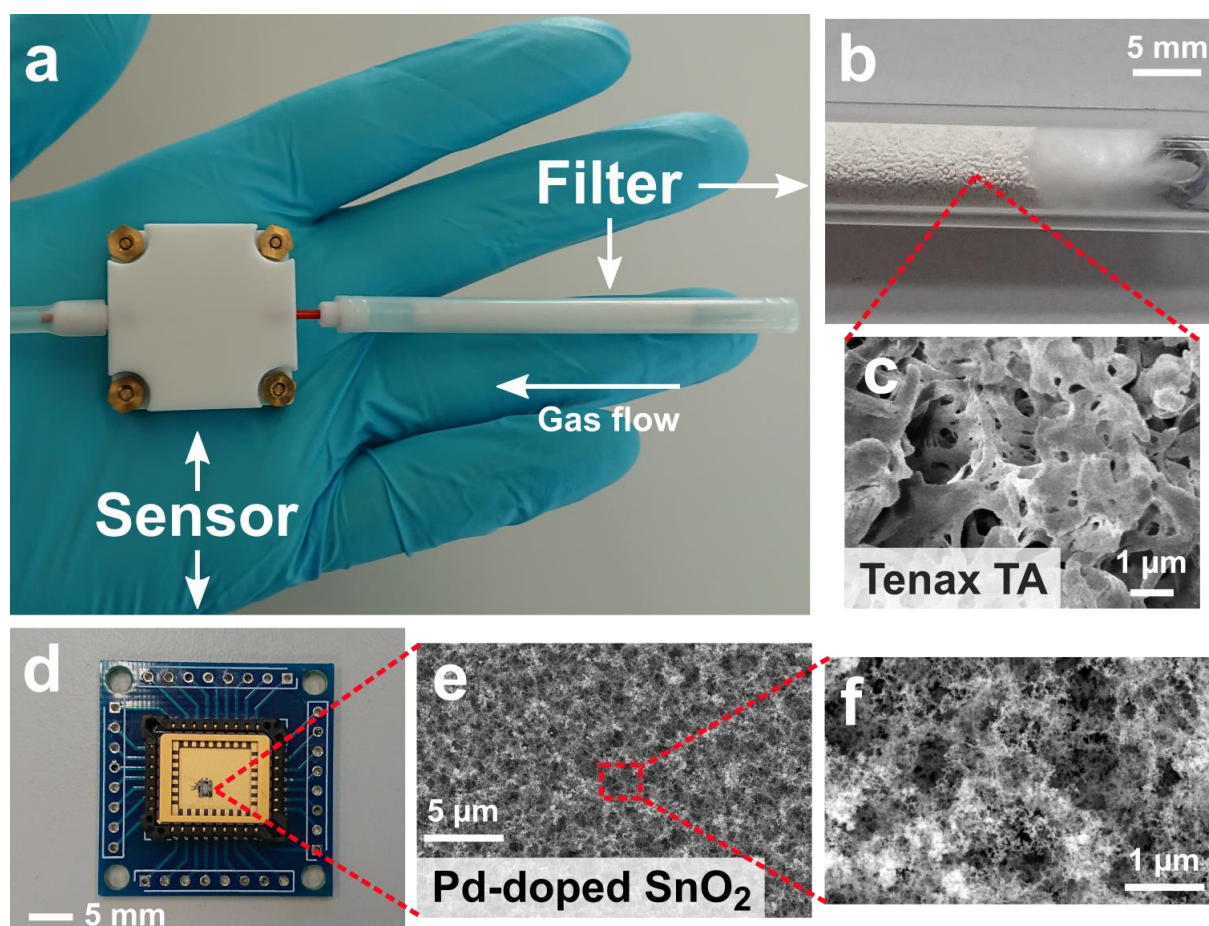


Figure 3.1: (a) Handheld methanol detector consisting of a microsensor (in Teflon housing) connected to a separation column (Tenax TA particles in Teflon tube). (b) Close-up of the separation column with particles inside a glass tube for better visibility. (c) Magnified images of a particle's surface. (d) The sensor chip carrier with a mounted microsensor. (e, f) Top-view images of the sensing films consisting of a fine network of agglomerated and aggregated Pd-doped SnO₂ nanoparticles.

highly sensitive, but non-specific microsensors (Figure 3.1d) consisting of flame-made Pd-doped SnO₂ nanoparticles on interdigitated sensing electrodes. In comparison to typical GC instruments,²² our device is much smaller and less expensive. It is benchmarked by detection of methanol in the relevant concentration range in the presence of much higher ethanol levels at high RH. Ultimately, the methanol detector is tested to sense toxic methanol levels in tainted rum and even in spiked human breath.

3.2 Experimental

3.2.1 Sensor fabrication

Palladium-doped SnO₂ nanoparticles were produced by flame spray pyrolysis (FSP). So, Pd-acetylacetonate (Sigma-Aldrich, 99%) was dissolved in tin(-II)-ethylhexanoate (Strem Chemicals, ~90% in 2-ethylhexanoic acid) and xylene (Sigma-Aldrich, ≥ 98.5%) to obtain a total metal molarity (Pd and Sn) of 0.5 M and nominal Pd content of 1 mol%.²⁶ This precursor solution was fed through a capillary at 5 mL min⁻¹, dispersed into a fine spray by 5 L min⁻¹ oxygen (pressure drop of 1.6 bar) and ignited by a surrounding premixed methane/oxygen flame (1.25/3.2 L min⁻¹). The FSP reactor design is described in more detail elsewhere.²⁷ Nanoparticles were directly deposited²⁷ for 4 min onto micromachined free-standing membrane-type sensor substrates (1.9 x 1.7 mm², MSGS 5000i, Microsens SA, Switzerland) attached to a water-cooled holder and at 20 cm height above the burner (HAB). The microsensors feature an integrated heater layer underneath the interdigitated sensing electrodes. Subsequent in-situ annealing with a particle-free flame for 30 sec at a HAB of 14.5 cm improved adhesion and cohesion of the highly porous sensing film.²⁸ Therefore, xylene was fed at 11 mL min⁻¹ through the nozzle with identical dispersion flow used during nanoparticle production. Finally, the sensors were annealed at 500 °C for 5 h in an oven (CWF13/23, Carbolite, United Kingdom) and wire-bonded onto leadless chip carriers (Chelsea Technology Inc., Massachusetts, US).

3.2.2 Separation column fabrication

The separation column is a packed bed of 150 mg Tenax TA (poly(2,6-diphenyl-p-phenylene oxide), 60–80 mesh, ~35 m² g⁻¹, Sigma Aldrich) packed inside a Teflon tube (4 mm inner diameter) and secured on both ends with silanized glass wool plugs and tension springs. Freshly prepared columns were flushed overnight with 100 mL min⁻¹ synthetic air (PanGas, C_nH_m and NO_x ≤ 0.1 ppm, Switzerland) at 50% RH to desorb impurities that might be adsorbed on the Tenax.

Scanning electron microscopy (SEM) images of the sensing film and the Tenax TA particle surface were made with a Hitachi S-4800 operated at 3 kV.

3.2.3 Gas evaluation

The methanol detector (Figure 3.1a) consists of the separation column followed by the Pd-doped SnO₂ sensor. A miniature rotary vane pump of only 12 g (135 FZ 3 VDC Schwarz Precision, Germany) downstream of the sensor draws the sample through the separation column at 25 mL min⁻¹. The flow was validated by a calibrated bubble flow meter connected to the pump outlet. The sensor was heated by providing DC current (R&S HMC8043, Germany) through the heater of the micromachined sensor substrate. The sensing film temperature was set to 350 °C requiring only 76 mW. The ohmic resistance of the sensing film between the interdigitated electrodes was monitored with a multimeter (Keithley, 2700, USA). Sensor responses were evaluated as

$$S = \frac{R_A}{R_S} - 1$$

where R_A and R_S denote the sensor film resistances measured in background air (synthetic air or ambient air in case of breath and liquor headspace analysis) and during sample measurement, respectively. The retention time t_R of an analyte was defined as the time from the start of analyte exposure to the sensor's maximum response, analogous to gas chromatography.²⁹ The breakthrough time t_B of an analyte was defined as the time from the start of analyte exposure to an analyte response equal to 5% of the response to 1 ppm methanol.

For characterization of the sensor with synthetic gas mixtures, the methanol detector was connected to a gas delivery system illustrated schematically in Figure 3.2. In specific, synthetic air was guided through a glass bubbler (Drechsel bottle, 125 mL, sintered glass frit, Sigma-Aldrich) containing ultrapure water (Milli-Q A10, Merck, Switzerland) and mixed with another stream of (dry) synthetic air to achieve 50% RH. All flows were accurately controlled by calibrated mass flow controllers (MFC, Bronkhorst, Netherlands) and the RH was verified by a humidity sensor (SHT2x, Sensirion AG, Switzerland). For generation of low analyte concentrations (5 ppm H₂, 1–5 ppm methanol, 5 ppm ethanol and 5 ppm acetone), analytes were admixed from calibrated gas standards (PanGas, in synthetic air) and added to the synthetic gas stream through a septum via a capillary. Thereby, the capillary was quickly inserted into the septum for 10 sec to generate well defined analyte exposures. The Teflon gas lines were heated to ~50 °C to avoid condensation and adsorption of water or analytes. The flow rates of the synthetic air and the analyte streams were varied in the range of 300–1,000

and 1–300 mL min⁻¹, respectively, while the flow rate to the sensor was always kept constant by the pump at 25 mL min⁻¹.

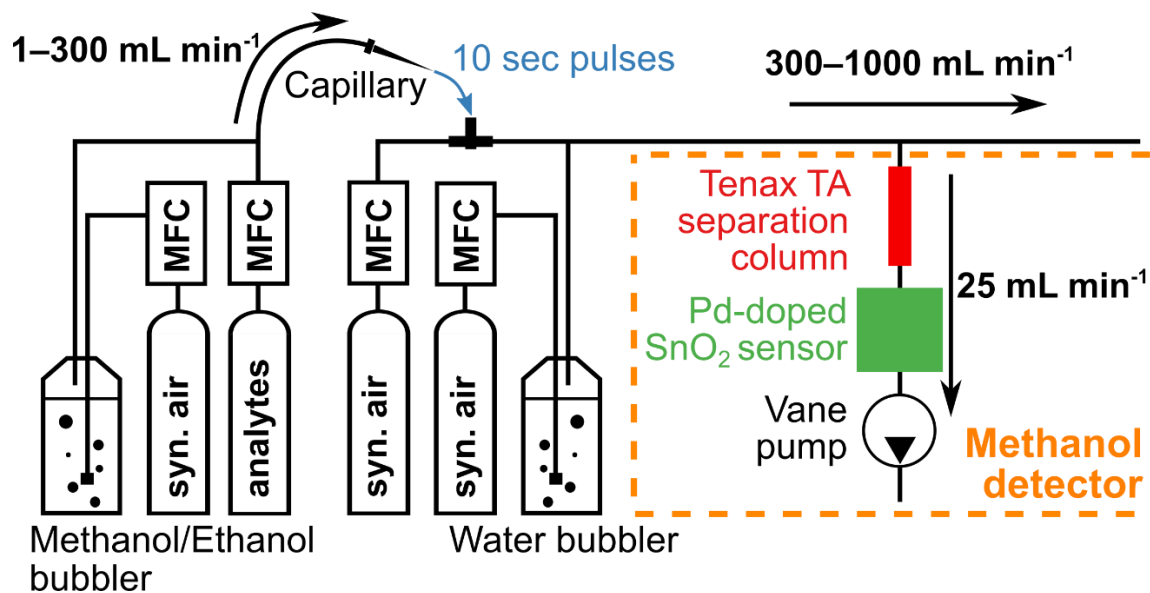


Figure 3.2: The methanol detector (orange box) consisting of the packed bed separation column of polymer (Tenax TA, red) particles, followed by the chemoresistive (Pd-doped SnO₂, green) sensor and the vane pump that draws 25 mL min⁻¹ of gas sample. For characterization with synthetic gas mixtures, the detector is connected to a gas delivery system. It supplies the detector with a constant flow of humidified air by mixing dry and humidified synthetic air (syn. air). Analyte exposures are generated by admixing analytes from calibrated gas standards or by syn. air bubbling through analyte/water mixtures to the humidified syn. air stream with a capillary through a septum. Flows are accurately controlled by calibrated mass flow controllers (MFCs).

For higher methanol concentrations (15–918 ppm), dry synthetic air was guided through a glass bubbler filled with ultrapure water and 1 vol% methanol (>99.9%, Sigma-Aldrich) and dilution with synthetic air. The generated methanol concentration from the bubbler was measured with a proton-transfer-reaction time-of-flight mass spectrometer (PTR-TOF-MS 1000, Ionicon, Austria) after further inlet dilution (1:200–1,000) with synthetic air to avoid device saturation. The ionization conditions were 600 V drift voltage, 60 °C drift temperature, and 2.3 mbar drift pressure. Methanol concentrations were determined in the H₃O⁺ mode by measuring the counts per second at a mass-to-charge ratio (m/z) of 33.0335³⁰ and comparison to a calibration curve obtained from the methanol gas standard. Higher ethanol concentrations (250–64,000 ppm) were generated similarly by bubbling air through pure ethanol (absolute, >99.8%, Fisher Chemical) and dilution with synthetic air. Generated concentrations were calculated from the weight loss of the bubbler after bubbling with air for 0, 2, 4, 6 and 8 h, while room temperature was kept constant at 22 °C.

3.2.4 Evaluation of the headspace of drinks and human breath

For testing of methanol spiked drinks and breath, sensors were stabilized in ambient air with analyte background concentrations of methanol <50 ppb, ethanol <500 ppb and acetone <100 ppb as determined by PTR-TOF-MS. Liquid samples were prepared in 25 mL glass bottles by mixing 5 mL of rum (40 vol% ethanol, Boven's echter Arrak, Indonesia) with 0, 0.3, 0.4, 0.5, 1, 5 and 10 vol% of methanol. Concentrations <0.3 vol% are not relevant for the liquor screening as the legal limit is 0.4 vol% in the US³¹ and EU³². To guarantee equilibrium headspace concentrations, the samples were vigorously shaken manually for 30 sec before sampling.³³ Headspace was sampled for 10 sec by injecting a capillary attached to the methanol detector through a septum into the glass bottle caps. During sampling, a second capillary was inserted to keep the vial at ambient pressure.

For breath sampling, a volunteer consumed an alcoholic beverage (40 vol% ethanol, Bacardi Rum Carta Blanca) containing an equivalent of 50 mL pure ethanol. After 1 h, blood alcohol concentration was estimated with a breathalyzer (Alcotest 3820, Dräger, Germany). Another two breath samples were collected in Tedlar bags (3 L, SKC Inc., USA) by direct and complete exhalation through a Teflon tube. One of the bags was spiked with 300 mL of 918 ppm methanol in synthetic air (100% RH), giving a final concentration of 135 ppm, as verified by PTR-TOF-MS (inlet dilution 1:40 with synthetic air). Also to the second bag, 300 mL of synthetic air (100% RH) without methanol was added to keep dilution of the breath samples similar. Breath samples were stored no longer than 1 h in the Tedlar bags to avoid analyte losses.³⁴ The detector was exposed to breath samples for 10 sec by injecting a capillary through a septum at the cap of the Tedlar bags. To validate the results of the methanol detector, the same breath samples were also analyzed by the PTR-TOF-MS (inlet dilution 1:40 with synthetic air) coupled to the separation column. Ethanol concentrations were determined in the H_3O^+ mode by measuring the counts per second at a mass-to-charge ratio (m/z) of 47.0490³⁰ and comparison to a calibration curve obtained from the ethanol gas standard. The experiment was approved by the ETH Zurich Ethics Commission and performed with written consent of the volunteer.

3.3 Results and discussions

3.3.1 Detector design

Figure 3.1a shows the handheld methanol detector. It consists of a separation column upstream of a micromachined metal-oxide gas sensor housed inside a Teflon chamber. Breath or the headspace of a beverage can be drawn by a pump through the separation column to the

sensor. The separation column is a miniaturized GC column with Tenax TA as the stationary phase (shown in Figure 3.1b) featuring lower adsorption strength to methanol over ethanol.²³ Figure 3.1c shows a scanning electron microscopy (SEM) image of a Tenax particle's surface revealing its high specific surface area ($35 \text{ m}^2 \text{ g}^{-1}$) and porosity (average pore size 200 nm). Compared to typical GC columns,²² the separation column used here is much shorter (4.5 cm) and thicker (4 mm inner diameter). Together with the small amount of adsorbent used (150 mg) and its large particle size ($\sim 200 \text{ }\mu\text{m}$), this results in a sufficiently small pressure drop ($<20 \text{ mbar}$) to provide the required flow rate (25 mL min^{-1}) to the sensor.

Figure 3.1d shows the sensor bonded on a chip carrier. It is micromachined, offering small size and minimal power requirement (76 mW at $350 \text{ }^\circ\text{C}$) readily suitable for integration into a handheld device. Figure 3.1e-f show top-view SEM images of the sensing film made of chemoresistive Pd-doped SnO_2 nanoparticles²⁷ offering high porosity and specific surface area ($\sim 80 \text{ m}^2 \text{ g}^{-1}$ for similarly prepared Pt-doped SnO_2)³⁵. The open film structure enables fast diffusion of analytes and interaction with the large surface area, important for rapid and highly sensitive methanol sensing. Such sensors had been used, for instance, for detection of only 3 ppb formaldehyde with fast response (140 sec) and recovery (190 sec) times, and good reproducibility ($<10\%$ response variation).²⁶

3.3.2 Selective methanol detection

Figure 3.3a shows responses of the Pd-doped SnO_2 sensor without separation column to 10 sec exposures of 5 ppm of hydrogen (purple line), methanol (red line), acetone (green line) and ethanol (blue line) at 50% RH. The sensor quickly reacts to all these analytes with responses between 10–25. However, it cannot differentiate between them. This becomes even more evident when exposing the sensor to a mixture of these analytes (Figure 3.3b). The sensor gives now a much higher response, slightly lower than the sum of the individual ones, as typically observed for chemoresistive sensors at such ppm concentrations.³⁶ As a consequence, this sensor cannot measure selectively methanol in the presence of such interferents.

When combined with the separation column, the sensor responses are separated as in a chromatograph. The response to hydrogen (purple line) remains the same (Figure 3.3c). This is expected as hydrogen features low molecular weight and is not retained by Tenax.³⁷ For the other analytes, however, a different behavior is observed. In fact, methanol (red line) is now detected after $>1 \text{ min}$ with a maximum sensor response (i.e., retention time t_R , dashed lines) after 1.7 min. Note that the maximum methanol response is lower than without separation column, as the column dissipates it over a longer time period, in line with theory³⁸. Most

importantly, ethanol (blue line, $t_R = 8.7$ min) and acetone (green line, $t_R = 33$ min) are retained for much longer, in agreement with literature ($t_R = 2.2, 10.8$ and 36 min) for methanol, ethanol and acetone, respectively, at 20 °C)³⁷. As a result, the separation column enables selective methanol detection. Interestingly also, the ethanol and acetone responses decrease with increasing t_R . In fact, the response to 5 ppm acetone is barely picked up by the sensor (while it was twice that of methanol without separation column, compare Figure 3.3a to c).

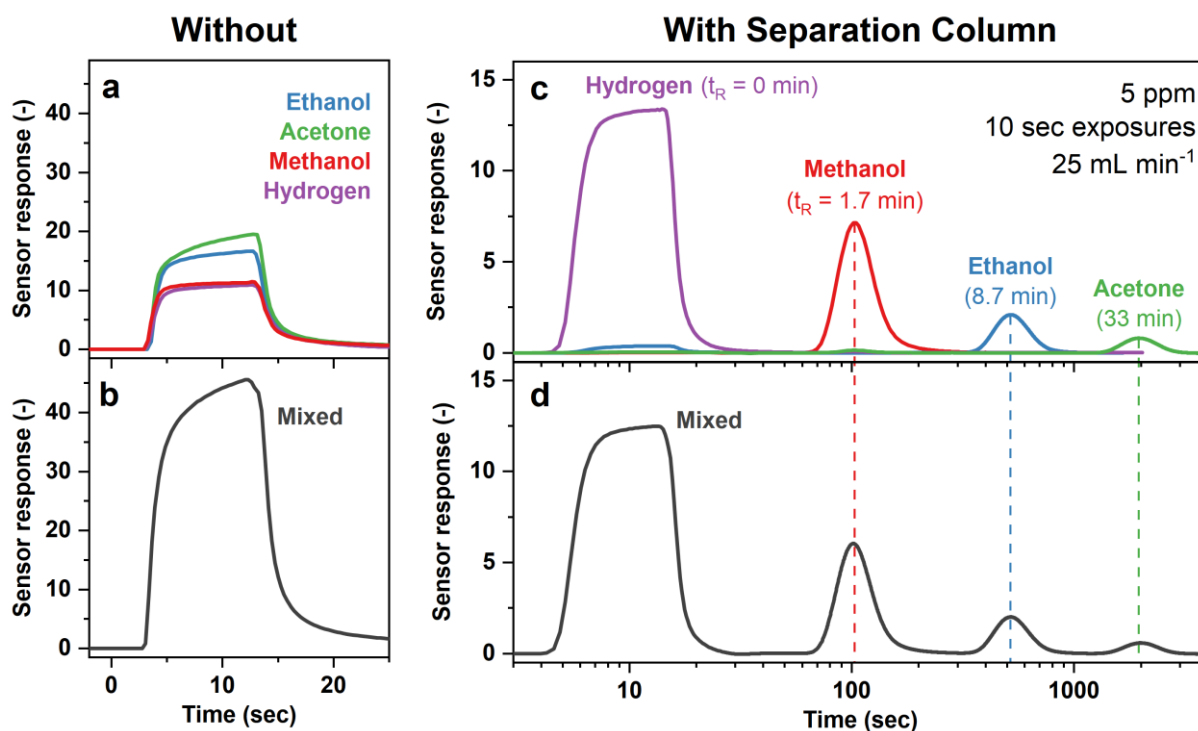


Figure 3.3: Response of the methanol detector (a, b) without and (c, d) with separation column to 10 sec exposures of 5 ppm hydrogen (purple line), methanol (red line), ethanol (blue line) and acetone (green line) as well as their mixture (black line in b and d) at 50% RH and 25 mL min^{-1} total flow rate. Also given are the corresponding retention times (t_R , dashed lines, for hydrogen $t_R = 0$ min as it is not retained). Note the different ordinate scale between a/b and c/d. The presence of the polymer sorbent packed bed upstream of the Pd-doped SnO_2 sensor facilitates the separation of the mixture components.

When exposing the sensor with separation column to a mixture of the same analytes and concentrations (Figure 3.3d), the analytes can be detected individually at their specific retention time with very high selectivity, identical to the single analyte exposures (Figure 3.3c). Most remarkably, for the targeted applications, methanol is detected without ethanol interference, superior to state-of-the-art methanol sensors where the highest selectivity to ethanol (>30) has been reported for imprinted Ag-doped LaFeO_3 core-shell particles³⁹.

As shown in Figure 3.3c,d, the detector fully regenerates from each analyte or mixture exposure by flushing with air. The recovery time depends on the analyte and is about 2–3 times its retention time, in agreement with literature⁴⁰. The recovery time can be decreased

considerably by simply increasing the flow rate or by slight heating of the separation column (e.g., acetone from ~60 min to 20 sec³⁷ when increasing column temperature and flow rate briefly to 80 °C and 100 mL min⁻¹).²³

3.3.3 Dynamic range

Methanol concentrations in the targeted applications may occur from several ppm in breath¹⁰ up to several hundred ppm in the headspace of beverages³¹. Figure 3.4 shows the Pd-doped SnO₂ sensor response with separation column when exposed for 10 sec to 1–918 ppm of methanol at 50% RH. The median methanol concentration in healthy breath⁴¹ (green line), the range of exogenous³² (orange line) and toxic breath methanol concentrations¹ (red area) are also indicated. The response curve is non-linear, in-line with diffusion-reaction theory³⁶ for such semiconductive metal-oxide films at high analyte concentrations. Nevertheless, as a result, this separation column–sensor system can discriminate clearly toxic from nontoxic levels and even detect low concentrations of 1 ppm with a signal-to-noise ratio >100. Lower concentrations are not relevant for the liquor headspace and breath analyses, but such Pd-doped SnO₂ gas sensors can detect volatile organic compounds down to single ppb levels (e.g., 3 ppb formaldehyde²⁶). In contrast, other bench-top methanol detectors (e.g., PTR-TOF-MS) can detect such low concentrations as well, but they have a much smaller dynamic range and require dilution to measure the high ppm concentrations present in breath or the headspace of beverages.

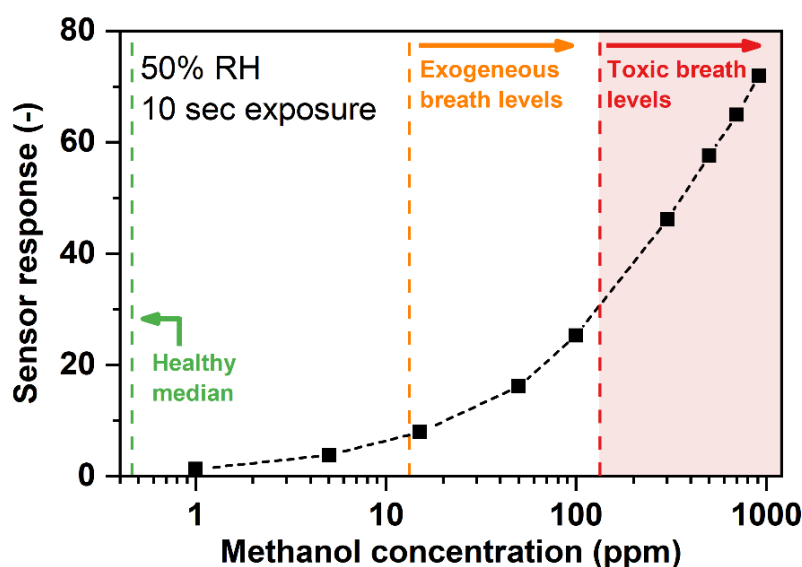


Figure 3.4: Response of the detector (Tenax separation column + Pd-doped SnO₂ sensor) to 1–918 ppm methanol concentrations (black squares and dashed line). The median methanol concentration in healthy breath⁴¹ (green dashed line), exogenous³² (orange dashed line) and toxic¹ breath levels (red dashed line and shaded area) are indicated. Measurements were performed with 10 sec exposure of all methanol concentrations at 50% RH and a flow rate of 25 mL min⁻¹ through the detector.

Please note that the response curve in Figure 3.4 is valid for a separation column temperature of 22 °C at 50% RH. With increasing column temperature, the sensor responses become higher as t_R decreases (Figure C.1a). Most importantly, however, methanol is clearly separated and detected individually from ethanol even at 40 °C. Such temperature effects could be accounted for by a temperature sensor. At higher humidity, t_R does not change, in-line with literature,²³ but the responses decrease (Figure C.1b). This is typical for such doped SnO₂ sensors²⁰ and can be addressed by using a sensor material less sensitive to humidity (e.g., Sb-doped SnO₂⁴²) or by correction with a humidity sensor as done with sensor arrays to monitor volatile emission from human breath and skin.⁴³

3.3.4 High ethanol background

To analyze methanol in the headspace of alcoholic beverages or in intoxicated breath, the detector must remain accurate in the presence of very high ethanol concentrations. Figure 3.5a shows the response of the detector when exposed to 1 ppm methanol with interfering ethanol concentrations of 5 (green line), 650 (1% relative saturation, blue line) and 32,500 ppm (50% relative saturation, red line). Despite the significantly higher ethanol concentration, methanol is detected first ($t_R = 1.5\text{--}1.7$ min) giving comparable responses to the single gas calibration (Figure 3.4). Ethanol is detected later with breakthrough times (t_B , dashed lines) that decrease with increasing concentration (5.7 min at 5 ppm to 2.2 min at 50% saturation) but are always higher than the t_R of methanol. In GC, the same phenomenon is observed when overloading the column with analyte.⁴⁴

Interestingly, at 50% ethanol saturation concentration, methanol is detected slightly earlier with higher peak maximum and narrower peak width. Probably, this is due to competitive adsorption on Tenax where methanol is displaced by ethanol that adsorbs more strongly.⁴⁵ Nevertheless, the resulting error of 17% is sufficiently small for the targeted applications as the difference between normal and toxic methanol concentrations in liquor and breath are much larger (e.g., human breath median 0.46 ppm⁴¹ vs. intoxicated >133 ppm¹). If higher accuracy is required, alternatively, the area below the methanol response could be evaluated, as commonly done in gas chromatography.²² In fact, the peak areas below the methanol responses are basically identical (within 2%), irrespective of the ethanol concentration (Figure C.2).

Most importantly, the methanol response is clearly separated from that of ethanol even at very high concentrations. This is shown in Figure 3.5b where the t_R of methanol (solid line) and t_B of ethanol (dashed line) are plotted for ethanol concentrations in the range 5–62,000 ppm

(95% saturation). The t_B decreases exponentially with increasing concentration, in line with literature at lower concentrations.³⁸ Even at the most extreme conditions of 95% saturated ethanol atmosphere, methanol is detected independently of ethanol as its response is clearly separated from the breakthrough of ethanol. These results are astonishing considering the simplicity of this device and outperform other methanol detectors.

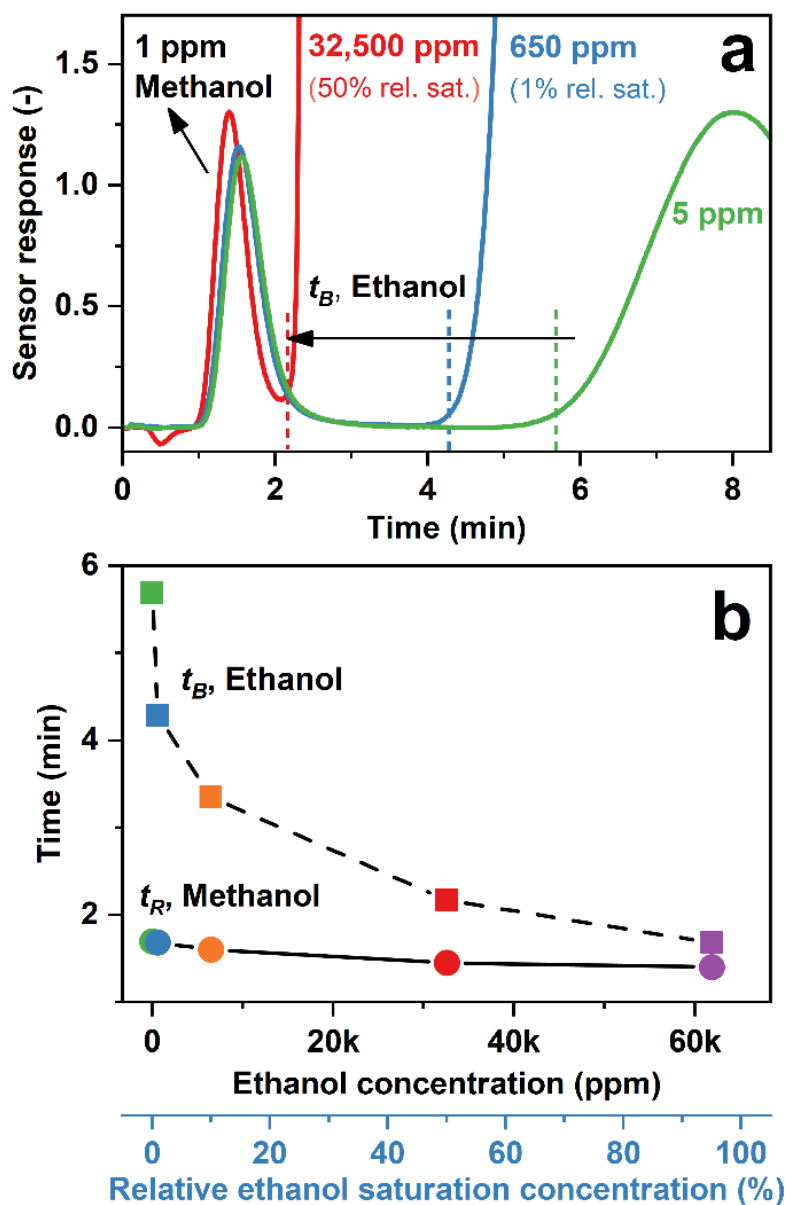


Figure 3.5: (a) Responses of the methanol detector upon exposure to 1 ppm methanol in the presence of 5 (green line), 650 (1% relative saturation, blue line) and 32,500 ppm (50% relative saturation, red line) ethanol. Corresponding ethanol breakthrough times (t_B , dashed lines) are indicated. (b) The ethanol t_B (squares and dashed line) and methanol retention time (t_R , circles and solid line) as a function of interfering ethanol concentration of 5 (green), 650 (1% relative saturation, blue), 6,500 (10% relative saturation, orange), 32,500 ppm (50% relative saturation, red) and 62,000 ppm (95% relative saturation, purple).

3.3.5 Methanol-spiked liquor and breath

Drinking as little as 6 mL methanol can be fatal.⁴⁶ Thus, a methanol detector for screening of alcoholic beverages could help to prevent methanol poisoning outbreaks. The safety threshold for naturally occurring methanol in liquor (40 vol% ethanol) is 0.4 vol% (US³¹ and EU³²), as such low levels occur naturally since methanol is a byproduct of fermentation.³¹ The detector must therefore be able to distinguish “safe” alcoholic beverages from tainted ones with typically much higher methanol content. Figure 3.6a shows the responses to pure (green) and laced Arrack (common liquor in Southeast Asia) with 0.3 (blue line), 0.4 (orange line), 0.5 (purple line) and 1 vol% (red line) methanol. The detector clearly recognizes the added methanol at the expected $t_R = 1.7$ min, matching the retention time of methanol in laboratory gas mixtures (see Figures 3.3 and 3.6).

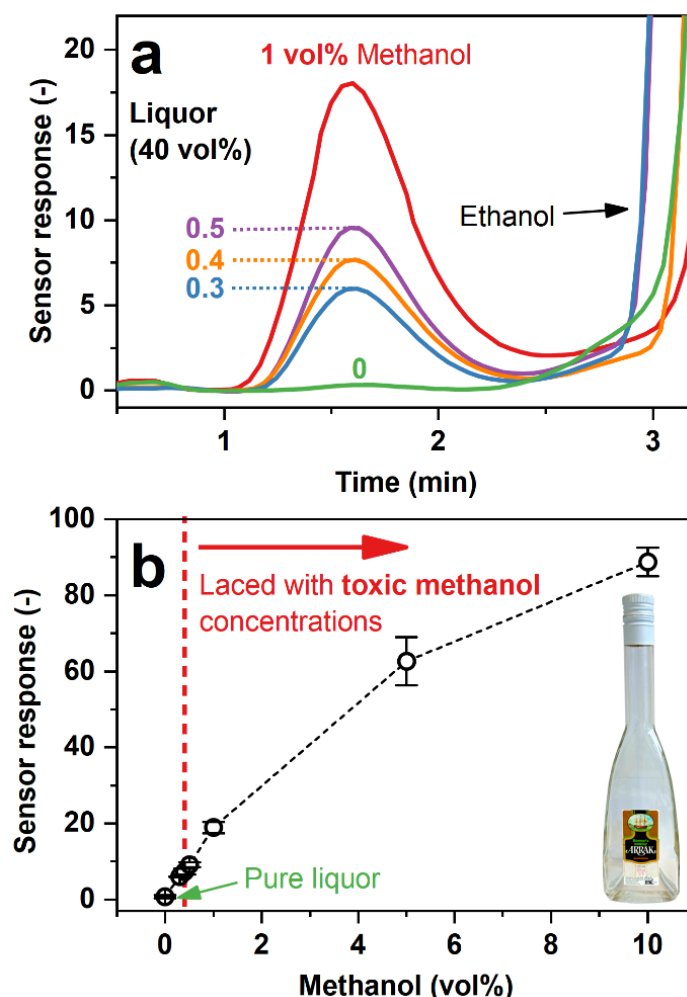


Figure 3.6: (a) Response of the detector to pure liquor (green line) containing 40 vol% ethanol and laced with methanol of 0.3 (blue line), 0.4 (orange line), 0.5 (purple line) and 1 vol% (red line). (b) Sensor responses as a function of methanol content (0–10 vol%) in the liquor (black circles). The red dashed line indicates the legally allowed (US³¹ & EU³²) naturally occurring methanol content in liquor (40 vol% ethanol). Error bars indicate the standard deviation of at least three measurements (i.e., repeatability) with less than 15% variation.

Most importantly, the response increases with increasing methanol concentration and even small differences between 0.3 to 0.4 and 0.5 vol% (i.e., close to the allowed limit) can be clearly resolved by the sensor with high signal-to-noise ratio >100 . In all cases, the response steeply increases after 3 min, corresponding to the high concentration of ethanol. Also at higher methanol contents of 5 and 10 vol% the sensor response continues to increase (Figure 3.6b). As a result, the methanol detector can clearly distinguish pure Arrack from that laced with toxic levels of methanol with good repeatability ($<15\%$ variation, error bars in Figure 3.6b). Due to the high signal-to-noise ratio, also lower concentrations of methanol should be detectable, which may be interesting for the production monitoring and quality control of alcoholic beverages (e.g., naturally occurring methanol in wine⁴⁷).

The methanol detector features also good stability with a sensor baseline drift of 0.7% per day during 18 days of testing (Figure C.4). Such drifts could be corrected by an additional processing algorithm.⁴⁸ By purging with ambient air, it fully regenerates within 15 min (Figure C.3a), enabling rapid screening and multiple uses with no observed saturation or degradation effects over, at least, two weeks of repeated testing (Figure C.4).

As a proof-of-concept for breath analysis, we evaluated the methanol detector on the original and methanol-spiked breath of an intoxicated (after ingestion of ethanol) volunteer (blood alcohol level 0.54‰ as measured with a Dräger Alcotest). Poisoning volunteers with methanol is unacceptable. However, spiking the analyte to the sample (i.e., standard addition method⁴⁹) is a standard approach in analytical chemistry as the complexity of the gas matrix (i.e., intoxicated breath) is preserved. Figure 3.7a shows the detector response for the normal (blue dashed line) and methanol-spiked breath (135 ppm methanol, red solid line). Note that a methanol concentration of 135 ppm was chosen as it is just above the threshold of serious methanol intoxication ($>133\text{ ppm}^1$). In both cases, the detector shows identical responses to hydrogen at $t = 0\text{--}30$ sec (not retained) and ethanol ($t_R = 8.3$ min) with full recovery thereafter (Figure C.3a). A clear peak associated with methanol is visible at $t_R = 1.7$ min with high signal-to-noise ratio (>1000), identical to laboratory gas mixtures (Figure 3.2c). To verify the methanol (Figure 3.7b) and ethanol (Figure 3.7c) peaks, the same breath samples were analyzed by benchtop PTR-TOF-MS equipped with the same separation column. Note that these high concentrations were only measurable by PTR-TOF-MS by additional dilution (please see experimental). Methanol and ethanol were detected at t_R identical to the sensor, confirming the sensor results.

As a result, this detector can clearly differentiate between normal and methanol-spiked breath. Therefore, this it is promising for fast and non-invasive sensing of methanol poisoning.

Given the high signal-to-noise ratio at 135 ppm methanol, it also shows promise for monitoring methanol elimination during treatment.¹⁰ Of course, the results are rather preliminary (only one subject tested) and further validation with extended cohorts is required as done recently with breath acetone and a similar sensor (Si-doped WO_3) for body fat burn monitoring during exercise⁵⁰ and dieting⁵¹.

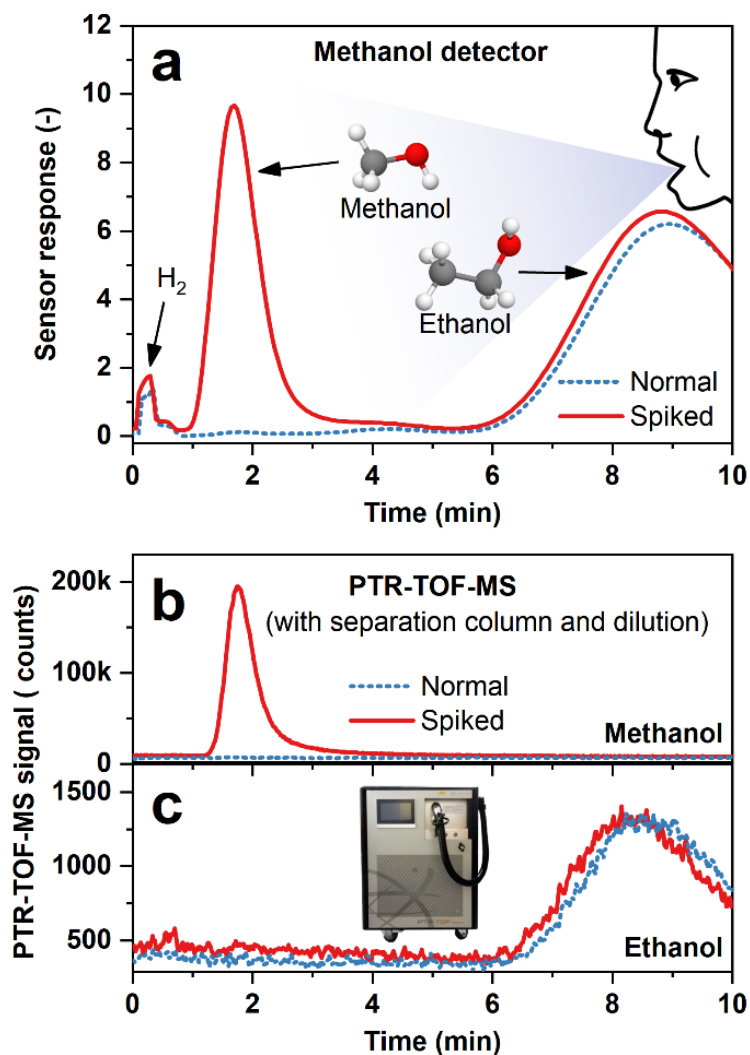


Figure 3.7: (a) Response of the methanol detector to breath of an intoxicated volunteer (0.54‰ blood alcohol level) sampled from Tedlar bags. The blue dashed line shows the measurement from the normal breath sample and the red solid line from the spiked sample with 135 ppm methanol, indicating methanol intoxication. The PTR-TOF-MS measurements (with separation column and dilution) of the same samples for (b) methanol and (c) ethanol. The instrument shown in c is a PTR-TOF-MS 1000 (Ionicon, Austria) used for sensor validation. Hydrogen (H_2) is not retained by the separation column and does not interfere with the methanol detector.

Interestingly, in liquor (Figure 3.6) and human breath (Figure 3.7), only methanol, ethanol and hydrogen (breath) are clearly detected by the sensor, although both liquor and breath are complex mixtures with more than 100⁵² and 800⁵³ analytes, respectively. This is probably due to the higher molecular weight and different functional groups (e.g., diols or

glycols) of most interferants, resulting in longer retention in the separation column than methanol (e.g., ethylene glycol 100 times longer than methanol³⁷). Most likely reason, however, is the much lower concentration of most confounders (e.g., 0.003 ppm trimethylamine in breath⁵⁴ compared to >133 ppm of methanol in case of intoxication¹).

To the best of our knowledge, this is the first methanol sensor for the detection of relevant concentrations in the presence of ethanol in realistic samples of liquor and breath. Other sensors are either liquid sensors that cannot be used for breath (e.g., photoluminescent Tb³⁺-based metal-organic framework sensor⁵⁵), do not offer the required detection limit (e.g., Quartz tuning fork-based sensor⁵⁶) or were not tested in gas mixtures (e.g., optical fiber sensor⁵⁷).

3.4 Conclusions

We created an inexpensive, handheld and reliable methanol detector based on a separation column–sensor concept. The separation column is a small packed bed of polymer adsorbent (Tenax TA) that separates methanol from ethanol and other interferants including hydrogen and acetone analogous to a column in gas chromatography. So, methanol is detected within 2 min by a nonspecific but highly sensitive nanostructured Pd-doped SnO₂ gas sensor in a wide concentration range from 1–918 ppm without interference of much higher ethanol concentrations (up to 62,000 ppm). The detector successfully quantified methanol concentrations in laced rum (Arrack) down to 0.3 vol% by analyzing its headspace and distinguished it from pure liquor. As first proof-of-concept, the detector was also tested on breath of an intoxicated volunteer, where it could clearly identify the sample spiked with toxic methanol concentrations. Thus, it shows promise for quick and non-invasive screening of methanol poisoning from breath and laced alcoholic beverages and could be used by first responders in developing countries, where most outbreaks occur.

In a broader sense, the present detector demonstrates how to possibly address a long-standing challenge of chemical sensors: the discrimination between analytes from the same chemical family. Giving comparable performance to a gas chromatographic column, such separation columns are much simpler in design, modular and can be combined flexibly with other sensor technologies that often lack selectivity, such as optical sensors (e.g., plasmonic,⁵⁸ fluorescent⁵⁹), gas ionization detectors,⁶⁰ electrochemical cells,⁶¹ carbon-nanotube⁶²- or graphene-based sensors.⁶³ Based on their small size and low price, such separation columns could enable highly selective, compact and portable gas detectors for emerging applications including medical breath analysis, food spoilage and air quality monitoring.

3.5 References

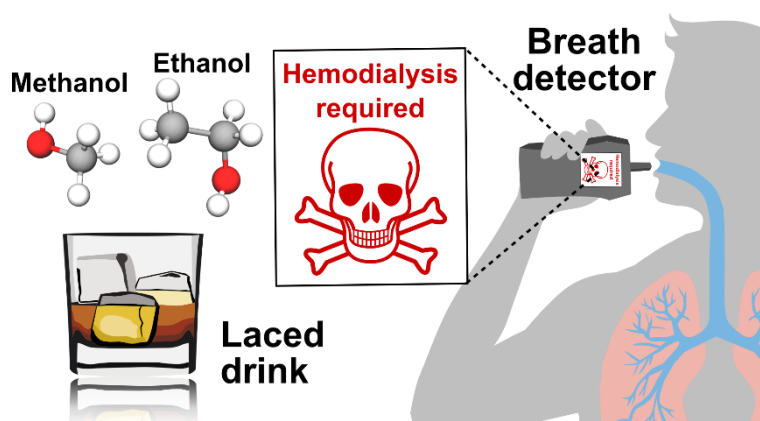
1. D. G. Barceloux, G. Randall Bond, E. P. Krenzelok, H. Cooper and J. Allister Vale, *J. Toxicol., Clin. Toxicol.*, **2002**, 40, 415-446.
2. J. A. Kruse, *Intensive Care Med.*, **1992**, 18, 391-397.
3. K. E. Hovda, O. H. Hunderi, A. B. Tafjord, O. Dunlop, N. Rudberg and D. Jacobsen, *J. Intern. Med.*, **2005**, 258, 181-190.
4. Agence France-Presse. *Voice of America News: Death toll in Iran alcohol poisoning jumps to 84*, **2018**, <https://www.voanews.com/a/death-toll-in-iran-alcohol-poisoning-jumps-to-84/4633468.html>.
5. S. David. *Khmer Times: More than 100 villagers return home after methanol poisoning*, **2018**, <https://www.khmertimeskh.com/50487671/more-than-100-villagers-return-home-after-methanol-poisoning/>.
6. K. Schultz and H. Kumar. *The New York Times: Over 90 killed in India by toxic homemade liquor*, **2020**, <https://www.nytimes.com/2019/02/23/world/asia/india-poison-alcohol.html>.
7. L. Lin, W. Zhou, R. Gao, S. Yao, X. Zhang, W. Xu, et al., *Nature*, **2017**, 544, 80-83.
8. J. A. Kraut, *Clin. Toxicol.*, **2015**, 53, 589-595.
9. J. D'Silva, *Br. Med. J.*, **2015**, 351, h4536.
10. O. Laakso, M. Haapala, P. Jaakkola, R. Laaksonen, K. Luomanmäki, J. Nieminen, et al., *J. Anal. Toxicol.*, **2001**, 25, 26-30.
11. R. F. Borkenstein and H. Smith, *Med., Sci. Law*, **1961**, 2, 13-22.
12. J. A. Kraut, *Am. J. Kidney Dis.*, **2016**, 68, 161-167.
13. A. T. Güntner, S. Abegg, K. Königstein, P. A. Gerber, A. Schmidt-Trucksäss and S. E. Pratsinis, *ACS Sens.*, **2019**, 4, 268-280.
14. M. M. Shulaker, G. Hills, R. S. Park, R. T. Howe, K. Saraswat, H. S. P. Wong and S. Mitra, *Nature*, **2017**, 547, 74-78.
15. W. Gao, S. Emaminejad, H. Y. Y. Nyein, S. Challa, K. Chen, A. Peck, et al., *Nature*, **2016**, 529, 509-514.
16. A. T. Güntner, N. J. Pineau, D. Chie, F. Krumeich and S. E. Pratsinis, *J. Mater. Chem. B*, **2016**, 4, 5358-5366.
17. S. H. Lim, L. Feng, J. W. Kemling, C. J. Musto and K. S. Suslick, *Nat. Chem.*, **2009**, 1, 562-567.
18. D. Han, P. Song, S. Zhang, H. Zhang, Q. Xu and Q. Wang, *Sens. Actuators B Chem.*, **2015**, 216, 488-496.
19. E. M. Caravati and K. T. Anderson, *Ann. Emerg. Med.*, **2010**, 55, 198-200.
20. A. T. Güntner, S. Abegg, K. Wegner and S. E. Pratsinis, *Sens. Actuators B Chem.*, **2018**, 257, 916-923.
21. J. van den Broek, A. T. Güntner and S. E. Pratsinis, *ACS Sens.*, **2018**, 3, 677-683.
22. H. M. McNair and J. M. Miller, *Basic gas chromatography*, John Wiley & Sons, **2011**.
23. I. Maier and M. Fieber, *J. High Resolut. Chromatogr.*, **1988**, 11, 566-576.
24. L. Franitza, M. Granvogl and P. Schieberle, *J. Agric. Food Chem.*, **2016**, 64, 9041-9053.
25. A. W. Jones, G. Mårdh and E. Änggård, *Pharmacol., Biochem. Behav.*, **1983**, 18, 267-272.
26. A. T. Güntner, V. Koren, K. Chikkadi, M. Righettoni and S. E. Pratsinis, *ACS Sens.*, **2016**, 1, 528-535.
27. L. Mädler, A. Roessler, S. E. Pratsinis, T. Sahm, A. Gurlo, N. Barsan and U. Weimar, *Sens. Actuators B Chem.*, **2006**, 114, 283-295.

28. A. Tricoli, M. Graf, F. Mayer, S. Kühne, A. Hierlemann and S. E. Pratsinis, *Adv. Mater.*, **2008**, 20, 3005-3010.
29. C. J. Geankoplis, *Transport processes and separation process principles*, Prentice Hall, **2003**.
30. P. Spanel and D. Smith, *Int. J. Mass Spectrom. Ion Processes*, **1997**, 167/168, 375-388.
31. P. Levy, A. Hexdall, P. Gordon, C. Boeriu, M. Heller and L. Nelson, *J. Toxicol., Clin. Toxicol.*, **2003**, 41, 23-28.
32. A. J. Paine and A. D. Dayan, *Hum. Exp. Toxicol.*, **2001**, 20, 563-568.
33. A. Tipler, *An introduction to headspace sampling in gas chromatography fundamentals and theory*. 2013. Available at SSRN: <https://ssrn.com/abstract=3668465>
34. M. M. Steeghs, S. M. Cristescu and F. J. Harren, *Physiol. Meas.*, **2006**, 28, 73-84.
35. L. Mädler, T. Sahm, A. Gurlo, J. D. Grunwaldt, N. Barsan, U. Weimar and S. E. Pratsinis, *J. Nanopart. Res.*, **2006**, 8, 783-796.
36. J. W. Gardner, *Sens. Actuators B Chem.*, **1990**, 1, 166-170.
37. Scientific Instrument Services (SIS), Tenax® TA breakthrough volume data, <https://www.sisweb.com/index/referenc/tenaxta.htm>, (accessed January 14, 2019).
38. M. Harper, *Ann. Occup. Hyg.*, **1993**, 37, 65-88.
39. R. Qian, Z. Yumin, L. Tianping, S. Kaiyuan, Z. Baoye, Z. Zhongqi, et al., *Nanotechnology*, **2018**, 29, 145503.
40. J. J. Manura, Application note: Calculation and use of breakthrough volume data, <https://www.sisweb.com/index/referenc/resin10.htm>, (accessed March 12, 2019).
41. C. Turner, P. Španěl and D. Smith, *Physiol. Meas.*, **2006**, 27, 637-648.
42. K. Suematsu, M. Sasaki, N. Ma, M. Yuasa and K. Shimano, *ACS Sens.*, **2016**, 1, 913-920.
43. A. T. Güntner, N. J. Pineau, P. Mochalski, H. Wiesenhofer, A. Agapiou, C. A. Mayhew and S. E. Pratsinis, *Anal. Chem.*, **2018**, 90, 4940-4945.
44. K. Yabumoto, D. Ingraham and W. Jennings, *J. High Resolut. Chromatogr.*, **1980**, 3, 248-252.
45. P. Comes, N. Gonzalez-Flesca, T. Menard and J. O. Grimalt, *Anal. Chem.*, **1993**, 65, 1048-1053.
46. I. L. Bennett, F. H. Cary, G. L. Mitchell and M. N. Cooper, *Medicine*, **1953**, 32, 431-463.
47. C.-Y. Zhang, N.-B. Lin, X.-S. Chai, L. Zhong and D. G. Barnes, *Food Chem.*, **2015**, 183, 169-172.
48. T. Artursson, T. Eklöv, I. Lundström, P. Mårtensson, M. Sjöström and M. Holmberg, *J. Chemom.*, **2000**, 14, 711-723.
49. M. Bader, *J. Chem. Educ.*, **1980**, 57, 703-706.
50. A. T. Güntner, N. A. Sievi, S. J. Theodore, T. Gulich, M. Kohler and S. E. Pratsinis, *Anal. Chem.*, **2017**, 89, 10578-10584.
51. A. T. Güntner, J. F. Kompalla, H. Landis, S. J. Theodore, B. Geidl, N. A. Sievi, et al., *Sensors*, **2018**, 18, 3655-3655.
52. H. Maarse and M. C. ten Noever de Brauw, *J. Food Sci.*, **1966**, 31, 951-955.
53. B. de Lacy Costello, A. Amann, H. Al-Kateb, C. Flynn, W. Filipiak, T. Khalid, et al., *J. Breath Res.*, **2014**, 8, 014001.
54. N. Alkhouri, F. Cikach, K. Eng, J. Moses, N. Patel, C. Yan, et al., *Eur. J. Gastroenterol. Hepatol.*, **2014**, 26, 82-87.
55. R. R. F. Fonseca, R. D. L. Gaspar, I. M. Raimundo and P. P. Luz, *J. Rare Earths*, **2019**, 37, 225-231.

-
56. S. A. Sampson, S. V. Panchal, A. Mishra, S. Banerjee and S. S. Datar, *Microchim. Acta*, **2017**, 184, 1659-1667.
 57. D. Liu, R. Kumar, F. Wei, W. Han, A. K. Mallik, J. Yuan, et al., *Sens. Actuators B Chem.*, **2018**, 271, 1-8.
 58. B. S. Hoener, S. R. Kirchner, T. S. Heiderscheid, S. S. E. Collins, W.-S. Chang, S. Link and C. F. Landes, *Chem*, **2018**, 4, 1560-1585.
 59. Y. Hu, Z. Zhou, F. Zhao, X. Liu, Y. Gong, W. Xiong and M. Sillanpää, *Scientific reports*, **2018**, 8, 10277.
 60. A. Modi, N. Koratkar, E. Lass, B. Wei and P. M. Ajayan, *Nature*, **2003**, 424, 171-174.
 61. J. Gebicki, *TrAC, Trends Anal. Chem.*, **2016**, 77, 1-13.
 62. J.-H. Kim, D. A. Heller, H. Jin, P. W. Barone, C. Song, J. Zhang, et al., *Nat. Chem.*, **2009**, 1, 473-481.
 63. J. Yun, Y. Lim, G. N. Jang, D. Kim, S.-J. Lee, H. Park, et al., *Nano Energy*, **2016**, 19, 401-414.

Chapter 4

Screening methanol poisoning with a portable breath detector



Abstract

Methanol poisoning outbreaks after consumption of adulterated alcohol frequently overwhelm health care facilities in developing countries. Here, we present how a recently developed low-cost and handheld breath detector can serve as a non-invasive and rapid diagnostic tool for methanol poisoning. The detector combines a separation column and a micromachined chemoresistive gas sensor fully integrated into a device that communicates wirelessly with a smartphone. The performance of the detector is validated with methanol-spiked breath of 20 volunteers (105 breath samples) after consumption of alcoholic beverages. Breath methanol concentrations were quantified accurately within 2 min in the full breath-relevant range (10–1000 ppm) in excellent agreement ($R^2 = 0.966$) with benchtop mass spectrometry (PTR-TOF-MS). Bland-Altman analysis revealed sufficient limits of agreement (95% confidence intervals), promising to indicate reliably the clinical need for antidote and hemodialysis treatment. This simple-in-use detector features high diagnostic capability for accurate measurement of methanol in spiked breath, promising for rapid screening of methanol poisoning and assessment of severity. It can be applied readily by first responders to distinguish methanol from ethanol poisoning and monitor in real time the subsequent hospital treatment.

4.1 Introduction

There are thousands of registered¹ methanol poisoning cases every year with devastating consequences including organ failure, blindness and even death.² Often, a single batch of methanol-contaminated spirit results in a poisoning outbreak with dozens of victims overwhelming local clinics,³ particularly in developing countries with insufficient diagnostic and treatment capacities.⁴ So also recently during the COVID-19 pandemic in Iran⁵ and even the US⁶ where the consumption of methanol-contaminated hand-sanitizers led to >700 deaths. After ingestion of laced products, methanol is absorbed rapidly from the gastrointestinal tract within 30–60 min.⁷ While methanol itself has low toxicity, it is metabolized in the liver (Figure 4.1a) at a rate⁸ of $85 \text{ mg L}^{-1} \text{ h}^{-1}$ to toxic formaldehyde by the enzyme alcohol dehydrogenase (ADH) and within only several minutes to formic acid⁹ which is directly correlated with increased morbidity and mortality.¹⁰ Thereby, ADH metabolizes ethanol preferentially over methanol. As methanol is typically consumed with ethanol, symptoms of methanol poisoning often start more than 24 h after consumption.⁹ Early diagnosis is therefore crucial to initiate immediate treatment and increase the chance of patient recovery.

The “gold standard” for diagnosis of methanol poisoning is the direct measurement of methanol in blood by benchtop liquid (LC) or gas chromatography (GC).¹¹ However, this is laborious, expensive and typically performed in specialized laboratories delaying diagnosis for several hours to days.¹² Instead, often a combination of physical examination and blood chemistries like pH, osmolal and anion gap is used.¹³ These are non-specific to methanol (e.g., cannot distinguish it from common alcohol intoxication) and only weakly correlate with intoxication severity.¹⁴ For instance, a retrospective study of 346 patients associated an increased osmolal gap more likely to other conditions (e.g., ketoacidosis, kidney failure) rather than methanol intoxication.¹⁵ Other methods include single¹⁶ or arrays¹⁷ of enzymatic assays to detect methanol or formic acid¹⁸ in blood, urine or saliva. But these only provide qualitative results, are non-specific and/or allow diagnosis only at a late stage. So, simple-in-use and low-cost diagnostic tools are needed for fast screening of methanol poisoning.¹⁹

Breath analysis is a non-invasive alternative to diagnose methanol poisoning,²⁰ as already widely established for ethanol intoxication by law enforcement.²¹ Thereby, the breath and serum alcohol concentrations are related at the alveolar membrane²² (Figure 4.1a) through the blood/breath partition ratio being ~ 2901 for methanol²⁰ and ~ 2100 for ethanol²³. This had been used for diagnosis and treatment of methanol poisoning in six subjects by a Fourier-transform infrared breath analyzer.²⁰ However, this technology (DX4000/DX4015 Gasmeter

Technologies) suffers from being bulky, heavy (15 kg) and rather costly (>\$50'000).²⁴ Chemical sensors (e.g., chemoresistive,²⁵ electrochemical,²⁶ quartz crystal microbalances²⁷) are inexpensive, feature compact size and can detect relevant methanol concentrations,²⁸ but cannot distinguish methanol from other alcohols due to their chemical similarity. Other chemical sensors are selective to methanol, but can only detect it in liquids (e.g., Pt-loaded reduced graphene oxide,²⁹ optofluidic Bragg fiber array³⁰) and are thus not applicable for non-invasive breath analysis.

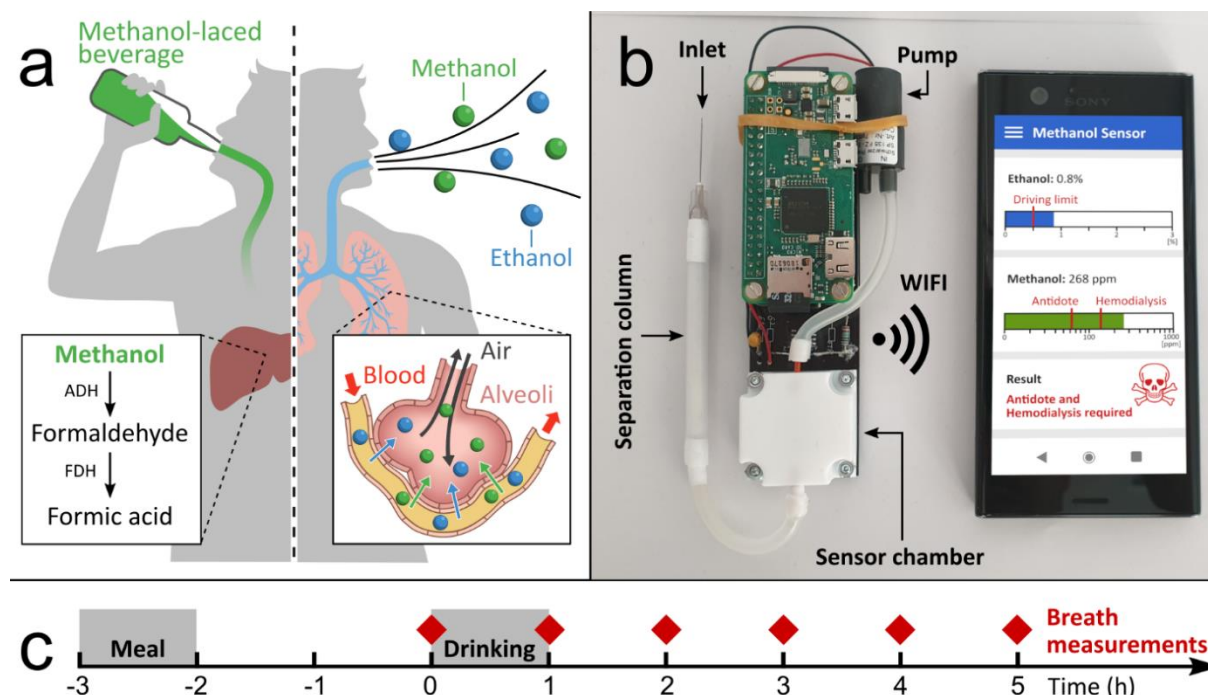


Figure 4.1: (a) After consumption of laced beverages, methanol is metabolized to toxic formaldehyde by alcohol dehydrogenase (ADH) and subsequently to formic acid in the liver. Methanol and ethanol diffuse from blood to breath in the alveoli. (b) Fully integrated and handheld methanol detector to analyze exhaled breath sampled in bags (e.g., Tedlar). Results are communicated by WiFi to a smartphone. (c) Experimental protocol: Volunteers consumed (grey shaded) a standardized meal 3 h before the onset of measurements and an individually calculated amount of ethanol within 1 h afterwards (grey shaded). Breath was sampled (red diamonds) every hour, ethanol concentration was measured by a commercial breathalyzer (Dräger) and subsequently spiked with 10–1000 ppm methanol. Every methanol-spiked breath sample was then measured with the handheld detector and the PTR-TOF-MS for characterization and validation.

Here, we explore the capacity of a previously developed³¹ low-cost and handheld breath detector (Figure 4.1b) for fast screening of methanol poisoning by validation under realistic conditions with humans. The detector combines a compact separation column and a chemoresistive micro gas sensor³¹ fully integrated into a device that can communicate wirelessly with a smartphone app for control and display of results.³² We tested the detector with 105 breath samples that were spiked with relevant methanol concentrations (10–1000 parts per million by volume, ppm) from 20 volunteers after consumption of different

alcoholic drinks to simulate poisoning (Figure 4.1c). Sample analysis was done simultaneously with the handheld detector and a high-resolution proton-transfer-reaction time-of-flight mass spectrometer (PTR-TOF-MS) for statistical analysis. Finally, the receiver operating characteristics (ROC) of the device were determined to assess its diagnostic ability for methanol poisoning.

4.2 Experimental

4.2.1 Detector design and measurement

The handheld detector is shown in Figure 4.1b and described elsewhere.³² In brief, it consists of a capillary inlet for sampling from Tedlar bags, a separation column consisting of a packed bed of Tenax TA polymer sorbent to separate the breath mixture,³¹ a chemoresistive Pd-doped SnO₂ microsensor to quantify the methanol and ethanol concentrations, and a rotary vane pump (SP 135 FZ 3 V, Schwarzer Precision, Germany) drawing the sample through the column to the sensor. A microcontroller (Raspberry Pi Zero W, Great Britain) with integrated circuits on a custom-designed printed circuit board (PCB) is used for autonomous sensor heating, film resistance readout, pump flow control as well as wireless communication with a computer or smartphone. This handheld (size 2×4×12 cm³) detector is lightweight (94 g) and needs minimal power of ~1 W, suitable for battery-driven operation. In this study, it was powered via a USB port and measurement data were saved on an on-board SD card for later analysis.

For sampling, the inlet capillary is injected into Tedlar bags containing the breath samples through a septum in their cap. The pump is turned on, pulling 25 mL min⁻¹ constantly as verified by a calibrated bubble flow meter, to bring the sample to the device. After sampling for 10 s, the capillary is removed from the sampling bag and room air is drawn for 13 min to sequentially determine the methanol and ethanol concentrations and recover the device before the pump is turned off. While off-line sampling from Tedlar bags was necessary in this study to spike breath samples with methanol, the detector could also be used with an end-tidal breath sampler³³ as applied for fat burn monitoring during exercise and rest.³⁴

The sensor response is calculated as:

$$S = R_b/R_s - 1$$

where R_b and R_s denote sensor resistances at the beginning of the test (i.e., baseline) and during analysis, respectively. Methanol and ethanol responses were evaluated at their respective peak maximum and after subtracting the minimum response before their respective peaks to minimize background interference. Retention times (t_R) of analytes are defined as the

time to reach the maximum analyte response, analogous to gas chromatography.³⁵ Please note that at high ethanol concentrations encountered in headspace sampling of adulterated beverages, also the t_R of ethanol can be used to estimate its concentration.³² Lower level of detection (LOD) was defined³⁶ as the lowest measurable concentration distinguishable from three times the sensor noise (standard deviation of the baseline). Ethanol and methanol concentrations were obtained by comparison to daily five-point calibration curves from calibrated gas mixtures of methanol (10–1000 ppm) and ethanol (10–300 ppm) in dry synthetic air, as elaborated elsewhere.³¹ Calibration curves for both analytes were fitted by a power law minimizing the relative error to the measured sensor responses. Note that the detector can also be calibrated less frequently (e.g., once a week, Figure D.5), which slightly lowers the accuracy but might be sufficient for quick screening of methanol poisoning.

4.2.2 Study design

To test the robustness of the device to individual differences in breath composition after alcohol consumption, a cohort of 20 volunteers (15 male and 5 female) 22–65 year old was tested with demographic and anthropometric data listed in Table S1. The main exclusion criteria were alcohol intolerance, history of drug or alcohol abuse (assessed by the AUDIT test³⁷), pregnancy, physical or psychological impairment or health conditions that prevent participation in study, as well as medications known to interact adversely with alcohol consumption. This study had been approved by the ETH Zurich Ethics Commission (EK 2019-N-142). Each subject gave written informed consent prior to the tests and could withdraw at any time. The volunteers were asked to abstain from alcohol for 24 h prior to the study. Further, they were asked not to smoke, eat or drink (except water) and not to brush their teeth nor use mouthwash for 2 h before and during the study to avoid exogenous interference.

The experimental protocol is illustrated in Figure 4.1c. A standardized meal of pasta (dry weight 100 g) with sauce and a salad was consumed 3 h before the start of the test within 60 min to guarantee similar ethanol adsorption and elimination rates.³⁸ At the test start (i.e., $t = 0$), each volunteer consumed a calculated amount of ethanol within 60 min to reach a target blood alcohol concentration of 1000 mg L^{-1} (0.1%) corresponding to a breath alcohol concentration of 0.476 mg L^{-1} (eq. in SI). The amount of ethanol was calculated according to the Widmark formula taking into account the volunteer's gender, weight and drinking duration.³⁹ Volunteers were randomly assigned to consume either beer (6 volunteers, Quöllfrisch, 4.8 vol%, Brauerei Locher AG, Switzerland), wine (7 volunteers, Faustino V, 13.5 vol%, Bodegas Faustino, Spain) or liquor (6 volunteers, Bacardi Carta Blanca, 37.5 vol%,

Bacardi Limited, Bermuda) in order to evaluate differences in the alcoholic beverage type on the detector performance. An additional volunteer served as control and did not consume any alcoholic beverage. During the test, volunteers were under medical supervision. The test was concluded and subjects were released only after their breath ethanol concentration reached a level below 0.238 mg L^{-1} (as checked with a commercial breathalyzer, Dräger, Alcotest 3820, Germany) and after examination by a physician.

4.2.3 Breath sampling and methanol spiking

Breath was sampled at the start, right after the drinking period and every hour thereafter (Figure 4.1c, diamonds). To obtain late expiratory breath containing the most relevant information on blood-borne biomarkers,⁴⁰ volunteers were asked to exhale approximately half of their lung volume (first 2–3 s of exhalation) into the air and the remaining part until exhaustion into Tedlar bags (3 L, SKC Inc., US) through a Teflon tube.⁴¹ This was repeated 4–10 times until a volume of $\sim 2 \text{ L}$ breath was obtained. Breath samples were first measured with the Dräger breathalyzer before spiking with methanol followed by the analysis with our detector and the PTR-TOF-MS. All samples were analyzed within 2 h to limit methanol and ethanol concentration changes to below 3% (Figure D.1), in agreement with experiments performed at lower analyte concentrations.⁴² Tedlar bags were cleaned after each use by filling with nitrogen (PanGas, purity: 99.99%) and pulling vacuum for at least three times.⁴³

Breath samples were spiked with methanol (i.e., standard addition method in analytical chemistry⁴⁴) to simulate methanol poisoning without intoxicating volunteers. Breath was spiked with randomly selected methanol concentrations in the range of 10 to 1000 ppm. This was done on a dynamic gas mixing setup controlled by calibrated gas flow controllers (Bronkhorst, Netherlands), as described in detail elsewhere.⁴⁵ Thereby, methanol vapor was generated by guiding synthetic air (C_nH_m and $\text{NO}_x \leq 100 \text{ ppb}$, Pan Gas) through gas bubblers containing ultrapure water (Milli-Q A10, Merck, Switzerland) and 1 vol% (for 10 – 100 ppm) or 12 vol% (for 100–1000 ppm) methanol (>99.9%, Sigma-Aldrich). The added volume was always <10% of the original breath sample to minimize dilution. Every sample was analyzed by PTR-TOF-MS (PTR-TOF-MS 1000, Ionicon, Austria) operated at 600 V drift voltage, 60 °C drift temperature, 2.3 mbar drift pressure and using H_3O^+ as precursor ion. Ethanol⁴⁶ and methanol⁴⁷ concentrations were determined at mass-to-charge ratios (m/z) of 47.049 and 33.034 by comparison to calibration curves obtained from ethanol and methanol gas standards (495 and 19.7 ppm, respectively, in synthetic air, Pan Gas). To avoid PTR-TOF-MS saturation at high analyte concentrations, samples were diluted with synthetic air (50% RH) by a factor

of 1:10–400 before analysis to measure within their calibrated range, 0–10 and 0–3 ppm for ethanol and methanol, respectively.³¹

4.2.4 Statistical analysis

For Bland-Altman analysis,⁴⁸ measurement data were transformed by a cube root transformation resulting in a normal distribution of the transformed measurement differences according to a Shapiro-Wilk normality test ($p = 0.88$) and absolute differences that are independent of their mean ($p = 0.72$).⁴⁹ Please note that cube root transformation was chosen among cube root, logarithmic and reciprocal transformations as it best satisfied the requirement for normal and independent variance.⁵⁰ Calculations of the mean difference and limits of agreement (95% confidence intervals, CI) were performed on the transformed data and back-transformed at the end.⁵¹ Device bias and precision⁵² were evaluated under intermediate precision conditions⁵³ from all measured breath samples.

Receiver operating characteristic curves were calculated for two classifiers, in specific the need for antidote (>52 ppm methanol measured by PTR-TOF-MS) and hemodialysis (>131 ppm) treatment. These methanol concentrations were estimated from respective blood concentrations⁹ of >200 and >500 mg L⁻¹ using the afore-mentioned blood/breath partition ratio (eq. in SI). Confidence intervals for areas below the ROC curves (AUC) were calculated with the package pROC (v. 1.16.2) in R using the bootstrap method with 10,000 stratified replicates.

4.3 Results and discussions

4.3.1 Selective methanol over ethanol detection

The main challenge for chemical sensors is the *selective* detection of breath methanol over high ethanol concentrations present after consumption of contaminated beverages or during methanol poisoning treatment where ethanol is even used as an antidote.⁹ The present detector achieves this with a packed bed of porous, non-polar Tenax TA polymer sorbent particles (Figure 4.2a), where ethanol absorbs stronger (and thus is retained longer) than methanol,⁵⁴ analogous to GC. A downstream chemoresistive microsensor based on Pd-doped SnO₂ nanoparticles quantifies the methanol and ethanol sequentially with high sensitivity⁵⁵ due to its high surface area (54.5 m² g⁻¹)⁵⁶ and highly porous ($>95\%$)⁵⁷ film morphology. Upon catalytic conversion of analytes,⁵⁸ the chemoresistive sensing film changes its electric resistance proportionally⁵⁹ to the analyte concentration that is read out as sensor response.

Figure 4.2b shows that response to a synthetic gas mixture of methanol (81 ppm) and ethanol (92 ppm). The sensor first detects a peak at a retention time (t_R) of 1.8 min,

corresponding to methanol. This response is not interfered by ethanol, which elutes later and is detected at a t_R of 8.5 min, as was verified³¹ by mass spectrometry. As a result, methanol and ethanol are both detected with high selectivity in gas mixtures and also from other alcohols (e.g., propanol present in disinfectants) that are retained even longer⁶⁰ due to their stronger van-der-Waals interaction with the separation column. This outperforms other state-of-the-art chemoresistive methanol sensors (e.g., GaN pillars,⁶¹ SnO₂-ZnO nanofibers⁶² or In₂O₃-SnO₂ nanofibers⁶³). Also other technologies, like quartz crystal microbalances²⁷ or electrochemical sensors, typically used in breath alcohol detectors,²⁶ fail to differentiate methanol from ethanol poisoning.

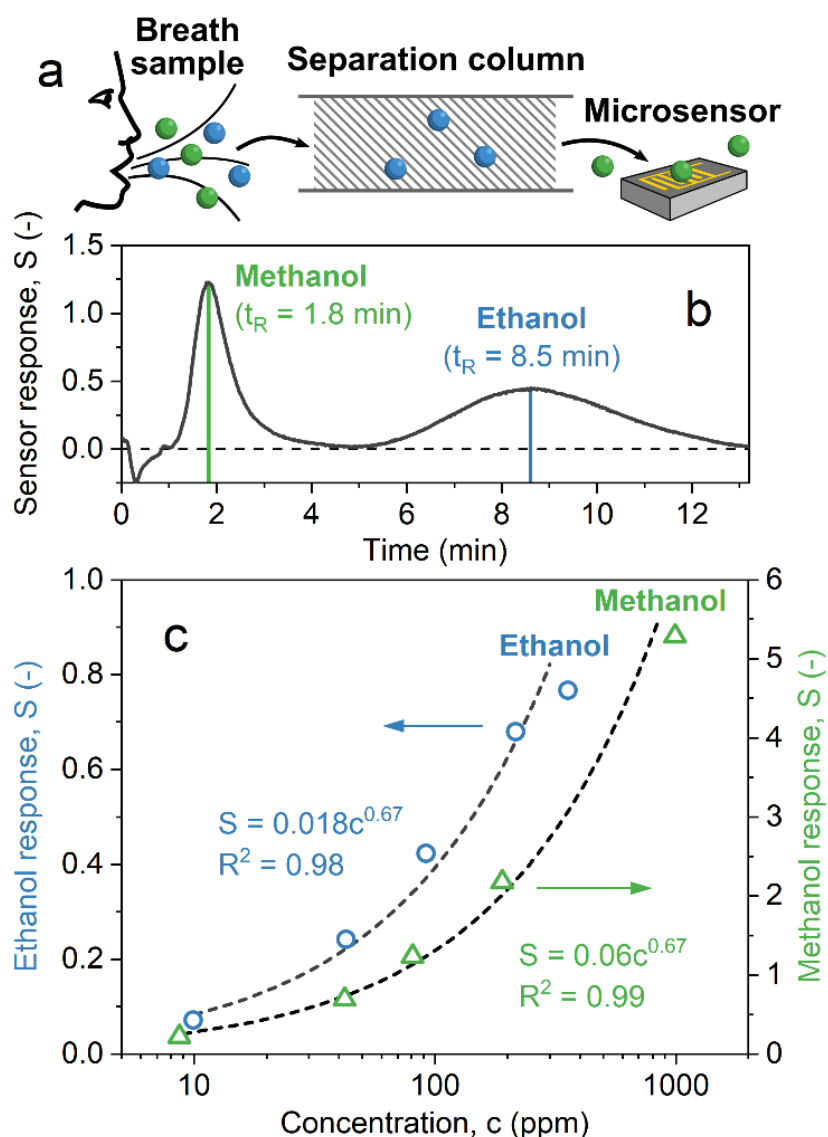


Figure 4.2: (a) Concept of selective breath methanol and ethanol sensing. (b) Sensor response to a mixture of methanol (81 ppm) and ethanol (92 ppm) with indicated retention times (t_R). (c) Sensor calibration with synthetic mixtures of methanol (triangles) and ethanol (circles) in the relevant concentration ranges. Power laws (dashed lines) fitting the sensor calibrations are indicated together with their R^2 values.

The detector was calibrated in the relevant ranges of 10 to 1000 ppm for methanol (triangles) and 10 to 300 ppm for ethanol (circles), as shown in Figure 4.2c. This corresponds to blood methanol and ethanol concentrations of 38–3,824 and 40–1,194 mg L⁻¹, respectively, covering the range observed after methanol poisoning²⁰ and corresponding to mild to medium ethanol intoxication.⁶⁴ Both calibration curves follow a power law in line with theory⁵⁹ for such porous metal-oxide gas sensing films. Also low concentrations of 10 ppm result in clear sensor responses with high signal-to-noise ratios (SNR) of 86 and 28 for methanol and ethanol, respectively. Actually, even lower levels of 0.5 ppm (SNR 4.2) methanol and 2 ppm (SNR 3.2) ethanol are detected just above their LODs (Figure D.2). However, the detector was calibrated only at concentrations >10 ppm relevant for the targeted application and well below toxic⁹ breath methanol concentrations of 52 ppm. Most importantly, the detector covers the entire relevant methanol concentration range without interference of ethanol.

4.3.2 Breath methanol quantification and intra-sample repeatability

The detector performance is shown best on real breath with its over 800 compounds⁶⁵ at high (up to 100%)⁶⁶ relative humidity. Although most of these compounds are present at concentrations <100 ppb, some of their individual or cumulative response might confound the measurement. Figure 4.3a shows the sensor response to breath (green) after consumption of an alcoholic beverage and when spiked with 23 (blue), 66 (purple) and 148 ppm (red) methanol. These methanol levels correspond to endogenous (0–10 ppm),⁶⁷ harmless exogenous (10 – 52 ppm) and toxic concentrations (>52 ppm), respectively.⁹

For all samples, similar ethanol concentrations of 285 ± 11 ppm are detected at $t_R = 8.2$ min, comparable to the calibrated gas mixtures (Figure 4.2b) and in agreement with PTR-TOF-MS (i.e., 248 ppm). Most importantly, the sensor detects no significant methanol concentration in the original breath (PTR-TOF-MS, <1 ppm) with sensor response below the LOD, as expected from physiological breath methanol concentrations (median 0.26 ppm),⁶⁸ while the spiked concentrations are recognized distinctly ($t_R = 1.8$ min). For instance, a sensor response of 1.72 is detected corresponding to 155 ppm from the calibration (see Figure 4.2c) at a nominal methanol concentration of 148 ppm. As a result, methanol and ethanol are quantified individually (to differentiate ethanol from methanol poisoning) and without interference also in spiked breath. Thereby, primarily poisoning-relevant levels are recognized, similar to other diagnostic tests (e.g., hormone HCG for pregnancy⁶⁹ or breath hydrogen for lactose malabsorption⁷⁰) and a variety of gas alarms (e.g., fire detector). Apart from a small response at $t = 0$ –30 s corresponding to non-retained breath compounds (e.g., hydrogen,

methane), no additional peaks are detected, in line with previous results.³¹ Probably this can be attributed to the much lower concentration of most breath molecules (e.g., <1 ppm acetone⁷¹) and longer retention in the separation column,⁵⁴ resulting in lower and practically invisible responses.

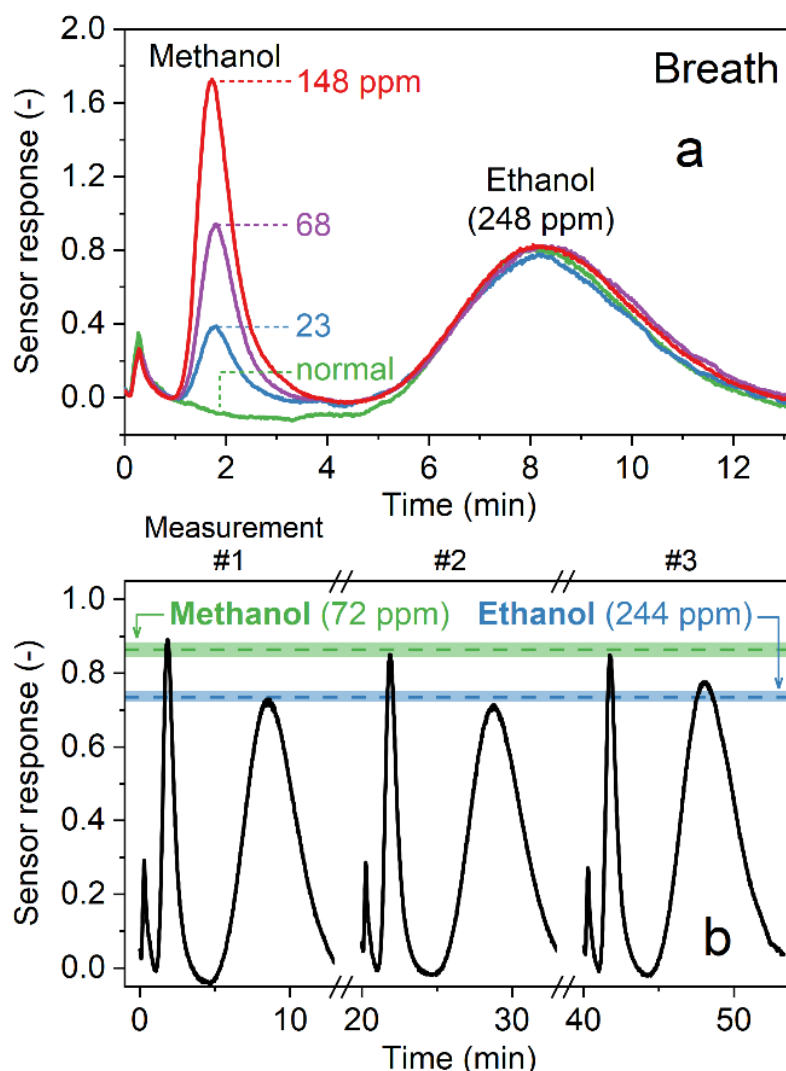


Figure 4.3: (a) Sensor response to breath (green, 248 ppm ethanol) and when spiked with 23 (blue), 68 (purple) and 148 ppm (red) methanol. (b) Sensor response of three consecutive measurements of a breath sample spiked with 72 ppm methanol and 244 ppm ethanol. Indicated are the averages (dashed lines) and standard deviations (shading) that are below 7%.

A major limitation of “gold standard” serum methanol/ethanol measurement gas chromatography is the off-site analysis in laboratories.⁷² As a result, confirmation of methanol poisoning often takes hours or even days¹¹ – too long considering the immediate need for treatment to improve clinical outcome. In contrast, our detector allows non-invasive and near real-time (<2 min) detection of methanol poisoning on site by first responders or non-professionals.

Furthermore, the detector is also reusable as demonstrated by measuring the same spiked breath sample three consecutive times (Figure 4.3b). After each measurement, the detector fully recovers within 15 min by flushing with ambient air and can be used for the next measurement. The intra-sample repeatability shows little variation (standard deviation, shaded in Figure 4.3b) for methanol and ethanol, both below 7%. As a result, the detector permits immediate diagnosis and screening of many patients in quick succession. In addition, the detector performed quite stably over three months of continuous³² testing.

4.3.3 Agreement to PTR-TOF-MS and diagnostic capability

Figure 4.4a,b shows breath ethanol concentrations of two volunteers (see all their profiles in Figures D.3–D.4) measured by the handheld detector (triangles) and the PTR-TOF-MS (circles). The exhaled ethanol concentrations shows a peak within 1 h after drinking for all subjects and thereafter an average elimination rate of $33 \pm 10 \text{ ppm h}^{-1}$ (i.e., $131 \pm 40 \text{ mg L}^{-1} \text{ h}^{-1}$ using the blood/breath partition ratio), both in line with the literature.⁷³ The detector follows this ethanol trend in reasonable agreement with PTR-TOF-MS and quite similar to a commercial breath alcohol tester (Figures D.3–D.4) for all volunteers.

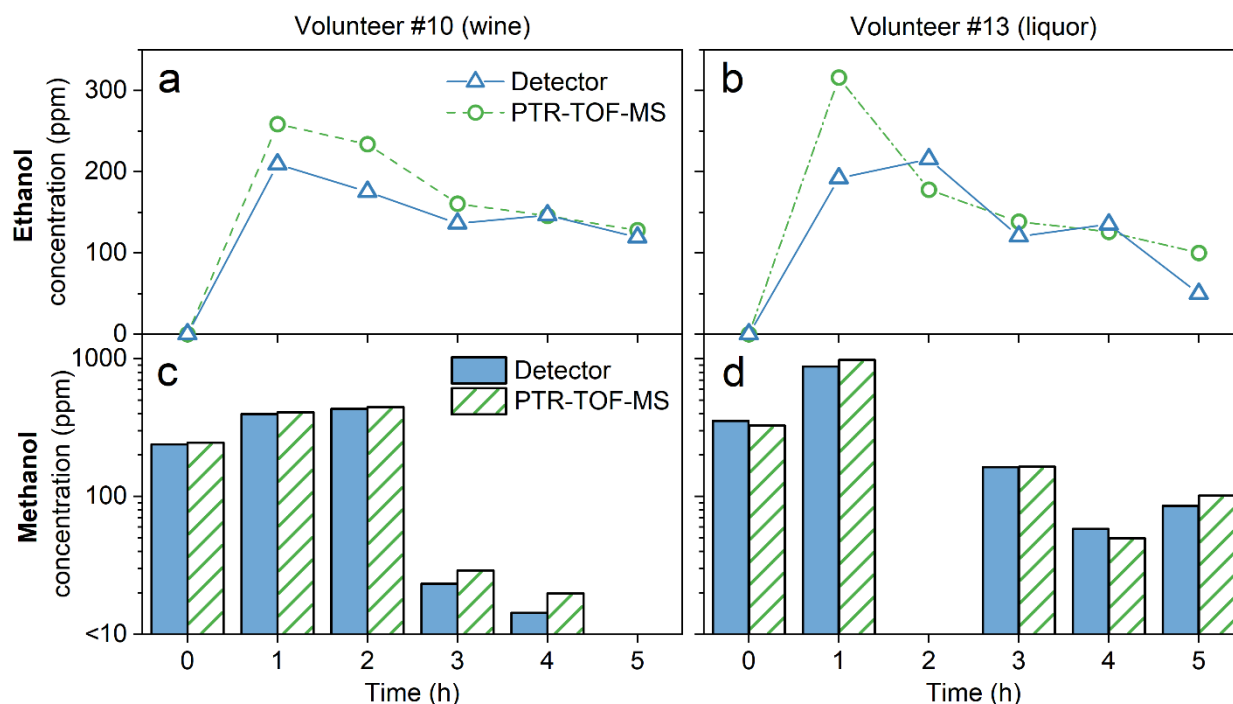


Figure 4.4: (a, b) Breath ethanol concentration dynamics from two volunteers before ($t = 0$) and after consumption of wine (a) and liquor (b), as measured by our detector (triangles) and the PTR-TOF-MS (circles). (c, d) Methanol concentrations from the corresponding spiked breath samples measured by our detector (solid bars) and the PTR-TOF-MS (hatched bars). Note the logarithmic ordinate scale in (c, d).

Most importantly, the detector correctly predicts the spiked methanol in the breath samples over the entire concentration range (Figure 4.4c,d, solid bars), despite high and changing breath ethanol levels (Figure 4.4a,b), in good agreement with PTR-TOF-MS (Figure 4.4c,d, hatched bars). For instance, for volunteer #10 at $t = 1$ h, a high methanol concentration of 397 ppm (Figure 4.4c, solid bar) was predicted, matching well the PTR-TOF-MS value of 409 ppm (hatched bar), despite the presence of 259 ppm ethanol (Figure 4.4a, circle). Lower methanol levels are detected accurately as well. In fact, for the same volunteer at $t = 3$ h, the detector predicts 23 ppm compared to 29 ppm by PTR-TOF-MS at more than 5 times higher ethanol levels (161 ppm).

In total, 105 methanol-spiked breath samples from 20 volunteers were evaluated and the measured methanol concentrations of the detector and PTR-TOF-MS are shown in Figure 4.5a. Indicated also are the concentration ranges where antidote (>52 ppm, grey shaded) and hemodialysis (>131 ppm, red shaded) treatments are recommended from the corresponding blood methanol concentrations.⁹ The detector shows excellent agreement with PTR-TOF-MS ($R^2 = 0.966$) over the entire concentration range (14–1079 ppm) and in the presence of 0–316 ppm ethanol. This is remarkable considering the device's compact and low-cost design (Figure 4.1b). Most importantly, the type of consumed beverage, liquor (squares), wine (triangles), beer (diamonds) and water (circles), does not influence the measurement. Indeed, prediction errors after consumption of different alcoholic beverages are not significantly different ($p > 0.05$) from each other. So, flavoring additives do not seem to interfere with the detector. Note that seven measurements are not shown as samples were not spiked with methanol and eight data points were excluded, as not enough breath sample was provided by the volunteer or problems surfaced during the sensor measurement (four cases each).

To evaluate the agreement between our handheld detector and PTR-TOF-MS further, we performed Bland-Altman analysis⁴⁸ (Figure 4.5b). The measurement error shows heteroscedasticity, i.e., increasing error with increasing methanol concentration, which is typical for such measurements of a physical property.⁷⁴ As a result, also the mean difference (bias, solid blue) and limits of agreement (95% confidence intervals, dash-dotted blue) are a function of the methanol concentration. Analysis of the relative differences (Figure D.6) reveals the detectors bias and precision,⁵² which is $-12 \pm 15\%$ at 131 ppm methanol. However, they and the limits of agreement are sufficiently narrow for a high diagnostic power, as illustrated when applying the detector as a binary classifier to distinguish spiked breath methanol concentrations corresponding to different degrees of poisoning, resulting in areas below the curve of >0.996 (Figure D.7). Of course, these results are based on the detection of

spiked methanol in breath and further validation during field tests with actual methanol poisoning victims are required to correlate breath methanol levels with corresponding concentrations in blood and evaluate unforeseen matrix effects (e.g., disinfectants in the clinical environment).

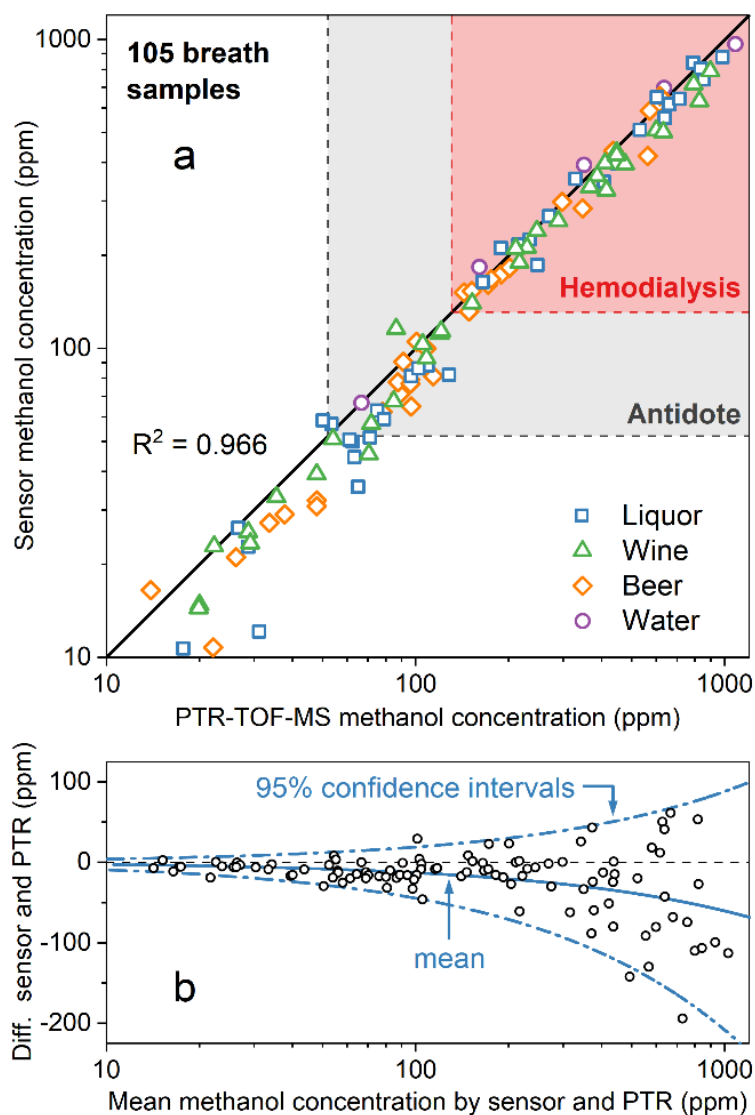


Figure 4.5: (a) Scatter plot of methanol concentrations in all breath samples measured by the detector and PTR-TOF-MS. Volunteers consumed either liquor (squares), wine (triangles), beer (diamonds) or water (circles). Corresponding ideal line (black solid line), R^2 to that line and concentrations requiring treatment with an antidote (grey shaded) or hemodialysis (red shaded) are indicated. (b) Bland-Altman plot showing the difference in methanol concentration measured by sensor and PTR-TOF-MS as a function of the mean of both measurements. Mean and limits of agreement (95% confidence intervals) of these differences are indicated as solid and dashed lines, respectively.

Estimation of blood methanol concentrations relies on the blood/breath ratio, which shows individual variations ($\pm 15\%$)²⁰ similar to ethanol ($\pm 10\%$)²³. It should depend slightly also on the inhaled air temperature through cooling of the airway (analogous to ethanol with 10% lower breath concentrations at 5 °C compared to 23 °C),⁷⁵ which can be addressed by

sampling under standardized conditions.⁷⁶ However, these variations are much smaller than the difference of physiological⁷⁷ to toxic⁹ blood methanol concentration (e.g., 1.7 vs. 200 mg L⁻¹) and should not compromise the screening of methanol poisoning.

It is important to note that such detectors could underestimate the degree of poisoning, similar to blood methanol analysis, when part of the methanol has been converted to toxic metabolites. Thus, the detector should be used complementary to current anamnesis and physical examination to indicate the time of poisoning. Most importantly, however, breath methanol offers non-invasive detection within minutes, so it can be done frequently and on site to initiate immediate treatment and even track the methanol washout. Additionally, through separation of analytes in its column, the detector could be optimized also for additional measurement of formic acid in breath to estimate the level of poisoning more accurately using kinetic models.⁷⁸

4.4 Conclusions

We show how an inexpensive and multi-use detector could be used for rapid (<2 min) and non-invasive diagnosis of methanol poisoning by simple breath sampling. The detector is handheld, can be operated with a battery and communicates results wirelessly with a smartphone or computer. We tested this detector on the breath of 20 volunteers (105 samples) after consumption of liquor, wine and beer. The detector accurately predicted spiked toxic methanol concentrations and differentiates them from elevated ethanol levels, in excellent agreement to high-resolution mass spectrometry ($R^2 > 0.96$) with LOD's close to 0.5 and 2 ppm for methanol and ethanol, respectively. As a result, this device is promising to screen methanol poisoning and classify severity to reliably distinguish the clinical need for antidote or hemodialysis treatment. This detector can be equipped with a disposable mouthpiece, as for commercial breath alcohol testers, and readily applied as a point-of-care diagnostic tool for fast screening of methanol poisoning by first responders and clinicians. Due to its simple use and low price, it is especially promising in developing countries, where most methanol poisonings occur.

4.5 References

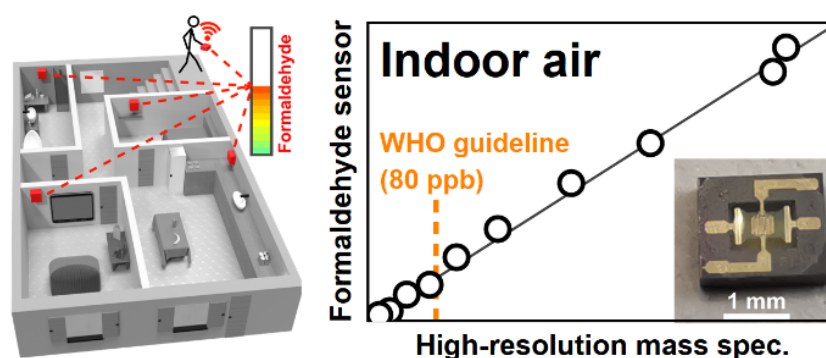
1. Doctors without borders, The methanol poisoning initiative, <https://legerutengrenser.no/mpi/index.html>, (accessed February 2020).
2. J. A. Kruse, *Intensive Care Med.*, **1992**, 18, 391-397.
3. H. Hassanian-Moghaddam, N. Zamani, D. M. Roberts, J. Brent, K. McMartin, C. Aaron, et al., *Clin. Toxicol.*, **2019**, 57, 1129-1136.
4. J. D'Silva, *Br. Med. J.*, **2015**, 351, h4536.
5. *Aljazeera: Iran: Over 700 dead after drinking alcohol to cure coronavirus*, **2020**, <https://www.aljazeera.com/news/2020/04/iran-700-dead-drinking-alcohol-cure-coronavirus-200427163529629.html>.
6. M. Fazio. *The New York Times: 3 Die in New Mexico After Drinking Hand Sanitizer, Officials Say*, **2020**, <https://www.nytimes.com/2020/06/26/us/3-dead-drinking-hand-sanitizer.html>.
7. C. E. Becker, *J. Emerg. Med.*, **1983**, 1, 51-58.
8. D. Jacobsen, R. Webb, T. D. Collins and K. E. McMartin, *Med. Toxicol. Adverse Drug Exper.*, **1988**, 3, 418-423.
9. D. G. Barceloux, G. Randall Bond, E. P. Krenzelok, H. Cooper and J. Allister Vale, *J. Toxicol., Clin. Toxicol.*, **2002**, 40, 415-446.
10. J. Brent, K. McMartin, S. Phillips, C. Aaron and K. Kulig, *N. Engl. J. Med.*, **2001**, 344, 424-429.
11. J. A. Kraut and I. Kurtz, *Clin. J. Am. Soc. Nephrol.*, **2008**, 3, 208-225.
12. J. A. Kraut and M. E. Mullins, *N. Engl. J. Med.*, **2018**, 378, 270-280.
13. K. E. Hovda, O. H. Hunderi, N. Rudberg, S. Froyshov and D. Jacobsen, *Intensive Care Med.*, **2004**, 30, 1842-1846.
14. J. A. Kraut, *Am. J. Kidney Dis.*, **2016**, 68, 161-167.
15. M. D. Krasowski, R. M. Wilcoxon and J. Miron, *BMC Clin. Pathol.*, **2012**, 12.
16. B. Vinet, *Clin. Chem.*, **1987**, 33, 2204-2208.
17. J. M. Shin, G. Sachs and J. A. Kraut, *Transl. Res.*, **2008**, 152, 194-201.
18. K. E. Hovda, G. Gadholt, V. Evtodienko and D. Jacobsen, *Scand. J. Clin. Lab. Invest.*, **2015**, 75, 610-614.
19. M. Rostrup, J. K. Edwards, M. Abukalish, M. Ezzabi, D. Some, H. Ritter, et al., *Plos One*, **2016**, 11, e0152676.
20. O. Laakso, M. Haapala, P. Jaakkola, R. Laaksonen, K. Luomanmäki, J. Nieminen, et al., *J. Anal. Toxicol.*, **2001**, 25, 26-30.
21. M. P. Hlastala, *J. Appl. Physiol.*, **1998**, 84, 401-408.
22. M. Phillips, *Sci. Am.*, **1992**, 267, 74-79.
23. A. W. Jones, *J. Stud. Alcohol*, **1978**, 39, 1931-1939.
24. P. Emanuel and M. Caples, Global CBRN Detector Market Survey, <https://www.wmddetectorselector.army.mil/library/Global%20CBRN%20Detector%20Market%20Survey%20page%20final%20sm.pdf>, (accessed March 2019).
25. J. J. Vijaya, L. J. Kennedy, G. Sekaran, B. Jeyaraj and K. S. Nagaraja, *J. Hazard. Mater.*, **2008**, 153, 767-774.
26. E. M. Caravati and K. T. Anderson, *Ann. Emerg. Med.*, **2010**, 55, 198-200.
27. M. M. Ayad, G. El-Hefnawey and N. L. Torad, *J. Hazard. Mater.*, **2009**, 168, 85-88.
28. A. T. Güntner, S. Abegg, K. Königstein, P. A. Gerber, A. Schmidt-Trucksäss and S. E. Pratsinis, *ACS Sens.*, **2019**, 4, 268-280.
29. H. Ma, Y. Jiang, J. Ma, X. Ma, M. Xue and N. Zhu, *Anal. Chem.*, **2020**, 92, 5897-5903.
30. A. Yildirim, F. E. Ozturk and M. Bayindir, *Anal. Chem.*, **2013**, 85, 6384-6391.

31. J. van den Broek, S. Abegg, S. E. Pratsinis and A. T. Güntner, *Nat. Commun.*, **2019**, 10, 4220.
32. S. Abegg, L. Magro, J. van den Broek, S. E. Pratsinis and A. T. Güntner, *Nat. Food*, **2020**, 1, 351-354.
33. S. Schon, S. J. Theodore and A. T. Güntner, *Sens. Actuators, B*, **2018**, 273, 1780-1785.
34. A. T. Güntner, N. A. Sievi, S. J. Theodore, T. Gulich, M. Kohler and S. E. Pratsinis, *Anal. Chem.*, **2017**, 89, 10578-10584.
35. C. J. Geankoplis, *Transport processes and separation process principles*, Prentice Hall, **2003**.
36. A. D. McNaught and A. Wilkinson, *Compendium of chemical terminology*, Blackwell Science Oxford, **1997**.
37. WHO, *AUDIT: The alcohol use disorders identification test: Guidelines for use in primary health care*. 2001. Available at SSRN: <https://ssrn.com/abstract=3668465>
38. R. T. Gentry, *Alcohol.: Clin. Exp. Res.*, **2000**, 24, 403-404.
39. K. Kypri, J. Langley and S. Stephenson, *Alcohol Alcohol.*, **2005**, 40, 447-452.
40. W. Miekisch, S. Kischkel, A. Sawacki, T. Liebau, M. Mieth and J. K. Schubert, *J. Breath Res.*, **2008**, 2, 026007.
41. O. Lawal, W. M. Ahmed, T. M. E. Nijssen, R. Goodacre and S. J. Fowler, *Metabolomics*, **2017**, 13, 110.
42. J. Beauchamp, J. Herbig, R. Gutmann and A. Hansel, *J. Breath Res.*, **2008**, 2, 046001.
43. P. Mochalski, J. King, K. Unterkofler and A. Amann, *Analyst*, **2013**, 138, 1405-1418.
44. M. Bader, *J. Chem. Educ.*, **1980**, 57, 703-706.
45. J. van den Broek, A. T. Güntner and S. E. Pratsinis, *ACS Sens.*, **2018**, 3, 677-683.
46. C. Turner, P. Španěl and D. Smith, *Rapid Commun. Mass Spectrom.*, **2006**, 20, 61-68.
47. C. Turner, P. Španěl and D. Smith, *Physiol. Meas.*, **2006**, 27, 637-648.
48. M. J. Bland and D. G. Altman, *Lancet*, **1986**, 327, 307-310.
49. N. M. Razali and Y. B. Wah, *J. Stat. Model. Ana.*, **2011**, 2, 21-33.
50. J. M. Bland and D. G. Altman, *BMJ*, **1996**, 313, 106.
51. J. M. Bland and D. G. Altman, *BMJ*, **1996**, 312, 1079-1079.
52. JCGM, The international vocabulary of metrology—basic and general concepts and associated terms (VIM). 3rd ed: BIPM, **2012**, https://www.bipm.org/utis/common/documents/jcgm/JCGM_200_2012.pdf, (accessed September 2020).
53. M. Thompson, *Anal. Methods*, **2012**, 4, 1598-1611.
54. I. Maier and M. Fieber, *J. High Resolut. Chromatogr.*, **1988**, 11, 566-576.
55. A. T. Güntner, V. Koren, K. Chikkadi, M. Righettoni and S. E. Pratsinis, *ACS Sens.*, **2016**, 1, 528-535.
56. J. van den Broek, D. K. Cerrejon, S. E. Pratsinis and A. T. Güntner, *J. Hazard. Mater.*, **2020**, 399, 123052.
57. L. Mädler, A. Roessler, S. E. Pratsinis, T. Sahm, A. Gurlo, N. Barsan and U. Weimar, *Sens. Actuators B Chem.*, **2006**, 114, 283-295.
58. N. Yamazoe, G. Sakai and K. Shimano, *Catal. Surv. Asia*, **2003**, 7, 63-75.
59. J. W. Gardner, *Sens. Actuators B Chem.*, **1990**, 1, 166-170.
60. A. T. Güntner, L. Magro, J. van den Broek and S. E. Pratsinis, *iScience*, **2021**, 24, 102050.
61. H.-F. Ji, W.-K. Liu, S. Li, Y. Li, Z.-F. Shi, Y.-T. Tian and X.-J. Li, *Sens. Actuators B Chem.*, **2017**, 250, 518-524.
62. W. Tang, J. Wang, P. Yao and X. Li, *Sens. Actuators B Chem.*, **2014**, 192, 543-549.

-
63. W. Zheng, X. Lu, W. Wang, B. Dong, H. Zhang, Z. Wang, et al., *J Am Ceram Soc*, **2010**, 93, 15-17.
 64. L. Vonghia, L. Leggio, A. Ferrulli, M. Bertini, G. Gasbarrini and G. Addolorato, *Eur. J. Intern. Med.*, **2008**, 19, 561-567.
 65. B. de Lacy Costello, A. Amann, H. Al-Kateb, C. Flynn, W. Filipiak, T. Khalid, et al., *J. Breath Res.*, **2014**, 8, 014001.
 66. L. Ferrus, H. Guenard, G. Vardon and P. Varene, *Respir. Physiol.*, **1980**, 39, 367-381.
 67. W. Lindinger, J. Taucher, A. Jordan, A. Hansel and W. Vogel, *Alcohol.: Clin. Exp. Res.*, **1997**, 21, 939-943.
 68. P. Španěl, K. Dryahina, P. Vicherková and D. Smith, *J. Breath Res.*, **2015**, 9, 047104.
 69. S. A. Butler, S. A. Khanlian and L. A. Cole, *Clin. Chem.*, **2001**, 47, 2131-2136.
 70. A. Rezaie, M. Buresi, A. Lembo, H. Lin, R. McCallum, S. Rao, et al., *Am. J. Gastroenterol.*, **2017**, 112, 775-784.
 71. A. T. Güntner, N. J. Pineau, P. Mochalski, H. Wiesenhofer, A. Agapiou, C. A. Mayhew and S. E. Pratsinis, *Anal. Chem.*, **2018**, 90, 4940-4945.
 72. J. A. Kraut, *Clin. Toxicol.*, **2015**, 53, 589-595.
 73. J. M. Cowan Jr, A. Weathermon, J. R. McCutcheon and R. D. Oliver, *J. Anal. Toxicol.*, **1996**, 20, 287-290.
 74. A. Nevill, *J Sports Sci*, **1997**, 15, 457-458.
 75. A. W. Jones, *Clin. Sci.*, **1982**, 63, 441-445.
 76. A. Jones, *Alcohol Drugs Driving*, **1990**, 6, 1-25.
 77. S. A. Batterman and A. Franzblau, *Int. Arch. Occup. Environ. Health*, **1997**, 70, 341-351.
 78. K. E. Hovda, K. S. Andersson, P. Urdal and D. Jacobsen, *Clin. Toxicol.*, **2005**, 43, 221-227.

Chapter 5

Selective formaldehyde detection at ppb in indoor air with a portable sensor



Abstract

Formaldehyde is a carcinogenic indoor air pollutant emitted from wood-based furniture, building materials, paints and textiles. Yet, no low-cost sensor exists for on-site monitoring to fulfill stringent current and upcoming (e.g., 8 parts-per-billion by volume, ppb, in France by 2023) exposure guidelines. Here, we present an inexpensive and handheld formaldehyde detector with proven performance in real indoor air. Selectivity is achieved by a compact packed bed column of nanoporous polymer sorbent that separates formaldehyde from interferants present in ambient air. Downstream, a highly sensitive nanoparticle-based chemoresistive Pd-doped SnO₂ sensor detects formaldehyde in the relevant concentration range down to 5 ppb within 2 min. As a proof-of-concept, we measured formaldehyde in indoor air and from different wood product emissions, in excellent agreement ($R^2 > 0.98$) with high-resolution proton-transfer-reaction time-of-flight mass spectrometry. This detector is simple-in-use and readily applicable for on-site formaldehyde exposure monitoring at home or work. It is promising for internet-of-things (IOT) sensing networks or even wearables for personal exposure assessment.

5.1 Introduction

Air pollution has been associated with more than 3 million deaths per year.¹ Thus, needed are portable or even wearable gas sensors for personal exposure monitoring of key toxicants. When interconnected, such next-generation sensors could enable distributed chemical recognition² to identify pollution hotspots³ and to monitor air quality in “smart” buildings⁴ and “future” cities⁵. This can mitigate air pollution and associated health risks. Yet, such sensors with validated performance in the application are often missing.⁶ For instance, commercial NO₂ sensors showed higher signals from interferants than from actual NO₂, while ozone concentrations measured by 20 identical ozone sensors varied by a factor of six.⁷

An omnipresent carcinogenic⁸ indoor air pollutant is formaldehyde. It is emitted most notably from wood-based materials (e.g., furniture), coatings, insulation and flooring materials, where it is used in the adhesives.⁹ Thus, stringent formaldehyde exposure guidelines exist for indoor air (e.g., 80 ppb by the WHO¹⁰) that can be even lower at the national level (e.g., France 8 ppb by 2023¹¹). To date, formaldehyde is measured by *on-site* batch sampling (taking typically >30 min) followed by *off-site* quantification in an external analytical laboratory. While various methods exist (e.g., described in ISO 16000-3), they all have in common that formaldehyde is trapped (i.e., pre-concentrated) and often derivatized in an adsorbent (e.g., Tenax TA, silica gel) and then analyzed with chromatography and/or spectroscopy.⁹ This procedure is expensive, time-consuming, requires skilled personnel and does not allow on-site monitoring.

Chemical gas sensor (e.g., electrochemical, chemoresistive, acoustic wave) could address this, featuring simple application, reusability, high miniaturization potential and low power consumption at minimal cost, ideal for on-site and distributed monitoring.¹² By nanotechnology, such sensors with large specific surface area can be designed capable to detect even the smallest traces of formaldehyde (e.g., 3 ppb by Si-doped SnO₂¹³). Yet, such single sensors fail in real-world environments (e.g., indoor air monitoring) as they lack the required selectivity (Table 5.1) to detect ppb-level formaldehyde concentrations in ambient air consisting of hundreds¹⁴ of compounds. Although high (10–100) selectivities to *some* interferants can be achieved by sensor material design (e.g., flame-made In₄Sn₃O₁₂,¹⁵ bacterial cellulose/polyethyleneimine bilayers,¹⁶ graphene/polymer composites,¹⁷ ZnO/ZIF-8 core-shell structures,¹⁸ Co-doped In₂O₃ nanorods¹⁹ or NiO-SnO₂ microflowers²⁰), this is typically not sufficient considering that ambient air contains orders of magnitude higher confounder²¹

concentrations (e.g., H₂, ethanol, acetone). Also, sensor arrays suffer from decreasing accuracy with an increasing number of analytes in gas mixtures.¹³

Table 5.1: Comparison of portable sensors for monitoring formaldehyde concentrations.

Working principle	Material	LOQ ^a (ppb)	Analysis time (min)	Formaldehyde selectivity, $S_{\text{formaldehyde}}/S_x$ (-)						Reuse-able ^b	Validated in indoor air	Ref.	
				H ₂	CH ₄	CO	Acet-aldehyde	MeOH	EtOH				Acetone
Chemoresistive	NiO-SnO ₂ microflowers	1,000	<1					7	3	42	✓		20
	Co/In ₂ O ₃ nanorods	1,000	1			>1,000		16	4	3	✓		19
	Graphene/polymer composite	50	12					7	7	11	✓		17
	In ₄ Sn ₃ O ₁₂	20	6			>1,000 ^e				>100 ^e	✓		15
	Urchin-like In ₂ O ₃ hollow spheres	50	<1			>1,000 ^e	>100 ^e				✓		22
	ZnO/ZIF-8 core-shell structures	10,000	<1					7	8	11	✓		18
	Pd/SnO ₂ with zeolite membrane	30	8					>1,000	>1,000	>100	✓		23
	Pd/SnO ₂ with Tenax column	5	1.8	∞	∞	∞	∞	∞	∞	∞	✓	✓	This work
Optical	Flow cell (NADH reaction)	2.5	1				77	∞	∞	∞	✓	f	24
	Fluorescent probe	2.5	1				>100						25
	Carbon dots@ SiO ₂ -NH ₂ -Ag ⁺	10	30				3	38	54	4		f	26
	Microfluidic chip (AHMT reaction)	10	18				>100 ^e	>1,000 ^e	>1,000 ^e	>1,000 ^e		f	27
	RKI FP-31	5	30			∞	∞			∞		✓	28
EC ^c	Hydrazinium polyacrylate-based	500	>60										29
SAW ^d	Bacterial cellulose/polyethyleneimine	100	<1	>100		86	14				✓		16

^aLowest concentration measured, ^bCan be used repeatably without exchange of reagents after a measurement, ^cElectrochemical,

^dSurface acoustic wave, ^eLinearly interpolated to same concentrations ($S = R_{\text{air}}/R_{\text{analyte}} - 1$),

^fIndoor air measured but without validation with a benchtop method

Very high (>1,000) selectivity was only achieved with microporous membranes that separate molecules by size, but these introduce increased response time and recovery time (8 and 72 min, respectively).²³ Also, such membrane–sensor systems could be interfered by small molecules (e.g., H₂). Other portable devices are based on formaldehyde derivatization followed by optical (e.g., colorimetric, spectroscopic) or electrochemical quantification. They typically suffer from long sampling times (>30 min), low sensitivity (e.g., hydrazinium polyacrylate-based electrochemical sensor²⁹), irreversibility (e.g., tetraphenylethylene-based fluorophores²⁵ or commercial detector FP-31²⁸), high complexity and price (e.g., fiber-optic flow cell²⁴), or interference (e.g., other aldehydes²⁶), impeding their application and leaving off-site analysis the current method of choice.

Here, we present a low-cost and handheld formaldehyde detector with validated performance in indoor air. Selectivity is achieved by a compact separation column containing a nanoporous non-polar sorbent. A non-specific but highly sensitive chemoresistive microsensor based on flame-made Pd-doped SnO₂ nanoparticles³⁰ is used for formaldehyde

quantification at low ppb concentrations. The formaldehyde sensitivity and selectivity of the detector are characterized with synthetic gas mixtures of indoor air relevant analytes (hydrogen, alcohols, ketones, aldehydes). Finally, the device performance is validated under real-world conditions by high-resolution mass spectrometry. This includes the quantification of formaldehyde emitted from different wood-product samples and in formaldehyde-spiked indoor air with concentrations covering the WHO exposure limit and where sensory irritation occurs.

5.2 Experimental

5.2.1 Microsensor & column fabrication

The handheld formaldehyde detector consists of a separation column and a chemoresistive microsensor. The Separation column is made in-house and consists of a packed bed of Tenax TA powder (500 mg poly(2,6-diphenyl-p-phenylene oxide), 60–80 mesh, $\sim 35 \text{ m}^2 \text{ g}^{-1}$, Sigma-Aldrich) packed inside a Teflon tube (4 mm inner diameters) and secured on both ends with silanized glass wool plugs. Freshly prepared columns were checked visibly for voids and flushed for 24 h with 300 mL min^{-1} synthetic (syn.) air (PanGas, C_nH_m and $\text{NO}_x \leq 0.1 \text{ ppm}$, Switzerland) to remove any previously adsorbed molecules.

The sensor is based on a Pd-doped SnO_2 nanoparticle film prepared by flame spray pyrolysis (FSP)³¹ and directly deposited onto microsensor substrates, described in detail elsewhere.³² The microsensor substrates ($1.9 \times 1.7 \text{ mm}^2$, MSGS 5000i, Microsens SA, Switzerland) feature a free-standing membrane with integrated sensing electrodes and heating layer. Before particle deposition, substrates were pre-annealed in an oven (CWF13/23, Carbolite, United Kingdom) for 20 h at $500 \text{ }^\circ\text{C}$. Finished microsensors were fixed onto leadless chip carriers (LCC, Chelsea Technology Inc., Massachusetts, US) with carbon paste (No. 16057, Pelco). The paste was dried at room temperature for 2 h and subsequently cured in an oven (100-800, Memmert, Germany) for 2 h at $93 \text{ }^\circ\text{C}$. Sensors were then wire-bonded (F&K Delvotec, Germany) to the LCC with aluminum wires ($30 \text{ }\mu\text{m}$ in diameter). The LCC is mounted on a socket (E-Tec, Switzerland) on a printed circuit board and covered by a Teflon sensor chamber ($30 \times 30 \times 5 \text{ mm}^3$).

Polyvinylidene fluoride tube unions (Serto, Switzerland) connect the column to the sensor chamber and to the gas delivery system used for characterization and testing. Downstream of the sensor, a miniature vane pump (135 FZ 3 VDC Schwarz Precision, Germany) draws syn. air or sample gas, respectively, at 25 mL min^{-1} through the separation

column to the sensor. The flowrate was validated by a calibrated bubble flow meter at the pump outlet.

5.2.2 Characterization

Nitrogen gas adsorption-desorption (Tristar II Plus, Micromeritics) was performed to determine the specific surface area and pore size distribution of Tenax TA. Prior to measurement, the sample was degassed for 2 h at 150 °C under nitrogen. The specific surface area was determined by the Brunauer-Emmet-Teller (BET) method and the pore size distribution was extracted from the gas desorption curve by the Barrett-Joyner-Halenda (BJH) method.

Scanning electron microscopy (SEM) cross-sections of sensing films were made with a Hitachi S-4800 operated at 4.1 kV. Pd-doped SnO₂ nanoparticles were thereby directly deposited on alumina sensor substrates (15×13×0.8 mm³, Electronic Design Center, Case Western Reserve University) as these are cleavable, in contrast to the microsensor substrates used for the detector.

5.2.3 Gas evaluation

The microsensor was heated to 350 °C by DC current (R&S HMC8043, Germany) through the heater of the sensor substrate. The separation column was operated at room temperature. The ohmic resistance of the sensing film was monitored between the interdigitated electrodes with a multimeter (Keithley 2700, USA). The sensor response is

$$S = \frac{R_{Air}}{R_{Analyte}} - 1 \quad (1)$$

where R_{Air} and $R_{Analyte}$ denote the sensing film resistance in syn. air and during sample measurement, respectively. All analyte measurements were recorded after equilibrating the sensor with the separation column and achieving a stable baseline (Figure E.1) with relative standard deviation <1%. Retention times, t_R , of analytes are defined as the time from the start of the exposure to the maximum response, analogous to gas chromatography.³³ For sensor calibration, the response was evaluated at the t_R of formaldehyde.

A schematic of the sensor testing setup is shown in Figure 5.1. For characterization, the detector is connected to the mainline supplying humidified syn. air (33–100 mL min⁻¹) generated by mixing dry and humidified syn. air (Figure 5.1a). All flows were accurately controlled by calibrated mass flow controllers (MFC, Bronkhorst, Netherlands) and relative humidity (RH) was monitored by a humidity sensor (SHT2x, Sensirion AG, Switzerland) at

the outlet of the mainline. Heated ($\sim 50\text{ }^{\circ}\text{C}$) Teflon gas lines were used to avoid condensation of water or adsorption of analytes.

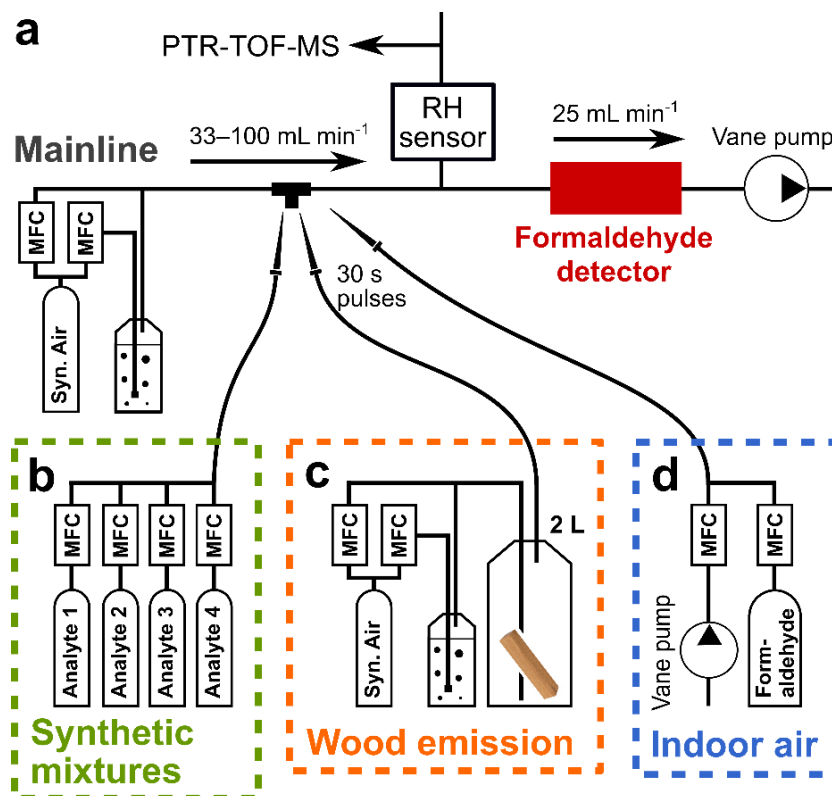


Figure 5.1: Schematic of the Measurement Setup. (a) The formaldehyde detector (consisting of the Tenax TA separation column upstream of a Pd-doped SnO₂ microsensor, red) is connected to the mainline of the gas mixing setup, supplying humidified syn. air by calibrated MFCs. A vane pump downstream of the detector draws air from the mainline or sample through the detector. At the outlet of the mainline, RH and analyte concentrations can be measured by a RH sensor and a PTR-TOF-MS, respectively. For characterization of the detector with (b) synthetic gas–vapor mixtures (green box), (c) wood emissions (orange box) and (d) indoor air (blue box), the respective samples are admixed to the mainline via a hypodermic needle through a septum.

For tests with syn. analyte (hydrogen, formaldehyde, methanol, acetaldehyde) mixtures from calibrated gas standards (Pan Gas, in syn. air or N₂), wood product emission or indoor air were admixed to the mainline with a hypodermic needle ($\varnothing 0.5 \times 40$ mm, Braun) through a septum (Figure 5.1b). The needle was thereby inserted into the septum for 30 s to generate well-defined analyte exposures.

5.2.4 Wood product emission testing

The measurement of emissions from wood products was based on standard testing protocol EN-717-1 (Figure 5.1c) to ensure comparable results. Thereby, humidified syn. air was flushed at 33 mL min⁻¹ (one air exchange per hour) through a 2 L glass bottle containing the samples (chamber loading 1–25 m² m⁻³) at 22 °C. The RH of the inlet air was adjusted to maintain 45% RH at the chamber outlet as validated with a RH sensor. Tested wood products,

in specific, natural wood, oriented strand board (OSB), particle board and medium density fiberboard (MDF) were freshly cut into pieces to achieve the needed surface area (including edges). They were equilibrated in the chamber for at least 12 h before testing. For sensor measurements, the outlet air of the sampling chamber was exposed to the detector for 30 s via a hypodermic needle through a septum in the mainline. The syn. air in the mainline was turned off during exposure to not dilute the sample. To quantify the formaldehyde concentration, the detector was regularly calibrated with a 3-point calibration in the expected concentration range of different wood samples (example in Figure E.2).

5.2.5 Indoor air testing

Indoor air (from the laboratory) was continuously drawn by a vane pump through a MFC at 200 mL min⁻¹ and formaldehyde from the gas standard was admixed to spike it with additional formaldehyde (Figure 5.1d). For sensor measurements, the RH in the mainline was adjusted to that measured in indoor air (40–55% RH at 22 °C). Formaldehyde-spiked indoor air samples were then exposed to the detector for 30 s by hypodermic needle injection via a septum to the mainline. The syn. airflow in the mainline was turned off during exposures to not dilute the sample. To quantify the formaldehyde concentration, the detector was regularly calibrated with a 5-point calibration.

5.2.6 PTR-TOF-MS validation

Analyte concentrations were measured at the outlet of the mainline with a proton-transfer-reaction time-of-flight mass spectrometer (PTR-TOF-MS 1000, Ionicon, Austria). It was operated at 600 V drift voltage, 60 °C drift temperature and 2.3 mbar drift pressure. In the PTR-TOF-MS, hydronium H₃O⁺ ions are produced as precursor and protonate analytes (A) according to equation (2)³⁴. Product ions AH⁺ are separated by their m/z ratio (i.e., mass-to-charge ratio) and recorded as counts per second by the time-of-flight mass spectrometer.



Analytes were recorded at their m/z of 31 (formaldehyde³⁵), 33 & 47 (methanol & ethanol³⁶), and 59 (acetone³⁷). Their concentrations were determined by comparison of measured counts per second to calibration curves prepared from calibrated gas standards on the gas mixing setup (Figure 5.1b). Calibration curves were recorded daily before each measurement and were linear in the relevant range for all compounds.

For validation of wood product emissions, the obtained formaldehyde intensity was compared to a 5-point calibration curve obtained from the gas standard at 45% RH (at 22 °C).

For the measurement of formaldehyde in pristine and spiked indoor air, additional corrections for RH and interference from species fragmentation were considered.³⁸ The formaldehyde sensitivity³⁸ decreases linearly with increasing RH in the relevant range of 40–55% RH (at 22 °C), as determined by four 5-point formaldehyde calibrations at different RH (Figure E.3a,b). This was corrected by measuring RH before every indoor air measurement. The laboratory air sometimes also contained high concentrations of acetone and ethanol that interfere with the formaldehyde signal due to their fragmentation.³⁹ Therefore, a linear correction was applied based on the PTR-TOF-MS calibrations of acetone and ethanol (Figure E.3c,d).

5.3 Results and discussion

5.3.1 Detector design

The concept of the formaldehyde detector is illustrated in Figure 5.2a–c. Indoor air contains >250 different analytes¹⁴ that are separated by a packed bed separation column of Tenax TA particles. Tenax TA was chosen as it is commercially available (thus inexpensive and readily accessible by other scientists), widely used in air analysis and features excellent desorption recovery and temperature stability.⁴⁰ It offers a high surface area ($25 \text{ m}^2 \text{ g}^{-1}$) due to its macroporous structure (Type II adsorption isotherm, Figure 5.2d) with a volume-average pore size of 120 nm (inset in Figure 5.2d). This enables efficient adsorption and retention of analytes, similar to a gas chromatographic column, though much more compact (13 cm length), inexpensive (< \$20 for the Tenax TA powder) and without the need for column heating. After the column, formaldehyde is detected separately from interferants (e.g., hydrogen, methanol), thus selectively, by a highly sensitive but non-specific chemoresistive microsensor (Figure 5.2e). It consists of a highly porous film of flame-made and directly deposited⁴¹ Pd-doped SnO₂ nanoparticles (Figure 5.2f) that form fine networks with large surface area ($54.5 \text{ m}^2 \text{ g}^{-1}$). Formaldehyde rapidly diffuses through this open structure and is oxidized on the surface of the heated metal-oxide nanoparticles, resulting in a modulation of the electrical film resistance that is detected as sensor response.⁴² Similar flame-made Pt-doped SnO₂ sensors showed stable performance for up to 20 days,⁴³ while Pd-doped SnO₂ sensors coupled to sorption filters showed that they are multi-use with good operational stability for selective sensing of isoprene⁴⁴ and methanol³² over three months.

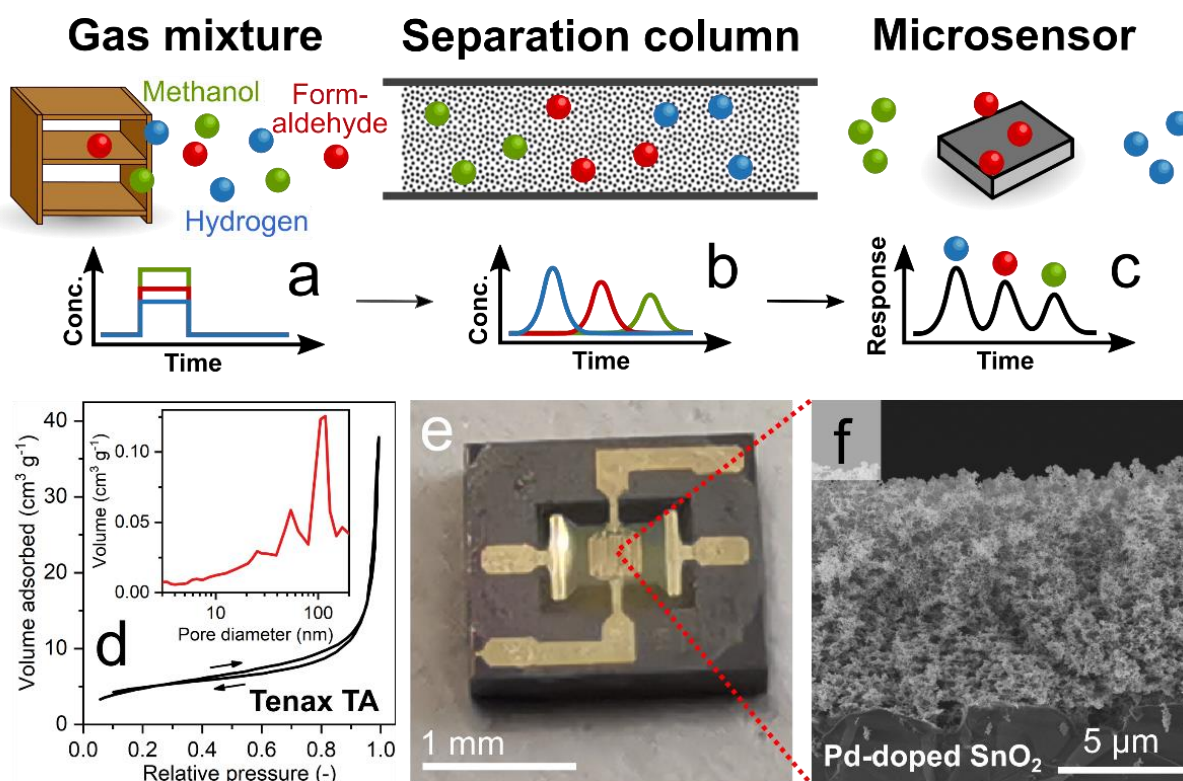


Figure 5.2: Concept for selective formaldehyde detection in (a) complex indoor air enabled by (b) separating a gas mixture with a separation column (packed bed) of Tenax TA particles. (c) Formaldehyde is subsequently detected by a highly sensitive Pd-doped SnO₂ microsensor. (d) Nitrogen gas adsorption-desorption isotherm and derived pore size distribution (inset) of Tenax TA particles. (e) Microsensor featuring a micro-hotplate with a gas-sensitive nanoparticle film. (f) Cross-section scanning electron microscopy image of such a film consisting of flame-aerosol deposited Pd-doped SnO₂ nanoparticles.

5.3.2 Selectivity and lower detection limit

First, the device was tested in synthetic gas mixtures to characterize selectivity and the limit of detection. Figure 5.3a shows the responses of the Pd-doped SnO₂ sensor without separation column when exposed for 30 s to 1 ppm hydrogen (blue), formaldehyde (red), methanol (green) and acetaldehyde (purple), as well as their mixture (black) at standard (EN 717-1) 45% relative humidity (RH). These compounds were chosen as their retention times on Tenax TA are closest to the one of formaldehyde⁴⁵ and they typically occur in indoor air at elevated concentrations.⁴⁶ The sensor quickly (within seconds) responds to all compounds, but cannot differentiate between them, in line with literature.³⁰ As a result, a cumulative response is obtained for their mixture that prohibits accurate formaldehyde quantification. Please note that the mixture response is lower than the sum of the individual compounds, as expected from non-linear reaction-diffusion theory.⁴⁷

With the separation column (Figure 5.3b), non-retained compounds such as hydrogen⁴⁵ are not affected while the others are detected as individual peaks at their specific retention time

(t_R), analogous to gas chromatography.³³ Formaldehyde is detected after 70 s, reaching a peak at 107 s and fully elutes from the column after 600 s. Note that the distinct tailing ($130 < t < 600$ s) might be an effect of adsorption on sites with different adsorption energy.⁴⁸ Methanol and acetaldehyde are retained longer with t_R of 330 and 840 s, respectively. Most importantly, the peak formaldehyde response does not overlap with other compounds, enabling *selective* formaldehyde detection without interference (i.e., infinite selectivity). This is also preserved in their mixture where analytes are detected at identical t_R (Figure 5.3c, dashed lines).

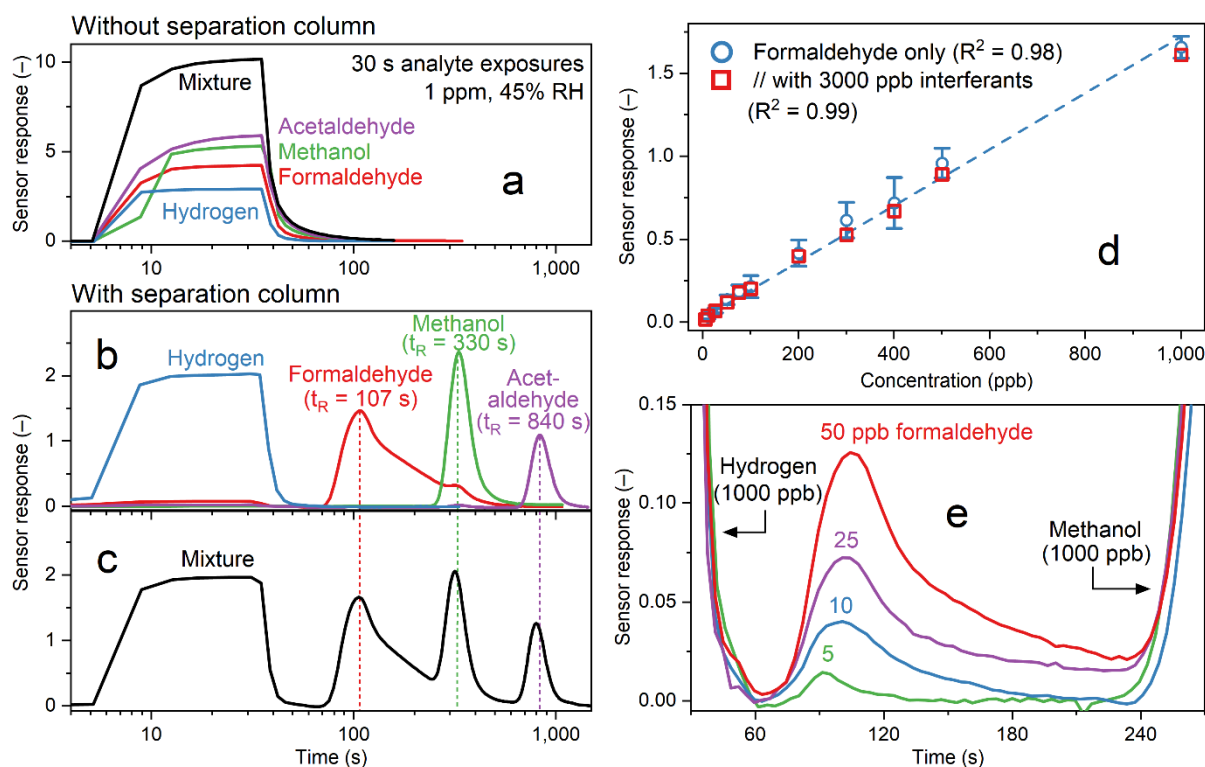


Figure 5.3: Selective formaldehyde detection in synthetic gas mixtures. Response of the Pd-doped SnO₂ microsensor (a) without and (b, c) with separation column to 30 s exposures of 1 ppm hydrogen, formaldehyde, methanol and acetaldehyde as well as their mixture at 45% RH. Analyte retention times (t_R) are given in parentheses. (d) Sensor response with separation column to formaldehyde concentrations between 5–1,000 ppb (circles) at 45% RH. Data are represented as mean \pm standard deviation of three sensors. Squares indicate the same measurement when simultaneously exposed to 3,000 ppb interferants (i.e., hydrogen, methanol, acetaldehyde each 1,000 ppb). Coefficients of determination are provided as R^2 . (e) Responses to 5, 10, 25 and 50 ppb formaldehyde with the same interferants are clearly distinguished at high signal-to-noise ratio (>20).

The non-polar Tenax TA particles separate molecules mainly by unspecific adsorption due to van der Waals forces.⁴⁰ These depend on the analyte's functional groups and molecular weight,⁴⁰ in line with Figure 5.3b. In particular, heavier molecules within the same chemical group are retained longer (e.g., methanol $<$ ethanol $<$ propanol, *etc.*).⁴⁰ So from a broader perspective, this eliminates interference not only of the tested compounds but of entire molecule classes present in indoor air, including the non-retained ones (e.g., H₂, NO_x, CO),

alcohols, higher aldehydes, ketones, carboxylic acids and hydrocarbons with more than three carbon atoms.⁴⁵ We validated this for additional common indoor air interferants (Figure E.4). While also other sorbents could be used if the retention times of formaldehyde and interferants are sufficiently different, they often show stronger adsorption resulting in prolonged analysis time (e.g., charcoal 30 times longer for formaldehyde than Tenax TA⁴⁹).

Average formaldehyde concentrations in conventional homes are typically below 50 ppb,⁹ but are higher in new or renovated houses (e.g., average 149 ppb in ~6000 renovated Chinese homes⁵⁰) and can even reach >1,000 ppb in mobile homes.⁵¹ Figure 5.3d shows the response of the formaldehyde detector (column & microsensor) over the entire relevant concentration range of 5–1,000 ppb (circles). The response increases linearly ($R^2 = 0.98$, fitted trend, dashed line) with good device-to-device reproducibility (20% relative standard deviation, error bars), a critical issue for most low-cost air pollution sensors.⁶ Please note, this calibration curve is RH-dependent, as was shown for the same Pd-doped SnO₂ sensor for formaldehyde at 50 and 90% RH.²³ However, this can be corrected with a co-located humidity sensor.⁵²

The major challenge in formaldehyde sensing is the presence of confounders at much higher⁴⁶ concentrations. Most remarkably, the presence of 3,000 ppb interferants (hydrogen, methanol and acetaldehyde, each at 1,000 ppb) does not affect the formaldehyde response ($R^2 = 0.99$), highlighting the excellent selectivity of the detector. Even 50, 25, 10 and 5 ppb formaldehyde are clearly distinguished (Figure 5.3e) with a high signal-to-noise ratio (SNR, >20). As a result, the WHO guideline of 80 ppb¹⁰ and even stricter upcoming limits (8 ppb)⁵³ are met by our device.

5.3.3 Formaldehyde emissions from wood products

Current formaldehyde detectors mostly failed in the transition from laboratory to real-world gas mixtures, a general challenge in gas sensor research.⁶ Therefore, we tested our detector on the complex emissions of wood products (Figure 5.4a), the main source of formaldehyde in indoor air,⁹ and validated its performance by high-resolution proton transfer reaction time-of-flight mass spectrometry (PTR-TOF-MS). Figure 5.4b shows the detector's response to natural wood (dash-dotted), oriented strand board (OSB, solid), particle board (dotted) and medium-density fiberboard (MDF, dashed) at a loading of 1 m² m⁻³ following a standardized protocol (EN 717-1). For all wood samples, a first response is detected from non-retained analytes (e.g., H₂, CO).⁵⁴ Thereafter, a second peak is detected at identical t_R (107 s) of formaldehyde from laboratory gas mixtures (Figure 5.3b). This formaldehyde response is

clearly separated from emitted methanol, acetaldehyde and ethanol, as verified by simultaneous PTR-TOF-MS measurements using the same separation column (Figure E.5) and synthetic gas mixtures (Figure E.4). The detector thereby indicates the highest formaldehyde concentrations from the MDF followed by the particle board, as expected from the urea-formaldehyde-based adhesive used in their production.⁵⁵ Lower and quite similar formaldehyde concentrations are detected for the natural wood and OSB samples, containing no formaldehyde from adhesives,⁵⁵ which should originate solely from the wood itself.⁵⁶

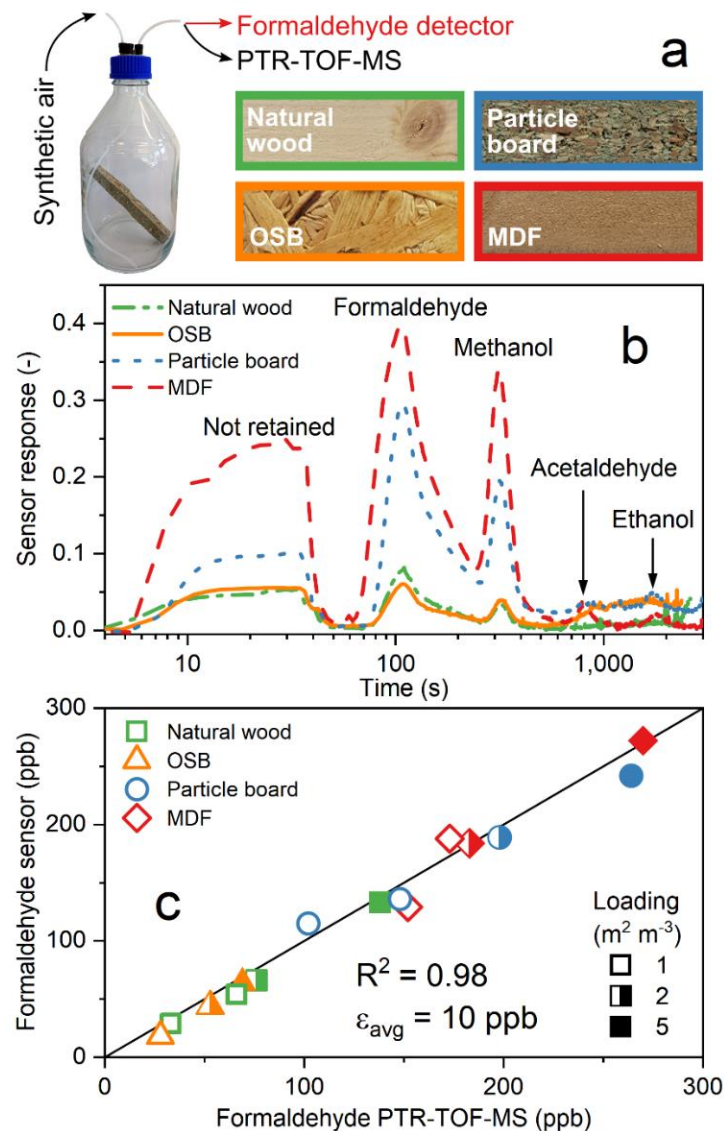


Figure 5.4: Measurement of formaldehyde emissions from wood products. **(a)** Emission testing following the norm EN 717-1: Samples of natural wood, oriented strand board (OSB), particle board and medium-density fiberboard (MDF) are kept in a 2 L glass bottle at 22 °C and 45% RH with an air change rate of 1 h⁻¹. Chamber air is sampled and analyzed with the formaldehyde detector and PTR-TOF-MS. **(b)** Sensor response with a loading of 1 m² m⁻³ natural wood (dash-dotted line), OSB (solid line), particle board (dotted line) and MDF (dashed line). **(c)** Scatter plot of formaldehyde concentrations measured by the detector and PTR-TOF-MS for natural wood (squares), OSB (triangles), particle board (orange circles) and MDF (diamonds) at different loadings of 1 (open), 2 (half-filled), 5 (filled) m² m⁻³.

The detector is applicable for repeated formaldehyde measurements. In fact, after flushing with air for 45 min, the sensor and separation column are regenerated and can be applied for consecutive measurements with <5% formaldehyde response deviation (Figure E.6). This indicates fully reversible interaction of the analytes with the Pd-doped SnO₂ and Tenax TA surfaces without degradation, in line with previous results for methanol sensing³² and literature.⁵⁷ This regeneration time could be decreased significantly by short heating of the separation column and increasing the air flow rate.⁴⁰

Figure 5.4c shows the formaldehyde concentrations by the calibrated (as in Figure 5.3d) detector and PTR-TOF-MS at different wood sample loadings of 1 (open symbols), 2 (half-filled) and 5 m² m⁻³ (filled) in the chamber. The detector is in excellent agreement ($R^2 = 0.98$) to the PTR-TOF-MS with an average error of only 10 ppb, a remarkable result considering the detector's inexpensiveness, simplicity and small size (Figure 5.2). These measurements were performed with a single device during two weeks of repeated exposures, indicating good operational stability.

5.3.4 Indoor air measurements

Finally, the detector was tested with *real* indoor air sampled from our laboratory (Figure 5.5a). It shows first a large response from non-retained compounds that might be CH₄,⁵⁸ CO⁵⁸ and H₂⁵⁹ (please see also Figure E.4). These gases are all usually present at hundreds of ppb in indoor air. Thereafter, a smaller formaldehyde peak is detected (SNR >40, see inset) at $t_R = 107$ s, identical to the synthetic gas mixture (Figure 5.3b) and wood emissions (Figure 5.4b). This peak corresponds to 45 ppb according to PTR-TOF-MS. It is not interfered by methanol and ethanol, which are both eluted later, in line with synthetic gas mixtures (Figure 5.3b and Figure E.4) and wood products (Figure 5.4b). In fact, exposing the detector to the same formaldehyde concentration in synthetic air gives an identical response (Figure E.7). Note that a clean reference gas is required for such indoor air measurements, as done here using bottled synthetic air. Alternatively, reference gas could be generated by switching on-demand to an additional sorption filter (e.g., activated carbon), as already done routinely in commercial devices (e.g., Quintron BreathTracker for H₂).

Figure 5.5b shows the scatter plot of the formaldehyde concentration measured by the detector and PTR-TOF-MS for pristine (squares, measured on two different days) and formaldehyde-spiked indoor air (circles) in the range of 14–475 ppb. Note that spiking was done to test the device also at higher formaldehyde levels. Both instruments show excellent agreement with an R^2 of 0.996, despite the challenging lab environment with high and varying

background concentrations of acetone (up to 1,000 ppb) and ethanol (up to 4,000 ppb), as measured by PTR-TOF-MS. Most importantly, the detector shows a low average error of only 10 ppb and can clearly differentiate safe levels from such above the WHO guideline (dashed line) and when immediate sensory irritation (dotted line) occurs.

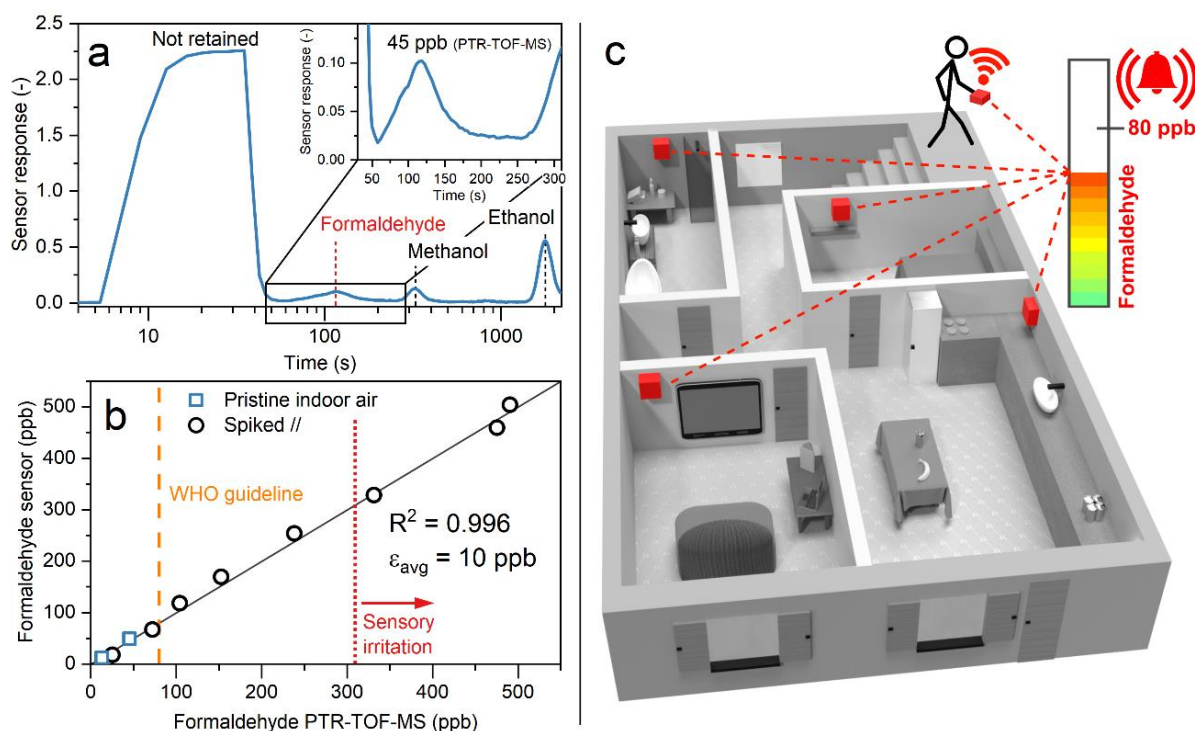


Figure 5.5: Formaldehyde measurement in indoor air. (a) Sensor response when sampling indoor air with a formaldehyde concentration of 45 ppb as determined by PTR-TOF-MS. Inset shows a higher magnification of the formaldehyde-relevant range ($t = 50\text{--}300$ s). (b) Scatter plot of the formaldehyde concentrations measured by the detector and PTR-TOF-MS for pristine (squares) and formaldehyde-spiked (circles) indoor air. Also shown as dashed lines are the WHO guideline (dashed line) for formaldehyde in indoor air and the concentrations where sensory irritation starts (dotted line). (c) Envisioned application of the formaldehyde detector as a sensor network for distributed chemical recognition that communicates with a data cloud for real-time mapping of air quality in “smart” buildings.²

To the best of our knowledge, this is the first low-cost, reusable and compact (75 g and fits in the palm of a hand) formaldehyde detector with *proven* performance in indoor air (Table 5.1). The detector needs minimal power of ~ 1 W (only 75 mW for the sensor heating and the rest for the pump), enabling ready integration into a fully autonomous, battery-driven device with wireless communication and real-time data visualization on a smartphone app. We envision that our detector could transmit data per wireless communication to a data cloud for distributed real-time monitoring of formaldehyde and active regulation of air exchange/purification systems in “smart” buildings,⁴ as illustrated in Figure 5.5c. This is urgently needed, considering that today’s indoor formaldehyde levels frequently exceed threshold levels,⁶⁰ while there is a clear trend to lower exposure guidelines.⁶¹

Even implementation as a portable exposure patch⁶² is feasible to prevent personal health risks. Furthermore, the detector is promising for measuring formaldehyde outdoors,⁶³ where it is an increasing concern due to formation from industrial plants, wildfires,⁶⁴ biofuel combustion⁶⁵ and photooxidation of smog.⁶⁶ The present detector could be mounted onto drones for real-time air quality mapping to identify emission hotspots,³ support smart traffic-management² and assist policymakers in their efforts for low emission zones⁶ in “future” cities.

5.4 Conclusions

A handheld and low-cost detector for the highly selective detection of carcinogenic formaldehyde at ppb-level in indoor air is presented. Formaldehyde is detected within 2 min without interference of the most challenging indoor air compounds at relevant ppb-levels (5 ppb), fulfilling current and upcoming exposure and emission guidelines. Validated with emissions of wood-based materials and real indoor air, it shows excellent agreement ($R^2 > 0.98$) to high-resolution mass spectrometry. This detector is simple-in-use and readily applicable for on-site monitoring of formaldehyde at home or work.

5.5 References

1. S. S. Lim, T. Vos, A. D. Flaxman, G. Danaei, K. Shibuya, H. Adair-Rohani, et al., *Lancet*, **2012**, 380, 2224-2260.
2. M. Mayer and A. J. Baeumner, *Chem. Rev.*, **2019**, 119, 7996-8027.
3. M. Rigby, S. Park, T. Saito, L. M. Western, A. L. Redington, X. Fang, et al., *Nature*, **2019**, 569, 546-550.
4. R. R. Murphy, *Sci. Robot.*, **2018**, 3, eaav6015.
5. M. O'Grady and G. O'Hare, *Science*, **2012**, 335, 1581-1582.
6. A. Lewis and P. Edwards, *Nature*, **2016**, 535, 29-31.
7. A. C. Lewis, J. D. Lee, P. M. Edwards, M. D. Shaw, M. J. Evans, S. J. Moller, et al., *Faraday Discuss.*, **2016**, 189, 85-103.
8. International Agency for Research on Cancer, *Oncol. Times.*, **2004**, 26, 72.
9. T. Salthammer, S. Mentese and R. Marutzky, *Chem. Rev.*, **2010**, 110, 2536-2572.
10. World Health Organization, *WHO guidelines for indoor air quality: Selected pollutants*, **2010**.
11. Ministère de L'Écologie, du Développement Durable, des Transports et du Logement. *Décret n° 2011-1727 du 2 Décembre 2011 relatif aux valeurs-guides pour l'air intérieur pour le formaldéhyde et le benzène*, **2011**.
12. A. T. Güntner, S. Abegg, K. Königstein, P. A. Gerber, A. Schmidt-Trucksäss and S. E. Pratsinis, *ACS Sens.*, **2019**, 4, 268-280.
13. A. T. Güntner, V. Koren, K. Chikkadi, M. Righettoni and S. E. Pratsinis, *ACS Sens.*, **2016**, 1, 528-535.
14. O. O. Hänninen, S. Alm, K. Katsouyanni, N. Künzli, M. Maroni, M. J. Nieuwenhuijsen, et al., *J. Exposure Sci. Environ. Epidemiol.*, **2004**, 14, 440-456.
15. J. A. Kemmler, S. Pokhrel, J. Birkenstock, M. Schowalter, A. Rosenauer, N. Barsan, et al., *Sens. Actuators B Chem.*, **2012**, 161, 740-747.

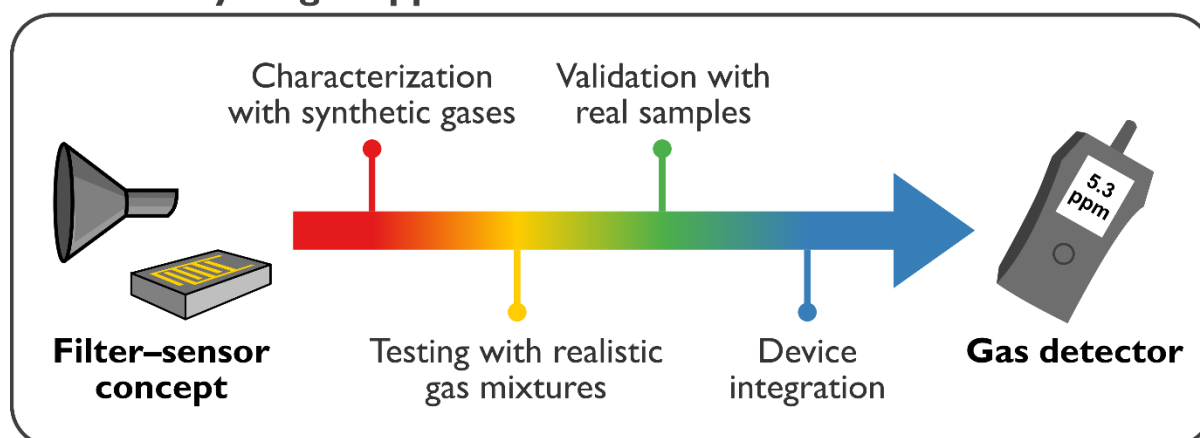
16. J. L. Wang, Y. J. Guo, G. D. Long, Y. L. Tang, Q. B. Tang, X. T. Zu, et al., *J. Hazard. Mater.*, **2019**, 388, 121743.
17. T. Alizadeh and L. H. Soltani, *J. Hazard. Mater.*, **2013**, 248-249, 401-406.
18. H. Tian, H. Fan, M. Li and L. Ma, *ACS Sens.*, **2016**, 1, 243-250.
19. Z. Wang, C. Hou, Q. De, F. Gu and D. Han, *ACS Sens.*, **2018**, 3, 468-475.
20. D. Meng, D. Liu, G. Wang, Y. Shen, X. San, M. Li and F. Meng, *Sens. Actuators B Chem.*, **2018**, 273, 418-428.
21. S. K. Brown, M. R. Sim, M. J. Abramson and C. N. Gray, *Indoor Air*, **1994**, 4, 123-134.
22. Z. Tao, Y. Li, B. Zhang, G. Sun, M. Xiao, H. Bala, et al., *Sens. Actuators B Chem.*, **2019**, 298, 126889.
23. A. T. Güntner, S. Abegg, K. Wegner and S. E. Pratsinis, *Sens. Actuators B Chem.*, **2018**, 257, 916-923.
24. H. Kudo, Y. Suzuki, T. Gessei, D. Takahashi, T. Arakawa and K. Mitsubayashi, *Biosens. Bioelectron.*, **2010**, 26, 854-858.
25. X. Zhao, C. Ji, L. Ma, Z. Wu, W. Cheng and M. Yin, *ACS Sens.*, **2018**, 3, 2112-2117.
26. W. Yang, G. Zhang, J. Ni and Z. Lin, *Microchim. Acta*, **2020**, 187, 137.
27. X.-L. Guo, Y. Chen, H.-L. Jiang, X.-B. Qiu and D.-L. Yu, *Sensors*, **2018**, 18, 3141.
28. RKI Instruments. *Technical Datasheet FP-31 Formaldehyde Detector*, <https://www.rkiinstruments.com/app/uploads/2016/10/FP-31.pdf> (accessed 20/10/20).
29. E. Menart, V. Jovanovski and S. B. Hočevar, *Sens. Actuators B Chem.*, **2017**, 238, 71-75.
30. N. J. Pineau, S. D. Keller, A. T. Güntner and S. E. Pratsinis, *Microchim. Acta*, **2020**, 187, 96.
31. L. Mädler, H. Kammler, R. Mueller and S. E. Pratsinis, *J. Aerosol Sci.*, **2002**, 33, 369-389.
32. J. van den Broek, S. Abegg, S. E. Pratsinis and A. T. Güntner, *Nat. Commun.*, **2019**, 10, 4220.
33. C. J. Geankoplis, *Transport processes and separation process principles*, Prentice Hall, **2003**.
34. A. M. Ellis and C. A. Mayhew, *Proton transfer reaction mass spectrometry: Principles and applications*, John Wiley & Sons, **2013**.
35. J. Beauchamp, J. Herbig, J. Dunkl, W. Singer and A. Hansel, *Meas. Sci. Technol.*, **2013**, 24, 125003.
36. P. Spanel and D. Smith, *Int. J. Mass Spectrom. Ion Processes*, **1997**, 167/168, 375-388.
37. T. Claire, Š. Patrik and S. David, *Physiol. Meas.*, **2006**, 27, 321-337.
38. L. Cui, Z. Zhang, Y. Huang, S. C. Lee, D. R. Blake, K. F. Ho, et al., *Atmos. Meas. Tech.*, **2016**, 9, 5763-5779.
39. S. Inomata, H. Tanimoto, S. Kameyama, U. Tsunogai, H. Irie, Y. Kanaya and Z. Wang, *Atmos. Chem. Phys.*, **2008**, 8, 273-284.
40. M. Schneider and K.-U. Goss, *Anal. Chem.*, **2009**, 81, 3017-3021.
41. L. Mädler, A. Roessler, S. E. Pratsinis, T. Sahm, A. Gurlo, N. Barsan and U. Weimar, *Sens. Actuators B Chem.*, **2006**, 114, 283-295.
42. N. Yamazoe, G. Sakai and K. Shimano, *Catal. Surv. Asia*, **2003**, 7, 63-75.
43. L. Mädler, T. Sahm, A. Gurlo, J. D. Grunwaldt, N. Barsan, U. Weimar and S. E. Pratsinis, *J. Nanopart. Res.*, **2006**, 8, 783-796.
44. J. van den Broek, A. T. Güntner and S. E. Pratsinis, *ACS Sens.*, **2018**, 3, 677-683.
45. I. Maier and M. Fieber, *J. High Resolut. Chromatogr.*, **1988**, 11, 566-576.
46. T. Salthammer, *Indoor Air*, **2016**, 26, 25-38.

-
47. J. W. Gardner, *Sens. Actuators B Chem.*, **1990**, 1, 166-170.
 48. J. C. Giddings, *Anal. Chem.*, **1963**, 35, 1999-2002.
 49. Y. Yokouchi, T. Fujii, Y. Ambe and K. Fuwa, *J. Chromatogr. A*, **1979**, 180, 133-138.
 50. X. Tang, Y. Bai, A. Duong, M. T. Smith, L. Li and L. Zhang, *Environ. Int.*, **2009**, 35, 1210-1224.
 51. K. Sexton, M. X. Petreas and K. S. Liu, *Environ. Sci. Technol.*, **1989**, 23, 985-988.
 52. A. T. Güntner, N. J. Pineau, P. Mochalski, H. Wiesenhofer, A. Agapiou, C. A. Mayhew and S. E. Pratsinis, *Anal. Chem.*, **2018**, 90, 4940-4945.
 53. T. Salthammer, *Int. J. Hyg. Environ. Health*, **2015**, 218, 433-436.
 54. P. R. Zimmerman, R. B. Chatfield, J. Fishman, P. J. Crutzen and P. L. Hanst, *Geophys. Res. Lett.*, **1978**, 5, 679-682.
 55. G. I. Mantanis, E. T. Athanassiadou, M. C. Barbu and K. Wijnendaele, *Wood Mater. Sci. Eng.*, **2018**, 13, 104-116.
 56. M. Böhm, M. Z. M. Salem and J. Srba, *J. Hazard. Mater.*, **2012**, 221-222, 68-79.
 57. H. Rothweiler, P. A. Wäger and C. Schlatter, *Atmos. Environ. B, Urban Atmos.*, **1991**, 25, 231-235.
 58. C. J. Weschler, *Indoor air*, **2000**, 10, 269-288.
 59. F. T. Mackenzie and J. A. Mackenzie, *Our changing planet: An introduction to earth system science and global environmental change*, Prentice Hall Upper Saddle River, NJ, **1998**.
 60. D. A. Sarigiannis, S. P. Karakitsios, A. Gotti, I. L. Liakos and A. Katsoyiannis, *Environ. Int.*, **2011**, 37, 743-765.
 61. S. Wi, M.-G. Kim, S.-W. Myung, Y. K. Baik, K.-B. Lee, H.-S. Song, et al., *J. Hazard. Mater.*, **2020**, 393, 122381.
 62. Y.-S. Kim, M. Mahmood, Y. Lee, N. K. Kim, S. Kwon, R. Herbert, et al., *Adv. Sci.*, **2019**, 6, 1900939.
 63. L. Zhu, D. J. Jacob, F. N. Keutsch, L. J. Mickley, R. Scheffe, M. Strum, et al., *Environ. Sci. Technol.*, **2017**, 51, 5650-5657.
 64. R. J. Yokelson, J. G. Goode, D. E. Ward, R. A. Susott, R. E. Babbitt, D. D. Wade, et al., *J. Geophys. Res.: Atmos.*, **1999**, 104, 30109-30125.
 65. J. C. Liao, L. Mi, S. Pontrelli and S. Luo, *Nat. Rev. Microbiol.*, **2016**, 14, 288.
 66. A. R. Garcia, R. Volkamer, L. T. Molina, M. J. Molina, J. Samuelson, J. Mellqvist, et al., *Atmos. Chem. Phys.*, **2006**, 6, 4545-4557.

Chapter 6

Research Recommendations

Guided by target application



This thesis presents the development of sensor systems enhanced by filters with unprecedented selectivity for applications in breath analysis, food quality assessment and indoor air monitoring. Today, many commercial sensors already use filters in specific applications (e.g., catalytic and sorption filters in CO¹ and CH₄² alarm sensors or GC columns for detection of H₂ and CH₄ in breath³). Furthermore, a plethora of next generation sensor technologies and advanced sensing materials are available with impressive performance in the laboratory. To fully assess their potential, they need to be validated under realistic conditions (e.g., detection of pollutants in indoor air⁴ or markers in exhaled breath⁵). In fact, today most commercial chemical sensors fail in such emerging applications as they lack the required selectivity.

Filters help single sensors and sensor arrays to overcome selectivity limitations as they can exploit a variety of molecular properties of analytes, including molecular size, surface affinity, diffusion properties and chemical reactivity. These are typically not accessible by the sensor alone, which is focused on reactivity (i.e., chemoresistive sensors), electromagnetic absorption (i.e., optical sensors), or molecular mass (i.e., quartz microbalances). By tuning

filter selectivity by material design and combination of filters with suitable sensors, an array of new and promising applications is unlocked.

Development of sensors should thereby not be focused solely on selectivity values but rather on their performance in specific applications. This requires careful consideration of expected confounders, analyte concentration ranges, operational conditions (e.g., humidity) and required device specifications (e.g., price, size and analysis time). Based on this, sensors should be developed step-by-step, going through stages with increasing complexity, including basic sensor characterization with synthetic gases, testing with realistic gas mixtures, validation with real samples and device integration. Only then, sensors can ultimately leave the laboratories and become useful products. The detectors presented in this thesis are all at different stages of this process and require further research and development to reach that goal.

While the isoprene sensor concept from chapter 2 showed promising performance with simulated breath, it must be validated next with real breath containing hundreds of additional compounds. As breath isoprene spikes during muscle activity,⁶ validation of the sensor with volunteers during and after exercise is attractive. Thereby, a large dynamic concentration range of isoprene could be covered, similar as done already for a breath acetone sensor.⁷ More diffuse seems to be the actual application of an isoprene sensor. While isoprene is a tentative breath marker for various physio- and pathological conditions, its origin and biophysical pathway is still mostly unknown.⁸ Here, collaborations with clinicians and breath analysis experts are required to define specific applications. As of now, atmospheric isoprene emitted from plants resulting in formation of secondary organic aerosols⁹ and isoprene as a unique sign of human life in search & rescue operations¹⁰ present the most tangible applications for isoprene sensors.

The methanol detector developed in chapter 3–4 and appendix A must be equipped with sampling mechanisms allowing automatic, simple-in-use and reproducible sampling of liquid headspaces and breath. While offline sampling of breath via Tedlar bags was necessary to spike samples with methanol, it is not practical for rapid screening of methanol poisoning by first responders. Needed is an online breath sampling mechanism using disposable mouthpieces, as already used by breath ethanol detectors. Reproducible sampling of end-tidal breath could be achieved by measuring exhalation volume¹¹ (through integration of exhalation flow measured by a pressure sensor), which is more accurate and cheaper than time¹²- and CO₂-controlled sampling, respectively. The next and crucial step is to validate the detector in collaboration with clinicians on breath of actual methanol poisoning victims to correlate breath to blood methanol concentrations and assess the detectors robustness in a clinical setting, as done similarly with a benchtop infrared spectrometer.¹³

For the formaldehyde sensor presented in chapter 5, the next step is integration of the sensor concept into a portable detector. The main challenge is thereby the generation of a formaldehyde-free reference gas, needed to obtain a sensor baseline and regenerate the separation column. Promising approaches are the use of other filters, such as commercial adsorption filters widely established already for generating zero-air for analytical instruments (e.g., Quintron BreathTracker³). Another, more compact, option that would not saturate over time are catalytic filters. Indeed, such catalytic filters of heated Pt-doped Al₂O₃ fully combusted most analytes present in indoor air including H₂.¹⁴ Another challenge that is especially pronounced for the formaldehyde detector but applies to all detectors with separation columns is fast regeneration to enable regular, quasi-continuous monitoring of compounds every few minutes. This could be achieved by quick heating of the column as already established for thermal desorption tubes.¹⁵ The filter and sensor then need to be integrated into a portable device, as done for the methanol detector, and validated in different indoor environments (e.g., homes, schools, offices or museums) to test its robustness and long term stability.

Through the immense flexibility of filters for analyte separation and their possible combination with different sensors, a plethora of additional applications becomes accessible. For instance, the methanol detector could also be used to monitor methanol during distillation to help producers control their production processes and their product's adherence to legal limits, and even to detect the presence of methanol in sanitizers, responsible for >700 deaths in Iran¹⁶ and U.S.A.¹⁷ during the recent COVID-19 pandemic. Or, a sensor enabled by a catalytic filter enables new the selective detection of acetone in breath.¹⁴ Integrated into a simple-in-use, portable detector, it enables for the first time longitudinal clinical studies with volunteers monitoring their breath acetone independently at home for metabolic profiling. Soon, tracking the effectiveness of different diets (e.g., ketogenic or intermittent fasting) and exercise protocols on fat burn rate or even the non-invasive detection of metabolic diseases might become reality, more important than ever given today's obesity epidemic.¹⁸

The devices developed in this thesis demonstrate how filters drastically increase the selectivity of sensors to meet demanding requirements in emerging applications. This results in useful devices with immediate societal impact. Given the immense potential of filters, they will almost certainly play a pivotal role in the future development of advanced sensor systems with unprecedented selectivity as they have done already for CO and CH₄.

6.1 References

1. M. Schweizer-Berberich, S. Strathmann, W. Göpel, R. Sharma and A. Peyre-Lavigne, *Sens. Actuators B Chem.*, **2000**, 66, 34-36.
2. H. Debéda, P. Massok, C. Lucat, F. Ménil and J.-L. Aucouturier, *Meas. Sci. Technol.*, **1997**, 8, 99-110.
3. Quintron, BreathTracker Analyzer, <https://www.breathtests.com/instrumentation>, (accessed 2020/06/02).
4. A. Lewis and P. Edwards, *Nature*, **2016**, 535, 29-31.
5. A. T. Güntner, S. Abegg, K. Königstein, P. A. Gerber, A. Schmidt-Trucksäss and S. E. Pratsinis, *ACS Sens.*, **2019**, 4, 268-280.
6. J. King, A. Kupferthaler, K. Unterkofler, H. Koc, S. Teschl, G. Teschl, et al., *J. Breath Res.*, **2009**, 3, 027006.
7. A. T. Güntner, N. A. Sievi, S. J. Theodore, T. Gulich, M. Kohler and S. E. Pratsinis, *Anal. Chem.*, **2017**, 89, 10578-10584.
8. R. Salerno-Kennedy and K. D. Cashman, *Wien. Klin. Wochenschr.*, **2005**, 117, 180-186.
9. M. Claeys, B. Graham, G. Vas, W. Wang, R. Vermeylen, V. Pashynska, et al., *Science*, **2004**, 303, 1173-1176.
10. P. Mochalski, V. Ruzsanyi, H. Wiesenhofer and C. A. Mayhew, *J. Breath Res.*, **2018**, 12, 027107.
11. W. Vautz, J. I. Baumbach, M. Westhoff, K. Züchner, E. T. Carstens and T. Perl, *Int. J. Ion Mobility Spectrom.*, **2010**, 13, 41-46.
12. W. Miekisch, S. Kischkel, A. Sawacki, T. Liebau, M. Mieth and J. K. Schubert, *J. Breath Res.*, **2008**, 2, 026007.
13. O. Laakso, M. Haapala, P. Jaakkola, R. Laaksonen, K. Luomanmäki, J. Nieminen, et al., *J. Anal. Toxicol.*, **2001**, 25, 26-30.
14. I. C. Weber, H. P. Braun, F. Krumeich, A. T. Güntner and S. E. Pratsinis, *Adv. Sci.*, **2020**, 7, 2001503.
15. M. Harper, *J. Chromatogr. A*, **2000**, 885, 129-151.
16. *Aljazeera: Iran: Over 700 dead after drinking alcohol to cure coronavirus*, **2020**, <https://www.aljazeera.com/news/2020/04/iran-700-dead-drinking-alcohol-cure-coronavirus-200427163529629.html>.
17. M. Fazio. *The New York Times: 3 Die in New Mexico After Drinking Hand Sanitizer, Officials Say*, **2020**, <https://www.nytimes.com/2020/06/26/us/3-dead-drinking-hand-sanitizer.html>.
18. A. C. Skinner, S. N. Ravanbakht, J. A. Skelton, E. M. Perrin and S. C. Armstrong, *Pediatrics*, **2018**, 141, e20173459.

Appendix A

A pocket-sized device enables detection of methanol adulteration in alcoholic beverages

Abstract

Alcoholic drinks contaminated, either accidentally or deliberately, by methanol claimed, at least, 789 lives in 2019, mostly in Asia. Here, a palm-sized, multi-use sensor-smartphone system is presented for on-demand headspace analysis of beverages. The analyzer quantified methanol concentrations in 89 pure and methanol-contaminated alcoholic drinks from 6 continents and performed accurately for 107 consecutive days. This device could help consumers, distillers, law-enforcing authorities and healthcare workers to easily screen methanol in alcoholic beverages.

A.1 Introduction

Alcoholic beverages are often intentionally adulterated with cheap methanol (up to 50 vol%¹) to increase beverage profit and potency. In 2017–2019, approximately 7104 intoxicated people and more than 1888 fatalities were reported in 306 registered methanol poisoning outbreaks, with more than 90% in Asia according to *Doctors Without Borders* (<https://legerutengrenser.no/mpi/>, 07.05.2020). Young men are most affected, as was shown in a 2018 case in Iran with 768 victims: 41% were aged 25 – 36 and 93% of the deaths were male.² Also, methanol occurs naturally in most alcoholic beverages, originating from the degradation of pectin during fermentation³. Methanol may reach high concentrations during improper distillation, particularly in fruit spirits (up to 2.4 vol%)⁴. In the European Union, the legal limits for distillates from fruit fermentation range from 0.09–0.71 vol% (at 36 vol% ethanol)⁵.

Chromatography is the “gold” standard for methanol testing, but it is costly, slow and confined to the laboratory. More compact gas sensors, such as fluorescent silica-gel plates⁶ or aluminum-doped nickel oxide nanofibers⁷, detect methanol in the container headspace above beverages, but can be unreliable owing to insufficient detection limits (e.g., 4 vol%⁶) and an inability to distinguish methanol from ethanol background⁷. Most importantly, they have not been validated under real conditions^{6,7}, which is a general challenge for sensor science⁸. Inexpensive, simple-to-use and portable methanol detectors are urgently needed by consumers, distributors and authorities (e.g., police and customs) to screen such beverages. These detectors would also be valuable for professional and even home distillers to assess product adherence to legal limits and monitor methanol concentrations during distillation and possibly even occupational exposure. Furthermore, such detectors could facilitate screening of methanol intoxication by breath analysis by first responders and emergency room workers.⁹

Thus, we introduce a fully integrated, handheld, smartphone-compatible and inexpensive analyzer (Figure A.1a) for rapid methanol and ethanol quantification, based on a previously developed⁹ separation column (Figure A.1b), with validated performance in real alcoholic beverages. The analyzer weighs 94 g and is small (2×4×12 cm³), comparable to commercial breath ethanol detectors (e.g., Dräger Alcotest 3820). The separation column consists of Tenax particles that retain ethanol longer than methanol⁹ and a highly sensitive chemo-resistive sensor, based on flame-deposited palladium-doped tin dioxide nanoparticles¹⁰, detects both chemicals sequentially and thus selectively.⁹ Owing to its low power consumption (~1.1 W), which is reduced by non-continuous operation (the pump is only switched on during

sampling, analysis and recovery, Figure A.1c), it can be powered by a battery. This protects the sensor and the column from unnecessary exposure to room air contaminants and reduces fluctuations in baseline resistance (Supplementary Figure A.3). Wireless communication by WiFi to a smartphone controls the device and displays the ethanol and methanol concentrations in real-time (Figure A.1d). In the field, the device can be operated also without an external network by direct communication through Bluetooth with the smartphone. The app can be used by Android- or iOS-based systems, thus, should be compatible with older smartphones as well, that are common in low-income regions where most outbreaks occur. Also, additional functionalities like text-to-speech features can be implemented flexibly.

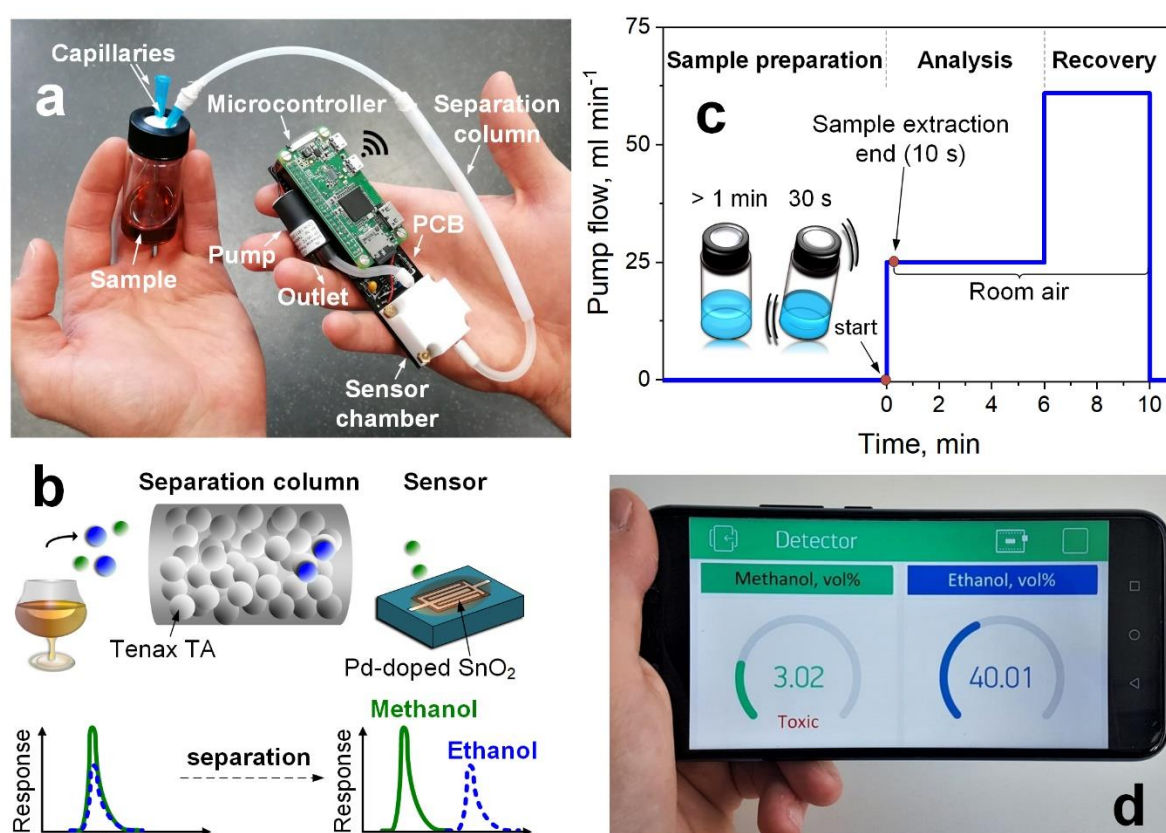


Figure A.1: (a) The handheld analyzer during measurement. (b) A schematic of the detection concept. (c) The sampling and analysis procedure. (d) The tailor-made app to visualize results on a smartphone transmitted through a wireless local area network.

A.2 Results and discussion

The device works by drawing a vapor/gas sample from the container headspace (Figure A.1) into the Tenax column. There methanol and ethanol are retained temporarily. Methanol elutes first and peaks at 1.5 min while ethanol starts to elute later (i.e., 1.9 min for Stroh rum and 3.8 min for beer) enabling the selective and quantitative detection of both (Figure A.2a). The simultaneous quantification of methanol and ethanol is critical as the legally

allowed methanol content depends on ethanol concentration.⁵ The present device offers a lower methanol detection limit (0.01 vol%) than previous sensors, as demonstrated in the relevant ethanol (5–80 vol%) concentration range (Supplementary Figures A.4 & A.5) and compared in the Supplementary Information. Alcoholic beverages are complex mixtures including flavoring additives that may interfere with the sensor. However, no additional peaks are observed as these compounds are present at much lower concentrations (e.g., 0.0015 vol% ethyl acetate¹¹) or retained longer (e.g., 1-propanol 29 times longer than ethanol (Supplementary Figure A.6).

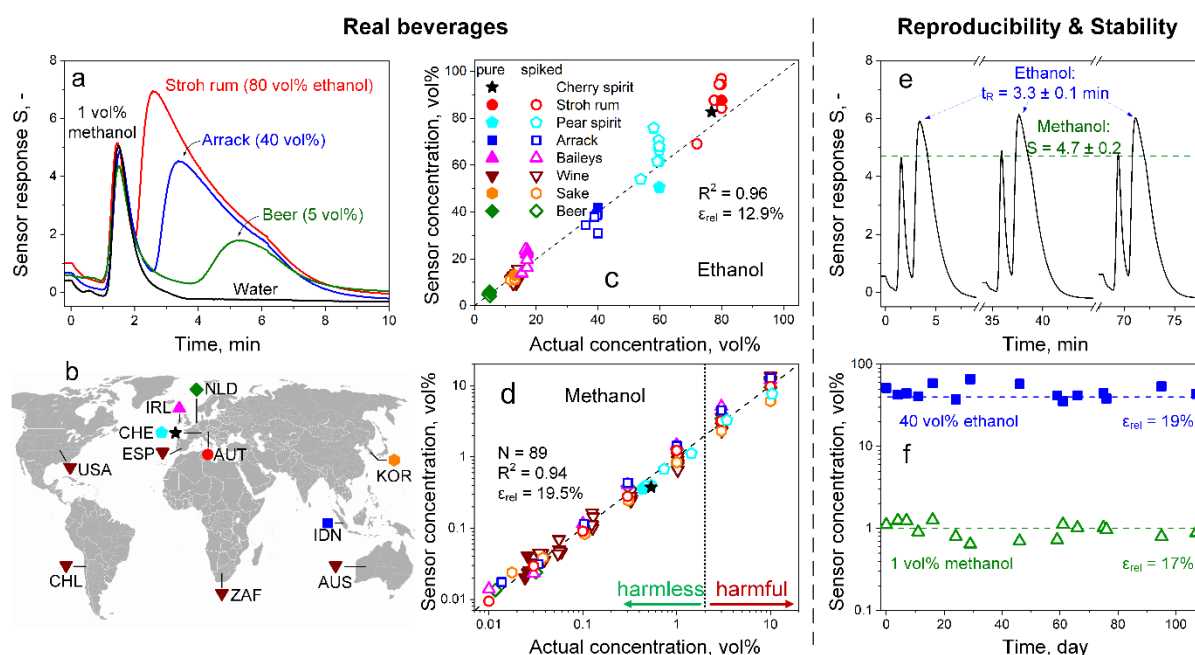


Figure A2: (a) The sensor response for water, beer, arrack and Stroh rum contaminated with 1 vol% methanol. (b) The origin of the tested alcoholic beverages indicated by country codes (ISO 3166). The corresponding actual and sensor-measured (c) ethanol and (d) methanol concentrations in pure (filled symbols) and 0.01, 0.03, 0.1, 0.3, 1, 3 and 10 vol% methanol-contaminated or -spiked (open symbols) cherry spirit (star), Stroh rum (circles), pear spirit (pentagons), arrack (squares), Baileys (up triangles), wines (down triangles), sake (hexagons) and beer (diamonds) ($n = 89$ independent samples). The methanol concentrations of pure beer, sake, Baileys, arrack and Stroh rum were below the sensor's detection limit (i.e., <0.01 vol%) and thus not included. The dashed line indicates the recommended limit (i.e., $2 \text{ vol}\%^{12}$). (e) Sensor responses to three consecutive headspace samples with 1 vol% methanol and 40 vol% ethanol in water. Methanol responses and ethanol t_R are indicated as mean \pm SD. (f) Methanol (triangles) and ethanol (squares) concentrations measured for 107 days. The dashed lines show the actual alcohol concentrations.

The device was evaluated on 89 pure and methanol-contaminated samples of beer, sake, wine (from five continents, Supplementary Figure A.7), Baileys, arrack, Stroh rum, pear and cherry spirits (Figure A.2b). The ethanol concentrations are quantified accurately—with a high R^2 (0.96) and low relative error ($\epsilon_{rel} = 12.9\%$) (Figure A.2c). Pear spirit errors are discussed in Supplementary Information. The device accurately detects methanol concentrations over three

orders of magnitude (0.01–10 vol%) with $R^2=0.94$ and 19.5% error (Figure A.2d). This includes the correct quantification of 0.39 and 0.54 vol% methanol in pure homemade pear and local cherry spirits, just below the EU legal limit⁵. Harmful concentrations of 3 and 10 vol% methanol, above the recommended limit (2 vol%¹², dashed line), are recognized.

The repeatability and stability were evaluated on laboratory mixtures containing 1 vol% methanol and 40 vol% ethanol in water. During three consecutive exposures (Figure A.2e), the peak methanol response and retention time, t_R , of ethanol vary by 4% and 3%, respectively, indicating reliable repeatability. The device provided stable results for 107 consecutive days, once per day for freshly prepared samples (Figure A.2f), with errors of 17 and 19% for methanol and ethanol, respectively. No deterioration was observed, meaning the recovery methodology (Figure A.1c) suffices to maintain the sensor's performance. Variations may be related to altered humidity (27.1–48.2%) and/or temperature (22.5–26.0 °C) during these 107 days – the response of chemo-resistive sensors is affected by humidity¹⁰ and the t_R of the separation column changes with temperature, as shown previously⁹. Nevertheless, the accuracy of the detector is sufficient to distinguish harmful from harmless methanol concentrations in alcoholic beverages (Figure A.2d). If higher accuracies are required, this can be corrected with co-located temperature and humidity sensors¹³.

In conclusion, we present a handheld, low-cost, simple-to-use and reliable methanol detector that can be readily used by beverage consumers, distillers, healthcare workers and law-enforcing authorities for easy methanol screening of alcoholic beverages and possibly even in the breath of intoxicated people. This modular design could be applied also for detection of other food contaminants, such as formaldehyde¹⁴, or food freshness markers, like ammonia from spoiling sea food¹⁵. Concepts for selective analyte sensing exist, including zeolite membranes (formaldehyde¹⁰) or porous CuBr (ammonia)¹⁶, which can be incorporated into the present device. Affordable detectors are particularly attractive for widely distributed use, especially in low-income economies where food safety is a concern.

A.3 Methods

The stand-alone analyzer is shown in Figure A.1a. It consists of a capillary (Sterican, B. Braun AG, Germany) to sample the headspace, a separation column to pre-separate the gas mixture, a sensor for analyte detection, a vane pump (135 FZ 3V, Schwarz Precision, Germany) providing the required flow of 25 mL min⁻¹ and a microcontroller (Raspberry Pi Zero W) to control the sensor and pump, extract the data and communicate wirelessly with a computer or smartphone. The components are integrated onto a PCB and powered by the microcontroller's

micro-USB port using a power adapter. The separation column, palladium-doped tin dioxide sensor and PCB are described in the Supporting Information. The device is inexpensive, consisting mostly of standard components.

The sensing film resistance is determined in the relevant range of 1–30 M Ω with an accuracy of 99.79%, as described in the Supporting Information. The sensor response S is defined as:

$$S = R_b / R_s - 1$$

Therein, R_s and R_b are the resistances during sampling and after overnight stabilization (without flow), respectively. The retention time t_R is defined as the time needed to reach the peak response, analogous to gas chromatography¹⁷. The breakthrough time t_B is extrapolated from a tangent to the ethanol peak¹⁸. Examples for the definition of t_R and t_B are shown in Supplementary Figure A.8. All signals are continuously processed and stored by the microcontroller. Methanol and ethanol concentrations are determined by comparison of the methanol peak response and ethanol t_R to calibration curves (Supplementary Figure A.5), which is more accurate than if the t_R of methanol and ethanol peak response are used, respectively (Supplementary Figure A.7). The microcontroller communicates wirelessly to a smartphone or computer to control its operation and display the results. The smartphone app was designed using the free mobile app constructor Blynk (Version 2.27.9, Blynk Inc., United States).

Sample preparation of laboratory mixtures and real beverages are described in the Supplementary Information. The detector is only exposed to an air flow during sampling, analysis and recovery (i.e., non-continuous operation, Figure A.1c). Before measurement, the prepared vials are at rest for at least 1 min and then shaken for 30 s to facilitate rapid phase equilibrium between liquid and headspace. To perform a measurement, the pump is turned on (25 mL min⁻¹) and the headspace above the liquid is sampled for 10 s, resulting in a total sample volume of about 4.17 mL. A second capillary compensates the pressure in the vial (Figure A.1a). Afterwards, the capillaries are removed from the vial and room air is sampled to carry the headspace sample through the separation column to the sensor. During analysis (0 \leq t \leq 6 min), the headspace sample containing methanol and ethanol passes the column and is analyzed by the sensor. Thereafter (6 $<$ t \leq 10 min), the flow is maximized (\sim 60 mL min⁻¹), to quickly remove analyte residues from the column, refresh the sensor chamber and prepare the device for rapid reuse.

A.4 Supplementary Methods

A.4.1 Column design

The separation column consists of 149.4 mg Tenax TA (poly(2,6-diphenyl-p-phenylene oxide), 60–80 mesh, $\sim 35 \text{ m}^2 \text{ g}^{-1}$, Sigma Aldrich) packed into a Teflon tube (4 mm inner diameter) between silanized glass wool plugs and tension springs at both ends⁹. Before operation, the packed bed column was checked visually for voids and flushed with synthetic air (C_nH_m and $\text{NO}_x \leq 100 \text{ ppb}$, Pan Gas) overnight at 100 mL min^{-1} and 50 % relative humidity (RH) to desorb possible impurities. Connections to the capillary and sensor are made of inert Teflon to minimize adsorption of the analytes during sampling.

A.4.2 Sensor design

The employed sensor consists of flame-made Pd-doped tin dioxide (SnO_2) nanoparticles directly deposited onto a microsensor substrate (Microsens SA, Switzerland, MSGS 5000i), as elaborated elsewhere⁹. The rest of the nanoparticles were collected on a glass-fiber filter (GF6 Albet-Hahnemuehle), downstream of the substrate as described in detail elsewhere¹⁹. Sensors and powder were annealed at $500 \text{ }^\circ\text{C}$ for 5 h. The specific surface area of the powder was determined by nitrogen adsorption, after degassing at $150 \text{ }^\circ\text{C}$ for 1 h (Tristar II Plus, Micromeritics). The particle size was calculated by the Brunauer-Emmett-Teller (BET) theory using the density of SnO_2 (6.95 g cm^{-3}) and assuming spherical morphology. The microsensor ($1.9 \times 1.7 \text{ mm}^2$) features interdigitated electrodes and a heating element integrated into a thin suspended membrane. The resulting power consumption is only 76 mW at the operating temperature of $350 \text{ }^\circ\text{C}$, as in previous studies⁹. For electrical connections, the sensor is attached onto a leadless chip carrier (LCC, Chelsea Technology Inc., United states) and wire-bonded (F&K Delvotec, Germany) with aluminum wires ($30 \text{ }\mu\text{m}$ in diameter). The LCC is mounted on a socket (E-Tec, Switzerland) soldered onto the PCB and covered by a homemade, inert Teflon sensor chamber ($30 \times 30 \times 15 \text{ mm}^3$). The cavity inside the chamber is designed to minimize dead volume and optimize the flow profile over the sensor by arranging the flow in- and outlet perpendicular to its surface (Supplementary Figure A.11).

A.4.3 PCB design

The PCB (Supplementary Figure A.12a) was designed in-house using the free software DesignSpark PCB 8.1. It features two main circuits (Supplementary Figure A.12b) to control the applied voltage to the sensor and pump (orange framed) and read out film resistances (green

framed). Pulse width modulation (PWM) is applied to heat the sensor and operate the vane pump. Thereby, the digital output of the microcontroller switches between 0 and 3.3 V with a frequency of 100 kHz at a given duty cycle. The PWM signal is passed through a low-pass filter for noise reduction and amplified by an operational amplifier (AD8656ARZ-R7, Analog Devices). A 12-bit analog-to-digital converter (ADC, MCP3208, Microchip Technology) is used to read out the applied voltage (Supplementary Figure A.13a) to the pump and determine the resistance of the sensor's heating element using a voltage divider. Based on the latter signal, the duty cycle is automatically adjusted by the microcontroller to sustain the sensor temperature of 350 °C. The respective circuit diagram is shown in the inset of Supplementary Figure A.13a. The sensor resistance was determined using a voltage divider and the ADC (green framed, Supplementary Figures A.12b and A.13b). The circuit diagram and validation are shown in Supplementary Figure 13b. A unity-gain amplifier (MCP6002T-I/SN, Microchip Technology) and a capacitance are used ahead of the ADC to reduce the influence of its internal resistance.

A.4.4 Sample preparation and analysis

For analysis with laboratory mixtures, methanol (>99.9%, Sigma-Aldrich, Germany) and ethanol (> 99.8 %, Fisher Chemical, Switzerland) were mixed with Milli-Q water (Milli-Q Synthesis A10, Merck, Germany) using high precision pipettes (Eppendorf, Germany and Mettler Toledo, United States). Samples contained methanol concentrations of 0, 0.01, 0.03, 0.1, 0.3, 1, 3 and 10 vol% in 5, 20, 40 and 80 vol% ethanol (total 32 samples). Each sample was 5 mL filled into a 20 mL glass vial (Wheaton, DWK Life Sciences, United States) for sufficient headspace volume that was immediately sealed with caps containing a septum (Polypropylene Hole Cap, Sigma Aldrich, Germany) for headspace extraction.

The following alcoholic beverages were tested: beer (5 vol% ethanol, Heineken, Netherlands), sake (13 vol%, Kook Soon Dang Brewery, Korea), five wines from different locations (Supplementary Figure A.7a and Supplementary Table A.1), Baileys Original (17 vol%, Diaego, Ireland), Boven's echter Arrak (40 vol%, Indonesia), pear spirit (homemade, Switzerland), cherry spirit (77 vol%, S. Fassbind AG, Switzerland) and Stroh rum (80 vol%, Stroh Austria, Austria). The liquid ethanol content of the pear spirit was determined by density measurements²⁰. The methanol content of the pure beverages was analyzed by liquid chromatography (Varian 3800, Agilent, USA) using a sample volume of 0.5 µL and pressure of 4 psi. The injector was operated at 210 °C with a split ratio of 20. During analysis, the column (Zebron ZB-624, Brechbühler AG, Switzerland) and flame-ionization detector were operated at 45 and 220 °C, respectively. A 9-point calibration was applied between 0.001 and

0.5 vol% methanol. For higher methanol concentrations, the alcoholic beverages are spiked with methanol contents of 0.01 – 10 vol%, as described above for laboratory mixtures. In total, 89 pure and methanol-spiked samples were tested.

The separation is validated by proton-transfer-reaction time-of-flight mass spectrometry (PTR-TOF 1000, Ionicon Analytik GmbH, Austria). The H_3O^+ primary ions are obtained from water vapor. The drift tube is operated at a voltage of 600 V and a pressure of 2.3 mbar. The value of the reduced electric field (E/N) is 130 Td. Methanol and ethanol are evaluated at a mass-to-charge ratio of 33.033 (CH_5O^+) and 47.049 ($\text{C}_2\text{H}_7\text{O}^+$), respectively. To avoid saturation of the detector, the sample (25 ml min^{-1}) is diluted by ambient air (250 ml min^{-1}).

A.4.5 Calibrations

For determination of methanol concentrations in real beverages, a relation is needed between sensor response (S) and methanol concentration. For methanol, the following calibration curves were applied, (based on Supplementary Figure A.5d):

$$c_M = \left(\frac{S+0.9}{5.5}\right)^{-2.08}, \quad R^2 = 0.99 \quad \text{for} \quad c_M > 0.1 \text{ vol\%}$$

$$c_M = \left(\frac{S+0.1}{25.2}\right)^{0.74}, \quad R^2 = 0.99 \quad \text{for} \quad 0.01 < c_M \leq 0.1 \text{ vol\%}$$

where c_M is the methanol concentration in vol%. The ethanol concentration (c_E in vol%) was determined from the retention time of ethanol ($t_{R,E}$ in min) by applying the following relation (based on Supplementary Figure A.5e):

$$c_E = \left(\frac{t_{R,E}}{8.3}\right)^{-4}, \quad R^2 = 0.95$$

Please note that the device prediction of methanol and ethanol with the applied calibration curves is much more accurate than if the t_R of methanol and ethanol peak response would have been used, respectively (compare Figure A.2c,d with Supplementary Figure A.9).

A.5 Supplementary Discussion

A.5.1 Sensor design and detection concept

The microsensor is a flame-deposited chemoresistive sensing film of Pd-doped SnO_2 nanoparticles. Methanol is adsorbed on the SnO_2 surface forming methoxide, as suggested by infrared spectroscopy²¹. There, it can react with oxygen- and hydroxyl-related species and decompose, for example, to CO , CO_2 and CH_4 , as measured by gas chromatography²². Thereby, the surface Pd catalyzes the reaction²² and electrons released into the conduction band of SnO_2

lower its resistance²³ resulting in the sensor response. Such flame-made metal oxide sensors feature high porosity (up to 98%²⁴) and surface area (i.e., 54.5 m² g⁻¹) obtained from their nanostructured morphology (average particle size 16 nm), that is finer than previous methanol sensors based on aluminum-doped nickel oxide fibers (100 nm diameter)⁷. Methanol and ethanol can easily penetrate into the sensing film resulting in fast response and recovery times and outstanding sensitivity to detect even the lowest analyte concentrations, e.g., 112 ppb ethanol²⁵.

A.5.2 Selective methanol and ethanol detection in laboratory mixtures

Supplementary Figure A.5a shows the sensor response to the headspaces of 1 vol% methanol (green) and 5 vol% ethanol (blue) contained as single analytes in water. Methanol and ethanol pass through the Tenax column and are detected with retention times (t_R) of 1.6 and 5.3 min, respectively, in agreement with a similar column and sensor⁹. Despite its higher concentration, the sensor response to ethanol (2.1) is lower than that to methanol (4.2) due to the larger dissipation in the column²⁶. Most importantly, when applied as a mixture (Supplementary Figure A.5b), the resulting response is exactly the superposition of those by the single analytes (Supplementary Figure A.5a), proving their selective detection. Furthermore, the filter column fully recovers as validated by high-resolution mass spectrometry (Supplementary Figure A.10).

Reliable methanol detection in alcoholic beverages requires that the methanol peak response is not affected even by their typically higher ethanol concentrations. In other words, the t_R of methanol must be smaller than the breakthrough time (t_B) of ethanol, for all relevant concentrations. Supplementary Figure A.5c shows the t_R of methanol (empty symbols) for concentrations of 0.01 vol% (triangles) and 10 vol% (circles) and the t_B of ethanol (filled squares) for relevant ethanol concentrations of 5 – 80 vol%. For all concentrations, the t_B of ethanol is always larger than the t_R of methanol. In specific, the t_R decreases for 0.01 and 10 vol% methanol from about 1.5 to 1.25 min, respectively. This is expected from gas chromatography, similar to an overloaded column when the gas concentration exceeds the column's capacity²⁷. Also, the t_R for both methanol concentrations are rather independent from those of ethanol. As expected, the t_B of ethanol decreases from 4.5 to 2.25 min with increasing ethanol concentration from 5 to 80 vol%. As a result, the separation by the column is sufficient for reliable methanol and ethanol discrimination at relevant concentrations, but changes in t_B and t_R need to be considered during evaluation.

Supplementary Figure A.5d shows the sensor peak response for methanol concentrations ranging from 0.01 to 10 vol%. These were selected to cover levels lower than the legal limit⁵ for distillers (i.e., 0.09 vol%) as well as harmful ones (>2 vol%)¹². The sensitivity (i.e., slope of the curve) decreases with increasing concentration, as typically observed for such semiconducting metal oxide (MOx) gas sensing films and in agreement with non-linear diffusion-reaction theory at elevated concentrations²⁸. Most importantly, the sensor can detect methanol over the entire concentration range (please see Supplementary Methods for mathematical description). Even the lowest 0.01 vol% (inset, Supplementary Figure A.5d) is quantified with high signal-to-noise ratio of 15 and distinguished from 0.03 vol%. Please note that the calibration curve has an offset, which is related to the non-continuous sampling. Below 0.01 vol%, concentrations cannot be detected anymore, as evident from the similar response to 0 vol% that is within the error bars. Detection of lower concentrations could be enabled, for instance, by optimizing the operational temperature⁷ and doping content¹⁹ of the Pd-doped SnO₂ sensor. This excellent detection limit can be attributed to the high sensitivity of the applied sensor and the low measurement noise (<1%) of the tailor-made readout circuitry (Supplementary Figure A.13b). The error bars resulting from different ethanol concentrations (5, 20, 40 and 80 vol%) are typically <10%, highlighting the outstanding selectivity of the analyzer that enables accurate quantification of methanol rather independently from the ethanol concentration.

The ethanol peak responses for relevant ethanol concentrations (5 – 80 vol%) are shown in Supplementary Figure A.5e (squares). They increase from about 3 to 8 when the concentration is increased from 5 to 80 vol% ethanol while the corresponding t_R (diamonds) decrease from 4.5 to 2.6 min, respectively. The decrease in t_R is related to an overloaded column, as observed also for methanol (Supplementary Figure A.5c) and in line with gas chromatography²⁷. This could be avoided by increasing the Tenax mass. Interestingly, however, the effect of methanol (0, 0.1, 0.3, 1 and 10 vol%) is smaller for ethanol's t_R (i.e., 3%) than for the ethanol peak response (10%), as indicated by the error bars in Supplementary Figure A.5e. Consequently, the t_R of ethanol was used to determine the ethanol concentration (please see Supplementary Methods for mathematical description). Please note that the device can also detect lower ethanol concentrations, e.g., 0.1 vol% (Supplementary Figure A.14), which are relevant in liquid medications for neonates and infants²⁹. This shows the versatility of this device for other foods and their processing.

A.5.3 Comparison to state-of-the-art methanol sensors

The detection limit of 0.01 vol% is superior to the 5 vol% for optical Bragg fiber arrays³⁰ and quartz tuning forks³¹, 0.15 vol% for electrolyte-free electrochemical cells³², 4 vol% for fluorescent silica-gel plates⁶, and comparable to 0.012 vol% for enzyme-based sensors³³. While different MOx have been proposed as methanol sensors³⁴, they typically fail to distinguish between methanol and ethanol due to their similar chemical interaction. Other systems overcome this issue with multiple sensors, so-called arrays, as done with optical Bragg fiber³⁰ or amperometric enzyme-based biosensors³³. However, such arrays feature increasing estimation errors with increasing complexity³⁵ of the gas mixture (e.g., >850 compounds in beer¹¹). In particular for enzyme-based biosensors, also stability issues are a concern³⁶.

A.5.4 Beer with various methanol contents

Supplementary Figure A.4 shows the sensor response to pure beer (5 vol% ethanol, dotted) and when spiked with 0.1 (dashed), 1 (solid) and 10 vol% (dash-dotted) methanol. Most remarkably, methanol and ethanol are identified at their characteristic peaks at $t_R = 1.28 - 1.5$ min and 5.1 – 5.5 min, respectively, and no other peaks from potential interferents are visible. While no methanol peak is observed for pure beer, the sensor response increases from 0.8 to 15.3 when spiked with 0.1 to 10 vol% methanol, respectively. These results are in excellent agreement with the laboratory mixtures (Supplementary Figure A.5c–e) and the separation in real beverages has also been validated with a high-resolution mass spectrometer (Supplementary Figure A.10b). As a result, the analyzer reliably identifies different methanol concentrations also in complex mixtures like beer. Please note that the ethanol peak responses decrease and the t_R increases when spiking with methanol, due to dilution.

A.5.5 Wines from five continents

Different wines were tested, as specified in Supplementary Table 1 and mapped in Supplementary Figure A.7a where the sensor-measured methanol concentrations are compared (Supplementary Figure A.9b) to their actual ones in pure (filled symbols) and 0.01, 0.03, 0.1, 0.3, 1, 3 and 10 vol% methanol-spiked samples (open symbols) from Spain (triangles down), Australia (circles), U.S.A (diamonds), Chile (hexagons) and South Africa (squares). In all wines, methanol was quantified accurately with an average error of 16.9% that is comparable to 19.5% for all alcoholic beverages in Figure A.2d. No distinct differences due to geographical origin were observed.

Table A.1: *Tested wines and origins.*

Name	Grape	Year	Country code (ISO 3166)	Ethanol content [vol%]
Casillero de Diablo	Cabernet Sauvignon	2016	CHL	13.5
Kangaroo Ridge	Cabernet Sauvignon, Shiraz	2015	AUS	14.0
Makana	Cabernet Sauvignon, Shiraz	2018	ZAF	13.0
Foxhollow	Cabernet Sauvignon	2016	USA	13.0
Las Flores Rioja	Tempranillo	2018	ESP	14.0

A.5.6 Response analysis of pure and methanol-spiked pear spirit

Supplementary Figure A.15 shows the sensor response of pure (solid line) and 3 vol% methanol-spiked (dashed line) pear spirit. These samples were measured with the largest under- and over-prediction from the actual ethanol content in Figure A.2c. The profiles show distinct methanol and ethanol peaks, in agreement with other beverages (Figure A.2a) and laboratory mixtures (Supplementary Figure A.5a). More specifically, the t_R of ethanol were 2.77 and 3.06 min, respectively, corresponding to ethanol concentrations of 75.8 and 50.5 vol%. The actual ethanol concentration, however, are 59.8 (pure) and 58.1 vol% (3 vol% methanol spiked), respectively. Such deviations may be caused by temperature variations in the environment that alter the t_R of analytes in the separation column⁹. These are larger at higher ethanol contents, where small changes in the t_R result in large changes in the predicted ethanol content (Supplementary Figure A.5e, diamonds).

A.6 Supplementary Figures

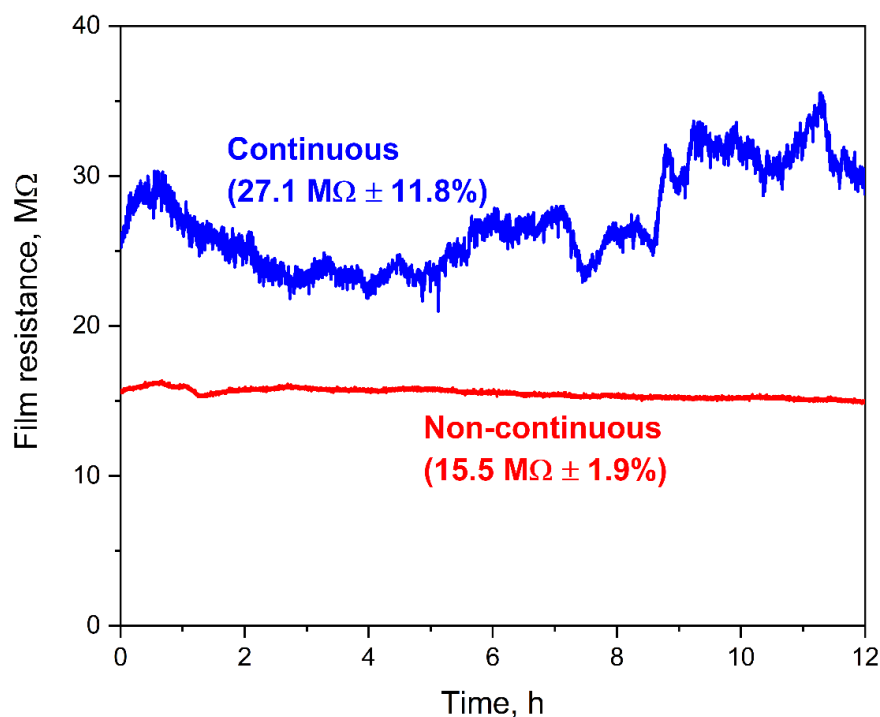


Figure A.3: Baseline resistance during continuous (blue, 25 mL min⁻¹) and non-continuous operation (red, 0 mL min⁻¹, no sampling). Fluctuations due to changes in ambient air composition are drastically reduced from 11.8 to 1.9% using non-continuous sampling.

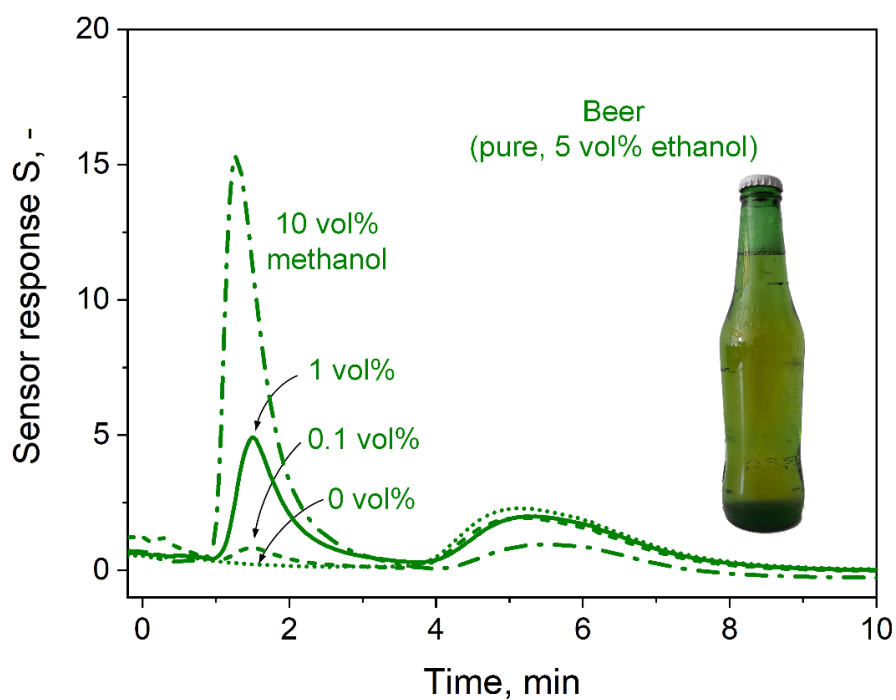


Figure A.4: Sensor response to pure beer (5 vol% ethanol, dotted) and spiked with 0.1 (dashed), 1 (solid) and 10 vol% (dash-dotted) methanol.

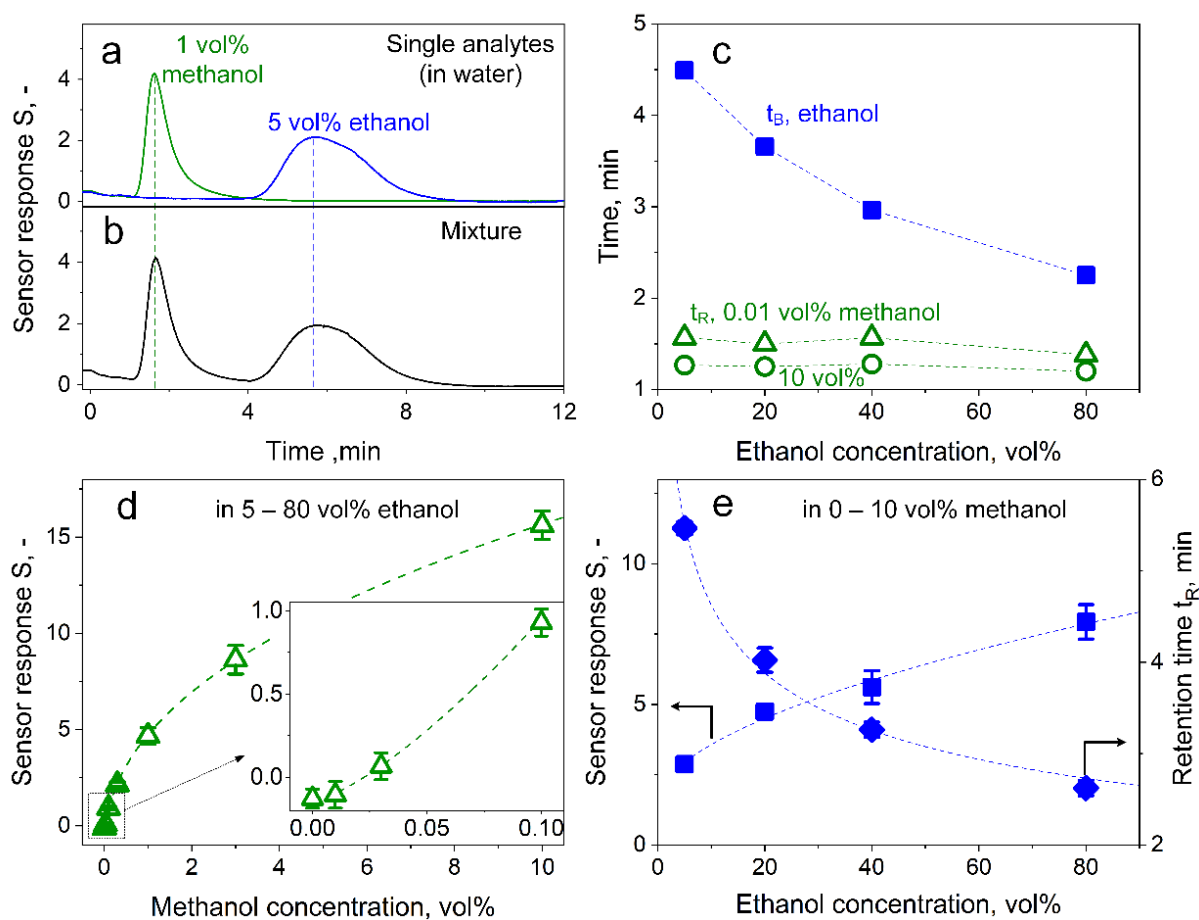


Figure A.5: Sensor responses to the headspace of containers with 1 vol% methanol in water (green) and 5 vol% ethanol in water (blue) as (a) single analytes and (b) their mixture. (c) Methanol retention times (t_R) of mixtures containing 0.01 (triangles) and 10 vol% methanol (circles) along with ethanol breakthrough times (t_B , squares) as a function of the mixture ethanol concentration. (d) Sensor responses (triangles) to 0, 0.01, 0.03, 0.1, 0.3, 1, 3 and 10 vol% methanol mixtures. Error bars represent the standard deviation from 5, 20, 40 and 80 vol% ethanol background. Inset shows higher magnification of 0 – 0.1 vol% methanol. (e) Sensor responses (squares) and retention times (diamonds) to 5, 20, 40 and 80 vol% ethanol. Error bars represent the standard deviation with 0, 0.1, 0.3, 1, 3 and 10 vol% methanol background. Some bars in d and e are hidden by the symbols.

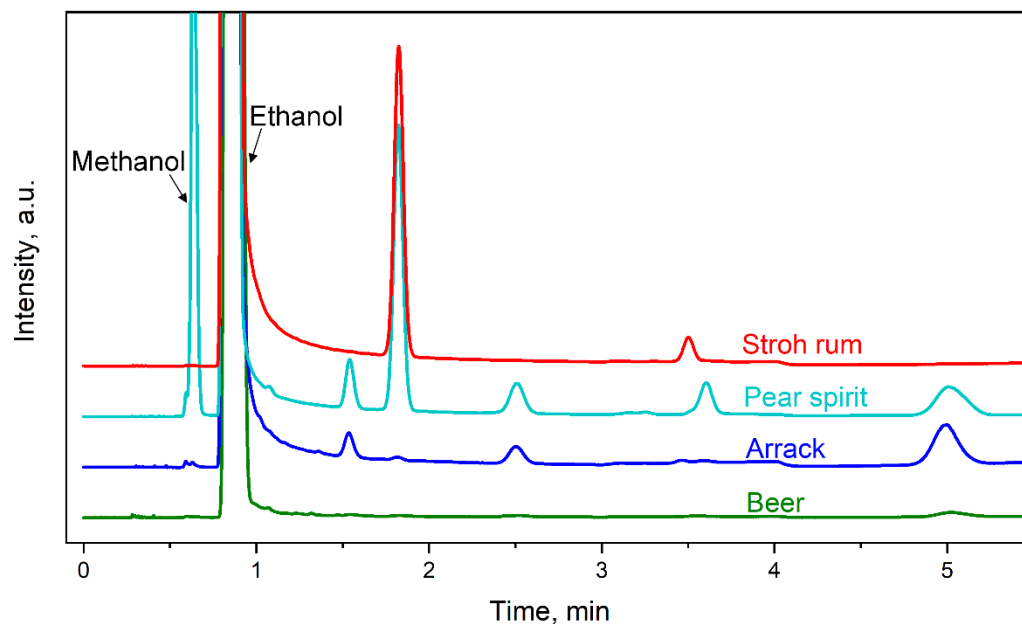


Figure A.6: Chromatograms of pure samples of beer (green), arrack (blue), pear spirit (cyan) and Stroh rum (red).

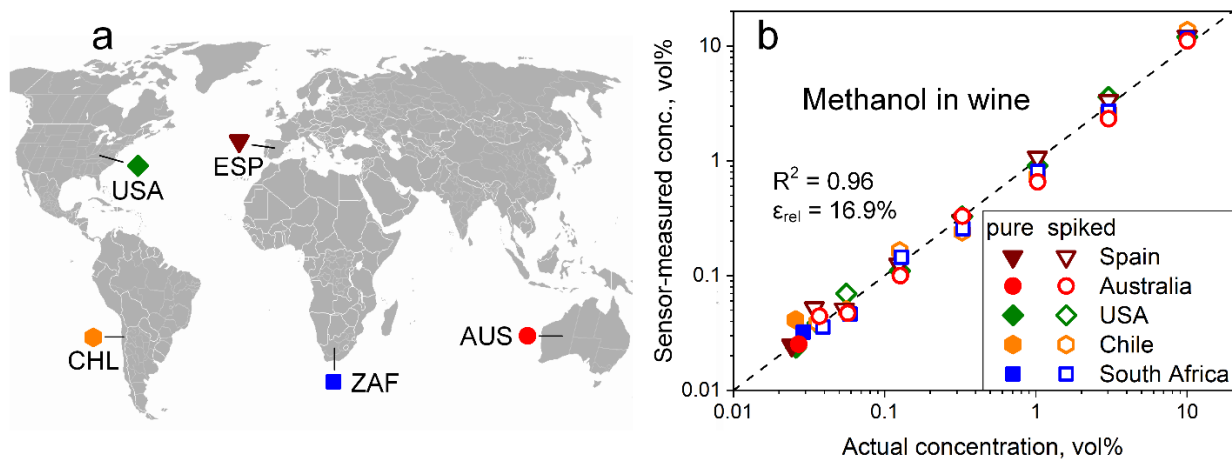


Figure A.7: (a) Geographical origin of wines as indicated by country codes (ISO 3166). (b) Sensor-measured and actual methanol concentrations in pure and 0.01, 0.03, 0.1, 0.3, 1, 3 and 10 vol% methanol-spiked wine (40 samples total) from Spain (triangles down), Australia (circles), U.S.A. (diamonds), Chile (hexagons) and South Africa (squares). The background world map has been obtained under the CC0 1.0 license (public domain).

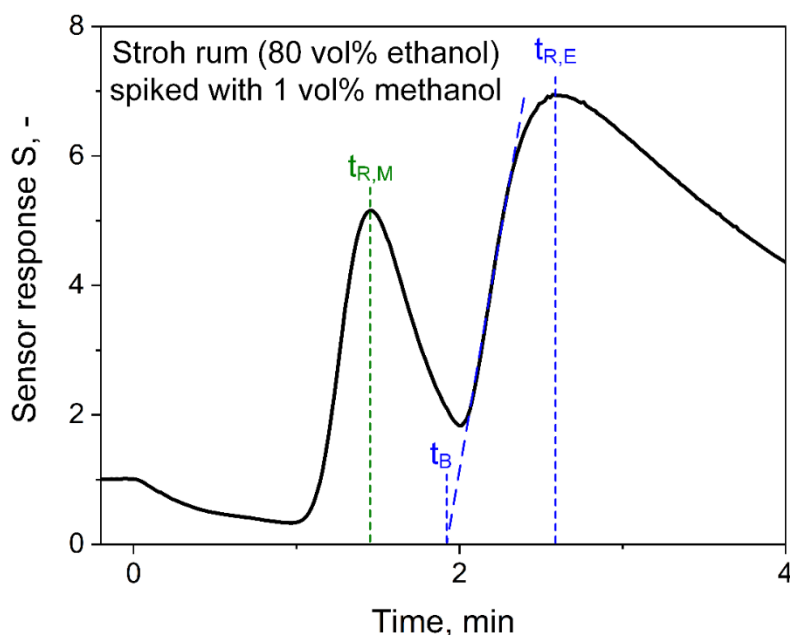


Figure A.8: Retention time t_R and breakthrough time t_B evaluation on the example of the sensor response to Stroh rum (80 vol% ethanol) spiked with 1 vol% methanol. The t_R is defined as the time needed to reach the peak response of methanol ($t_{R,M}$) and ethanol ($t_{R,E}$). The breakthrough time of ethanol is assessed by applying a tangent to the onset of the ethanol peak and evaluating the intercept at zero response.

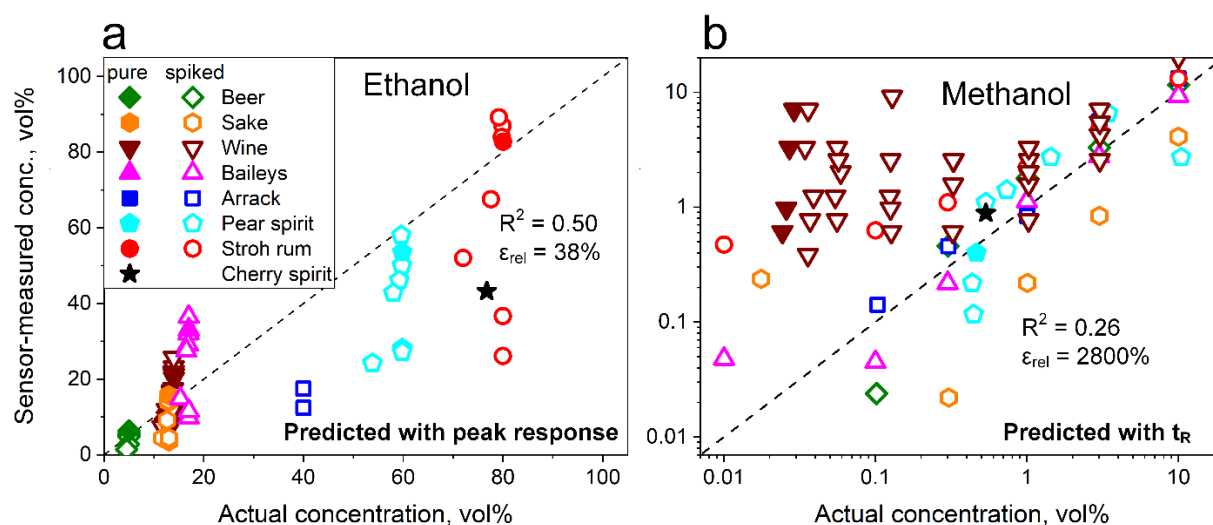


Figure A.9: Sensor-measured concentrations of (a) ethanol and (b) methanol compared to their actual concentrations in pure (filled symbols) and 0.01, 0.03, 0.1, 0.3, 1, 3 and 10 vol% methanol-spiked (empty symbols) beverages. Beer (diamonds), sake (hexagons), wine (triangles down), Baileys (triangles up), arrack (squares), pear spirit (pentagons), Stroh rum (circles) and cherry spirit (star) were tested. Please note that in contrast to Figure A.2c,d, the ethanol concentration was predicted here using the peak sensor response of ethanol, while methanol was predicted with the methanol retention time t_R . This results in worse prediction compared to the calibration done in the main text. Please note that the predicted ethanol concentration for arrack was mostly >100 vol%.

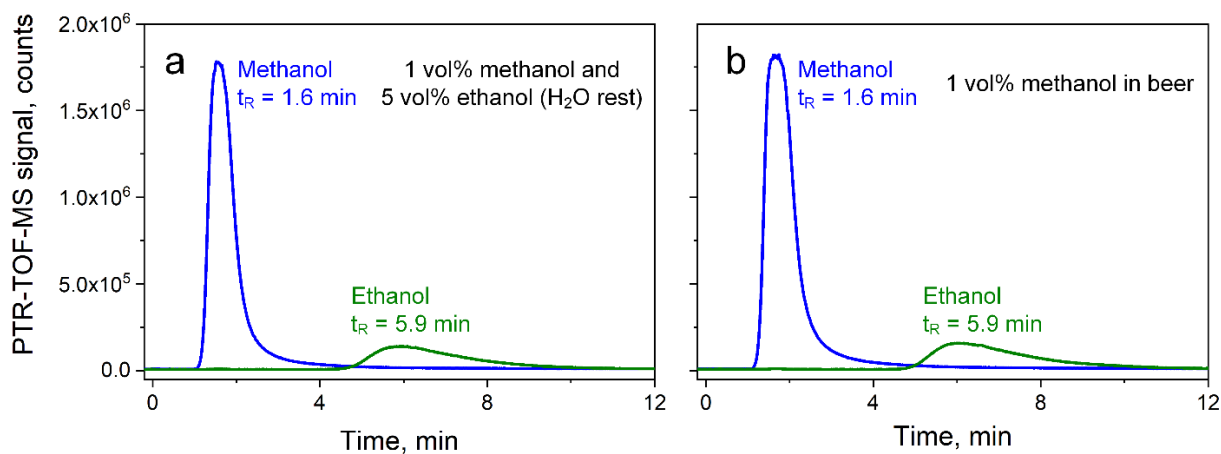


Figure A.10: Detector signal of a proton-transfer-reaction time-of-flight mass spectrometer (PTR-TOF-MS) to the headspace of a sample containing (a) 1 vol% methanol and 5 vol% ethanol in water and (b) 1 vol% methanol in beer (5 vol% ethanol) after separation by the filter column. Please note that the signal to ethanol is lower, despite the higher concentration, probably due to peak broadening in the column and reduced sensitivity. The Tenax separation column fully regenerates after sampling.

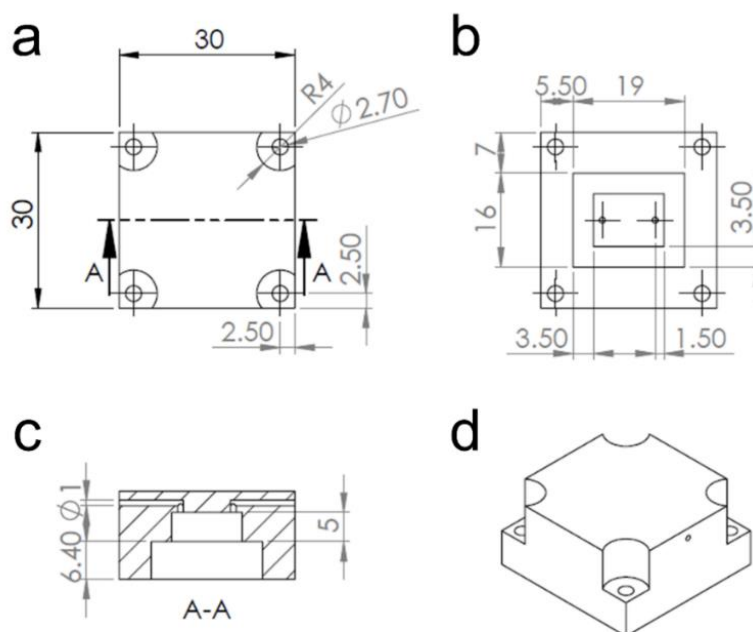


Figure A.11: CAD drawing of the in-house designed Teflon sensing chamber. Shown are (a) top view, (b) bottom view, (c) cross-sectional view and (d) 3D view of the chamber with the most important dimensions in mm.

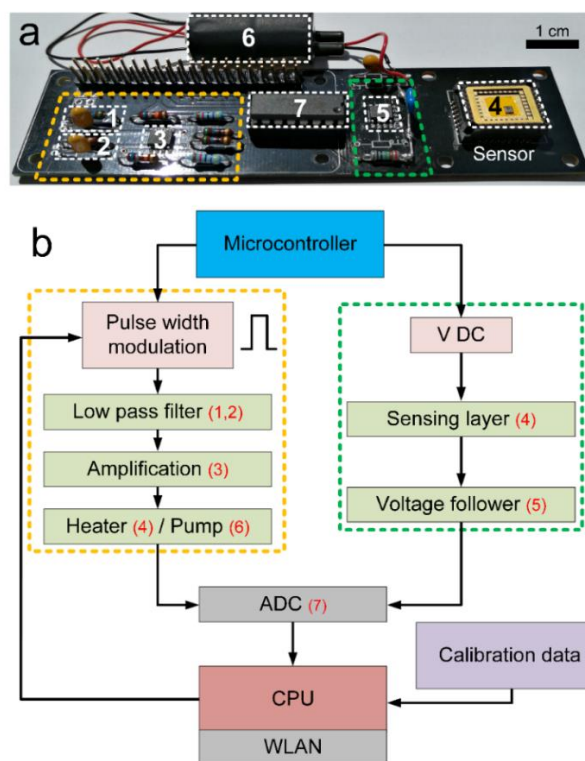


Figure A.12: (a) Image and (b) flow chart of the printed circuit board (PCB) featuring circuits to control/actuate the pump & sensor heater and resistance readout of the chemoresistive microsensor based on Pd-doped SnO₂ nanoparticles. The sensor heater (4) and pump (6) are operated by pulse width modulation. Before being applied to the heater and pump, the signal is passed through a low-pass filter (1, 2) and subsequently amplified (3). The applied voltages are determined by an analog-to-digital converter (7, ADC). The resistance of the sensing layer is determined by a voltage divider and the ADC. An additional voltage follower (5) is applied to reduce the influence of the internal resistance of the ADC.

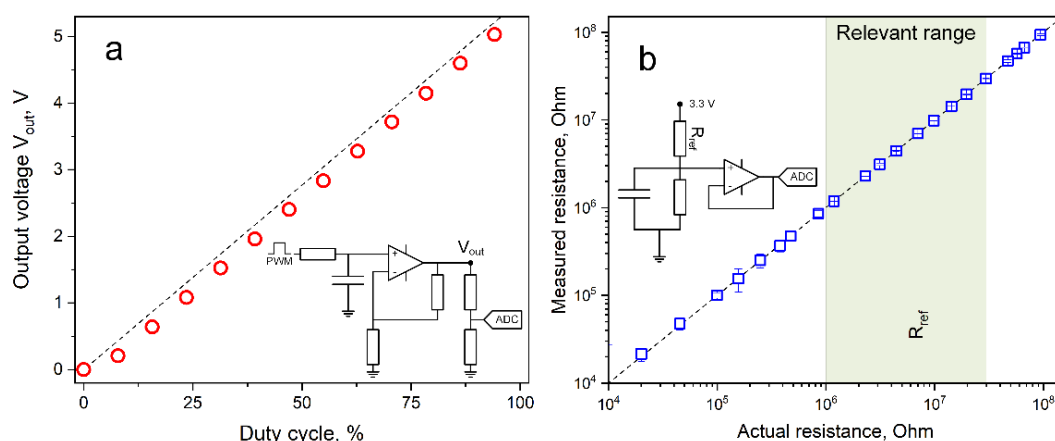


Figure A.13: (a) Output voltage V_{out} (circles) as a function of the duty cycle for adjusting the voltage to heat the sensor and operate the vane pump. The V_{out} is the voltage applied before the voltage divider. The circuit diagram is shown in the inset. (b) Validation and circuit diagram of the read-out circuitry to determine the sensing film resistance (squares). A known resistance was inserted into the circuit and measured with the analyzer. The reference resistance (R_{ref}) in the voltage divider was 9.92 MOhm. The error bars (some hidden by the symbols) denote the variation of the measured resistance, i.e., the noise (standard deviation of >100 measurements for each resistance). In the relevant range (green shaded) from 1–30 MOhm, the resistance is accurately determined with an average deviation from the actual value of only 0.21% and noise of only 1.0%.

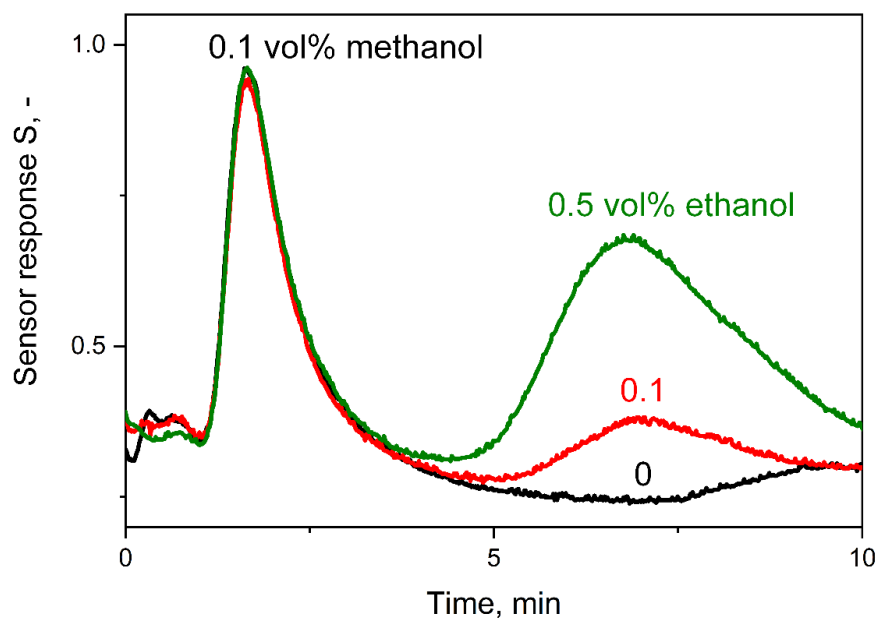


Figure A.14: Sensor response to the headspace of samples containing 0.1 vol% methanol and 0 (black), 0.1 (red) and 0.5 vol% ethanol (green) in water. Even the lowest ethanol signal of 0.1 vol% can be detected with a high signal-to-noise ratio of 48 compared to the sample without ethanol. Please note that detection of lower ethanol concentrations than 0.1 vol% are possible, but with compromised signal quality, showing the current limitations of the device.

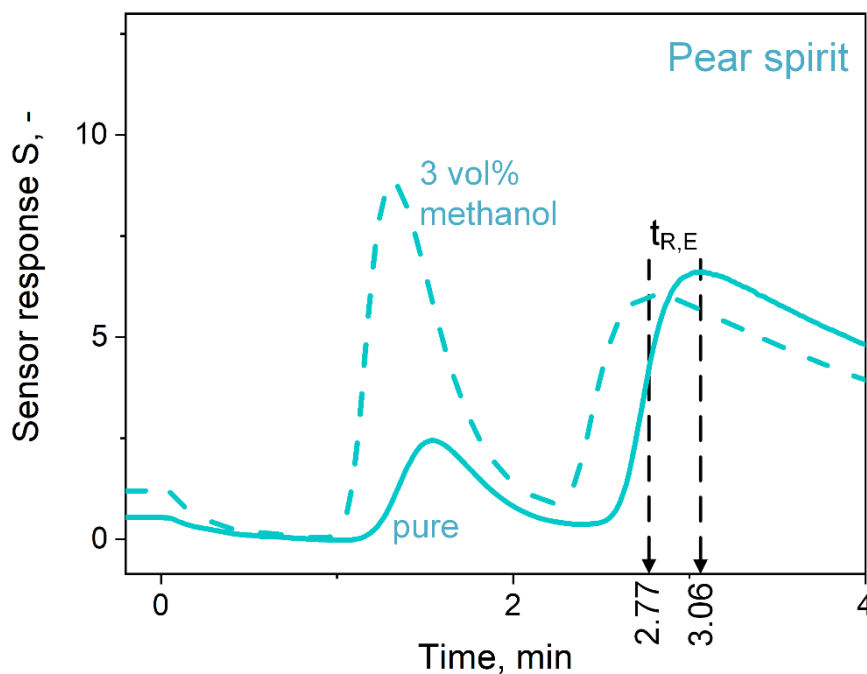


Figure A.15: Sensor response to pure (solid line) and 3 vol% methanol-spiked (dashed line) pear spirit samples. The t_R for ethanol are indicated.

A.7 References

1. H. Knowles. The Washington Post: *Tainted alcohol has led to 20 deaths in Costa Rica, authorities say*, **2019**, <https://www.washingtonpost.com/world/2019/07/22/tainted-alcohol-kills-costa-rica-ministry-says-urging-caution/>.
2. H. Aghababaeian, L. Araghi Ahvazi and A. Ostadtaghizadeh, *Alcohol Alcohol.*, **2019**, 54, 128-130.
3. F. Bindler, E. Voges and P. Laugel, *Food Addit. Contam.*, **1988**, 5, 343-351.
4. M. D. Croitoru, E. Topor, I. Fülöp and E. Fogarasi, *Acta Med. Marisiensis*, **2013**, 59, 206-208.
5. The european parliament and the council. *Official Journal of the European Union: Regulation (European Union) No 2019/787*, **2019**.
6. R. Huang, K. Liu, H. Liu, G. Wang, T. Liu, R. Miao, et al., *Anal. Chem.*, **2018**, 90, 14088-14093.
7. C. Feng, Z. Jiang, B. Chen, P. Cheng, Y. Wang and C. Huang, *Anal. Methods*, **2019**, 11, 575-581.
8. A. Lewis and P. Edwards, *Nature*, **2016**, 535, 29-31.
9. J. van den Broek, S. Abegg, S. E. Pratsinis and A. T. Güntner, *Nat. Commun.*, **2019**, 10, 4220.
10. A. T. Güntner, S. Abegg, K. Wegner and S. E. Pratsinis, *Sens. Actuators B Chem.*, **2018**, 257, 916-923.
11. M. C. Meilgaard, *J. Agric. Food Chem.*, **1982**, 30, 1009-1017.
12. A. Paine and A. Dayan, *Hum. Exp. Toxicol.*, **2001**, 20, 563-568.
13. A. T. Güntner, N. J. Pineau, P. Mochalski, H. Wiesenhofer, A. Agapiou, C. A. Mayhew and S. E. Pratsinis, *Anal. Chem.*, **2018**, 90, 4940-4945.
14. J. Chiou, A. H. H. Leung, H. W. Lee and W.-t. Wong, *J. Integr. Agric.*, **2015**, 14, 2243-2264.
15. R. Jia, W. Tian, H. Bai, J. Zhang, S. Wang and J. Zhang, *Nat. Commun.*, **2019**, 10, 795.
16. A. T. Güntner, M. Wied, N. J. Pineau and S. E. Pratsinis, *Adv. Sci.*, **2020**, 7, 1903390.
17. C. J. Geankoplis, *Transport processes and separation process principles*, Prentice Hall, **2003**.
18. H. M. McNair, J. M. Miller and N. H. Snow, *Basic gas chromatography*, John Wiley & Sons, **2019**.
19. A. T. Güntner, N. J. Pineau, D. Chie, F. Krumeich and S. E. Pratsinis, *J. Mater. Chem. B*, **2016**, 4, 5358-5366.
20. H. P. Robert, W. G. Don and O. M. James., *Perry's chemical engineers' handbook*, Mc Graw-Hills, New York, **1984**.
21. F. Ouyang, S. Yao, K. Tabata and E. Suzuki, *Appl. Surf. Sci.*, **2000**, 158, 28-31.
22. H. Cheong and M. Lee, *J. Ceram. Process. Res.*, **2006**, 7, 183.
23. N. Barsan, M. Schweizer-Berberich and W. Göpel, *Fresenius' J. Anal. Chem.*, **1999**, 365, 287-304.
24. L. Mädler, A. Roessler, S. E. Pratsinis, T. Sahn, A. Gurlo, N. Barsan and U. Weimar, *Sens. Actuators B Chem.*, **2006**, 114, 283-295.
25. N. J. Pineau, J. F. Kompalla, A. T. Güntner and S. E. Pratsinis, *Microchim. Acta*, **2018**, 185, 563-563.
26. M. Harper, *Ann. Occup. Hyg.*, **1993**, 37, 65-88.
27. K. Yabamoto, D. Ingraham and W. Jennings, *J. High Resolut. Chromatogr.*, **1980**, 3, 248-252.

28. J. W. Gardner, *Sens. Actuators B Chem.*, **1990**, 1, 166-170.
29. E. Marek and W. K. Kraft, *Curr. Ther. Res.*, **2014**, 76, 90-97.
30. A. Yildirim, F. E. Ozturk and M. Bayindir, *Anal. Chem.*, **2013**, 85, 6384-6391.
31. S. A. Sampson, S. V. Panchal, A. Mishra, S. Banerjee and S. S. Datar, *Microchim. Acta*, **2017**, 184, 1659-1667.
32. T.-H. Ou, Y. Wang, D. Fang, S. Narayanan and W. Wu, *ACS Appl. Mater. Interfaces*, **2019**, 11, 6217-6223.
33. B. Bucur, G. L. Radu and C. N. Toader, *Eur. Food Res. Technol.*, **2008**, 226, 1335-1342.
34. A. Mirzaei, S. Leonardi and G. Neri, *Ceram. Int.*, **2016**, 42, 15119-15141.
35. A. T. Güntner, V. Koren, K. Chikkadi, M. Righettoni and S. E. Pratsinis, *ACS Sens.*, **2016**, 1, 528-535.
36. N. J. Ronkainen, H. B. Halsall and W. R. Heineman, *Chem. Soc. Rev.*, **2010**, 39, 1747-1763.

Appendix B

Supplementary Data Chapter 2: Highly selective and rapid breath isoprene sensing enabled by activated alumina filter

B.1 Full sensor responses with filter

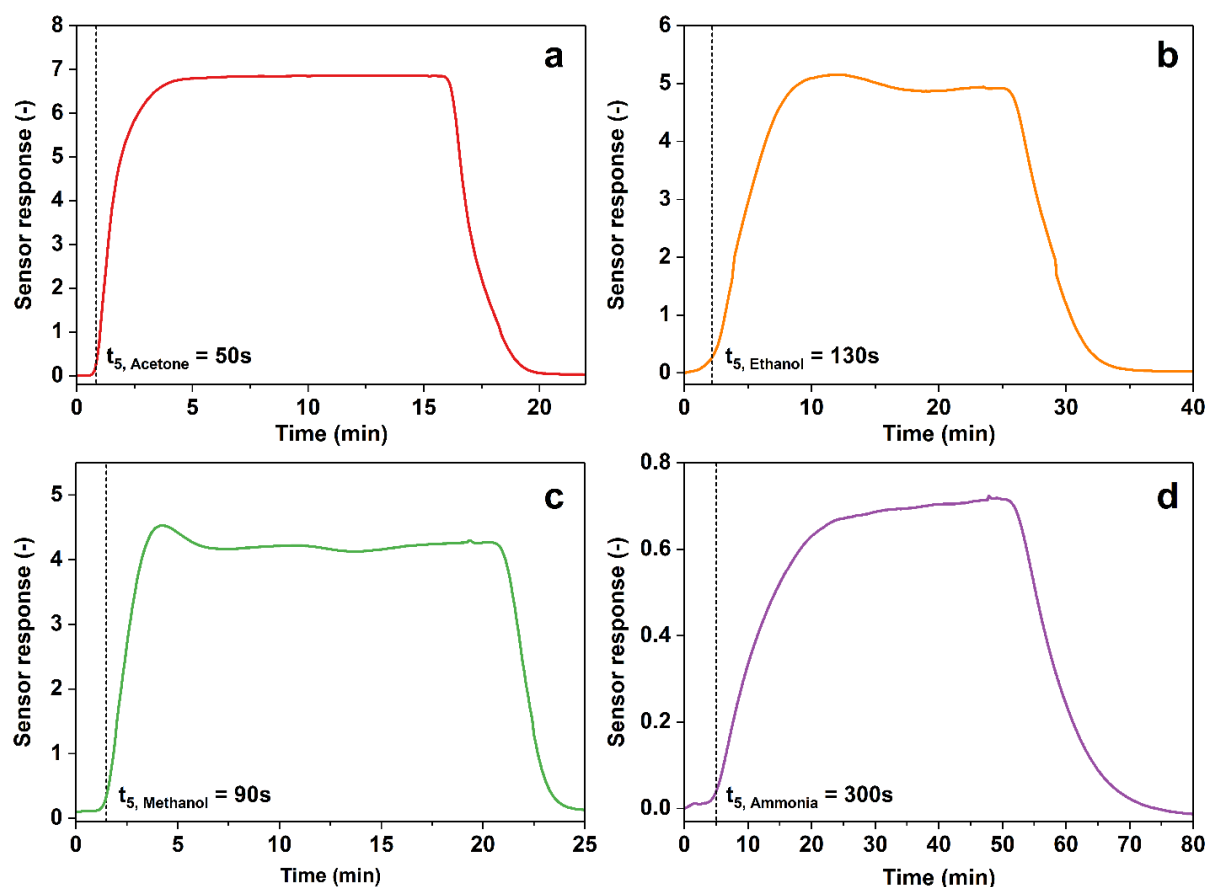


Figure B.1: The responses of a Pt-doped SnO₂ sensor with filter at 90% RH to 500 ppb concentrations of acetone (a), ethanol (b), methanol (c) and ammonia (d). The breakthrough times, t_5 , of the analytes through the filter are also indicated. Note the different time scale on the abscissa as analytes were exposed until a stable response was reached.

B.2 Filter characterization at different loadings

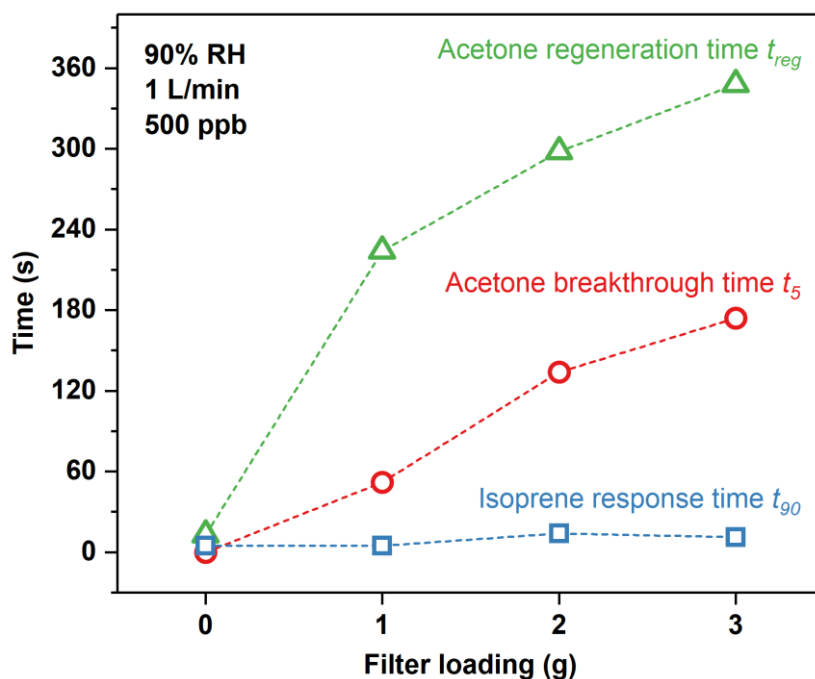


Figure B.2: Isoprene response time t_{90} (blue squares), acetone breakthrough time t_5 (red circles) and acetone recovery time t_{reg} (green triangles) for different activated alumina filter loadings. Measurements were performed with 500 ppb analyte concentrations at 90% RH and 1 L/min. The t_{reg} is the time needed to recover 95% of the response after switching back to air.

B.3 Effect of relative humidity

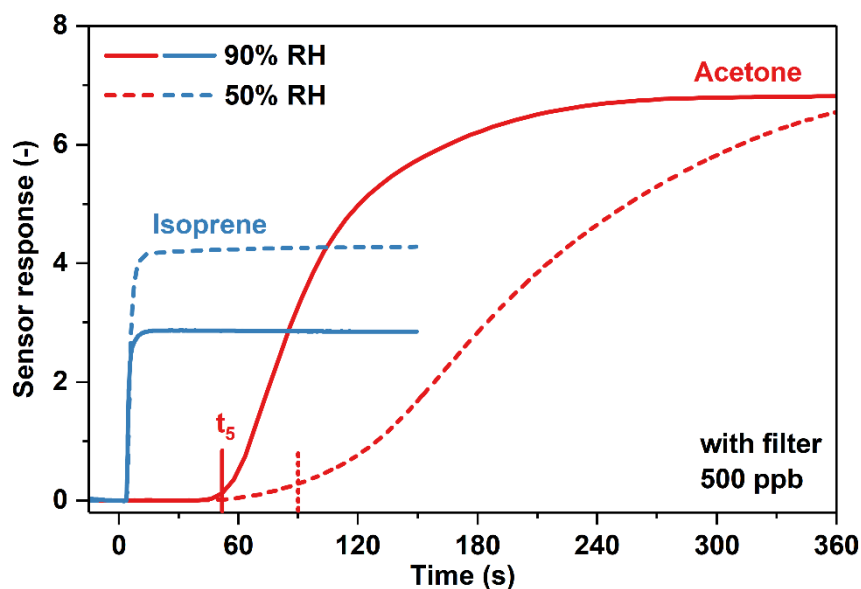


Figure B.3: The response of a Pt-doped SnO_2 sensor with 1 g activated alumina filter at 90 % RH (solid), 50 % RH (dashed) 500 ppb of isoprene (blue) and acetone (red). The sensor response time to isoprene is hardly affected by relative humidity but the response is reduced, which is typical for SnO_2 -based sensors. In case of acetone, the breakthrough time t_5 increases with decreasing humidity (i.e., lower degree of surface hydration) consistent with literature⁵³ showing that sorption coefficients of volatile organic compounds depend on the metal-oxide and decrease with increased surface hydration.

B.4 Filter validation by PTR-TOF-MS

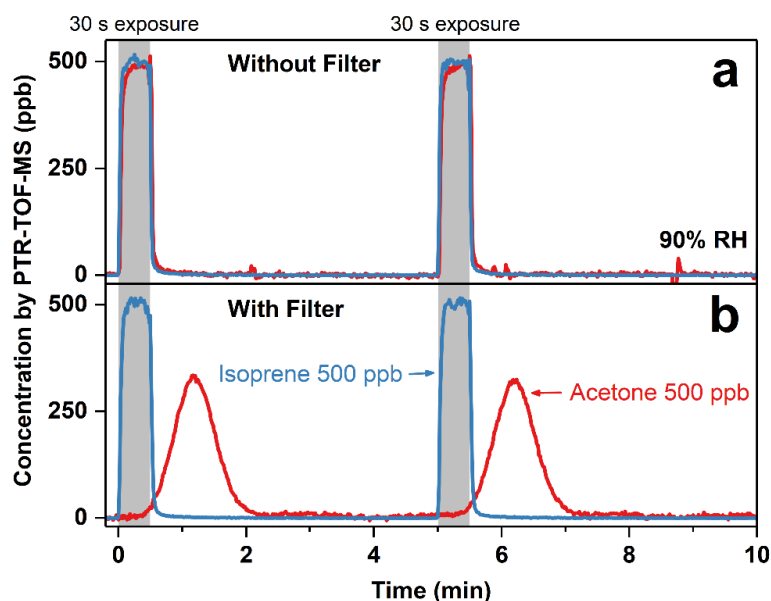


Figure B.4: Concentration of acetone (red lines) and isoprene (blue line) measured by a proton-transfer-reaction time-of-flight mass spectrometer (PTR-TOF-MS) for 30 s mixed pulses of 500 ppb acetone and 500 ppb isoprene at 90% RH. (a) Measured concentrations without filter showing the identical and simultaneous increase of acetone and isoprene during the exposure. (b) Concentrations measured with filter show the delay and spread of the acetone pulse, while isoprene is not affected, similar to the corresponding sensor results (Figure 2.4). Please note that response/recovery times of the PTR-TOF-MS differ from the one of the sensor. Importantly also, the area under the concentration curves for isoprene and acetone are identical (<5% deviation) without and with filter, confirming that the filter fully recovers after every exposure.

B.5 Sensor operational stability

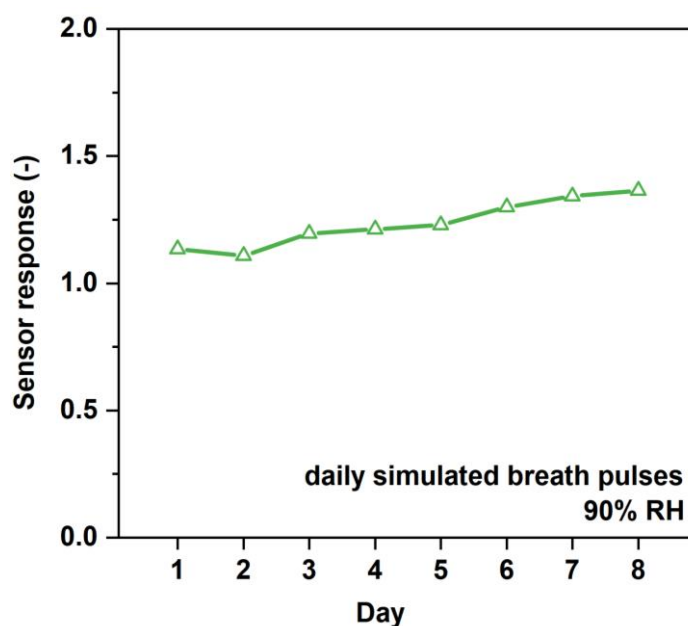


Figure B.5: Pt-doped SnO_2 response with filter during continuous operation for eight days. Response is evaluated after 30 s of exposure to simulated breath consisting of 106 ppb isoprene, 477 ppb acetone, 461 ppb methanol and 833 ppb ammonia at 90% RH.

Appendix C

Supplementary Data Chapter 3: Highly selective detection of methanol over ethanol by a handheld gas sensor

C.1 Effect of temperature and relative humidity

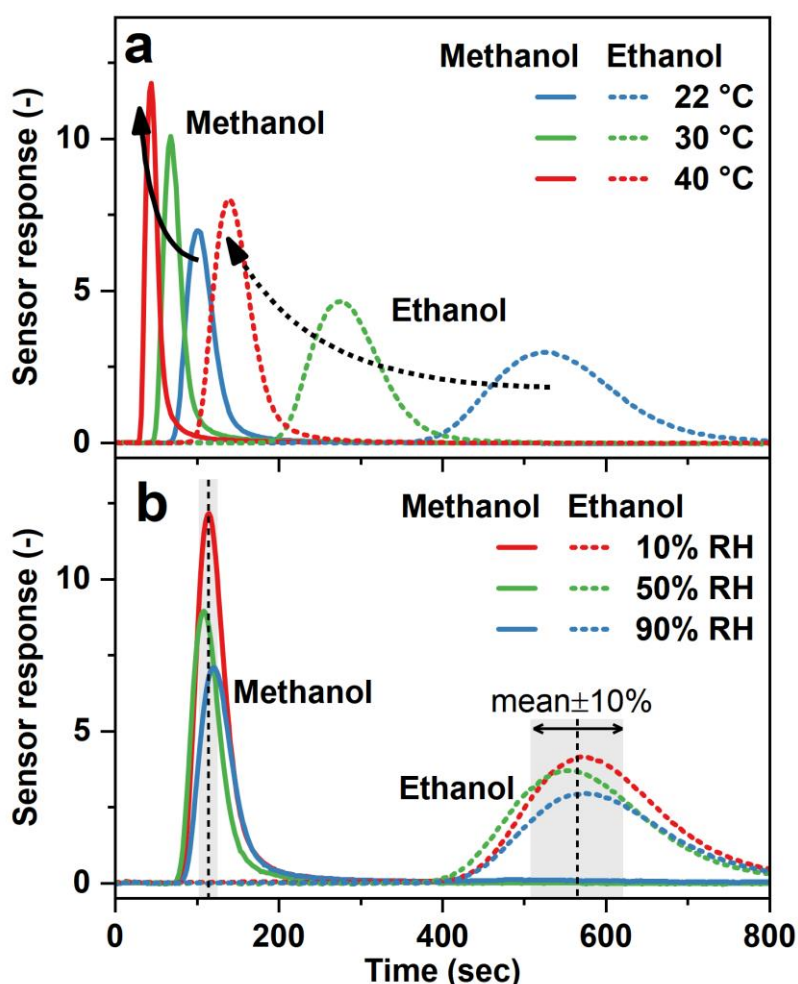


Figure C.1: (a) Response of the methanol detector to 10 sec pulses of 5 ppm methanol (solid lines) and ethanol (dashed lines) at different separation column temperatures of 22 (blue), 30 (green) and 40 °C (red). (b) Response of the methanol detector to 10 sec pulses of 5 ppm methanol (solid lines) and ethanol (dashed lines) at different relative humidity (RH) in the gas flow of 90 (blue), 50 (green) and 10% (red). Dashed black lines and grey shaded areas indicate the mean plus-minus 10% standard deviation of the methanol and ethanol retention times (t_R), respectively.

C.2 Methanol detection with high ethanol interference

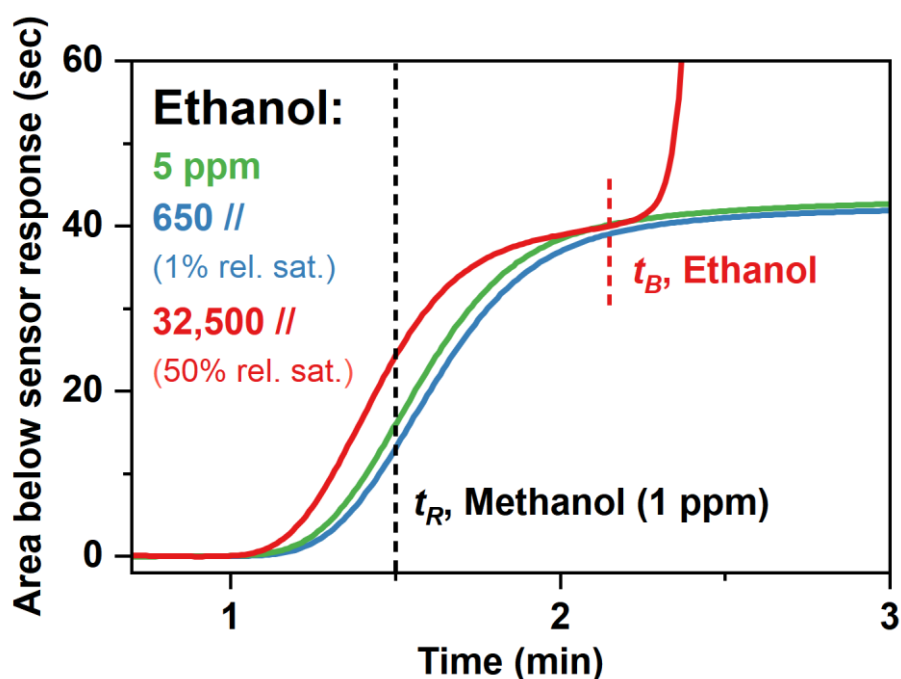


Figure C.2: Area below the response curve of the methanol detector upon exposure to 1 ppm methanol in the presence of 5 (green line), 650 (1% relative saturation, blue line) and 32,500 ppm (50% relative saturation, red line) ethanol. While the maximum peak height is slightly higher with high ethanol interference (see Figure 4a), the areas below the methanol response curves are equal when evaluated just before the breakthrough (t_B , red dashed line) of ethanol. Also shown is the retention time (t_R , black dashed line) of 1 ppm methanol.

C.3 Regeneration after liquor and breath sampling

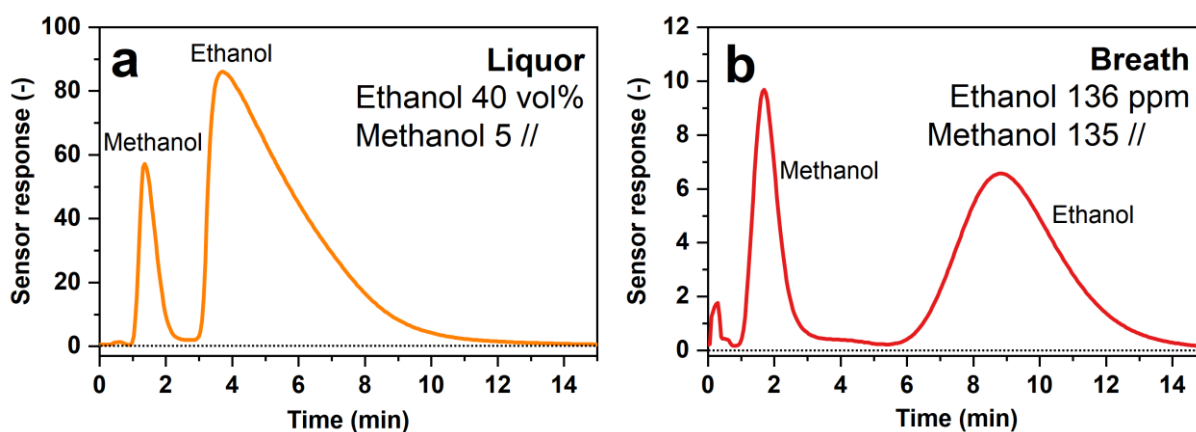


Figure C.3: Response of the detector to (a) Arrack liquor containing 40 vol% ethanol and laced with 5 vol% methanol (orange line), and (b) breath of an intoxicated volunteer after ingestion of ethanol spiked with 135 ppm methanol (red line) that is equivalent to the breath of a person being intoxicated with the above laced liquor according to the standard addition method⁴⁴. The 136 ppm of ethanol correspond to a blood alcohol level of 0.54‰ according to the Dräger Alcotest 3820 device manual. The sensor baseline (black dotted line) is recovered in both cases within 15 min by flushing with ambient air.

C.4 Operational stability in ambient air

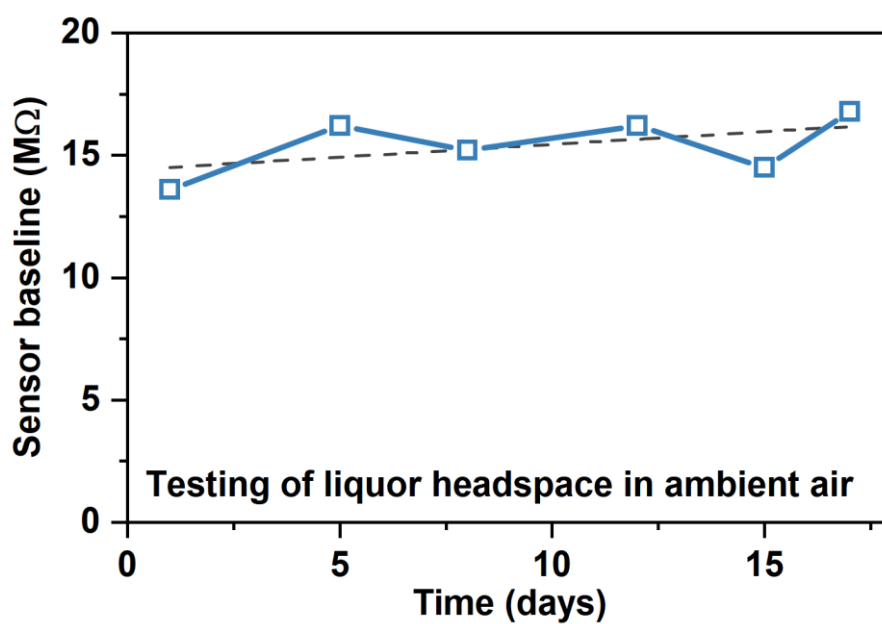


Figure C.4: Baseline resistance of the methanol detector in room air over 18 days with regular testing of liquor headspace (blue squares and solid line). A linear fit (black dashed line) indicates an upward drift of 0.7% per day.

Appendix D

Supplementary Data Chapter 4: Rapid diagnosis of methanol poisoning with a portable breath detector

D.1 Calculation of blood/breath concentrations

The following formula was used for conversion of blood to breath alcohol concentrations:

$$c_{Breath}(ppm) = \frac{c_{Blood}(mg L^{-1})}{r_{Blood/Breath} \cdot M_W(mg mol^{-1})} \cdot 24.31 L mol^{-1} \cdot 10^6 ppm \quad (1)$$

c_{Blood} : Alcohol concentration in blood

c_{Breath} : Alcohol concentration in breath

$r_{Blood/Breath}$: Blood/breath partition ratio, 2901 for methanol and 2100 for ethanol

M_W : Molecular weight of alcohol, 32.04 g mol⁻¹ for methanol and 46.07 g mol⁻¹ for ethanol

24.31 L mol⁻¹: Volume occupied per Liter of gas at standard temperature (22 °C) and pressure (1 atm)

D.2 Physiological data of subjects

Table D.1. Subject data.

Participant No.	Gender	Age (years)	Weight (kg)	Beverage	Ethanol (mL)	Max. blood ethanol concentration (mg L ⁻¹)
1	F	24	53.0	Liquor (37.5 vol%)	48	816
2	M	22	92.6	Liquor	99	782
3	M	23	60.0	Wine (13.5 vol%)	64	564
4	M	27	78.3	Wine	84	761
5	M	22	75.5	Beer (4.8 vol%)	81	526
6	M	24	95.5	Beer	102	961
7	M	28	55.3	Wine	59	816
8	M	26	80.0	Wine	85	779
9	M	29	98.9	Liquor	106	945
10	M	28	65.0	Wine	69	1030
11	F	65	62.4	Wine	56	920
12	F	52	60.6	Wine	55	880
13	M	32	97.0	Liquor	104	1257
14	F	23	68.2	Beer	61	783
15	M	23	70.3	Beer	75	820
16	F	24	58.4	Liquor	53	869
17	M	23	75.9	Beer	81	812
18	M	27	78.8	Beer	84	800
19	M	29	109.0	Liquor	116	935
20	M	26	86.2	Water	0	0

D.3 Analyte stability in Tedlar bags

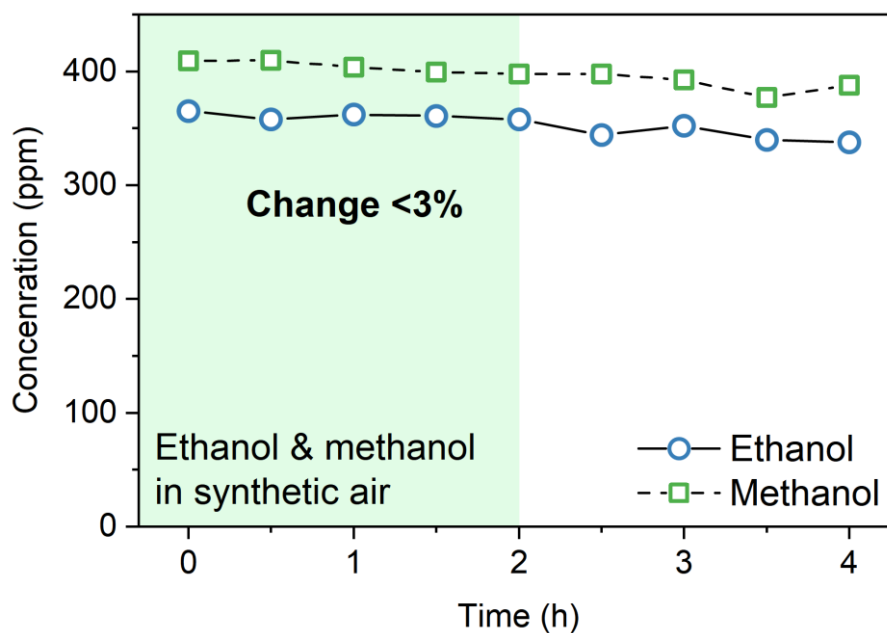


Figure D.1: Stability of ethanol (365 ppm, circles) and methanol (409 ppm, squares) in Tedlar bags as measured by PTR-TOF-MS. All samples were analyzed within 2 h where concentration changes are <3% (green shaded).

D.4 Level of detection

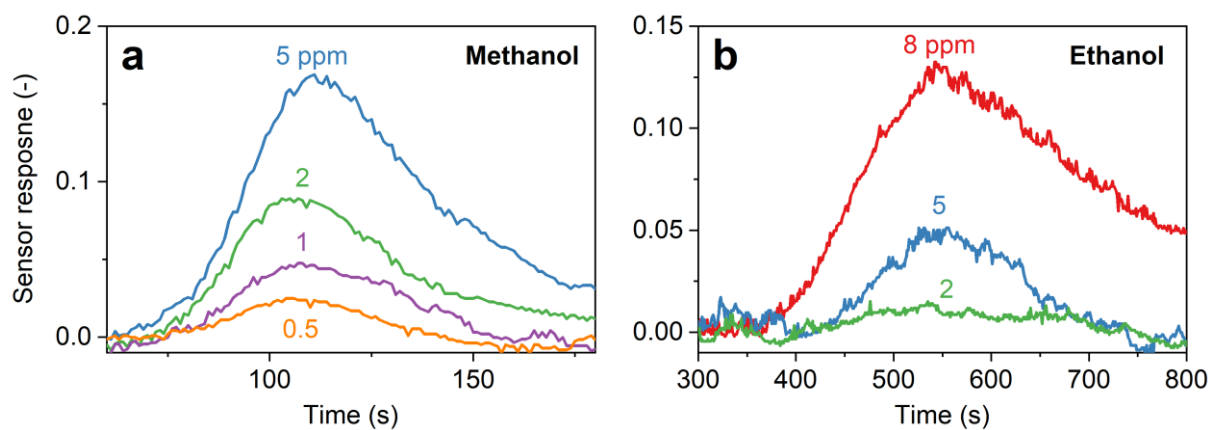


Figure D.2: Sensor responses to low concentrations of (a) methanol and (b) ethanol above the level of detection.

D.5 Measured methanol and ethanol concentrations of all subjects

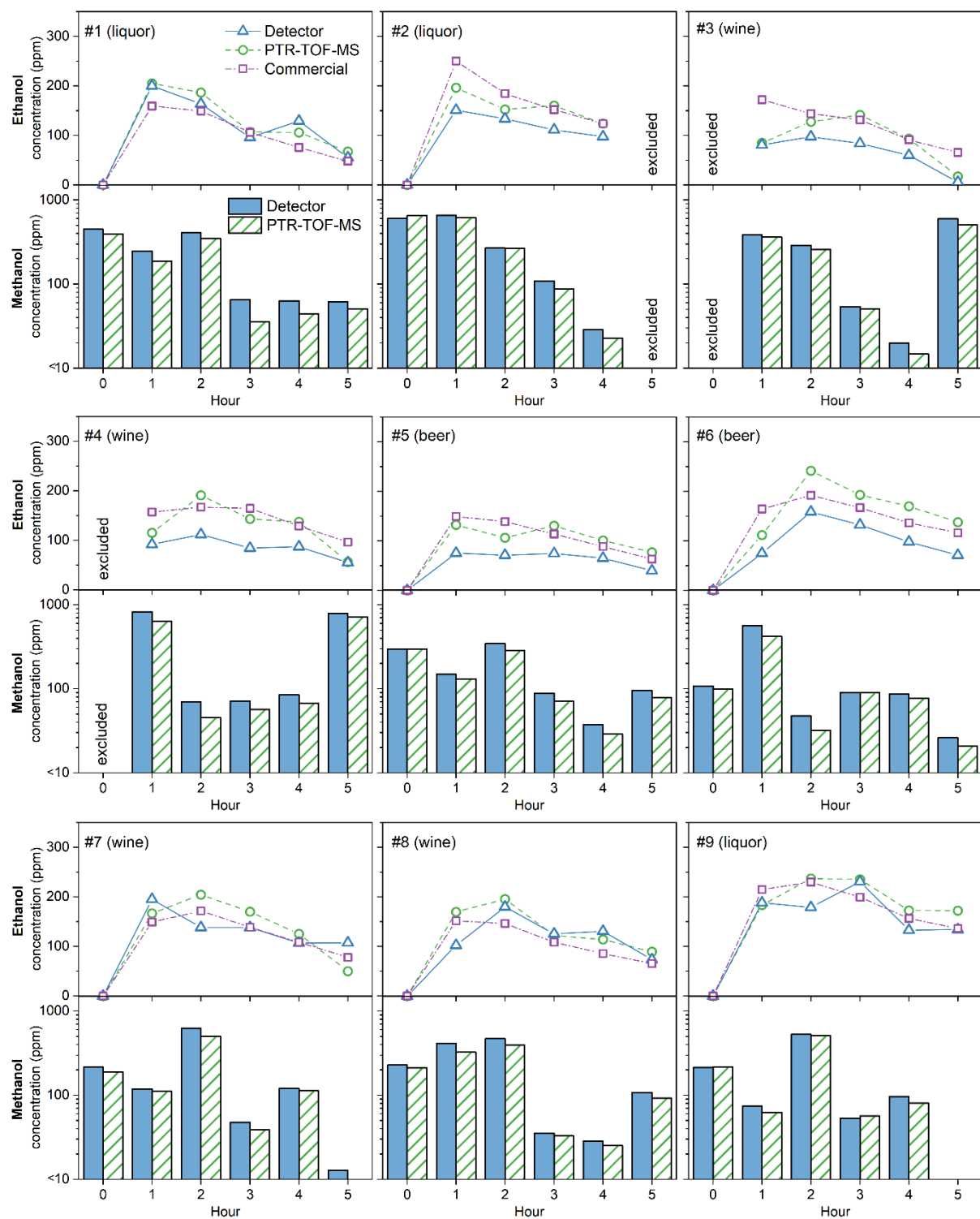


Figure D.3: Breath ethanol concentrations (line plots) from volunteers #1–9 as measured by our detector (triangles), a commercial breathalyzer (Dräger, squares) and the PTR-TOF-MS (circles). Methanol concentrations from the corresponding spiked samples (bar plots) as measured by the detector (solid bars) and PTR-TOF-MS (hatched bars). Excluded data points are due to insufficient breath sample provided by the volunteer or problems during sensor measurements.

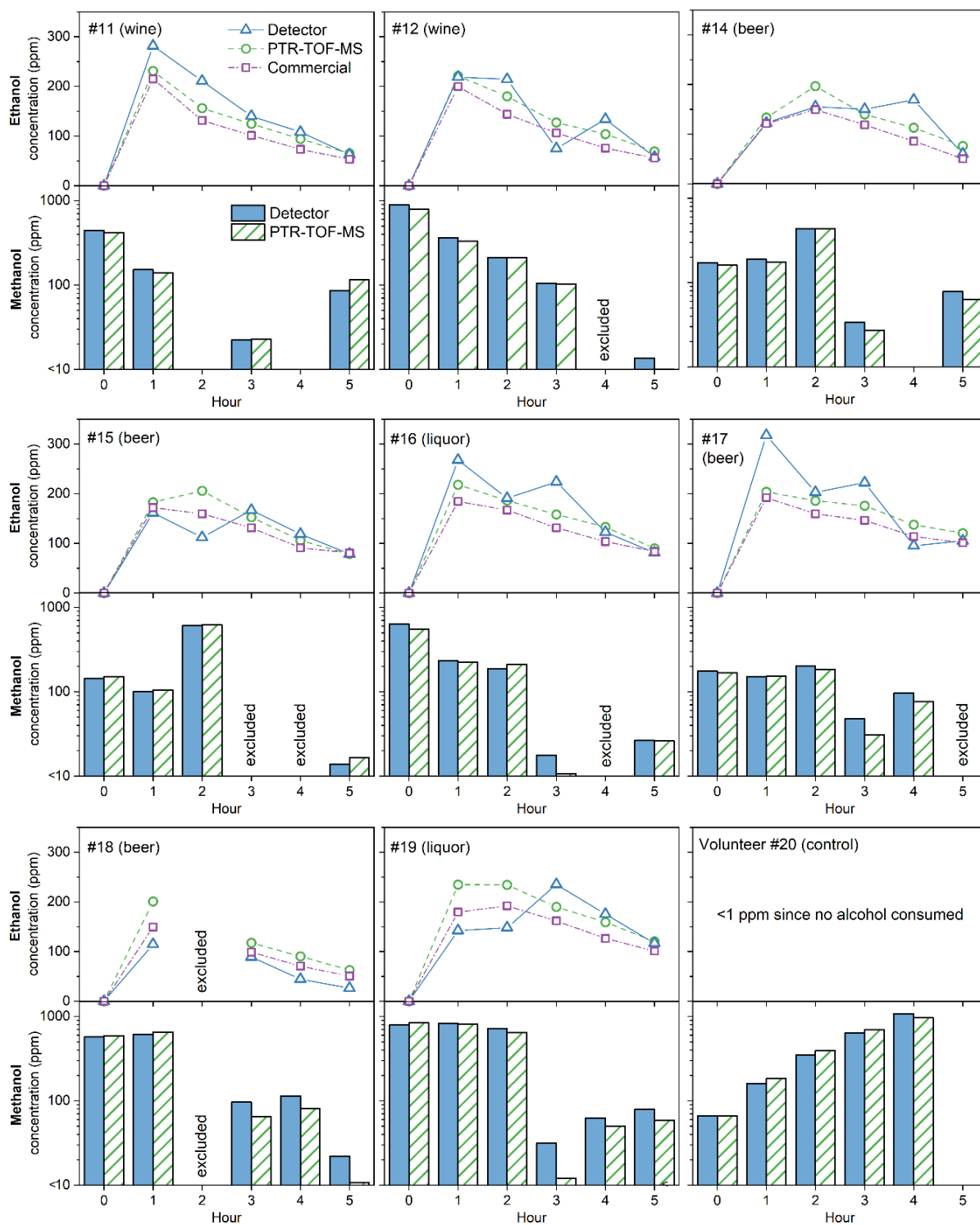


Figure D.4: Breath ethanol concentrations (line plots) from volunteers #11–20 as measured by our detector (triangles), a commercial breathalyzer (Dräger, squares) and the PTR-TOF-MS (circles). Methanol concentrations from the corresponding spiked samples (bar plots) as measured by the detector (solid bars) and PTR-TOF-MS (hatched bars). Profiles for volunteers #10 and #13 are given in the main manuscript. Excluded data points are due to insufficient breath sample provided by the volunteer or problems surfaced during sensor measurements.

D.6 Weekly calibration

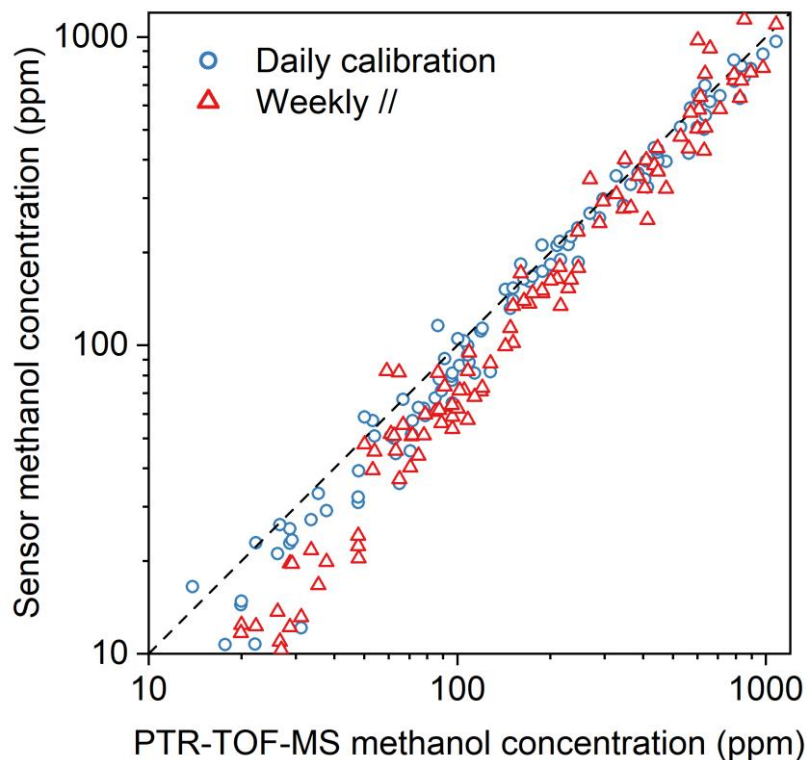


Figure D.5: Scatter plot of methanol concentrations in all breath samples when evaluated by daily (blue circles) and weekly calibrations (red triangles).

D.7 Relative Bland-Altman

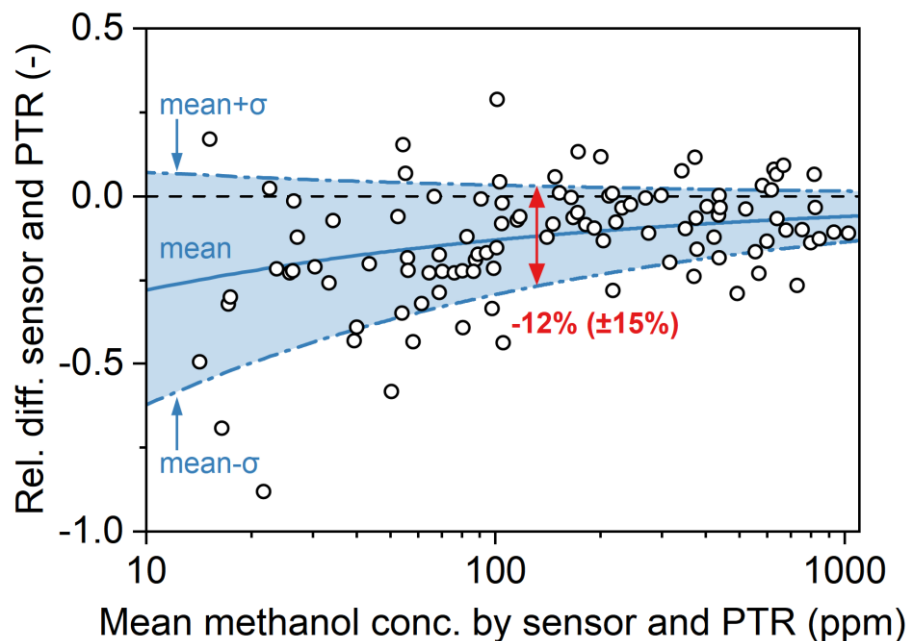


Figure D.6: Bland-Altman plot of the relative difference in measured methanol concentration by sensor and PTR-TOF-MS as a function of the mean of both measurements. Mean (i.e., bias) and mean \pm standard deviation (σ ; i.e., precision) are indicated as solid and dashed-dotted lines, respectively. Bias and precision are exemplarily shown at 131 ppm (red arrow).

Appendix E

Supplementary Data Chapter 5: Selective formaldehyde detection at ppb in indoor air with a portable sensor

E.1 Sensor baseline stability

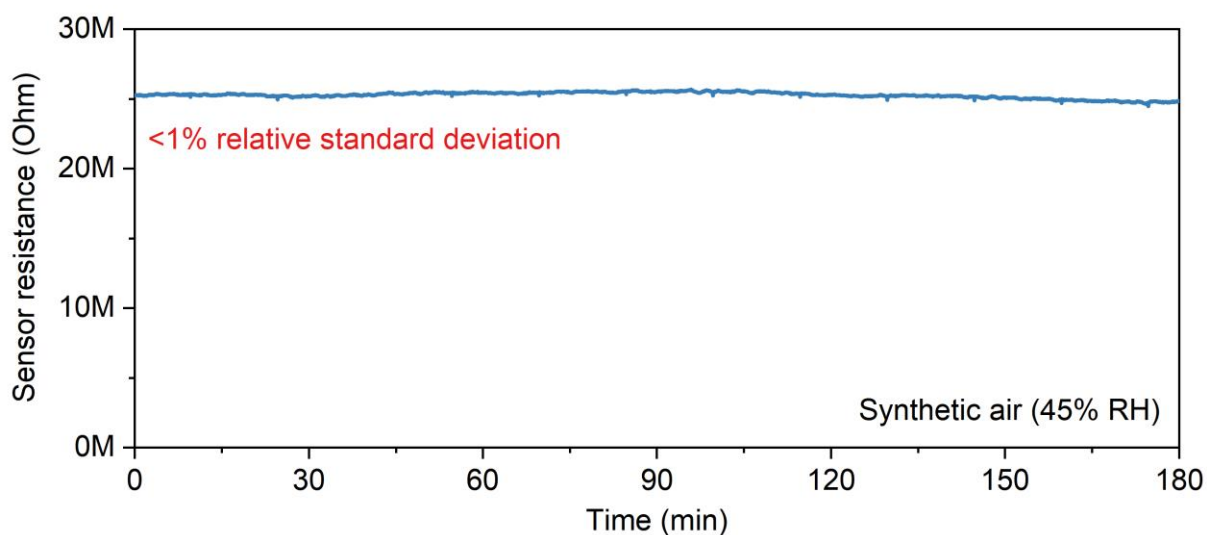


Figure E.1: Equilibrated baseline of the sensor with separation column in synthetic air at 45% RH. Such stable sensor baselines showed a relative standard deviation <1%.

E.2 Oriented strand board emission measurement

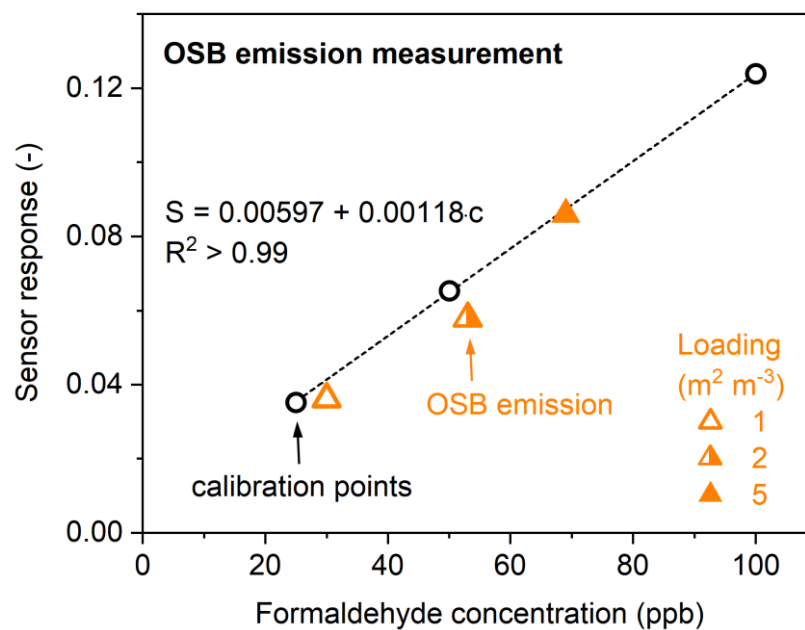


Figure E.2: Sensor calibration with formaldehyde (circles) and measurement of OSB emissions (triangles) at different loadings of 1 (open), 2 (half-filled) and 5 (filled) $m^2 m^{-3}$. OSB formaldehyde concentrations were determined by PTR-TOF-MS. Also shown is the linear calibration line (dashed) and corresponding fit equation and coefficient of determination.

E.3 PTR-TOF-MS calibration for indoor air measurements

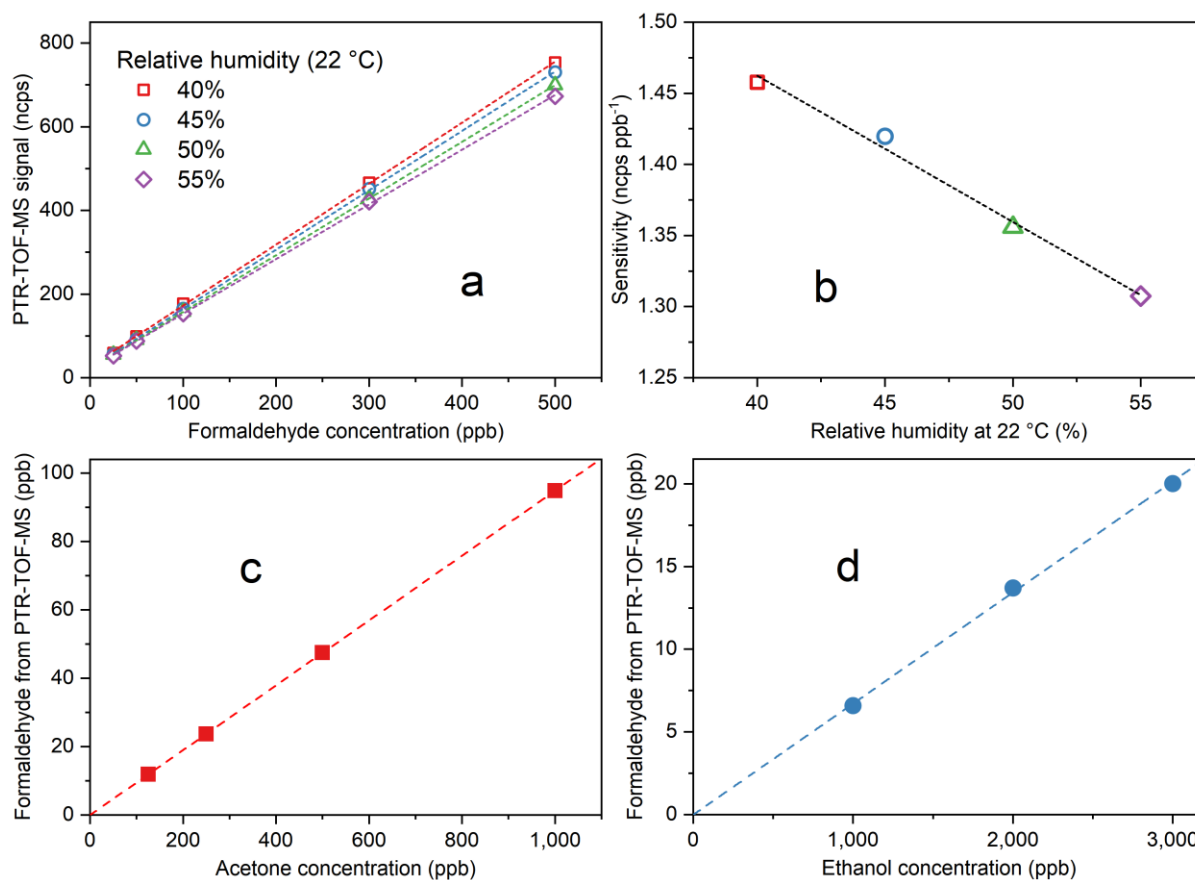


Figure E.3: PTR-TOF-MS calibration for indoor air measurements. **(a)** The formaldehyde signal ($m/z = 31$) from proton-transfer-reaction time-of-flight mass spectrometry (PTR-TOF-MS) as a function of the actual formaldehyde concentration (in synthetic air) at relative humidity of 40 (squares), 45 (circles), 50 (triangles) and 55% (diamonds, at 22 °C). Signals were normalized (ncps) to a H_3O^+ intensity of 10^6 (cps). **(b)** Slope of the calibration curves shown in (a) at different relative humidity. Interference of the formaldehyde PTR-TOF-MS signal ($m/z = 31$) from fragmentation of **(c)** acetone and **(d)** ethanol are 9.48 and 0.67%, respectively.

E.4 Retention times of relevant compounds

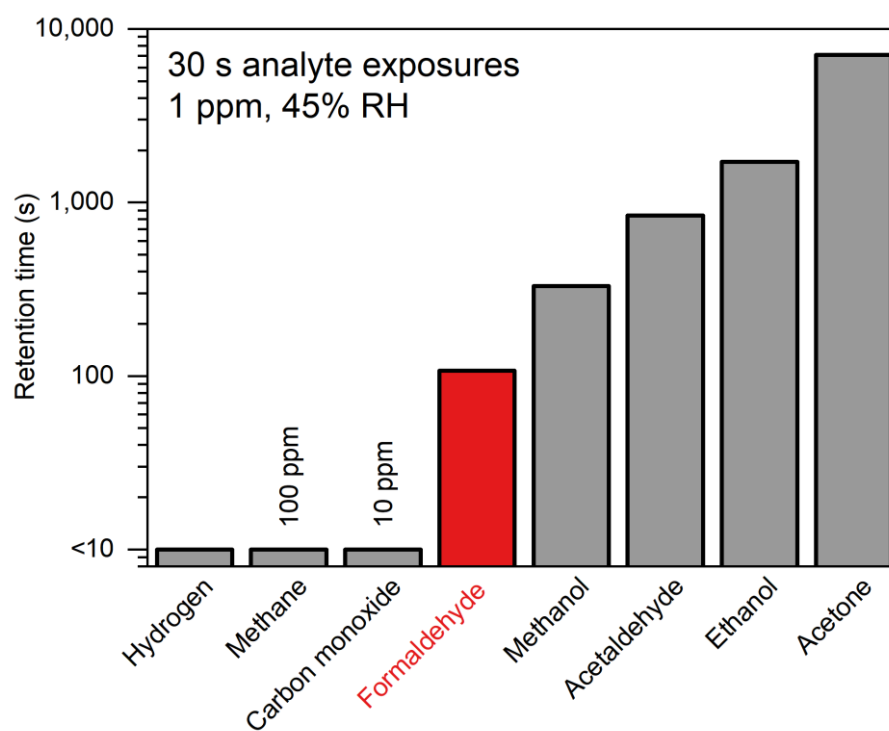


Figure E.4: Retention time of compounds in the separation column determined by the Pd-doped SnO₂ microsensor.

E.5 Validation of wood emission measurement

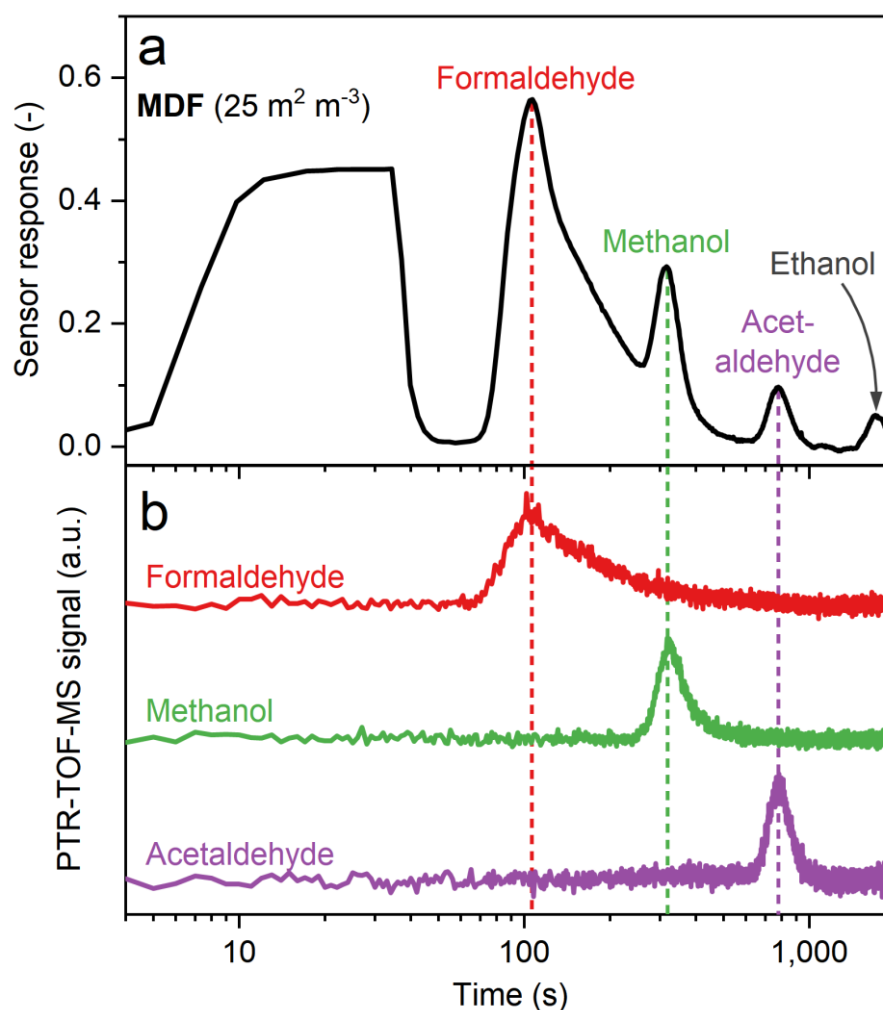


Figure E.5: Validation of wood emission measurements. (a) Response of the formaldehyde detector (Tenax TA column + Pd-doped SnO₂ microsensors) to wood chamber emission with a loading of 25 m² m⁻³ medium-density fiberboard (MDF). (b) Simultaneous measurement of formaldehyde (red), methanol (green) and acetaldehyde (purple) by the proton-transfer-reaction time-of-flight mass spectrometer (PTR-TOF-MS) downstream of the vane pump of the detector outlet. Please note that the concentration of ethanol was below the detection limit of the PTR-TOF-MS.

E.6 Sensor intra-sample repeatability

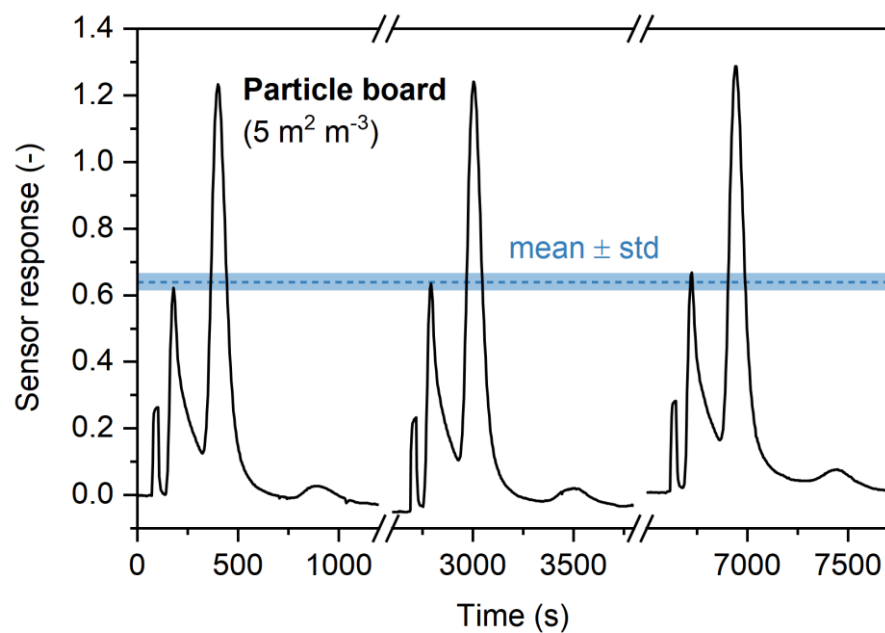


Figure E.6: Sensor response to three consecutive exposures to particle board at a chamber loading of 5 m² m⁻³. Indicated in blue is the mean and standard deviation (< 5%) of the formaldehyde response.

E.7 Validation of indoor air measurement

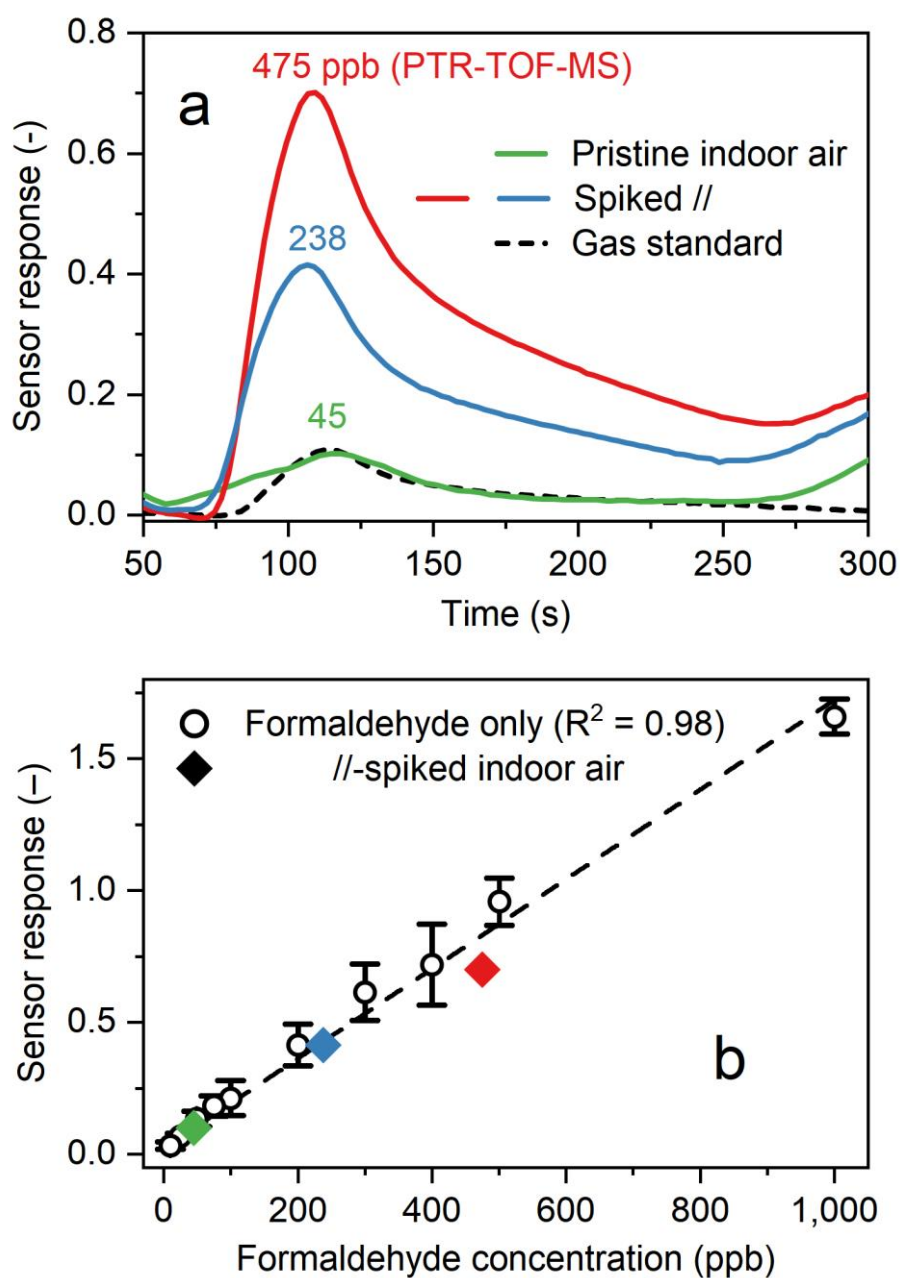


Figure E.7: (a) Response of the formaldehyde detector when sampling pristine indoor air (green) with a formaldehyde concentration of 45 ppb as determined by proton-transfer-reaction time-of-flight mass spectrometry (PTR-TOF-MS). Exposing the detector to the same formaldehyde concentration from the calibrated gas standard in synthetic air (black dashed) results in an identical response. Indoor air spiked with higher formaldehyde concentrations of 238 (blue) and 475 ppb (red) results in increased sensor response. (b) Formaldehyde sensor responses to formaldehyde only (circles) and to formaldehyde-spiked indoor air (diamonds). Colors of diamonds correspond to measurements shown in (a).

Curriculum Vitae

Jan van den Broek

September 16th 1990, born in Luzern, Switzerland, married.

Education

- 2020 *PhD* in Mechanical Engineering, ETH Zürich, Switzerland. Title: “Highly selective flame-aerosol-made gas sensors enabled by particle-based filters” at the Particle Technology Laboratory, Advisor: Prof. S.E. Pratsinis.
- 2015 *MSc*, Materials Science, ETH Zürich, Switzerland. Title: “All-solid-state Li-ion batteries based on garnet-type fast Li-ion conductor $\text{Li}_7\text{La}_3\text{Zr}_2\text{O}_{12}$ ” at the Electrochemical Materials Group, Advisor: Prof. J.L.M. Rupp.
- 2012 *BSc*, Materials Science, ETH Zürich, Switzerland.
- 2009 *Abitur*, Kantonsschule Luzern, Switzerland.

Experience

- 2020– Co-founder and CTO, Alivion AG, Switzerland.
- 2017– Research Associate & Teaching Assistant, Particle Technology Laboratory, ETH Zürich, Switzerland.
- 2016 Research Assistant, Electrochemical Materials, ETH Zürich, Switzerland.
- 2013–2015 Teaching Assistant, ETH Zürich, Switzerland.
- 2013 Industrial Internship (3 months), Sensirion, Zürich, Switzerland.
- 2012 Industrial Internship (6 months), RUAG Space, Zürich, Switzerland.
- 2009–2012 Part-time Job, Xinventa, Luzern, Switzerland.
- 2009 Industrial Internship (2 months), ABB Corporate Research, Baden, Switzerland.

Awards

- 2021 Best Poster Award, Chemical Sensors for Wearable Devices, March 3, Haifa, Israel.
- 2021 Fellow of the Global Young Scientist Summit, Jan. 12–15, Singapore.
- 2019 Best Poster Award for Exposure Measurement Methods and Techniques, European Aerosol Conference, Aug. 25–30, Gothenburg, Sweden.
- 2016 Zuger Science Award (2nd place) for outstanding master theses of distinguished inventions, Zug, Switzerland

Publications and Presentations

Refereed Publications

12. Pineau N., Magro L., van den Broek J., Güntner A.T., Pratsinis S.E., “Spirit distillation: Monitoring methanol formation with a hand-held device”, *ACS Food Sci. Technol.*, 1, 839-844, (2021).
11. van den Broek J., Weber I.C., Güntner A.T., Pratsinis S.E., “Highly selective gas sensing enabled by filters”, *Mater. Horiz.*, 8, 661-684, (2020). *Invited review article.*
10. Güntner A.T., Magro L., van den Broek J. and Pratsinis S.E., “Sniffing Methanol in Hand Sanitizers”, *iScience.*, 24, 102050, (2020).
9. van den Broek J., Bischof D., Derron N., Abegg S., Gerber P., Güntner A.T., Pratsinis S.E., “Screening methanol poisoning with a portable breath detector”, *Anal Chem.*, 93, 1170-1178 (2020).
8. van den Broek J., Cerrejon Klein D., Pratsinis S.E. and Güntner A.T., “Selective formaldehyde detection at ppb in indoor air with a portable sensor”, *J. Hazard. Mater.*, 399, 123052, (2020).
7. Abegg S., Magro L., van den Broek J., Pratsinis S.E. and Güntner A.T., “A pocket-sized device enables detection of methanol adulteration in alcoholic beverages”, *Nature Food*, 1, 351-354, (2020).
6. van den Broek J., Abegg S., Pratsinis S.E., Güntner A.T., “Highly selective detection of methanol over ethanol by a handheld gas sensor”, *Nature Commun.*, 10, 4220, (2019).
5. Afyon S., Kravchyk K.V., Wang S., van den Broek J., Hänsel C., Kovalenko M.V., Rupp J.L.M., “Building better all-solid-state batteries with Li-garnet solid electrolytes and metalloid anodes”, *J. Mater. Chem. A*, 7(37), 21299, (2019)
4. van den Broek J., Güntner A.T., “Highlights of Analytical Sciences in Switzerland: Analyzing breath with chemical sensors”, *CHIMIA*, 72, 425 (2018). *Invited feature article.*
3. van den Broek J., Güntner A.T., Pratsinis S.E., “Highly selective and rapid breath isoprene sensing enabled by activated alumina filter”, *ACS Sens.*, 3, 677-683, (2018).
2. van den Broek J., Rupp J.L.M., Afyon S., “Boosting the electrochemical performance of Li-garnet based all-solid-state batteries with Li₄Ti₅O₁₂ electrode: Routes to cheap and large scale ceramic processing”, *J. Electroceram.*, 38, 182, (2017). *Invitation for special issue.*
1. van den Broek J., Afyon S., Rupp J.L.M., “Interface-engineered all-solid-state Li-ion batteries based on garnet-type fast Li⁺ conductors”, *Adv. Energy Mater.*, 6(19), 1600736, (2016).

- van den Broek J., Mochalski P., Königstein K., Wang C., Unterkofler K., Schmidt-Trucksäss A., Mayhew C.A., Güntner A.T., Pratsinis S.E., “Portable breath isoprene detector validated during exercise and at rest”, *submitted*.

Patent Applications

1. Pratsinis S.E., Güntner A.T., van den Broek J., Abegg S., DE2019011109582800, 11/1/2019.

Press Release

- 2020 Swiss National Television (SRF) show 10vor10 (in German) on handheld detector for screening of methanol-adulteration:
<https://srf.ch/play/tv/redirect/detail/e1a07460-41be-44a6-b417-31eaf172b596>
- 2020 Nachrichten aus der Chemie article (in German) on sniffing methanol in breath and beverages:
<https://onlinelibrary.wiley.com/doi/full/10.1002/nadc.20204095027>
- 2019 Research highlight in ETH News and DerStandard on measuring methanol by a portable detector:
<https://ethz.ch/en/news-and-events/eth-news/news/2019/09/measuring-methanol.html>
<https://www.derstandard.de/story/2000108697019/wie-man-mit-methanol-gepanschten-alkohol-aufspuert>
- 2016 Research highlight in ETH News and NZZ am Sonntag on all-solid Li-ion batteries:
<https://ethz.ch/content/main/en/news-und-veranstaltungen/eth-news/news/2016/08/festkoerper-lithium-ionen-akku.html>
http://www.electrochem.mat.ethz.ch/news_events/NZZamSonntag_16102016_Geht_das_auch_ohne_Feuer.pdf

Oral Presentations

5. “Selective breath isoprene detection by filter-enhanced sensors”, *International Meeting on Chemical Sensor (virtual)*, USA (30/5–3/6/2021).
4. “Compact formaldehyde detector based on filter–sensor system with validated performance in indoor air”, *International Meeting on Chemical Sensor (virtual)*, USA (30/5–3/6/2021).
3. “Rapid diagnosis of methanol poisoning with a handheld detector”, *International Meeting on Chemical Sensor (virtual)*, USA (30/5–3/6/2021).
2. “Isoprene selective gas sensing by adsorption filter”, *International Meeting on Chemical Sensor*, Vienna, Austria (15–19/7/2018).
1. “Highly Selective and Rapid Breath Isoprene Sensing Enabled by Activated Alumina Filter”, *Zürich Exhalomics Workshop*, Zürich, Switzerland (27/2/2018).

Poster Presentations

7. “Handheld methanol and formaldehyde detectors enabled by adsorption filter”, *Chemical Sensors for Wearable Devices (virtual)*, Haifa, Israel (3/3/2021). Best Poster Award.

6. “Toxic methanol detection by handheld filter–sensor device”, *European Aerosol Conference*, Gothenburg, Sweden (25–30/8/2019). EAC Best Poster Award for Exposure Measurement Methods and Techniques.
5. “Selective isoprene sensor for air quality monitoring”, *European Aerosol Conference*, Gothenburg, Sweden (25–30/8/2019).
4. “Cholesterol monitoring with breath isoprene sensor?”, *Fall Meeting of the Material Research Society*, Boston, USA (25–30/11/2018).
3. “Highly selective and rapid breath isoprene sensing enabled by activated alumina filter”, *International Association of Breath Research Summit*, Maastricht, Netherlands (17–20/6/2018).
2. “Breath isoprene monitoring by highly selective filter–sensor system”, *ETH Zürich’s MaP Graduate Symposium*, Zürich, Switzerland (26/6/2018)
1. “Low temperature synthesized-processed garnet-type fast Li-ion conductor, $\text{Li}_{6.25}\text{Al}_{0.25}\text{La}_3\text{Zr}_2\text{O}_{12}$ for all solid state Li-ion batteries”, *The 31st PSI Electrochemistry Symposium*, Baden, Switzerland (6/5/2015)